2018 Florida Conference on Recent Advances in Robotics

May 10~11 at the University of Central Florida, Orlando

Invited Speakers

Roger Smith, PhD, Florida Hospital

Richard Davis, KUKA Robotics

Evan Herndon, Lockheed Martin

Dwayne McDaniel, PhD, Florida International University

Melissa Morris, PhD, Florida Polytechnic University

Christina Drake, PhD, Florida Polytechnic University

Jason Schuler, Kennedy Space Center

Organizers

Chair: Sang-Eun Song, PhD, University of Central Florida

Coordinator: Yaela Marks, PhD, University of Central Florida

Event Photographer: Pradipta Biswas, PhD student, UCF

Website and Proceeding Archive

URL: http://mae.ucf.edu/fcrar2018/

Website Designer: Michael Morris, Denise Tjon Ket Tjong

Faculty Reviewers

Doyoung Chang, PhD, University of Miami Miller School of Medicine

Hossein Dehghani, PhD, University of Central Florida

Christina Drake, PhD, Florida Polytechnic University

Qiushi Fu, PhD, University of Central Florida

Oren Masory, PhD, Florida Atlantic University

Melissa Morris, PhD, Florida Polytechnic University

Mehrdad Nojoumian, PhD, Florida Atlantic University

Zvi Roth, PhD, Florida Atlantic University

Lara Sharp, PhD, St. Petersburg College

Gita Sukthankar, PhD, University of Central Florida

Gloria Jean Wiens, PhD, University of Florida

Hanqi Zhuang, PhD, Florida Atlantic University

Sponsors

Florida Space Grant Consortium

Kuka Robotics

College of Engineering and Computer Science

UCF | **College of Engineering and Computer Science** — UNIVERSITY OF CENTRAL FLORIDA

NASA FLORIDA SPACE GRANT CONSORTIUM

KUKA

Table of Contents

Models and Framework for Supporting Humanoid Robot Planning & Exploration

Ahmad Hasanain, Troy Weekes, Michael Person, Kepinski Paul, Yonghui Chang, Aaron Rothman,
Zhu Rui, Rajaa Rahil, Muntaser Syed, Chris Wodd, Marius Silaghi
Florida Institute of Technology

ABSTRACT

While the Nao humanoid is among the most advanced intelligent robots accessible to the global public, it lacks high level support for advanced intelligent walking activities. The robot has remarkable low level intelligence embedded into itself, such as artificial life with breath motions, and reasonable situation awareness with human face recognition and tracing. It also has motion control support in terms of unreliable distance or velocity-based commands for walking. However, building high level intelligent applications on such robots still requires significant research and effort. In this work we propose a framework of Artificial Intelligence (AI) models that create a platform for easy high level tasks specification and implementation. The models are trained using a Nao humanoid undergoing experimentation and the results are evaluated based on a set of high-level tasks implemented with standard AI algorithms. The models are described, as well as the test-beds and benchmarks used for their evaluation. The work proves the large potential that humanoids hold in the area of applications offering human support in daily activities.

Keywords: Humanoid, framework, model, AI, Nao.

1. Introduction

In this work we propose a probabilistic model for addressing the Nao humanoid robot non-deterministic actions and sensors. These models are designed for integration with high level artificial intelligence techniques, usable for advancing towards a long term goal of providing a software architecture for supporting Nao's motion and localization activities for general tasks.

A plethora of robotic hardware and test-beds are available for educational, research, and application opportunities. However, while the Nao humanoid robots are among the most advanced widely available robots for household applications, there is a lack of widely available software for supporting it in high level intelligent activities. This may be explained in part by the uncertainty introduced due to the significant non-determinism in walking actions presented by the Nao robot. Each single movement command and corresponding localization with respect to the base introduce errors of dozen of degrees in rotation, and dozens of centimeters in translation. Such errors can be compensated with inputs from sensors such as sonars and vision, but sonars have high unreliability themselves, and the vision needs reliable landmarks as well as previous knowledge about these landmarks. While the robot has two cameras, they are not configured from factory for usage as a stereo rig, being oriented in different directions and lacking synchronization of capture.

The Nao robot is a humanoid robot that is designed to serve as a human companion and can sustain well household environments.

Figure 1. The benchmark setting: mazes with landmarks.

While its relatively small dimensions limit its usability for tasks requiring strength or height and dexterity, it is well adapted to home, hospital, and office environments to provide, for example, entertainment and emergency support for children and seniors. While its communication and emotional intelligence is meeting many expectations, its movement and ability to localize with standard software is reduced, and insufficient for most other tasks. A number of research efforts have led to the description of successful applications of *simultaneous localization and mapping* (SLAM) to certain tasks such as wall following in mazes and localization in spaces filled with landmarks [1]. However there is a lack of general software packages applicable to new scenarios. In this work we take a step towards designing such a general mapping and localization support software architecture.

After introducing a benchmark problem based on mazes with landmarks (Figure 1), and reviewing some of the related work, the rest of the paper details the definition and training of probabilistic models for the Nao sonars and visual landmark localization. These probabilistic models are being tested by integration into particle-filtering based SLAM reasoning or partially observable Markov decision process (POMDP) formulation of planning problems. These are significant building blocks for the software architectures that we plan de address. Preliminary experimental results are presented before the conclusions.

2. Problem Formalization

The problem is described by a grid of $m \times n$ cells where some of the separating walls are missing, creating a maze. This can be formalized as two Boolean matrices $H_{m+1,n}$, and $V_{m,n+1}$, where in our example above, $m = 4$ and $n = 4$. The matrix $H_{m+1,n}$ with $m+1$ rows and n columns specifies the presence of separating walls between east-west neighboring cells. The matrix $V_{m,n+1}$ specifies the presence of separating walls between north-south neighboring cells. The functions $h : [1..m+1] \times [1..n] \times \{S,N\} \to \mathbb{N}$ and

Figure 2. The shape of a maze used in experiments, in ASCII representation.

Figure 3. Landmark examples, each consists of a unique integer conveyed in the NAOmarks pattern.

$v : [1..m] \times [1..n+1] \times \{E,W\} \to \mathbb{N}$ assign a distinguishing label to each wall, corresponding to the elements in $H_{m+1,n}$ and $V_{m,n+1}$, respectively. The image of the functions h and v is not defined on inputs where $H_{m+1,n}$ and $V_{m,n+1}$ are false, respectively. The sets $\{S,N\}$ and $\{E,W\}$ specify the sides of the wall whose label is considered: *south, north, east,* and *west*, respectively. The image of the function can be a special pattern recognizable by a classifier, or something as simple as a NAOmark label. In an extreme case, where there is no distinguishing information between walls, the image of the two functions would consist in a single value.

A robot is placed in this maze in a potentially unknown original position and has to learn the elements H, V, h, and v. The robot can move with non-deterministic actions inducing transition probabilities that can be modeled as Gaussian. It also has noisy sensors that can detect H and V (sonars) or v and h (vision).

The position π of the robot at a moment in time is jointly defined by a maze cell (i,j) with $i, j \in [1..m] \times [1..n]$, as well as a position and orientation in the cell defined with respect to its south-west corner (x, y, θ).

The past trajectory of the robot, acts as a weight gauging the confidence of the robot in particular components of the belief. The trajectory can be maintained with various levels of detail. The a temporal trajectory of the robot is defined as a Boolean matrix $T_{m,n}$, where elements are set to true for maze cells that have been visited in the past.

A belief concerning the structure of the maze and position of the robot is a probability distribution b over the complete set of possible data structures T, H, V, h, v, and π.

For mapping or SLAM problems in this setting, the above data structures, namely H, V, h, and v, as well as the belief concerning the final position of the robot, are requested outputs while the inputs may consist in:

- values for *m* and *n*,

- specification of landmarks for distinguishing walls (e.g., NAO marks at 1/2 size)

- dimensions for cells (e.g., $21in \times 21in$), as well as

- a belief regarding the current position of the robot in the described space.

The task is to have a mobile robot explore and localize itself within a maze. The map of the maze is assumed initially unknown to the robot other than that it consists of cells, which are analogous to rooms or parts of rooms in an office environment, and the cells' shapes are in a predefined finite set of possibilities. For simplicity, the cells shapes are assumed empty squares with 53.34cm sides, each being possibly a wall/object as depicted in Figure 2.
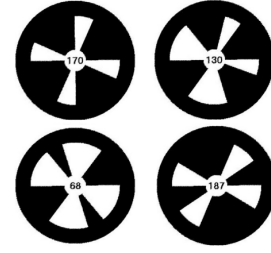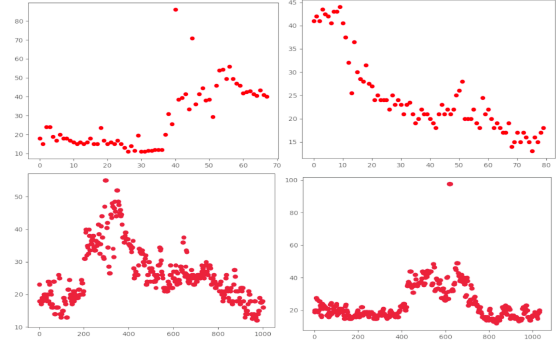

Figure 4. Probabilistic Sonar Model.

3. Nao5 Robot Specifications

Our experiments, and corresponding probabilistic models obtained for sensors and actions, are constructed with a Nao robot at version 5. This robot boasts 2 sonars on the chest, bumpers on the feet, and two cameras placed vertically on the face. Nao has multiple other sensors in its actuators. The sonars and landmark recognition modules have significant noise, as highlighted by the described experiments. The landmarks utilized, which require the software to only be informed about their size, are recognized by the built-in ALLandMarkDetection software package, and are shown in Figure 3. The package provides an estimate for the abscissa, ordinate, and projection angle of the smallest line of sight relative to the robot's camera and the NAOmarks. Furthermore, adjusting the yaw of the head and joints of the limbs can be performed with high accuracy, but walking and turning have significant error.

4. Probabilistic Sensor Model

Measurements of the Nao sensors response as a function of the distance between the Nao torso and walls, are shown in Figure 4. Sonar readings are taken while the robot is rotating its body 360°. In each image in the Figure 4, the robot was placed in the same cell but with different position and angle. The sonar reading are in cm in the y-axis, while the x-axis is in a unit of time, which is proportional to the robot's body rotational angle captured uniformly while the robot motion was active.

Although the robot was supposed to take 360° (degrees) to turn around, it usually needs approximately 390°. Consequently, the direct scattering of these distance readings in an x-y plane is apparently not straightforward. The x- and y- axes in the Figure 6 are in cm. The motion started when the robot was exactly facing the positive x-axis and ended around the axis. Notice that the initial distance to the wall was 10cm while it landed at 15cm from the same wall.
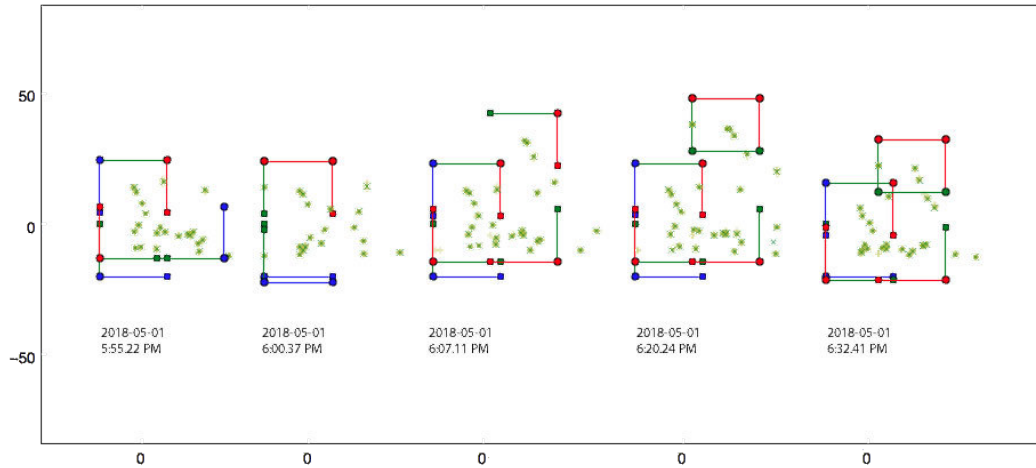
31st Florida Conference on Recent Advances in Robotics, May 10-11, 2018, University of Central Florida, Orlando, Florida

2

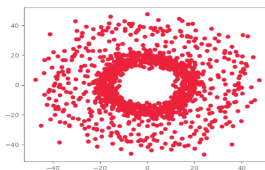**Figure 5.** The localization results of five tests.

Figure 6. Shape of sonar signal during robot rotation.

Based on such measurements, statistics are used for training a probability distribution of the sensor readings with respect to wall distance.

5. Landmark Detection Models

A visually based localization algorithm is proposed which utilizes a probabilistic sensor fusion approach. On-board the humanoid Nao robot are a stereo camera and two sonars. The Nao is preprogrammed to perform an image space search for NAOmarks, seen in Figure 3, and provide the vector separating the Nao robot from the marker. However, it is unknown what the underlying algorithm for this search is and it also provides noisy measurements, most likely due to its required generalizability to all scenarios. A naive approach to reduce the uncertainty due to the noise of the Nao's built-in localization would be to form an estimator of the true value by forming a sample and computing the expected value. The sample variance could also be computed to act as an error bound for the estimator. In any case, it is inconvenient to form a large enough sample required to place small enough bounds on the error.

An improvement is proposed, as follows. The robot is surrounded by at most three Nao marks if a wall is present. The Nao captures images using both camera's of what is directly in front of it. The images are then rectified using the known camera intrinsics and then the epipolar lines are searched to compute the stereo pair's disparity map. The disparity map is then mapped to a depth map using the camera extrinsics. This depth map provides two purposes; the first is to augment each pixel location with a depth value and also to create a Cartesian 3D point cloud using the camera's Projection matrix.

Next the reference camera's image is passed through the Hough Circle Transform to retrieve any possible circular like regions of interest (ROI) in the image. In order to separate out the NAOmarks

from this noisy set of ROI's, a Histogram of Oriented Gradients (HOG) feature vector is extracted from each region. Each ROI's feature vector is passed through a binary Support Vector Machine (SVM) to classify whether the ROI is a Nao mark or an extraneous detection. After the true Nao mark pixel locations have been identified, the mean depth for each mark is computed from the depth map and the mean offset, in both axis, is computed using the point cloud.

This provides a set of vector's to any potential Nao markers in the Nao's current field of view. During this processing time, samples from the Nao's application programming interface (API) have been collected and stored to be used later. If any Nao marks have been found, the sonar values are also aggregated. Although the sonar measurements will not directly pick up the Nao mark, they will pick up the distance to the wall it is placed upon. Finally we have a set of three different measurement types; our own visually based set of vectors, a set of Nao API based vectors, and a set of sonar radial distance measurements. The expected value of these three sets are then computed however each set has a different probability associated with it. We place a probability of 50% to our own measurement, a probability of 30% to the Nao API's sample mean, and finally a probability of 20% to the sonar depth measurement. This expected value performs a fusion on the three different sets of data to provide a more accurate localization than a single stream of data alone.

The process is then repeated with the Nao's head turned left and right. This eliminates the data stream from the sonar's however this is the more optimal solution to having Nao's entire body turn which introduces motion noise in addition to sensor noise.

6. Motion Planning

The Nao robot has a significant amount of noise in it's movements. The noise is primarily attributed to the asynchronicity of it's different operational threads; thus, making the Nao an ideal robot for developing probabilistic models. The first step in developing any autonomous capabilities of the Nao is creating an accurate motion model. In order to simplify the transition model, a priori knowledge of the maze and the Nao is used to reduce the set of possible transitions. For example, the Nao will be assumed to not be able to move in the direction opposite to the command. Since the location the Nao will occupy in a single cube is continuous, the position is

31st Florida Conference on Recent Advances in Robotics, May 10-11, 2018, University of Central Florida, Orlando, Florida

3

discretized into a four by four grid of possible locations the Nao could occupy. This discretization reduces the complexity of the transition model. The transition between the Nao going from one cube to another can be seen in Figure 7. The Nao is marked with a red circle, the current discretized cube is shown in green and the set of possible states it can transition to are shown in blue. The blue region extends past a single cube because its non-deterministic motion model allows for a small probability to pass beyond its given command.

In order to help decrease uncertainty that the Nao has moved to the expected location of the transition model, a NAOmark was located in the cell that the transition is set to move into. When the Nao is ready to move, it will lock with the NAOmark and gather readings continuously while transitioning into the next cell. The readings consist of x, y, z positions from the marker as well as rotation along each axis which can be converted to angles of view of the NAOmark. These angles of view allow the Nao to align perpendicularly to the NAOmark it has a lock onto. From there, the next set of readings can be taken to localize in that cell. The results of five tests are illustrated in Figure 5. It is assumed that there will be 2 or 3 NAOmarks in each cell, having distinct numbers within the cell; however, other cells in the maze can contain NAOmarks with the same number. It is also assumed that each NAOmark is placed in the center of a wall; with this known and the length of a single wall known, using just the sensor readings, the Nao can position itself very close to the center of the cell during transition. This can be used as input motion model to the Sequential Monte Carlo Method described in the next section.
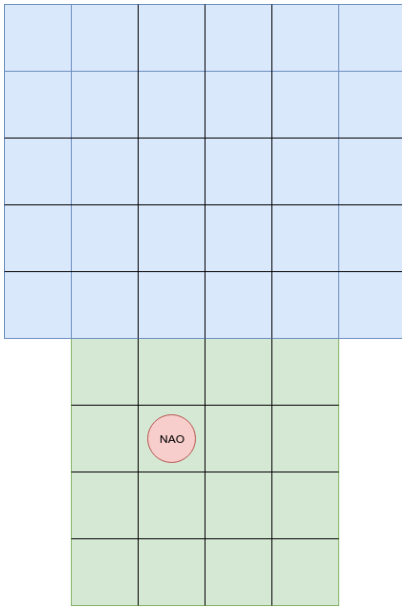

Figure 7. Transition of the Nao from one cell to another

7. Sequential Monte Carlo Method

The Kalman Filters are a powerful class of algorithms commonly used for a variety of probabilistic tasks [2]. However, they have strong requirements for both Gaussian distributions and linear models. In order to address these stringent limitations for real world applications, Extended Kalman filters and Unscented Kalman filters were introduced, allowing for the use of non-linear models [3, 4]. However, many applications cannot be assumed to be Gaussian,

making the Kalman Filter family of algorithms unsuitable. For example, skewed normal distributions also appear in several applications. On the other hand, the Sequential Monte Carlo Method, or Particle Filter, is a robust probabilistic method that is able to deal with any distribution and non-linear transitions. Although there is no general proof of convergence for particle filters, they empirically provide accurate results with much less time complexity. For our applications, particle filters will be used for both localization and for Simultaneous Localization and Mapping (SLAM).
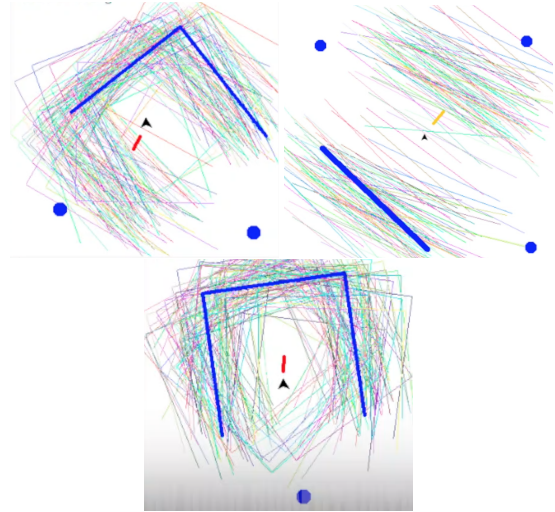

Figure 8. Particle filtering for Monte-Carlo Localization in a maze cell. The thick line represents a generated hypothesis whose attributes are proportional to the arithmetic mean of the population of the hypotheses.

For Monte Carlo localization, particles described by specific hypotheses (H, V, h, v, π), are generated and weighted according to the likelihood of the evidence (i.e. history of sensor readings) in the corresponding world. The robot first considers all possible world cases, in which the robot may be placed. The hypotheses space is weighted after each sensor reading taken after a robot motion. While the hypotheses are weighted, new particles are generated (resampled) according to the new weight distribution. In our settings, a particle directly conveys the state of the world as oppose to the state of the robot in the world, and thus the shape of the cell, in which the robot is, is one of the discrete parameters that a particle can describe. The other attributes, such as the x- and y- axes as well as the rotation of the hypotheses, have continuous dimensions. Since the Nao's sensors behave differently when the sensed objects are closer than 20cm, a Boolean distance measure sets the weights of the particles that match to a corresponding value (e.g., 0.5). Additionally, the particles whose features are beyond the hypothesis space are regenerated. Finally, a constant weight (e.g., 10 percent) is given to particles that have not been observed by the sensor model, to preserve the unseen hypotheses unless particles with very high certainty emerge in the hypothesis population.

Figure 9 depicts three iterations during a Monte Carlo Localization search in a situation when the robot is rotating in a single cell. Each assembly of same-color lines resembles a particle. The number of particles in each conducted experiment is 3000, and a momentum was added to the weights to compensate for the first degree Markov transition assumption. The later the iteration number, the more aligned the particles are, as can be seen in Figure 9. The thick blue lines, in the figure, resemble a particle whose placement was at the arithmetic means of the continuous attributes of
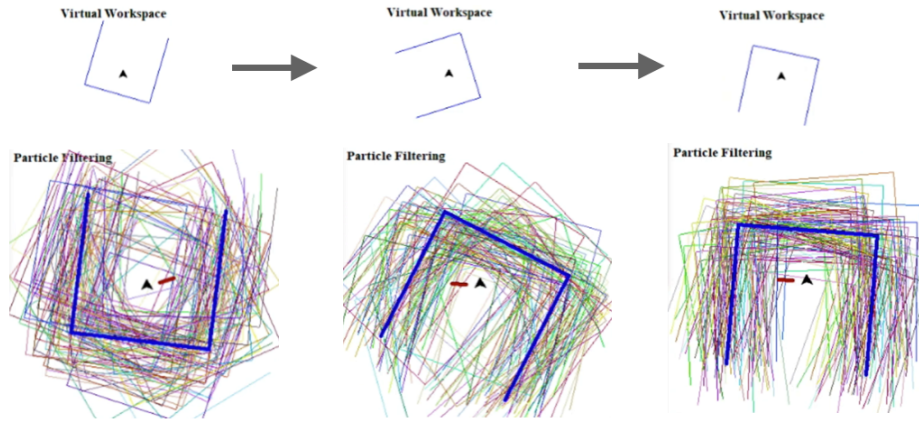
31st Florida Conference on Recent Advances in Robotics, May 10-11, 2018, University of Central Florida, Orlando, Florida

4

Figure 9. Particle filtering for Monte-Carlo Localization in a maze cell. The first row shows three iteration states. Time is illustrated from left to right, and the second row presents the particles in the three states.

the 3000 particles. The only discrete attribute is the shape of the cell; therefore, the shape of the resulting hypothesis is the shape of the majority of the particles. The module gave consistent results as the shape of the cell differed. Figure 10 portrays two other examples, from left to right, when the number of walls modeled by the particles was one and three respectively. Our configurations allow for more complex settings than the assumed simple squared cells. The stopping criterion of our algorithm was when 99% of the population had the same shape; hence, the convergence of the particles. The configuration with two parallel walls was also tested. The large blue and green discs picture the centers of the adjacent cells to which the robot could move. The module was backed by the breadth-first shortest path search and a database that records the cells and passages which were visited and found.
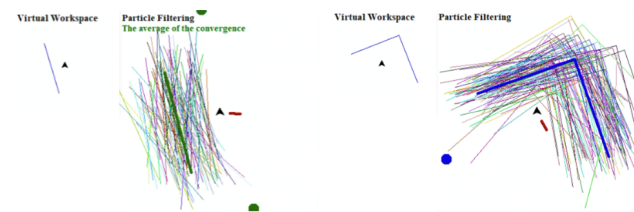

Figure 10. Two examples of the particle-filtering-based localization when the number of cell sides vary.

8.   Related Work

The problem of simultaneous localization and mapping (SLAM) for a Nao robot placed in a room with multiple Nao marks placed at random locations, at the height of the cameras of Nao, was addressed in [1]. The effort led to new SLAM approaches for real-time incorporation of new landmarks in exploration.

Probabilistic reasoning for localization has been used with mobile robots to address various types of problems. If the map of the explored world is known, then Monte Carlo Localization can employ particle filtering [5].

Motion planning in partially observable non-deterministic environments of this type can be modeled with Partially Observable Markov Decision Processes (POMDPs), for which various techniques have been proposed to tame the complexity challenges. All

these techniques can employ a dynamic belief network representation of the problem [6].

9.   Conclusion

In this work we build a probabilistic model of the humanoid robot Nao sensors and actions, enabling the application of high level intelligent algorithms for tasks such as localization, mapping, and planning. Preliminary results are described and several compact methods of representation that enable efficient reasoning were developed.

The Nao robot is found to have significant non-determinism in walking and rotation actions. Additionally, its sonar sensors have significant noise and built-in visual NAOmark landmark detection shows noise that increases when the head's yaw rotational angles are larger than 80 degrees. The proposed models can be used in POMDPs and SLAM solvers.

References

[1] Y. Zhang, *Real-time SLAM for Humanoid Robot Navigation Using Augmented Reality*. PhD thesis, Applied Sciences: School of Mechatronic Systems Engineering, 2014.

[2] R. E. Kalman, "A new approach to linear filtering and prediction problems," *Transactions of the ASME–Journal of Basic Engineering*, vol. 82, no. Series D, pp. 35–45, 1960.

[3] N. J. Muga and A. N. Pinto, "Extended kalman filter vs. geometrical approach for stokes space based polarization demultiplexing," *IEEE/OSA Journal of Lightwave Technology*, vol. 33, pp. 4826–4833, December 2015.

[4] E. A. Wan and R. V. D. Merwe, "The unscented kalman filter for nonlinear estimation," pp. 153–158, 2000.

[5] S. Thrun, D. Fox, W. Burgard, and F. Dellaert, "Robust monte carlo localization for mobile robots," *Artificial intelligence*, vol. 128, no. 1-2, pp. 99–141, 2001.

[6] S. J. Russell and P. Norvig, *Artificial intelligence: a modern approach*. Malaysia; Pearson Education Limited,, 2016.

[7] N. d. F. . N. G. Arnaud Doucet, ed., *Sequential Monte Carlo Methods in Practice*. Springer, 2001.

31st Florida Conference on Recent Advances in Robotics, May 10-11, 2018, University of Central Florida, Orlando, Florida

5

A Nondestructive Autograft Extraction Method for Autologous Osteochondral Transplantation

Pradipta Biswas, Sakura Sikander, Pankaj Kulkarni, Christopher Clifford, Sang-Eun Song

Department of Mechanical and Aerospace Engineering
University of Central Florida
Orlando, Florida

pvbiswas@knights.ucf.edu, sakura@knights.ucf.edu, pankajpkulkarni@knights.ucf.edu, chris.e.clifford@knights.ucf.edu,
s.song@ucf.edu

ABSTRACT

Osteoarthritis is the degeneration of articular cartilage and subchondral bone, often leading to pain, joint stiffness, and disability. Post Traumatic Osteoarthritis (PTOA) develops after a joint injury. Such injuries can damage the articular cartilage and/or the bone, changing the mechanics of the joint and making it wear out more quickly. Mosaicplasty is a well-established technique for cartilage repair for osteochondral cartilage transplantation for PTOA. Due to current technological limitations, harvesting large grafts is not practical. The success of harnessing a larger and complex shaped graft to replace the damaged osteochondral area lies in effective extraction of the cartilage-bone graft from the donor site. Currently, no method exists to perform this procedure. So, we have proposed a novel bone removal mechanism to harvest a personalized autologous graft irrespective of its shape and size. Our method involves drilling/milling the profile around the region of interest from a non-weight bearing site according to the damaged cartilage profile and slicing off the bottom part of the graft from the bone using a flexible string saw approach like Gigli saw used for bone amputation. We have designed a mechanism which inserts the flexible saw parallel to the transverse plane and slices the graft parallel to the coronal plane to extract the graft.

Keywords

Osteoarthritis, Autografting, Osteochondral Cartilage, Post Traumatic Osteoarthritis, Mosaicplasty, Cartilage Extraction.

1. INTRODUCTION

Osteoarthritis (OA) is the degeneration of articular cartilage and subchondral bone, often leading to pain, joint stiffness, and disability [1]. It is a well-known degenerative joint disease characterized by biochemical and molecular changes within the tissue that result in progressive erosion of the articular cartilage [2]. For more than 90% of the cases, there is no apparent etiology or initial cause for the disease and there appears to be a direct relationship to aging. This form of the disease is known as primary osteoarthritis. When the disease occurs in younger patients with a specific cause like traumatic injury or systemic metabolic disorders like obesity, then it is referred to as secondary osteoarthritis. Age-dependent changes in extracellular matrix components result in decreased mechanical strength and resiliency of the cartilage tissue.

Although the relationship to age and traumatic injury has often led to the oversimplification of the disease as a function of "wear and tear", research has shown more complex cellular pathogenesis. Post Traumatic Osteoarthritis (PTOA) develops after a joint injury. The injury may be in the form of fracture, cartilage damage, acute ligament sprain, or chronic ligamentous instability (or combination of these) [1]. Such injuries shown in Figure 1 can damage the articular cartilage and/or the bone, changing the mechanics of the joint and making it wear out more quickly.

Figure 1. Graphical representation of osteochondral (bone and cartilage) damage/osteoarthritis [3]

Mild PTOA can be treated with weight loss, low impact exercise, strengthening of the muscles surrounding the joint, and non-steroidal anti-inflammatory medicines. Arthritic joints can also be injected with corticosteroids to decrease inflammation or with hyalgan, which acts like an artificial joint fluid. These measures provide symptomatic relief but do not slow down or reverse the cartilage damage. Nearly 27 million adults aged 25 or above have a clinical diagnosis of OA [4]. Among those, PTOA affects 5.6 million people and is the cause of about 12% of osteoarthritis of the hip, knee, and ankle in the United States [5]. When osteoarthritis progresses to the point that conservative measures are no longer effective, then surgical treatments are often performed. Surgical treatment may include debriding, reconstructing, or replacing the worn out joint surfaces. There are numerous surgical procedures aimed to repair or regenerate osteoarthritic lesions which include microfracture, autologous osteochondral cylinder transplantation (mosaicplasty), artificial bone graft substitutes and cell-based repair techniques such as autologous chondrocyte implantation (ACI)[6]–[8]. Compared to mosaicplasty, ACI is more expensive,
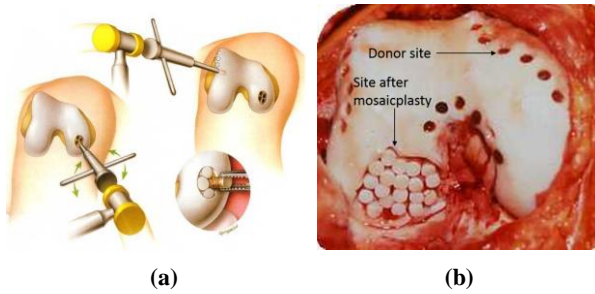
Figure 2. (a) Steps in mosaicplasty and (b) site after mosaicplasty [9].

requires two procedures and an open arthrotomy [10]. The microfracture technique is typically used for small defect areas while osteochondral transplantation is used for larger cartilage defects [6] and has advantages over microfracture.

For osteochondral transplantation, plugs of healthy cartilage with subchondral bone are extracted either from the joints of a cadaver (allografts) or from a non-load bearing area of the patient (autografting) and inserted into the arthritic defect (in case of mosaicplasty) shown in Figure 2 (a) and (b). Unlike allografts osteochondral autograft transplantation (OAT) uses the patient's own tissue eliminating any risk of infectious disease transmission [11]. Both cartilage and bone are harvested from the donor site, so OAT has the advantage of filling osteochondral defects, making OAT an option in treating smaller osteochondritis dissecans lesions [12].

For mosaicplasty, combination of grafts are able to resurface 80-100% of the damaged area [12]. Although, mosaicplasty is a well-established technique for cartilage repair, due to current technological limitations, harvesting large grafts is not practical. The success of harnessing a larger and complex shaped graft to replace the damaged osteochondral area lies in effective extraction of the cartilage-bone graft from the donor site. Currently, no method exists to perform this procedure.

In this paper, we are proposing a novel bone removal mechanism to harvest a personalized autologous graft irrespective of its shape and size.

Figure 3. Commercially available Gigli saw which is less flexible

2. Method

There are two components to our approach: 1) milling the profile around the region of interest, and 2) extracting the graft by using the proposed mechanism. The path drilling/milling can be performed using orthopedic robots such as Robodoc [13], Acrobot [14], Caspar [15], Mako [16] or a bone attached orthopedic robot HyBAR [17]. Potential donor sites must be in non-weight bearing

areas. The difficulty in extracting donor grafts for autografting lies in separating the bottom surface of the graft from the donor site. This problem does not exist for allografting because the cadaver tissue can be completely sliced. To accomplish this, our mechanism involves converting the typical saw motion from the transverse plane to coronal plane. We have used the concept of Gigli saw approach often used for amputation. But we are avoiding commercially available Gigli saw (Figure 3) due to its less flexible property which will hinder sharp bending in the cylindrical guide that we are using in our device.

For the proposed method there are two challenges: 1) to insert the flexible saw parallel to the transverse plane and slice the graft parallel to the coronal plane, and 2) to deal with irregular shaped contour. To optimize the travel path for the saw while having
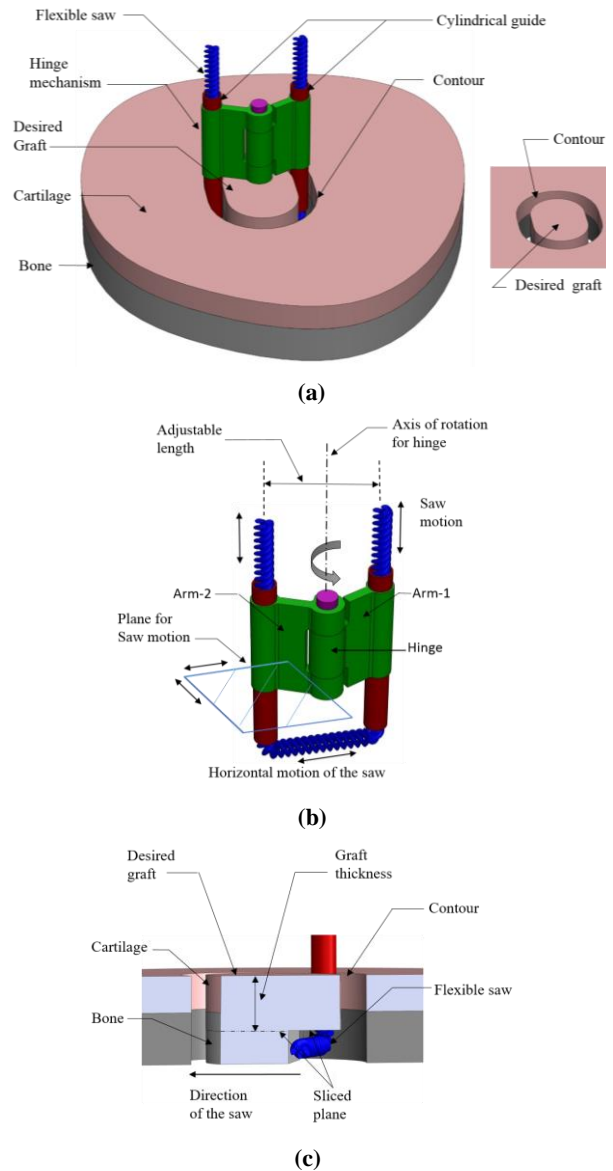

(a)

(b)

(c)

Figure 4. CAD model of (a) donor tissue removal setup, (b) detailed view of flexible string saw mechanism, and (c) cross-section of the donor tissue while being sliced.

31st Florida Conference on Recent Advances in Robotics, May 10-11, 2018, University of Central Florida, Orlando, Florida

7

motion parallel to coronal plane the strings must be parallel to each other throughout the procedure. To achieve the required motion configuration the saw is guided through two hollow cylindrical guides parallel to each other, as shown in Figure 4 (a). The two cylindrical guides are positioned along the contour path. These two cylinders are rigidly attached at the end of two arms which are linked with a hinge shown in Figure 4(b).

The hinge mechanism was used to allow varying distance between the two cylinders (Figure 4 (b)). Since the two arms of the guide can rotate about the hinge independent to each other the two cylinders can follow a complex shaped contour. This gives the flexibility to move the string saw along a contour with an irregular shape. It also ensures parallelism between the cylindrical guides at all time. It is important to have the two cylinders parallel to each other and perpendicular to the coronal plane (i.e. slicing plane) to follow the contour properly and extract a graft with a perpendicular edge. Since the receiving site has a perpendicular edge this will ensure a better fit for the extracted graft. The string saw will reciprocate in between guided cylinders and as a result, the bone will be sliced along the coronal plane as shown in Figure 4 (b) and (c). Figure 4 (c) shows how required thickness of the graft can be maintained if the string saw is reciprocating without changing the depth of its motion.
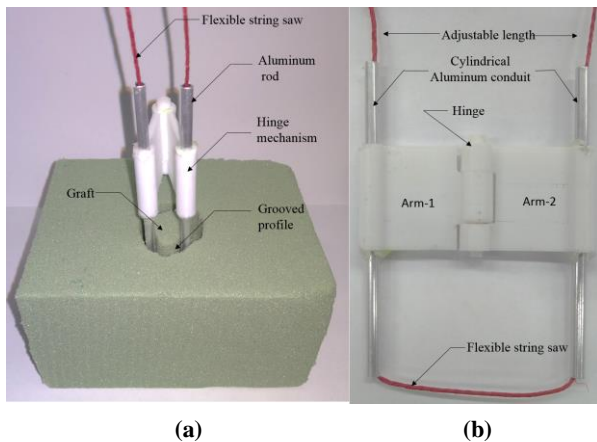
3. RESULTS

(a) **(b)**
Figure 5. A foam removal experiment using the prototype showing (a) experimental setup after precision milling of donor profile and (b) prototype device.

A proof-of-concept prototype was fabricated using a 3D printed arm-hinge mechanism and two aluminum conduits as a guide. A simple slicing experiment was performed on a floral foam using the prototype as shown in Figure 5 (a) and (b). The prototype could slice the desired thickness of graft producing a flat surface underneath, despite the profile being an irregular shape (e.g. non-circular, oval shape). It was possible to deal with an irregular profile and harness the graft because the hinge mechanism permitted the guides to move freely while remaining parallel, regardless of its shape.

4. DISCUSSION

The results show that the prototype can transfer reciprocating saw motion from the transverse plane to the coronal plane and harness a graft of desired thickness. At the same time the hinge mechanism including two arm provides the flexibility to guide the string saw along irregularly shaped profile. This new approach will enhance

current surgical techniques for osteochondral injuries and PTOA surgical treatments. This mechanism can be used for extracting hard tissue grafts of virtually any shape and size. A highly flexible string saw needs to be developed to operate in these confined areas and an optimized roughness of the string needs to be determined so that the grafts tissue doesn't deteriorate. This technology could enable precision hard tissue harvesting in various other surgical procedures. Future work will include development of a powered saw and integration with an orthopedic robot that removes damaged area and profiles autograft.

5. REFERENCES

[1] A. C. Thomas, T. Hubbard-Turner, E. A. Wikstrom, and R. M. Palmieri-Smith, "Epidemiology of Posttraumatic Osteoarthritis," *J. Athl. Train.*, vol. 52, no. 6, pp. 491–496, Jun. 2017.

[2] V. Kumar, A. Abbas, N. Fausto, and J. R. Aster,"Cotran pathologic basis of disease. 2010," *Saunders/Elsevier, 8th ed. P, vol. 784, 2010.*

[3] "Knee Arthritis Part Two, Pain by John Post, MD | Rock Star Triathlete Academy." [Online]. Available: https://rockstartriathlete.com/knee-arthritis-part-two-pain-by-john-post-md/. [Accessed: 04-May-2018].

[4] R. C. Lawrence *et al.*, "Estimates of the prevalence of arthritis and other rheumatic conditions in the United States. Part II.," *Arthritis Rheum.*, vol. 58, no. 1, pp. 26–35, Jan. 2008.

[5] T. D. Brown, R. C. Johnston, C. L. Saltzman, J. L.Marsh, and J. A. Buckwalter, "Posttraumatic Osteoarthritis: A First Estimate of Incidence, Prevalence, and Burden of Disease," *J. Orthop. Trauma*, vol. 20, no. 10, pp. 739–744, Nov. 2006.

[6] B. Kinner and M. Spector, "Cartilage–current applications," *Orthop. tissue Eng. basic Sci. Pract. Dekker, New York, NY*, 2004.

[7] R. S. Tuan, "Experimental Principles and Future Perspectives of Skeletal Tissue Engineering," *Tissue Eng. Musculoskelet. Clin. Pract. Ed. Rosemont, Am. Acad. Orthop. Surg.*, 2004.

[8] J. D. Harris, R. A. Siston, X. Pan, and D. C. Flanigan, "Autologous Chondrocyte Implantation," *J. Bone Jt. Surgery-American Vol.*, vol. 92, no. 12, pp. 2220–2233, Sep. 2010.

[9] Versier G. Bures C., "Surgical treatment of cartilage injuries in 2002." [Online]. Available: http://www.rhumatologie-bichat.com/versier02.htm. [Accessed: 04-May-2018].

[10] P. Hindle, J. L. Hendry, J. F. Keating, and L. C. Biant, "Autologous osteochondral mosaicplasty or TruFit™ plugs for cartilage repair," *Knee Surgery, Sport. Traumatol. Arthrosc.*, vol. 22, no. 6, pp. 1235–1240, 2014.

[11] C. L. Camp, M. J. Stuart, and A. J. Krych, "Current concepts of articular cartilage restoration techniques in the knee.," *Sports Health*, vol. 6, no. 3, pp.

[12] 265–73, May 2014. L. Hangody *et al.*, "Autologous osteochondral grafting—Technique and long-term results," *Injury*, vol. 39, no. 1, pp. 32–39, Apr. 2008.

[13] S. Nishihara, N. Sugano, T. Nishii, H. Miki, N. Nakamura, and H. Yoshikawa, "Comparison Between Hand Rasping and Robotic Milling for Stem Implantation in Cementless Total Hip Arthroplasty," *J. Arthroplasty*, vol. 21, no. 7, pp. 957–966, Oct. 2006.

31st Florida Conference on Recent Advances in Robotics, May 10-11, 2018, University of Central Florida, Orlando, Florida

8

[14]   F. Rodriguez *et al.*, "Robotic clinical trials of uni-condylar arthroplasty.," *Int. J. Med. Robot.*, vol. 1, no. 4, pp. 20–8, Dec. 2005.

[15]   W. Korb *et al.*, "Development and first patient trial of a surgical robot for complex trajectory milling.," *Comput. Aided Surg.*, vol. 8, no. 5, pp. 247–56, 2003.

[16]   R. Tarwala and L. D. Dorr, "Robotic assisted total hip arthroplasty using the MAKO platform," *Curr. Rev. Musculoskelet. Med.*, vol. 4, no. 3, pp. 151–156, Sep. 2011.

[17]   S. Song, A. Mor, and B. Jaramaz, "HyBAR: hybrid bone-attached robot for joint arthroplasty.," *Int. J. Med. Robot.*, vol. 5, no. 2, pp. 223–31, Jun. 2009.

31st Florida Conference on Recent Advances in Robotics, May 10-11, 2018, University of Central Florida, Orlando, Florida

9

Be Aware of Motorized Shopping Carts

Oren Masory

Department of Ocean and Mechanical Engineering, FAU
777 Glades Rd,

Florida Atlantic University
FAU, Boca Raton, FL 33431

masoryo@fau.edu

ABSTRACT

As the elderly population grows, the need for personal mobility devices such scooter and wheelchairs increases too. Most of these devices are being used in uncrowded environment except Motorized Shopping Carts (MSCs). MSCs are operated by elderly or people with disabilities in very confined and in times crowded environment. In a first glance, it appears that there are no safety issues in operating MSCs due to their low "walking" speed. On the contrary, there are few safety issues and this paper attempts to present some of the safety concerns related to the operation of MSCs in shopping facilities.

Keywords

Safety, Motorized Shopping Cart.

1. INTRODUCTION

There are 38441 supermarkets in the US [1] besides malls, pharmacies etc. Thus, the number of Motorized Shopping Carts (MSCs) can be estimated, with high probability, to be above 50,000. This number will increase dramatically in the future as the population of the US age. MSCs are used in confined, and in times very crowded, spaces and as a result accidents might occur.

Motorized Shopping Carts (MSCs) are fundamentally reduced speed scooters with large basket installed in their front and, in most cases, for three wheel scooters two small casters were added in the front for stability (see Figure 1).
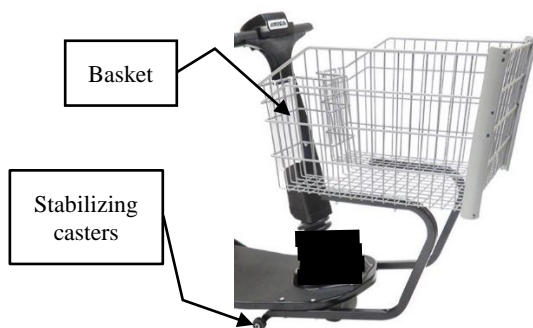

Figure 1: Modification to a typical scooter.

In [5] the new rules regarding to mobility aids, published by the American with Disabilities Act, are explained but safety remarks or recommendation were given. In [6] the following hazards were expressed: "A concern over the carts leading to injuries when used by those who do not know how to control them. Injuries can occur to the operator, to other persons and to property if they crash into an object or a person with the equipment. Frontal crashes leading to injuries and property damage are the most common injury. Most units have back-up alarms to warn person(s) when the equipment is in reverse". In [7] other concerns brought forward: 1) "The physical and mental capability of the person operating the device. Capabilities can include; reduced eyesight, diminished capacity due to medication, or alcohol, and limited physical movement (cannot turn around to view when backing up), etc. and 2) "The speed, and the combined weight of the equipment and the operator of the scooter or cart is the best indicator of the severity of the injury or extent of the damage".

The purpose of this paper is to discuss and to some degree quantify the hazards related to the use of Motorized Shopping Carts which were mentioned in the above references.

2. START-STOP ACCELERATIONS AND JERKS

It is quite clear that MSCs are use in GO – STOP mode as shopper are driving from one location to another and stop to pick up a certain item. All MSCs are using Direct Current motors to propel the cart and magnet brakes to stop it. Direct current characteristic is high torque at law speed that can result high accelerations. Magnetic brakes are on/off devices and when engaged might cause high decelerations. Experiments, in which the acceleration of the cart along a straight path, were performed on an empty basket commercial MSC driven by 156[lb] rider. The recorded acceleration is shown in Figure 1 (F stands for forward motion, R for reverse and S for Stop). The acceleration signal was samples at 100[Hz] and filtered with a first order low pass filter with time constant of 0.2 second.

As shown in Figure 2 the acceleration in the forward or reverse direction is practically the same and its peak reaches 0.075[g]. On the other hand, when the brake is applied the deceleration peaks at 0.14[g].

To determine the jerk the acceleration signal was numerically differentiated and then filtered by a first order low pass filter with time constant of 0.2 second (see Figure 3). As shown, stopping while moving in reverse generates jerk in the order of 0.42[g/second] and 0.3[g/second] when accelerating forward.

Similar results were reported in [2] where the following measurement were taken: maximum forward acceleration of 0.163[g] stopping deceleration of 0.183[g] forward jerk of 0.29[g/second] and stopping jerk of 0.345[g/second]. In [3] four different scooters were tested on horizontal surface. The measured maximum forward acceleration was found to be 0.194[g] and in the reverse direction 0.363[g].

ANSI/ASCE Standard 21.2-08 [4] the maximum acceleration and jerk allowed in public transportation is given (see Table 1). Comparing the results mentioned above, only one scooter exceeds the allowed acceleration but in two cases the jerk is larger than the allowed values. Although this standard is not directly related to MSCs it does dictate the necessary limitation on acceleration and jerk so that the rider will be kept in his seat.

Table 1: Maximum acceleration and jerk dictated by ANSI/ASCE standard [1].

Direction	Acceleration [g]	
	Standing	Seating
Lateral	±0.1	±0.25
Vertical	±0.05	±0.25
Longitudinal Normal	±0.16	**±0.35**
Longitudinal Normal*	±0.32	±0.60
	Jerk [g/s]	
Lateral	±0.06	±0.25
Vertical	±0.04	±0.25
Longitudinal	±0.10	**±0.25**

*Including effect of grade

3. IMPACT WITH BY STANDING SHOPPER

MSCs operate in facilities that might be extremely crowded in times such as department stores during the holiday seasons. As a result, collisions with by standers or walking shopper are not avoidable. The following are two simple model by which the impact force can be estimated.

Applying linear momentum principle to the shopping cart:

$$m_c v_1 = \int_0^T f(t)dt + m_c v_2 \qquad (1)$$

where m_c - cart's mass (including the defendant and the basket's contain)

v_1 - cart's speed before impact

v_2 - cart's speed after the impact

$f(t)$ - force impulse

T - Impact duration

Since the cart lost speed due to the impact we can rewrite Eq. 1 as:

$$m_c(v_1 - v_2) = m_c v_1(1 - L) = \int_0^T f(t)dt + m_c \qquad (2)$$

where L is the fraction of the velocity lost during the impact.

For a simple model, in which the impact force $f(t) = F_0$ [Lb] and impact duration of T [second], the magnitude of the impact force can be determined by:

$$F_0 = \frac{1}{T}m_c v_1(1 - L) = K m_c v_1 \qquad (3)$$
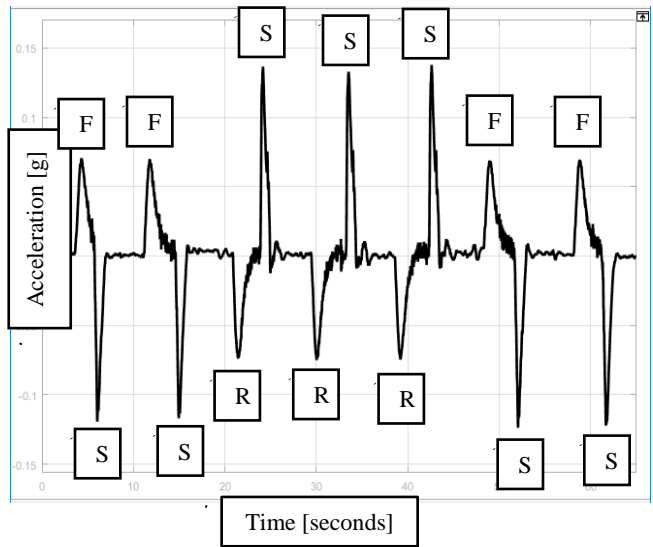
where $K = \frac{1}{T}(1 - L)$

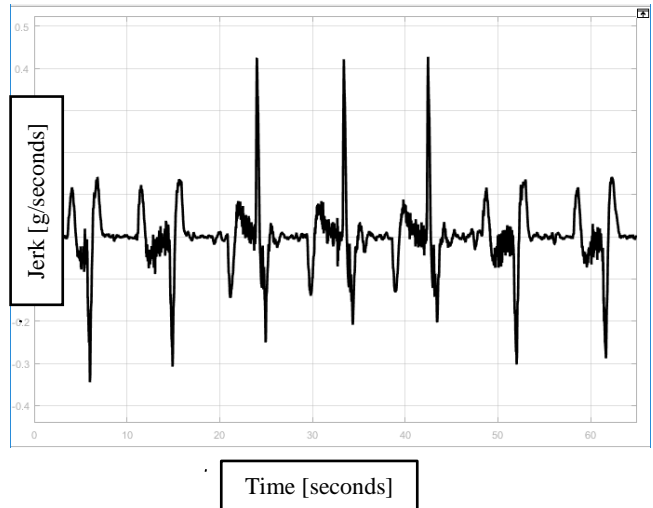**Figure 2: Acceleration recording**

Figure 3: Calculated jerk.

Considering the following case: rider weight – 170[Lb], Basket weight=50[Lb] and the data for cart A (see Table 2) (cart weight = 190[Lb] v_1 = 3.66[ft/sec]. Figure 4 illustrates the value of F_0 as function of the impact duration time, T, and the fraction of the MSC velocity loss L. As shown, even for a long impact time of 50[ms], MSC velocity loss of 30% the impact force is 70[Lb] which is substantially enough to cause injury.
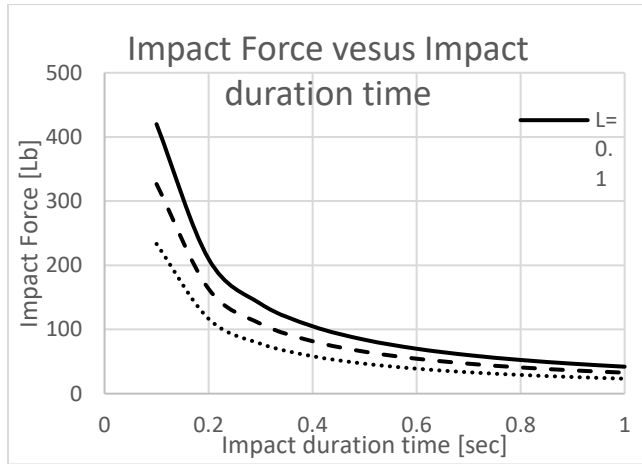

Figure 4: Impact force as function of impact duration time and cart's velocity lose.

Table 2: Data for two commercial MSCs.

Property		Cart A	Cart B
Weights [Lb]	Rider	750	500
	Cart	190	167
	Basket	250	250
	Total	1190	917
Cart Dimensions [in]		55L 26W 38H	56L 24W 33H
Basket dimensions [in]		23L 25.5W 20H	23.6L 19W 14.8H
Speed [mph]	Forward	2.5	2.3
	Reverse	1.5	1.4
Wheel diameter [in]		8	8 - rear 6 - front
Turning radius [in]		34	38
Stopping Distance [in]			18"

In a better model the force impulse behaves as sin function with half a period T/2[s] and is given by:

$$f(t) = F_0 \sin(\omega t) = F_0 \sin(\frac{2\pi}{T} t) \tag{4}$$

where F_0 is the maximum value of the force.

The total force impulse, I, is given by:

$$I = F_0 \int_0^{T/2} \sin\left(\frac{2\pi}{T} t\right) dt = F_0 \frac{T}{\pi} \tag{5}$$

Thus the magnitude of the force can be determined

$$F_0 = \frac{\pi}{T} m_c v_1 (1 - L) \tag{6}$$

Equation 6 indicates in this, which is more realistic response, the maximum value of the impact force is □ time larger. Figure 5 illustrates the impact force as function of time for F_0=300[lb] and MSC's speed used in Figure 3, with impact duration time of 0.25 [second] and L=0.25. The graph indicates that the MSC will exert a force of 250[Lb] for 0.1[second] during the impact.
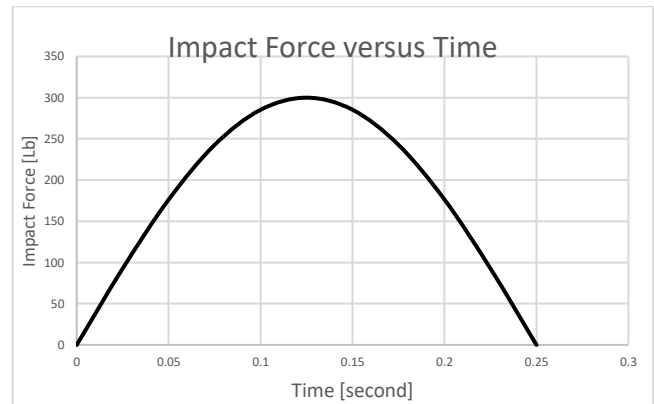
Figure 5: Impulse shape for a maximum force of 100[lb] and a period of 0.5[second].

This impact force might be exerted, with high probability, in two body locations: at the torso (impact with the top of the basket) or the ankle (impact with the cart's bumper) as shown in Figure 6. In the first case a person might lose his stability and fall and in the second case a person will injure or even brake his ankle which requires a long heeling time.

To estimate the magnitude of the impact force, exerted by the basket tip, required to tip over a person, a multibody human model must be used. However, a rough estimation can be obtained by considering the human body as a rigid body.

Figure 7 illustrates the Free Body Diagram which describes all the forces acting on a person at the tipping instant. The magnitude of the impact force, F_0, is given by:

$$F_0 = \frac{Wd}{2H} \tag{7}$$

where H is the height of the tip of the basket and d is the span between the feet of standing person.

For H=33[in] (above the center of gravity of the standing person) and d=12[in] Eq. yields $F_0 = 31[lb]$. As shown above the impact force can assume by far larger magnitude which for certain might cause a by stander to lose his balance, fall and possibly be injured.

31st Florida Conference on Recent Advances in Robotics, May 10-11, 2018, University of Central Florida, Orlando, Florida

12

Figure 6: High probability impact points.

Figure 7: Free body diagram of a person on a verge of tipping.

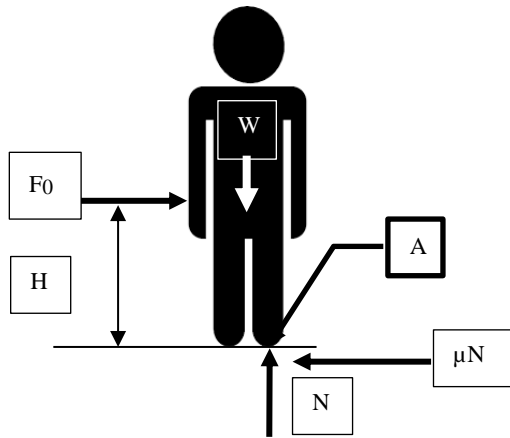**Figure 8: Turning radii of a car and a MSC**

4. OTHER ISSUES
4.1 Turning Radius

Users of MSCs most probably drove standard family vehicle for many years and got used to their performance. One issue in driving a car is to clear its corner while making a turn in a tight space. With a car the maximum radius of rotation is slightly larger than the radius of rotation of front wheel (left front in the Figure 8), In contrast, the maximum radius of rotation of a typical MSC is by far larger than the radius of rotation of front wheel. This fact presents a major difficulty when a tight turning maneuver is performed such as turning into a narrow isle since the rider has to clear the edge of the basket. In comparison, driving the MSC is like driving a mini excavator where the bucket is extended. Also, one has to realize that most of the MSCs users are probably using scooters for daily mobility. These scooters do not have baskets, or very small ones, thus they need some adjustment time to drive a MSC which has a large basket in is front.

4.2 Stopping Distance

The stopping distance provided by the manufacturer of cart B is 1.5[t] which relates to the capability of the brake to bring the cart to halt. This value agrees with measurements taken in several experiments. One such is shown in Figure 9 where the acceleration signal was integrated twice and the stopping distance was estimated. The actual stopping distance should include the distance the cart travels during the reaction time of the rider. Typical response time is 1.5[second] and for elderly people it might me higher. Thus for a traveling speed of 2.4[mph], as specified by the manufacturer of cart B, the stopping distance is:

$$S = 1.5 + 1.5 * 2.4 * 1.466 = 6.78[ft] \qquad (8)$$

Thus the stopping distance, if the rider pay full attention, is about 2[ft] assuming that the rider full attention is in driving. One has to realize that the attention of the rider in finding a particular product. While driving along an isle the products are located on shelves on both of his sides and as a result he is not looking forward in the driving direction. In this case stopping distance becomes very critical in particular in crowded store.

In [3] one of the four scooters tested had a stopping distance of 7.578[ft] from a speed of 2.51[ft/second]. This value is comparable to the calculated in Eq. 8.

31st Florida Conference on Recent Advances in Robotics, May 10-11, 2018, University of Central Florida, Orlando, Florida

13

Figure 9: Determination of stopping distance.

4.3 Tipping Over

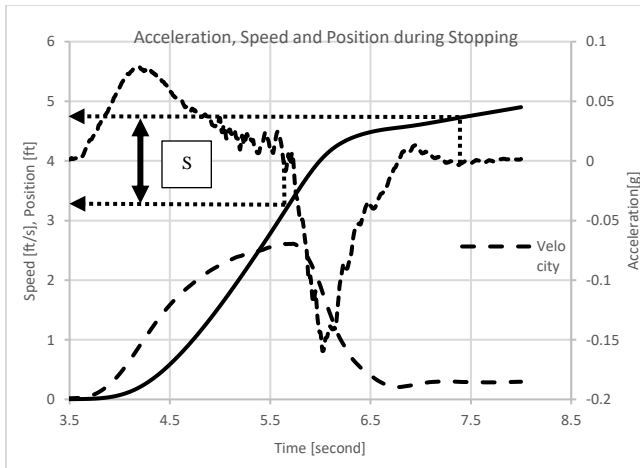Some three wheel MSCs do not have stabilizing casters and as a result, they are more susceptible to tipping. In this case, the MSC will tip to the right once the center combined center of gravity of the rider, the cart and the basket and its content will cross the tip over line that connects the centers of the right rear and the front wheel (see Figure 10). Tipping can occurs when the rider over extends his arm and shift his weight in order to reach a product or while standing on the platform and shifting his weigh to one foot in order to reach a product on a high shelf.

In this regard the label attached to the MSC warns: 1) "Do not stand on the platform; and 2) "Distribute weight evenly in basket". The only question is: "how many of the users actually reading the label?"
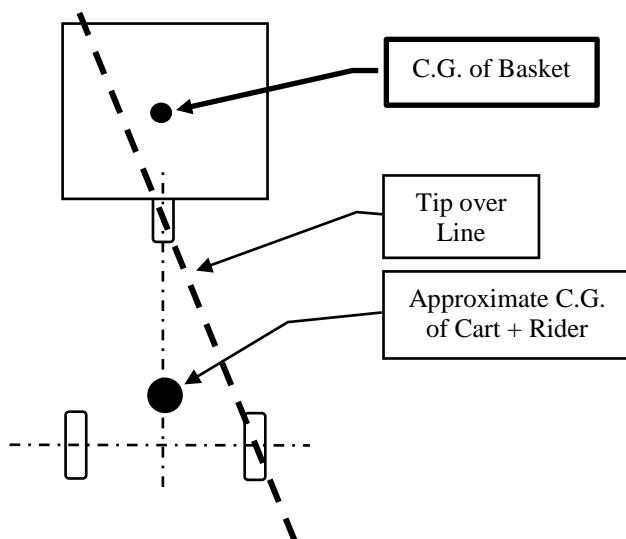

Figure 10: Tipping diagram of an MSC.

5. CONCLUSIONS

It is expected that the number of Motorized Shopping Cart will increase considerably in the near future as the population age. MSCs do present risk to an inexperienced rider and bystanders in particular in crowded spaces like department store during the holiday season.

Injuries due to impact with bystanders, tip over, high acceleration and other reasons were presented in this paper. Some changes in the design of these carts, such as soft bumpers and limiting the acceleration and decelerations, will certainly reduce the risk. However, the real problem is that the accessibility to these carts is not monitored by the facility personnel. Therefore anybody, capable or not, experienced or not, can use these carts. Since these facilities are providing these carts to their customers it is their responsibility for their safe usage. A few minutes of instructions will make the user aware of the safety issues and thus reduce the risk.

6. REFERENCES

[1] https://www.statista.com/statistics/240892/number-of-us-supermarket-stores-by-format/

[2] Andrew John Rentschler , "Analysis of the NASI-RESNA wheelchair standards A comparison study of 5 different electric powered wheelchairs", M.Sc. in Bioengineering thesis, submitted to Carnegie Mellon University, 1995.

[3] Ana E. Souza, Jonathan L. Pearlman, Rosemarie Cooper, Annmarie Kelleher, Benjamin Gebrosky, Rory A. Cooper, "Evaluation of scooters using ANSI/RESNA standards", Journal of Rehabilitation Research & Development (*JRRD*), Vol. 50 No 7, 2013,   Pages 1017 — 1034.

[4] ANSI/ASCE Standard 21.2-08, Automatic People Mover Standards – Part 2, Vehicle Propulsion and Braking, 2008.

[5] Wheelchairs, Mobility Aids, and Other Power-Driven Mobility Devices, U.S. Department of Justice Civil Rights Division *Disability Rights Section*

[6] ZURICH RISKTOPICS, "Safety of Mobility Scooters and shopping carts", Feb. 2015

[7] ZURICH Retail Newsletter.3rd Qtr. 2015

31st Florida Conference on Recent Advances in Robotics, May 10-11, 2018, University of Central Florida, Orlando, Florida

14

Multimodal Fusion Object Detection System

Michael Person, Mathew Jensen, Hector Gutierrez, Anthony O. Smith

IGVC Spec 2 Team

College of Engineering and Computing

Florida Institute of Technology, Melbourne, Florida 32901

mperson2016@my.fit.edu, mjensen@fit.edu, hgutier@fit.edu, anthonysmith@fit.edu

ABSTRACT

In order for autonomous vehicles to safely navigate the road ways, accurate object detection must take place before safe path planning can occur. Currently, general purpose object detection CNN models have the highest detection accuracies of any method. However, there is a gap in the proposed detection frameworks. Specifically, those that provide high detection accuracy necessary for deployment but do not perform inference in realtime, and those that perform inference in realtime but detection accuracy is low. We propose Multimodal Fusion Detection System MDFS), a sensor fusion system that combines the speed of a fast image detection CNN model along with the accuracy of light detection and range (LiDAR) point cloud data through a decision tree approach . The primary objective is to bridge the trade-off between performance and accuracy. The motivation for MDFS is to reduce the computational complexity associated with using a CNN model to extract features from an image. To improve efficiency, MDFS extracts complimentary features from the LIDAR point cloud in order to obtain comparable detection accuracy. MFDS achieves 3.7% higher accuracy than the base CNN detection model and is able to operate at 10 Hz. Additionally, the memory requirement for MFDS is small enough to fit on the Nvidia Tx1 when deployed on an embedded device.

Keywords: Autonomous Vehicle Perception, Obstacle Detection, Embedded GPU Computing, Convolutional Neural Networks, Sensor Fusion

1. INTRODUCTION

Vehicles are an integral part of the world, interweaved in our everyday tasks with the primary objective to provide point-to-point transportation. They transport goods between factories, shipping ports, stores, and also are a primary mode of transportation for many populations of the world. Vehicles may be very beneficial; however, their usefulness does not come without a cost. Every year roughly 30,000 are killed and over 2 million are injured in the US in automobile accidents [1]. Therefore, safety is a large concern not only for government regulators but also for automotive manufacturers. It is desired to have vehicles that are capable of driving themselves, since they would never be distracted leading to a significant improvement in vehicle safety. In 2005, Stanley the robotic vehicle from Stanford University (Figure 1), under the guidance of Sebastian Thrun won the DARPA Grand Challenge [2]. This success sparked a surge in research and commercial work towards the development of autonomous vehicles. This

Figure 1. Stanely, winner of the DARPA Grand Challenge in 2005 [2]

rush for autonomy was increased when Boss, from Carnegie Mellon University won the DARPA Grand Urban Challenge in 2007 [3]. Most vehicles are now equipped with Advanced Driver Assistance Systems (ADAS), such as Adaptive Cruise Control, that are classified as National Highway Traffic Safety Administration (NHTSA) level 1 or 2 autonomy (partial autonomy). However, one of the challenges in designing level 4 or 5 autonomous vehicles (highly or completely autonomous) is accurate perception in all environments of the world around the vehicle [4].

At the heart of perception lies computer vision. The vehicle must take in raw data from sensors such as cameras, LiDAR, and RADAR and then process it to form a meaningful representation of the world around it including object classification, detection, and localization. These different modalities of data provide unique benefits, but also have shortcomings and failure points. These different streams of data must be analyzed in order to gather important information from the environment around the vehicle in order to be passed to later stages of the autonomy system such as path planning.

A modern approach for object detection and classification is to use a convolutional neural network (CNN). The CNN is passed an image and will output a set of both bounding boxes and object labels for each bounding box. The CNN learns which features to extract by optimizing its convolutional kernels in order to form rich representational power to detect and classify objects. This class of algorithms yields high accuracy and generalizable detections. However LiDAR data is able to directly reason with the 3D world instead of a 2D projection of it. Directly manipulating 3D data allows detections to be used for path planning in the next stage of an autonomous vehicle, which would not be possible with the 2D detections of an image algorithm. Although LiDAR analysis

would be useful because of its 3D reasoning, detection accuracy is traditionally worse for LiDAR based algorithms than camera based ones, making LiDAR only algorithms unsuitable for autonomous vehicles [5].

In order to overcome the weaknesses of these independent modes of data, it is possible to fuse the data. The two defining types of data fusion between image and LiDAR data are decision and feature level fusion. Both of these fusion techniques have their own weaknesses, feature level fusion is difficult to find equivalent representations for each type of data and decision fusion can be less accurate as the system relies on both sets of features independently. The benefits though are increased detection quality over LiDAR only algorithms and 3D detections which can not be obtained by monocular camera algorithms, thus making sensor fusion algorithms the final output of an autonomous vehicle's perception system.

The purpose of this research was to develop MFDS to fuse camera and LiDAR data in order to provide accurate, fast object detection and classification. MFDS attempts to avoid large memory consumption while still being accurate, and operate at close to real time by using information from different types of sensors to efficiently augment one another, rather than greatly increase the computational cost of a single sensor for marginal benefit. The target deployment platform for MFDS is the Nvidia Tegra series, specifically the Tx1.

2.   LITERATURE REVIEW

Convolutional Neural Networks (CNNs) have seen great success in image classification [6][7][8][9][10]. CNNs have also proven successful in a variety of other computer vision tasks including, but not limited to, detection and segmentation [11][12][13][14][15][16]. Although classification, detection, and segmentation tasks are all different, neural networks are called universal approximators and are able to learn how to perform each of them with high levels of accuracy [17]. Each task requires specific network architectures for optimality, but due to their generality, many improvements to CNNs in one task also prove to be improvements in the others.

By 2017, image classification had reached the necessary accuracy levels for real world performance; however, to be useful for most applications, models would need to take up less memory and perform inference faster. The first major paper to address this problem of model deployment was MobileNets, which developed an accurate, small, fast classification network and was shown to perform well at transfer learning to more complicated tasks [18]. MobileNets was based upon the idea of the depthwise seperable convolution, which was shown to be nearly equivalent to normal convolution. Depthwise seperable convolution is faster than standard convolution because they are optimized for the General Matrix to Matrix (GEMM) function call from within the cuBLAS library of CUDA, which is utilized by the cuDNN library [19]. cuDNN is a library specifically dedicated to GPU implementations of CNNs due to their high computational complexity, making them intractable on standard CPUs.

Once classification networks had reached a high enough level of accuracy, CNNs were applied to more complicated tasks such as detection tasks. One such successful detection network is Single Shot MultiBox Detector (SSD) [20]. Instead of only outputting a class label, SSD outputs a list of detections where each detection consists of a class label, a confidence, and the four coordinates of a bounding box. SSD is a unified detection network meaning that it performs a single pass through a network without using a Region Proposal Network popularized by Fast and Faster RCNN [12][13].

Detections are outputted at different stages of the network because the feature map size decreases as the layer depth increases, meaning that larger objects will be outputted earlier on in the network since their feature maps are larger.

In addition to camera, or image, based methods are LiDAR, or point cloud, based methods for object detection. As range sensors such as LiDAR have become more affordable and more readily available, point cloud detection methods have increased in popularity but are still not as accurate as image based methods [21][22][23][24][25][26]. Unlike image methods which are almost entirely handled by deep learning methods, LiDAR methods utilize both modern deep learning techniques and traditional hand crafted feature extraction methods. This is largely due to the computational complexity of 3D convolution, making it difficult to form CNNs for a LiDAR point cloud. Therefore CNN algorithms that operate on LiDAR data typically perform some sort of projection or form a 2D representation of the point cloud which 2D convolution can be applied to.

There are also fusion based methods which take multiple modes of data as input and output detections similar to the camera and LiDAR methods previously mentioned. These fusion methods can generally be grouped into two classes, feature fusion and decision fusion. Feature fusion methods generally involve projecting the LiDAR point cloud into a 2D space and then processing both the image and the projection with some sort of CNN in order for the learned features that are extracted from both mediums to compliment one another [27][28][29]. The other group of fusion algorithms are decision level fusions, which perform independent detections in both mediums and then combine both sets of detections together in order to output a single set of superior detections [30]. The idea behind fusion methods is to utilize the advantages of each type of data to augment one another in order to provide superior detection quality over each independent medium alone.

3.   METHODOLOGY

The proposed Multimodel Fusion Detection System (MFDS) is a decision-feature fusion, seen in Figure 2. At the start of the algorithm, an image based CNN performs detection to output a set of possible objects represented as bounding boxes with classes and probabilities. After which, the synchronized point cloud is masking to the same viewing angle's as the camera, the ground plane is removed, the cloud is transformed into the camera coordinates, and the remaining points are separated into clusters based upon Euclidean distance. Then, image detections and clusters are associated and paired together. Next a vector of hand selected features is extracted from the cluster of each pair, if there are any, and run through a Multi-layer Perceptron (MLP) to regress class probability, object length, distance to the object's center, and orientation of the object. The pairs confidence's are adjusted, or could potentially be removed, based upon the output of the MLP. The output of the fusion algorithm are confident 3D localized detections.

3.1   Creation of Fusion Models

The first step was acquiring a pretrained image detection CNN model, specifically SSD, and then performing transfer learning on the SSD model to be fine tuned on the KITTI dataset [5]. The KITTI dataset was split to create training and validation sets, out of the 7481 images and point clouds, 5611 were used for training and 1870 were used for validation. Next, the LiDAR processing pipeline was built up to the feature extraction of identified clusters
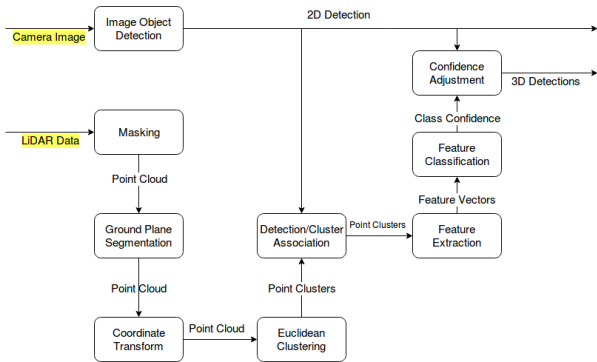
Figure 2. System Diagram for the operation of MFDS

Figure 3. Class Representation in the created MLP Cluster Dataset

stage. A converted LiDAR dataset was then created by running every LiDAR point cloud in the KITTI dataset through the processing pipeline to extract features of every cluster, which were then compared to KITTI's labels and saved to disk if they matched. After the converted dataset was formed, the classifying MLP was built and trained.

3.2 Feature Extraction

After point cloud clusters had been formed, the last step before the MLP was to perform feature extraction. The features that were decided upon was the sample mean and standard deviation of the clusters x, y, and z coordinates, ranges for all 3 dimensions, as well as ratios of x to y, x to z, y to x, y to z, z to x, and z to y. Although these ratios were redundant and included inverses, they proved to be beneficial as the MLP did not learn as well if some were removed. It is believed that this is because this redundancy slightly reduced the complexity of the nonlinear decision boundary that the network needed to learn.

These features were chosen because they represent important geometric information about the point cloud cluster while being computationally cheap to compute. The geometric data of the point cloud is used to augment the color intensity data stored in the camera image.

3.3 Dataset Creation

After the LiDAR point cloud pipeline had been created, the dataset needed to be created. To form the dataset, each point cloud in the separated training portion of KITTI was processed with the same pipeline that was used during inference, which included masking, ground plane extraction, transformation, and clustering. Each cluster was checked against each labeled cuboid to determine if that cluster represented one of the labeled objects. Since the labels were not perfect, a cluster was considered a labeled object if no more than 5% of the points existed outside the label cuboid. In addition to the KITTI labels of Vehicle, Pedestrian, or Cyclist, clusters with no class label were included in the final dataset in order for the network to learn to be able to reject objects that were not relevant, which meant that the MLP would output a score for four classes instead of three. Therefore, the final classes used were Don't Care, Vehicles, Pedestrians, and Cyclists. In total there were 17,382 point clouds, 17% was other, 69% was vehicles, 10% was pedestrians, and 3% was cyclists, seen in Figure 3. Therefore, cyclists were the most difficult class to classify since they had the least number of training examples. After the datasets clusters were identified, each cluster had their features extracted and their class, distance to
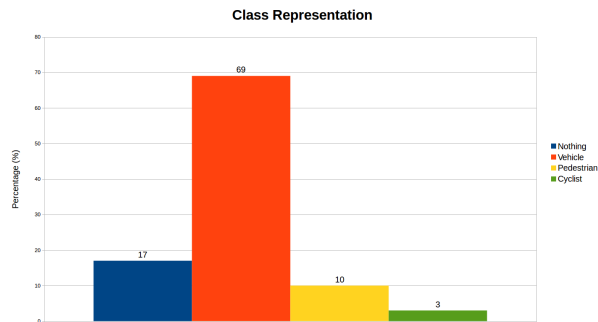
center, length, orientation, and features saved to disk. 75% of the point clouds were used for training and the remaining 25% were used for validation.

3.4 Mutli Layer Perceptron Architecture

The MLP to classify point cloud clusters was built in Python with the Tensorflow library. The MLP's jobs were to predict the class of the object's cluster, the distance to the center of the object from the LiDAR sensor's origin, the size of the object along the z axis, and the rotation of the object given the cluster's features and the trained model. The class probability distribution is an unknown nonparametric distribution. The MLP is used to form an estimate of the posterior distribution given the trained model and input feature vector. The class probability is mathematical stated in Equation 1.

$$\hat{P}(C_i|\mathbf{f}_i, \Theta) \qquad (1)$$

C_i represents the class probability for the ith feature vector and Θ represents the trained MLP model parameters. The distance to the center of the object, z_i, the size of the object, l_i, and the rotation of the object, α_i, are all estimated values.

The MLP needed one output layer for every value that needed to be regressed, therefore the MLP had four different output layers. The MLP architecture is seen in Figure 4 but should be noted that the nodes are not draw to scale according to their size. The input layer for the feature vector had a size of 15 since that was the length of the feature vector, the class output layer had a size of 4 to be able to regress each class probability, and distance, size, and rotation layers each had a size of 1.

The number and shape of the MLP's hidden layers needed to be determined. The number of layers tested varied from 1-7 and the number of neurons in each layer was varied between 10-200. The hidden layer configuration that converged to the best accuracy had a single hidden layer with 150 neurons.

A truncated normal distribution with a standard deviation of .01 was sampled from to initialize all parameters. As is standard for detection networks, the distance, length, and rotation was not predicted outright, an encoding was used instead. The entire dataset was analyzed and the maximum distance was 50m as was the maximum length. The maximum length was this large because of random clusters that were included in the dataset. Therefore, the distance and length did not need to be predicted but instead an encoding was predicted, which was easier for the network to learn. In addition, the rotation value can only assume values between $-\pi$ and π so the natural scaling factor used was π. The encodings are seen below:
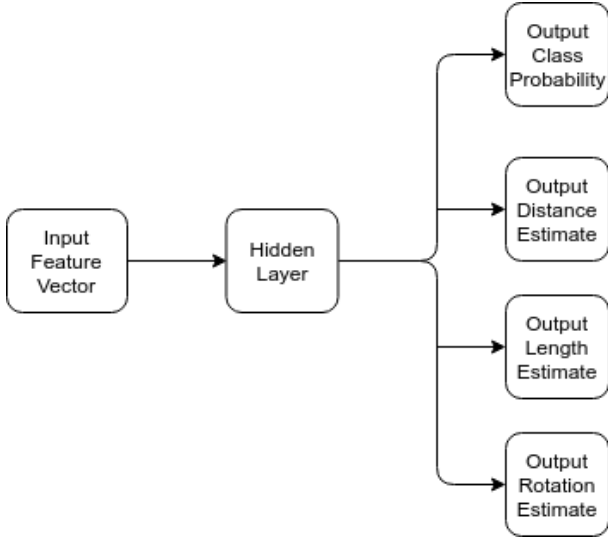
Figure 4. MLP Network Architecture

Figure 5. MLP Total Loss

$$\phi(z_{pred}, l_{pred}, \alpha_{pred}) = \left[\frac{z_{pred}}{50}, \frac{l_{pred}}{50}, \frac{\alpha_{pred}}{\pi} \right] \quad (2)$$

The activation function that was used for the hidden layer was a rectified linear unit (RELU), the class output layer was a softmax, the distance and length output layers were both sigmoids, and the rotation layer was a hyperbolic tangent [7]. The class layer used the softmax to squash all class probabilities between 0 and 1 and to make the sum of the probabilities equal 1. The distance and length layers used the sigmoid because the predictions fell between 0 and 1 since neither of the values could be negative and also the scaled value could never be over 1. The rotation layer used a hyperbolic tangent since the values fell between -1 and 1.

3.5 Training

In order to train the MLP to regress all four values simultaneously, a multi-part loss function was created. The total loss would be the summation of a weight regularization penalty term, L_{reg}, the weighted class error, L_{class}, and the weighted distance, length, and rotation errors, $L_{dist}, L_{size}, L_{rot}$, respectively. The final multi-part loss equation can be seen below:

$$L = L_{reg} + \frac{1}{N_{total}} \sum_{i=0}^{N_{total}} (\lambda_{class} L_{class}) + \quad (3)$$

$$\frac{1}{N_{care}} \sum_{j=0}^{N_{care}} ((\lambda_{dist} L_{dist}) + (\lambda_{size} L_{size}) + (\lambda_{rot} L_{rot})) \quad (4)$$

L_{class} was Cross Entropy Loss and L_{dist}, L_{size}, and L_{rot} were Smooth L1 Loss or Huber Loss [?]. L_{reg} was the summation of the l2 norm of all trainable parameters with decay value of 0.001. Finally, $\lambda_{class} = .8$, and $\lambda_{dist} = \lambda_{size} = \lambda_{rot} = \frac{1-.8}{3}$. The class loss weight, λ_{class}, was set higher than the other three weight terms as that output was the most important and needed to be emphasized to learn to the highest degree of accuracy possible. N_{total} is the total number of training examples per batch and N_{care} is the number of training examples that do not have a Don't Care class label. The reason why the summations were over N_{total} and N_{care} and not the
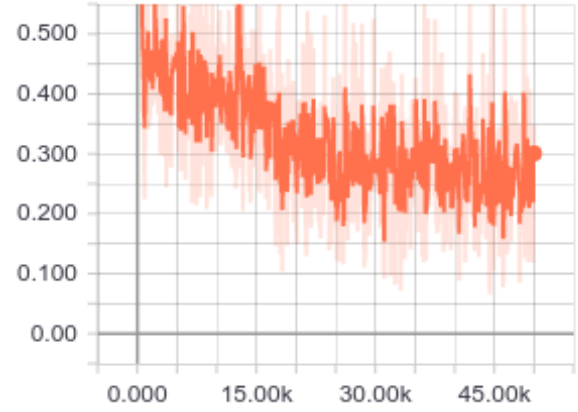
same is that there were no labels for length, size, or rotation of the clusters that were labeled Don't Care. Therefore, the Don't Care terms in the summation needed to be avoided when computing loss, which would impact the gradients and degrade the performance of the MLP.

The batch size was set to 12 on each GPU so there was an effective batch size of 36, since three GPUs were used. The network was trained for 50,000 iterations. Both Nesterov Momentum, with learning rate of 0.1 and momentum of 0.9, and Adam were tested; however, Adam converged to a higher class accuracy and was therefore used. The Total Loss during training can be seen in Figure 5.

Due to the unknown shape of the error surface, the MLP accuracy was extremely sensitive to initial conditions used for the learnable parameters. Since the MLP was so sensitive, the network was trained 75 times and the network that scored the highest classification accuracy on the validation set was selected to be the final network.

3.6 Association Problem

In order to perform the fusion algorithm after trained models were created for the image detection CNN and LiDAR classifying MLP, image detections and clusters needed to be associated together due to potentially noisy sensor readings detecting the same object. The projection matrix from 3D LiDAR space to 2D camera image space is provided for every timestep in the KITTI dataset. The projection matrix allows to compute the pixel location for each 3D point within the cloud, seen in Figure 6. The projection can be computed in the following way:

$$\begin{bmatrix} u \\ v \\ 1 \end{bmatrix} = \mathbf{P} \begin{bmatrix} x \\ y \\ z \\ 1 \end{bmatrix} \quad (5)$$

$$\mathbf{P} \in \mathbb{R}^{3,4} \quad (6)$$

After the matrix multiplication had been computed, the output vector needed to be normalized by the last element and the projection from 3D LiDAR to 2D camera image space. After the projection had been developed, clusters mean x, y, and z coordinates were projected into image space, along with forming the centroids of each of the CNN detection's bounding box. With the two sets of projected cluster centroids and bounding box
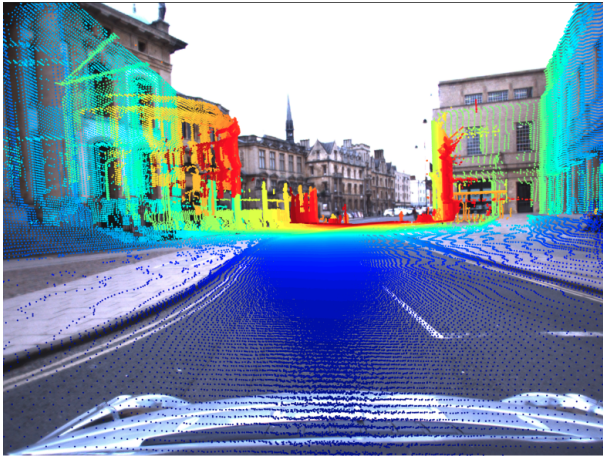
31st Florida Conference on Recent Advances in Robotics, May 10-11, 2018, University of Central Florida, Orlando, Florida

18

Figure 6. Example LiDAR Projection to Image Pixel Space, [31]

Figure 7. Fusion Algorithm's Compute Graph

Figure 8. MLP Accuracy

centroids, a simple Euclidean distance comparison in pixel space was performed. Any pair of centroids that were under a certain threshold were considered to to be a pair of the same object. The threshold that was used was 75 pixels due to the large variance of the cluster centroid's means.

3.7 Confidence Adjustment

After each pair's cluster had been classified, a check was performed between the pair's image detection class and cluster classification class. If the classes were not the same then the detection was eliminated, however if the classes were the same then the detections confidence was increased by 50%. The class probability was normalized afterwards. This confidence adjustment allowed for uncertain image detections, which would be eliminated, to gain the required confidence to be considered true detections.

3.8 MFDS Deployment Details

The fusion algorithm was jointly implemented in Python and C++ using ROS as the communication and build platform. ROS serves multiple purposes in this code; first to allow for messages to be passed with between the two languages, second for the use of powerful debugging tools such as topic monitoring and it's visualization package RVIZ, and third because MFDS needs to be easily deployable on robotic systems [32].

MFDS requires two ROS nodes to operate concurrently, seen in Figure 7; the first of which is a Python node to perform image detection and the second is a C++ node to perform point cloud manipulation, classification, and fusion. The Python node is subscribed to a Compound Data Message (CDM) containing both an image and a synchronized point cloud. Once the CNN finishes computing detections, another compound message is formed containing the detections and the CDM, which is published to the C++ node. The C++ node performs all point cloud preprocessing, cluster formation, cluster detection pairing, feature extraction, feature classification, and fusion. The output of the C++ node is the final set of fused 3D localized detections. Python was chosen for the image detection CNN because of Python's easy access to the Tensorflow library, eliminating the need to write the network inference code. C++ was chosen for the fusion node because PCL only operates in C based languages.

Since the LiDAR classifing MLP was trained with Tensorflow in Python, but inference was performed in C++, the MLP needed
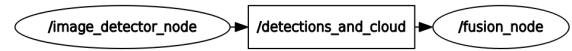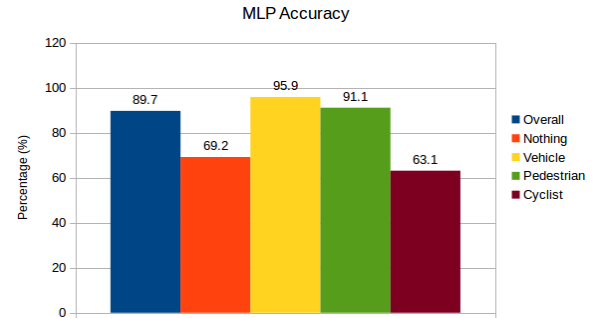
to be ported over to C++ [33]. Since the network involved no convolutions and only a simple MLP, the cuDNN library did not need to be called. A MLP is a series of matrix multiplications followed by nonlinear activation functions so naturally an efficient, large scale matrix multiplication library was required. cuBLAS was decided upon over Eigen due to the size of the matrices that needed to be multiplied. cuBLAS is a library of CUDA that operates similarly to the Basic Linear Algebra Subprograms (BLAS) library in C++; however, cuBLAS performs the same operations on a GPU instead of a CPU. The cuBLAS function call Sgemm that is used to implement the MLP is the same function call that MobileNets optimized their depthwise seperable convolutions around [18].

4. RESULTS

4.1 LiDAR Cluster MLP

The MLP was able to learn to classify each cluster with 90% accuracy, on average, without the need for a complicated feature extraction method. The MLP struggled with classifing the nothing, or Don't Care class, as well as cyclists. It is believed that classifying the nothing class was difficult due to the large variance in shapes and sizes, making it difficult for the network to form a relationship between the high variance features and the class label. Cyclists were difficult to classify due to the relatively low number of training examples to learn from.

All distance, length, and rotation errors presented are after rescaling the MLP's outputs and labels back to dimensional values from their nondimensional outputs. The MLP output of predicted distance to the object had a Mean Square Error (MSE) of 1-2 square meters, which is a much better predictor than the centroid of the cluster (MSE of 39.52 square meters), but not an optimal value. The MLP distance prediction is an order of magnitude more accurate than the naive analysis of the point cloud. The length of the object's prediction had an MSE of approximately a quarter of a meter squared when the average length of vehicles, pedestrians, and cyclists were 18.3 meters. Unlike distance, there is no easy way to predict object length or rotation without making strong assumptions about each class's shape. Therefore, the MLP provides access to reasonable predictions for these values very quickly at the expense of some accuracy.
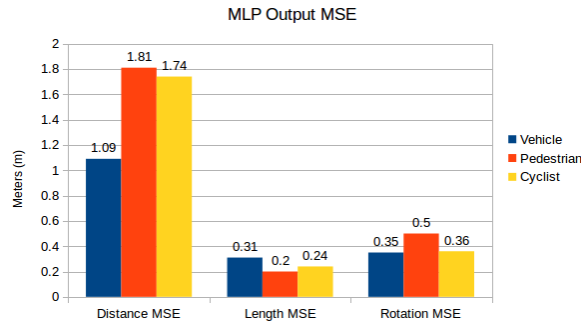
31st Florida Conference on Recent Advances in Robotics, May 10-11, 2018, University of Central Florida, Orlando, Florida

19

Figure 9. MLP Output MSEs

As the MLP was progressing through its 75 separate training initializations, the network appeared to converge to only three different levels of accuracy. It became apparent that these three levels of accuracy were proportional to each classes representation in the dataset. The network would converge to roughly 79%, 87%, or 90%. The networks that converged to 79% had not learned how to predict pedestrians or cyclists and instead only predicted class labels of vehicles and nothing since they made up the majority of the training examples. 87% convergence represented not learning cyclists and 90% represented learning how to predict all classes. This theory was tested by tallying each of the outputs of the test set and it was confirmed that the network never outputted the corresponding class labels.

4.2 MFDS and Image Detection CNN

Testing was performed on the remaining 1870 images and point clouds that were set aside in the test set. The image only detection method was analyzed in order to see how well the primary SSD model, as well as the RFCN and FRCNN reference models, performed on the KITTI dataset, as well as to act as a benchmark to see how much improvement MFDS provided. The KITTI dataset uses the mean Average Precision (mAP) metric for reporting results and is computed by finding the area under the precision recall curve. KITTI defines a true positive as a detection that scores over 70% IOU for cars and 50% for pedestrians and cyclists. However, mAP is a poor indicator of MFDS's detection quality since it is dependent on how many detections an algorithm can output.

Recall is a measure of how completely the detector's output detection set covers all labeled objects, while precision is a measure of how few incorrect detections are in the output set. Recall is largely dependent on how many detections a detector can output, generally in the range of 10 to 300 [34]. This variable number of detections, at varying confidence levels, allows for increased recall. As more detections are outputted, the likelihood of covering all labeled objects increases. MFDS operates in direct opposition to the idea of a variable number of detections with different confidence levels and works to only output as many detections as necessary, each with high confidence. This difference in output ideology means that recall is not a good evaluation metric for MFDS and as a result, neither is mAP. As the few high confidence outputs of MFDS are used to compute the systems recall, the precision recall curve drops to zero when there are no more available detections to cover the labels. Therefore a more applicable metric to evaluate the improvement of MFDS over the base SSD image detection CNN was used.

In order to determine the viability for deployment of the image detection CNN model, three main metrics were considered; the

	RFCN	FRCNN	SSD	MFDS
CPU Memory (GB)	2.592	2.816	1.824	2.176
GPU Memory (GB)	1.962	7.876	0.554	0.703
Inference Time (s)	0.073	0.54	0.0167	0.1083
Adjusted Accuracy (%)	58.11	57.84	37.18	40.89

Table 1. SSD Results in MFDS

memory footprint on the CPU and GPU, the inference time, and our own accuracy metric called adjusted accuracy. We define Adjusted accuracy, Equation 7, as the percentage of accurate detections with a penalty for incorrect detections, divided by the total numbed of labeled objects. In addition to these three metrics, it was beneficial to view the distribution of different types of detections in order to see the room for improvement that MFDS could add. The different types of detections were based upon varying combinations of confidence and correctness. Correctness was defined as the detection predicting the correct class with appropriate IOU. Confidence was defined as the confidence MFDS had in the detection's class, and a miss was defined as the detection CNN placing a detection around no labeled object. MFDS's main objective was to reduce the number of unconfident but correct detections and also reduce the number of confident misses. Therefore, MFDS is best suited to be used in conjunction with a CNN detection model that has a high number of unconfidently correct detections, a high number of confident misses, and performs inference at a high rate of speed.

$$\text{Adjusted Accuracy} = \frac{\text{True Positives} - \text{False Positives}}{\text{True Positives} + \text{False Negatives}} \quad (7)$$

The command line tool nvidia-smi was used to find each model's GPU memory consumption and the command line top was used to find each model's CPU memory consumption, which included all memory required by the process. The memory consumption is much larger than the size of the trained models because the memory consumption includes the amount of memory for storing temporary values and all additional required libraries for performing inference.

The SSD model was chosen for its small memory footprint, fast inference time, and ideal detection type distribution. Roughly 11% of SSD detection's fell within the categories of unconfidently correct and confidently incorrect, seen in Figure 13, as the targeted types of detections for MFDS to eliminate. MFDS takes the small, lightweight SSD model and increases the confidence of it's detections in order to output high confidence, correct detections with a minimal increase in memory demands, while still being able to operate at 10 Hz, seen in Table 1. Figures 10, 11, and 12 show that MFDS increases the confidence of detections that are able to become confident enough to become final detections. MFDS' output is 96% high confidence, correct detections, which is roughly a 50% improvement over the base SSD model, seen in Figure 13. MFDS suffers from a slight, roughly 0.8%, increase in confidently incorrect detections and misses. With the increase in the number of confident detections, MFDS was able to increase the adjusted accuracy by 3.7%. A comparrison to the popular RFCN and Faster RCNN models are supplied in Table 1.

In order to evaluate the inference speed of MFDS, each function in MFDS was timed, shown in Table 2. Cluster formation took up roughly half of the entire MFDS inference time with the other half evenly spread out amongst the other functions. Although the MFDS processing is roughly as fast as the RFCN and faster than the FRCNN inference time, they are not directly comparable because
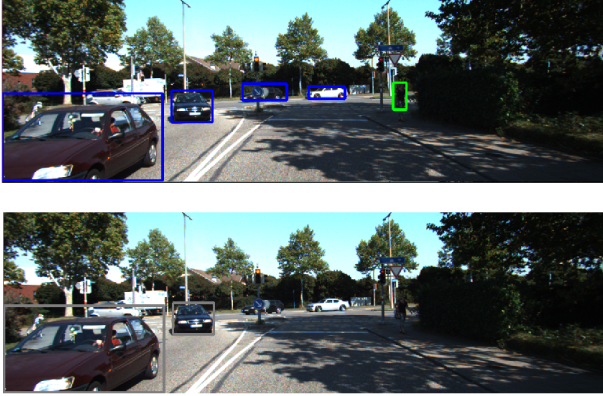
31st Florida Conference on Recent Advances in Robotics, May 10-11, 2018, University of Central Florida, Orlando, Florida

20

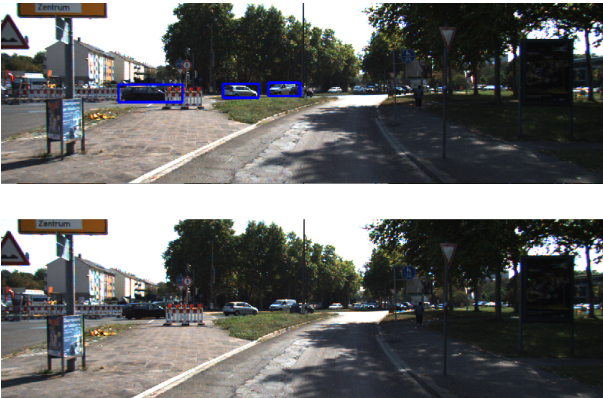**Figure 10.** SSD to MFDS Comparison; MFDS above, SSD below

Figure 11. SSD to MFDS Comparison; MFDS above, SSD below

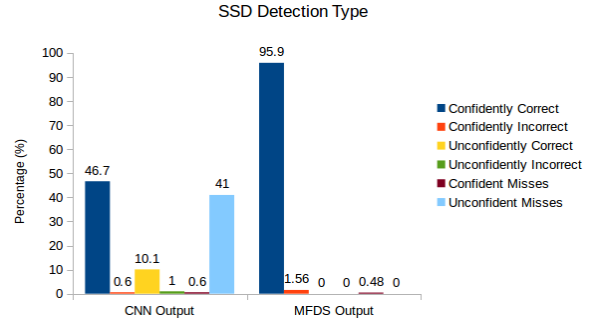**Figure 12.** SSD to MFDS Comparison; MFDS above, SSD below

Figure 13. SSD Model Detection Type

Task	Time (s)
CNN	.0167
Masking	0.014
Segmenting Ground Plane	0.009
Coordinate Transform	0.015
Cluster Formation	0.039
Detection/Cluster Association	0.001
Feature Extraction	0.0004
Classification	0.008
Confidence Adjustment	0.0001
Total	0.1083

Table 2. Time Analysis of MFDS Inference

Figure 14. Occluded Objects from the Image Viewpoint

the CNN detection models operate on the GPU and MFDS operates on the CPU and GPU with non optimized functions.

One of the main sources of error in MFDS proved to be the detection-cluster association. A known problem is when objects appear very close to one another, their bounding boxes will be nearly on top of one another and will be erased by NMS [35]. MFDS is very susceptible to this problem due to the way it associates detections and clusters together. An example of this can be seen in Figures 14 and 15 where a cyclist partially occludes a pair of pedestrians. There is only a single bounding box after NMS, due to their high IOU, however, there are two different clusters that are paired with it, visualized as the pink and blue points in Figure 15. There will be two final detections with the same bounding box, but with different 3D localized values which, by KITTIs definition, is one true positive and one false positive since labels can only have one detection after which all detections are considered errors.

Another source of error for MFDS was the false positive detection rate due to confident misses. Since many clusters are generated from a point cloud and are then paired with image detections with MFDS's association method, non object clusters make it to the cluster classification stage. The classifying MLP has a classification accuracy of 90%, which means that for every
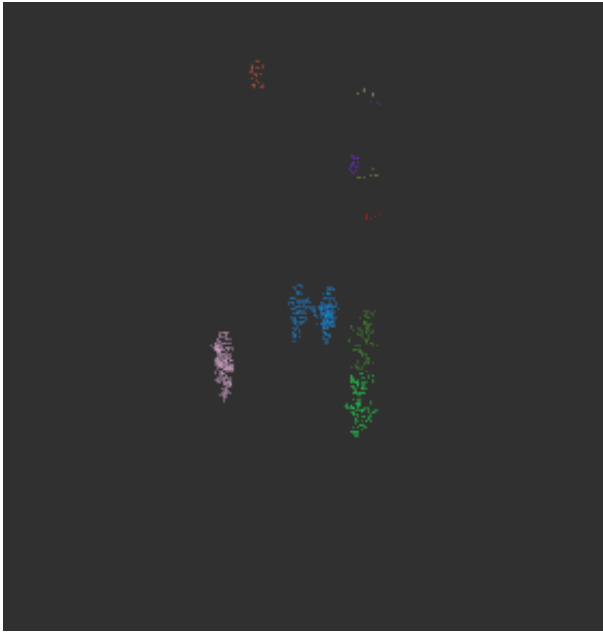
31st Florida Conference on Recent Advances in Robotics, May 10-11, 2018, University of Central Florida, Orlando, Florida

21

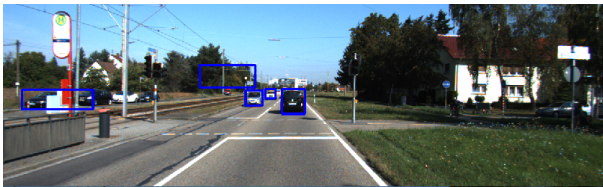**Figure 15.** Occluded Objects from the Point Cloud Cluster Viewpoint

Figure 16. False Detection Much Higher than Ground Plane

non object to reach the MLP, 10% will be viewed as confident detections due to false cluster classification and a poor confidence image detection. An example of this can be seen in Figure 16 where the treetop canopy's cluster is falsely detected as a car.

5. CONCLUSSIONS

An object detection system for autonomous vehicles was discussed in this article. MFDS was able to increase the adjusted accuracy by 3.7% over SSD while providing detections at 10 Hz. This increase in adjusted accuracy was achieved by changing unconfident into confident detections by performing an analysis on the corresponding point cloud cluster. MFDS performed inference comparably or faster than the reference CNN image detectors, takes up significantly less memory, and provided 3D localized detections. MFDS was able to take unconfident detection proposals from the image CNN and use LiDAR data to add enough confidence for the detection proposals to be considered true detections. MFDS was a step towards a deployable object detection system for autonomous vehicles. It fused information from multiple sensors to produce outputs directly usable by the path planning module of an autonomous vehicle. Although there are limitations to MFDS; the benefits and information that MFDS produces outweigh the problems it faces.

6. ACKNOWLEDGMENTS

7. REFERENCES

References

[1] Nation Highway Traffic Safety Administration. Traffic safety facts 2015, a compilation of motor vehicle crash data from the fatality analysis reporting system and the general estimates system. 2015.

[2] Sebastian Thrun, Mike Montemerlo, Hendrik Dahlkamp, David Stavens, Andrei Aron, James Diebel, Philip Fong, John Gale, Morgan Halpenny, Gabriel Hoffmann, Kenny Lau, Celia Oakley, Mark Palatucci, Vaughan Pratt, Pascal Stang, Sven Strohband, Cedric Dupont, Lars-Erik Jendrossek, Christian Koelen, Charles Markey, Carlo Rummel, Joe van Niekerk, Eric Jensen, Philippe Alessandrini, Gary Bradski, Bob Davies, Scott Ettinger, Adrian Kaehler, Ara Nefian, and Pamela Mahoney. Stanley: The robot that won the darpa grand challenge: Research articles. *J. Robot. Syst.*, 23(9):661–692, September 2006.

[3] Christopher Urmson, Joshua Anhalt, Hong Bae, J. Andrew (Drew) Bagnell, Christopher R. Baker, Robert E. Bittner, Thomas Brown, M. N. Clark, Michael Darms, Daniel Demitrish, John M. Dolan, David Duggins, David Ferguson, Tugrul Galatali, Christopher M. Geyer, Michele Gittleman, Sam Harbaugh, Martial Hebert, Thomas Howard, Sascha Kolski, Maxim Likhachev, Bakhtiar Litkouhi, Alonzo Kelly, Matthew McNaughton, Nick Miller, Jim Nickolaou, Kevin Peterson, Brian Pilnick, Raj Rajkumar, Paul Rybski, Varsha Sadekar, Bryan Salesky, Young-Woo Seo, Sanjiv Singh, Jarrod M. Snider, Joshua C. Struble, Anthony (Tony) Stentz, Michael Taylor, William (Red) L. Whittaker, Ziv Wolkowicki, Wende Zhang, and Jason Ziglar. Autonomous driving in urban environments: Boss and the urban challenge. *Journal of Field Robotics Special Issue on the 2007 DARPA Urban Challenge, Part I*, 25(8):425–466, June 2008.

[4] C. Berger and B. Rumpe. Autonomous Driving - 5 Years after the Urban Challenge: The Anticipatory Vehicle as a Cyber-Physical System. *ArXiv e-prints*, September 2014.

[5] A Geiger, P Lenz, C Stiller, and R Urtasun. Vision meets robotics: The kitti dataset. *Int. J. Rob. Res.*, 32(11):1231–1237, September 2013.

[6] Yann LeCun, LÃl'on Bottou, Yoshua Bengio, and Patrick Haffner. Gradient-based learning applied to document recognition. In *Proceedings of the IEEE*, volume 86, pages 2278–2324, 1998.

[7] Alex Krizhevsky, Ilya Sutskever, and Geoffrey E Hinton. Imagenet classification with deep convolutional neural networks. In F. Pereira, C. J. C. Burges, L. Bottou, and K. Q. Weinberger, editors, *Advances in Neural Information Processing Systems 25*, pages 1097–1105. Curran Associates, Inc., 2012.

[8] Karen Simonyan and Andrew Zisserman. Very deep convolutional networks for large-scale image recognition. *CoRR*, abs/1409.1556, 2014.

[9] C. Szegedy, W. Liu, Y. Jia, P. Sermanet, S. Reed, D. Anguelov, D. Erhan, V. Vanhoucke, and A. Rabinovich. Going Deeper with Convolutions. *ArXiv e-prints*, September 2014.

[10] K. He, X. Zhang, S. Ren, and J. Sun. Deep Residual Learning for Image Recognition. *ArXiv e-prints*, December 2015.

31st Florida Conference on Recent Advances in Robotics, May 10-11, 2018, University of Central Florida, Orlando, Florida

22

[11] Ross B. Girshick, Jeff Donahue, Trevor Darrell, and Jitendra Malik. Rich feature hierarchies for accurate object detection and semantic segmentation. *CoRR*, abs/1311.2524, 2013.

[12] R. Girshick. Fast R-CNN. *ArXiv e-prints*, April 2015.

[13] S. Ren, K. He, R. Girshick, and J. Sun. Faster R-CNN: Towards Real-Time Object Detection with Region Proposal Networks. *ArXiv e-prints*, June 2015.

[14] J. Redmon, S. Divvala, R. Girshick, and A. Farhadi. You Only Look Once: Unified, Real-Time Object Detection. *ArXiv e-prints*, June 2015.

[15] J. Redmon and A. Farhadi. YOLO9000: Better, Faster, Stronger. *ArXiv e-prints*, December 2016.

[16] Jifeng Dai, Yi Li, Kaiming He, and Jian Sun. R-FCN: object detection via region-based fully convolutional networks. *CoRR*, abs/1605.06409, 2016.

[17] Gerald H. L. Cheang. Approximation with neural networks activated by ramp sigmoids. *J. Approx. Theory*, 162(8):1450–1465, August 2010.

[18] Andrew G. Howard, Menglong Zhu, Bo Chen, Dmitry Kalenichenko, Weijun Wang, Tobias Weyand, Marco Andreetto, and Hartwig Adam. Mobilenets: Efficient convolutional neural networks for mobile vision applications. *CoRR*, abs/1704.04861, 2017.

[19] S. Chetlur, C. Woolley, P. Vandermersch, J. Cohen, J. Tran, B. Catanzaro, and E. Shelhamer. cuDNN: Efficient Primitives for Deep Learning. *ArXiv e-prints*, October 2014.

[20] Wei Liu, Dragomir Anguelov, Dumitru Erhan, Christian Szegedy, Scott E. Reed, Cheng-Yang Fu, and Alexander C. Berg. SSD: single shot multibox detector. *CoRR*, abs/1512.02325, 2015.

[21] Charles Ruizhongtai Qi, Hao Su, Kaichun Mo, and Leonidas J. Guibas. Pointnet: Deep learning on point sets for 3d classification and segmentation. *CoRR*, abs/1612.00593, 2016.

[22] Yin Zhou and Oncel Tuzel. Voxelnet: End-to-end learning for point cloud based 3d object detection. *CoRR*, abs/1711.06396, 2017.

[23] Dominic Zeng Wang and Ingmar Posner. Voting for voting in online point cloud object detection. In *Proceedings of Robotics: Science and Systems*, Rome, Italy, July 2015.

[24] M. Engelcke, D. Rao, D. Zeng Wang, C. Hay Tong, and I. Posner. Vote3Deep: Fast Object Detection in 3D Point Clouds Using Efficient Convolutional Neural Networks. *ArXiv e-prints*, September 2016.

[25] Shuran Song and Jianxiong Xiao. *Sliding Shapes for 3D Object Detection in Depth Images*, pages 634–651. Springer International Publishing, Cham, 2014.

[26] Shuran Song and Jianxiong Xiao. Deep Sliding Shapes for amodal 3D object detection in RGB-D images. 2016.

[27] X. Chen, H. Ma, J. Wan, B. Li, and T. Xia. Multi-View 3D Object Detection Network for Autonomous Driving. *ArXiv e-prints*, November 2016.

[28] Danfei Xu, Dragomir Anguelov, and Ashesh Jain. Pointfusion: Deep sensor fusion for 3d bounding box estimation. *CoRR*, abs/1711.10871, 2017.

[29] V. Hegde and R. Zadeh. FusionNet: 3D Object Classification Using Multiple Data Representations. *ArXiv e-prints*, July 2016.

[30] Sang-Il Oh and Hang-Bong Kang. Object detection and classification by decision-level fusion for intelligent vehicle systems. *Sensors*, 17(1), 2017.

[31] Will Maddern, Geoff Pascoe, Chris Linegar, and Paul Newman. 1 Year, 1000km: The Oxford RobotCar Dataset. *The International Journal of Robotics Research (IJRR)*, 36(1):3–15, 2017.

[32] Morgan Quigley, Ken Conley, Brian P. Gerkey, Josh Faust, Tully Foote, Jeremy Leibs, Rob Wheeler, and Andrew Y. Ng. Ros: an open-source robot operating system. In *ICRA Workshop on Open Source Software*, 2009.

[33] Martín Abadi, Ashish Agarwal, Paul Barham, Eugene Brevdo, Zhifeng Chen, Craig Citro, Greg S. Corrado, Andy Davis, Jeffrey Dean, Matthieu Devin, Sanjay Ghemawat, Ian Goodfellow, Andrew Harp, Geoffrey Irving, Michael Isard, Yangqing Jia, Rafal Jozefowicz, Lukasz Kaiser, Manjunath Kudlur, Josh Levenberg, Dan Mané, Rajat Monga, Sherry Moore, Derek Murray, Chris Olah, Mike Schuster, Jonathon Shlens, Benoit Steiner, Ilya Sutskever, Kunal Talwar, Paul Tucker, Vincent Vanhoucke, Vijay Vasudevan, Fernanda Viégas, Oriol Vinyals, Pete Warden, Martin Wattenberg, Martin Wicke, Yuan Yu, and Xiaoqiang Zheng. TensorFlow: Large-scale machine learning on heterogeneous systems, 2015. Software available from tensorflow.org.

[34] J. Huang, V. Rathod, C. Sun, M. Zhu, A. Korattikara, A. Fathi, I. Fischer, Z. Wojna, Y. Song, S. Guadarrama, and K. Murphy. Speed/accuracy trade-offs for modern convolutional object detectors. *ArXiv e-prints*, November 2016.

[35] Navaneeth Bodla, Bharat Singh, Rama Chellappa, and Larry S. Davis. Improving object detection with one line of code. *CoRR*, abs/1704.04503, 2017.

[36] Ian Goodfellow, Yoshua Bengio, and Aaron Courville. *Deep Learning*. MIT Press, 2016. `http://www.deeplearningbook.org`.

31st Florida Conference on Recent Advances in Robotics, May 10-11, 2018, University of Central Florida, Orlando, Florida

Towards the development of Junkyard Hacks: Networked Robotics Applications

Eric Williams, Moshe Acvecedo, Mohammad Ammar Bharmal, Vladislav Fomitchev, Luke Nichols, Kendon Ricketts, Balasubramaniyan Chandrasekaran, Ercan Ellibol, Melissa Morris, Ryan Integlia

Florida Polytechnic University
4700 Research Way
Lakeland, Florida, 33805

ewilliams3590@floridapoly.edu, macevedo5094@floridapoly.edu, mbharmal5916@floridapoly.edu, vfomitchev5004@floridapoly.edu, lukenichols0504@floridapoly.edu, kricketts6237@floridapoly.edu, bchandrasekaran@floridapoly.edu, eelibol@floridapoly.edu, mmorris@floridapoly.edu, rinteglia@floridapoly.edu

ABSTRACT

In this paper, we outline the ongoing development of a hackathon designed to raise awareness of electronic-waste, alternative uses for it, and what can be done to mitigate the damage caused by it. Nonfunctioning electronics are brought in for participants to salvage functioning parts out of for use in projects. An upcycling hackathon will be the focus of the event, which is designed to encourage STEM educational engagement and sustainability focused cultural development. An example project in which broken Roomba vacuum cleaner robots were repaired and modified for use in a swarm robotics application is also detailed. The expected outcomes are enhanced student engagement in STEM educational technology; awareness of the sustainability issues related to e-waste; and enhanced accessibility of educational technology as a platform for application innovation, development, research, and discovery.

Keywords

Educational Robotics, Roomba, ROS, Raspberry Pi, Hackathons

1.   INTRODUCTION

1.1   E-Waste

E-waste, or electronic waste, is a term for garbage generated in the form of discarded electronic devices. This includes, among other things, household appliances, home computers, and cell phones. E-waste management is a growing problem around the world. According to the EPA [2], the United States alone produced over 2.3 million tons of E-waste in 2009. Worldwide e-waste production was 44.5 million metric tonnes (49.3 US tons) in 2016[3]. As a form of pollution, E-waste provides major challenges. Electronics commonly contain heavy metals such as tin, copper, lead, and gold, along with other potentially dangerous substances, including flame retardants and the contents of batteries. [1]

In additions to the materials themselves being toxic, the methods commonly used to process E-waste for recycling can result in further contamination of the environment. E-waste is often shipped to developing countries for recycling, where the common practices involves the use of acid baths and even open air burning of the waste to recover valuable metals. This results in further exposure to potentially toxic substances for the workers.[2]

Due to the difficulties posed by recycling E-waste, we have decided to instead focus on the second of the three R's from the old slogan "reduce, reuse, recycle" -- we are looking at ways of reusing functional components of discarded electronics, rather than stripping them down to their component materials.

1.2   Educational Robotics

Educational robotics is the application of robotics to education. This is most commonly used in STEM education, both as a means of introducing students to fundamental scientific, engineering, and computing concepts, and for teaching robotics as a subject in its own right, but the term is broad enough to also apply to educational techniques which merely make use of robots for teaching some other subject.[7]. In their review of educational robotics platforms, Karim et al identified three broad classes of educational robot: what they called "brick based robot assembly kits," exemplified by the ubiquitous Lego Mindstorm kits; what they called "Modular Robotic Kits," which are designed to be assembled from common off the shelf components, and strike a balance between cost and the flexibility of Lego Mindstorm and its immediate competitors; and pre-assembled robots, such as the E-puck and the iRobot Create. [7], which tend to be smaller and less individually expensive, but also less flexible than robots from either of the other categories. Most of the designs which are currently in use are wheeled ground robots, but there are exceptions, such as the Nao, a humanoid robot from Aldebaran Robotics.[8]

Educational robot platforms are in use at all levels of education, from early childhood clear through post-secondary. At the lowest levels it can act as an engaging extension activity, particularly for math lessons. At intermediate levels robots provide a convenient means for engaging students with concepts of programming and introductory engineering topics. At the post-secondary level, uses range from something similar to the above, to use in actual robotics research.[4][5][7][8]

2.   Junkyard Hacks

Junkyard hacks is a concept for a hackathon focused on sustainability and e-waste reduction. Planning is currently in a

highly preliminary The basic idea is to provide participants with a selection of broken and discarded electronics, and to task them with creating something from the working components. This could be anything from individual sensors and motors up to the entire device, depending on the reason the original owner discarded it. Equipment, such as workbench power supplies and 3D printers, should be available, and a reasonable supply of batteries and basic electronics components (such as resistors and capacitors) should also be available. Partnerships with recycling centers and manufacturers should be considered, but donations from the community, and even items listed as "for parts" or "as is" on online retailers might be potential sources of broken or otherwise non-functioning electronics for the hackathon. The remainder of this paper will focus on a robotics project that itself serves as an example of the kind of project which participants in the hackathon might create.

3. REPURPOSING DISCARDED ROOMBAS FOR NETWORKED EDUCATIONAL ROBOTICS APPLICATIONS

3.1 Why Roombas?

The iRobot Roomba is an automated vacuum cleaner meant for home use. When purchasing new equipment, the iRobot Create, a robot built on the same platform but explicitly designed for use in educational robotics, may be a better choice, but when acquired used, the Roomba has quite a few reasons for recommendation, beyond the obvious reasons of price and availability.

For starters, all but the earliest models have a serial port which gives access to all functions of the robot, including motor control and sensor data.[6] The Create uses the same port with a slightly expanded set of features, but the point here is that the Roomba already provides an adequate interface for applications outside of their primary function as robotic vacuum cleaners.

Figure 1. The serial port on a 500 Series Roomba

Further, the platform itself is robust -- both mechanically reliable, as it is designed to be always on, automatically cleaning a room at scheduled intervals and autonomously returning to its charging base, and large enough to carry a heavier payload than many smaller entry level robotics kits, such as the GoPiGo from Dexter Industries. Even units produced before iRobot introduced the

serial interface have these advantages, and my be of interest for hackathon participants looking to control the motors directly, but the additional work involved in getting control over that has thus far precluded their use in the current preliminary work.

Finally, as a home appliance, there is extensive documentation available online for repairing nearly any problem a given unit might have. Odds are if something is wrong with a roomba, somebody else has already encountered the problem, figured out how to fix it, and made a text or video guide for others with the same problem. This is useful both in the case that a specific unit has an actual problem, and as a source of documentation for the inner workings of the robot in the case that an extension of functionality is desired.

3.2 Current Progress on the Project

Work has progressed at a glacial pace this semester due to various bureaucratic and logistical issues unrelated to the project itself, but some work has been done towards building a functioning prototype. Four Roombas were acquired from ebay, all listed as non functioning units being sold for parts or repairs, at a price of about $50 a piece -- a significant savings over a new iRobot Create 2, at $199.99. Of these, two turned out to be 500 series roombas, one turned out to be an older model that is still new enough to have the serial port, but unfortunately uses a different battery from the 500 series, and thus has not yet been tested, and the third was an even older, pre-serial port model, which takes the same kind of battery as the third Roomba.
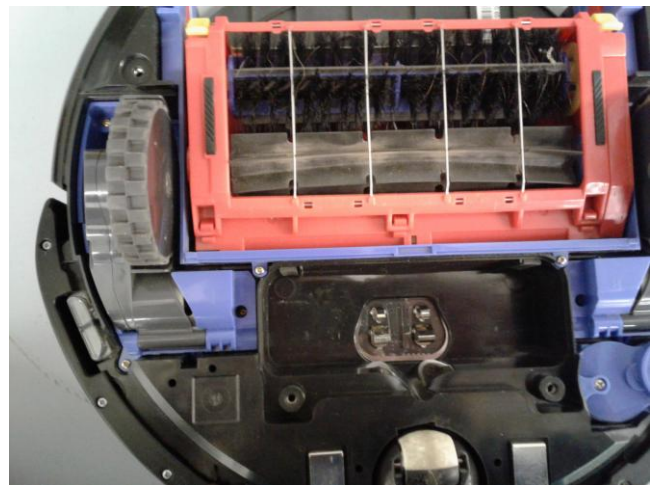

Figure 2. The battery compartment of a 500 series Roomba, with cover plate removed

31st Florida Conference on Recent Advances in Robotics, May 10-11, 2018, University of Central Florida, Orlando, Florida

25

Figure 3. The battery compartment on a pre-500 series Roomba.

Of the 500 series roombas, one turned out to simply need its battery contacts cleaned and a new battery slotted in. Once this was done, the unit started right up and proceeded to work as designed, vacuuming the floor of the lab. The other one had a damaged bump sensor in addition to needing a new battery, causing the unit to think one side of the robot is always in contact with an obstruction, but it should be possible to control over serial even without the use of this sensor, and if time and resources permit, instructions are available on the internet for the repair and replacement of the sensor. Unfortunately, at present time control via the serial port has not been tested, but doing so is the immediate next step.

3.3 Future Work

The immediate next step in the research process is, as mentioned above, connecting a computer to the serial interface and ensuring that everything on that end is working. The plan is to initially use the GPIO pins on a Raspberry Pi microcomputer for this task, moving to more powerful (and expensive) hardware only if necessary. Once the physical connection and serial logic are confirmed to be working, the next step will be to move from Raspbian to ROS as the operating system on the pi. ROS, short for Robot Operating System, is an open source operating system designed specifically for controlling robots, and is used on a wide variety of platforms, and comes with a driver for controlling Roombas. Using ROS will also allow us to leverage previous work done by members of the research group on networked applications involving an in house mesh network and a different robotics platform, the GoPiGo. Keeping things on ROS should, in general, allow us to transfer the higher level aspects of the work done with this platform to other robotics platforms should a reason to do so arise. Once this has been done, the plan is to connect the robots in a mesh network, and start adding additional sensors, such as ultrasonic sensors, accelerometers, and LIDAR, and use the data collected to make decisions within the swarm. Eventually, a set of classroom activities could be developed for educational use.

4. CONCLUSION

In conclusion, e-waste is a growing problem which needs to be confronted. We believe that the planned hackathon could result in ideas for novel ways of dealing with it. The example project above could be one such method; at the very least, it provides the genesis of an interesting alternative to more expensive educational robotics platforms.

5. ACKNOWLEDGMENTS

6. REFERENCES

[1] Anon. 2017. Electronic waste. (August 2017). Retrieved April 14, 2018 from http://www.who.int/ceh/risks/ewaste/en/

[2] Anon. 2017. Cleaning Up Electronic Waste (E-Waste). (December 2017). Retrieved April 14, 2018 from https://www.epa.gov/international-cooperation/cleaning-electronic-waste-e-waste

[3] C.P. Baldé, V. Forti , V. Gray, R Kuehr., P Stegmann. The Global E-waste Monitor – 2017, United Nations University (UNU), International Telecommunication Union (ITU) & International Solid Waste Association (ISWA), Bonn/Geneva/Vienna.

[4] T.L.A.Crenshaw 2013. Using Robots and Contract Learning to Teach Cyber-Physical Systems to Undergraduates. *IEEE Transactions on Education* 56, 1 (2013), 116–120. DOI:http://dx.doi.org/10.1109/te.2012.2217967

[5] Yen Air Caballero Gonzalez, Ana Garcia-Valcarcel Munoz-Repiso. 2017. Educational robotics for the formation of programming skills and computational thinking in childish. *2017 International Symposium on Computers in Education (SIIE)* (2017). DOI:http://dx.doi.org/10.1109/siie.2017.8259652

[6] iRobot. 2005. iRobot® Roomba® Serial Command Interface (SCI) Specification. *iRobot® Roomba® Serial Command Interface (SCI) Specification* (2005). Archived copy retrieved from https://web.archive.org/web/20131202230831/http://www.irobot.com/images/consumer/hacker/Roomba_SCI_Spec_Manual.pdf

[7] Mohammad Ehsanul Karim, Severin Lemaignan, and Francesco Mondada. 2015. A review: Can robots reshape K-12 STEM education? *2015 IEEE International Workshop on Advanced Robotics and its Social Impacts (ARSO)* (2015). DOI:http://dx.doi.org/10.1109/arso.2015.7428217

[8] Gauthier Sellin and Pierre LaRochelle. 2017. Internship Training in Robotics Lab: Exploring Robotics through hands-on experience. 30th Florida Conference on Recent Advances in Robotics (May 2017)

31st Florida Conference on Recent Advances in Robotics, May 10-11, 2018, University of Central Florida, Orlando, Florida

26

SOFT ROBOTICS: FIBER REINFORCED SOFT PNEUMATIC MULTIDIRECTIONAL MANIPULATORS, DESIGNING, FABRICATING, AND TESTING

Mohammad Holdar, Erik D. Engeberg

Ocean &Mechanical Engineering Department
College of Engineering and Computer Science.
Florida Atlantic University
Boca Raton, FL

mholdar2016@fau.edu, eengeberg@fau.edu

ABSTRACT

Traditional robots are made from hard materials like hard plastic or metal and consist of regular rigid mechanical parts. Using those parts has some limitations, like limited dexterity and lack of flexibility. Some of these limitations could be avoided through using a compliant material, because it has higher flexibility and dexterity. It is also safer to be in direct contact with humans. This research studies soft pneumatic manipulator (SPM) that move in multi degrees of freedom (MDOF), which makes it able to perform various functions. The study will include designing, fabricating, and testing for the range of bending and elongation. The SPM consists of three soft pneumatic chambers to reach unlimited points on its workspace through implementing bending and elongating movements. There are a lot of applications for this kind of soft actuators, like rehabilitation, underwater utilizes, and robots for surgery and rescues. Most soft pneumatic actuators provide one kind of movement, for bending, twisting, or elongating. Combining more than one kind of movement in one soft pneumatic actuator provides considerable contributions to the body of research. The SPM was controlled and tested to evaluate the achieved bending and elongating range.

Keywords

Soft actuator, Soft Robot, Pneumatic actuator.

1. INTRODUCTION

The latest advancements in the robotics field have changed from inflexible instruments using gears, pulleys, and bearings to elastic and flexible actuators [1]. One of the benefits of soft robotics is the ability to deal with delicate and sensitive items. Regular robots are less reliable to work with a person because they are made from hard materials that are subject to malfunction at any time. Nowadays, robots are involved in several fields, so establishing a safe contact with humans is necessary. Moreover, traditional robots have limited ability to handle delicate items without harming them. Soft robots provide an ideal solution to deal with human and sensitive objects. These difficulties in traditional robots can be minimized by utilizing soft actuators made of elastic materials like catalyzed silicones.

The functional part in the soft robot is the soft actuator. For that reason this research is focused on improving soft actuators with high capabilities. The working concept of the soft actuator is similar to the concept of a balloon when it is inflated. The pneumatic soft actuator is completely made out of elastic material, so it can be shaped easily when fluid inflates the cavities. There are a lot of applications for those kinds of actuators, like rehabilitation [2], underwater utilization [3], and medical robots for surgery [4], [5], [6], and [7]. Soft actuators are turning into an interesting area for research, because it helps to treat some of the traditional robots problems [8].

Additionally, it is interesting field for the researchers because they are affordable, safe, have more dexterity and not heavy. These adequacies help the researchers to use the soft robotics technology in designing some animals [9]. By taking the advantage of the compliance material that used in soft robotics, it is possible to mimic some biological organism such as fish [10], jellyfish [11], squid, octopus [12] and earthworm [13].

The research communities always focus in developing soft actuators with high capabilities because that enhance the ability of the soft robot to perform various tasks. The soft actuator made of soft material such as silicon rubber [1] and polymers [14] and that can be translated to either circular or bending motion [1]. Further, it can be designed to provide slow pnue-net or fast pneu-net [15]. There are two main outputs that evaluate the efficiency of the soft actuators which are the generated force and the end effector speed [15].

The SPM is a soft pneumatic actuator work by pumping gas or liquid into channel that blows up flexible fiber-reinforced chamber to achieve bending or elongating motion. Most of the current soft

31st Florida Conference on Recent Advances in Robotics, May 10-11, 2018, University of Central Florida, Orlando, Florida

27

pneumatic actuators afford only one type of movement: bending, elongating, or twisting. So, it is interesting to create more than one chamber imbedded in one soft actuator to manipulate in multi-DOF.

2. METHODOLOGY

The goal of this research work is providing SPM with high capability, dexterity, and flexibility. To accomplish this goal, many trials have been applied through design and fabricate soft pneumatic actuator that can manipulate in multi degrees of freedom (MDOFs). The SPM is made of catalyzed silicone Ecoflex 50-00[16].

2.1 Designing the SPM

The design of the SPM is cylindrically and has three chambers inflate independently. The movement of the module depends on pumping air on the chambers, so that will force it to inflate and leads to bend the SPM body. Thinner faces on chambers wall subjected to high expanding and may cause undesired bubbles. To avoid that radial expansion, the outer surface of the SPM is restricted helically with fiber to force the actuator to perform bending movement. The main body for all of the SPM are made of Ecoflex 00-50 but the end closer (end effectors) are created from Dragon Skin Silicones 10 [16]. The purpose of using Dragon Skin Silicones 10 in the end closer is preventing the expansion from the end effector side because Dragon Skin Silicones 10 has higher stiffening. The mold of the main body consists of five pieces. Figure 1 show the components of the mold which are the threaded container, pneumatic template, central channel template, and base mold.
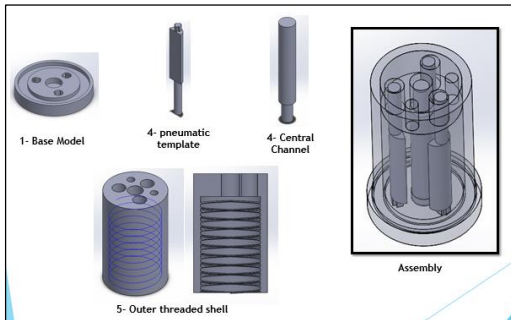

Figure 1. The components and assembly of the molds

2.2 3D Printing Molds

3D printing technology adopts to create the molds for casting the elastomer material. SolidWorks is a solid modeling computer-aided design (CAD) that used to draw and modify the SPMs and their molds. After drawing any component of the whole mold, the component is saved in STL format in order to be printed. The 3D-printer reads the STL file then generates a G code to implement the printing commands. The mold for SPM is shown in figure 2.

Figure 2. 3D printed molds

2.3 SPM Fabrication

Fabricating the SPM require six main steps; collecting the material and components, 3D printing, preparing and pouring the soft material, bonding the soft parts, wrapping the actuator with fiber thread, coating the outer surface with layer of Ecoflex 00-50, and tube insertion. The internal thread in the container mold may cause undesired tearing on the outer surface of the main body of the actuator due to its roughness. XTC-3D is an ideal product to achieve smooth surface. The threaded container, pneumatic template, and central channel template molds are placed on the base mold as shown on figure 3. The entire mold was assembled with hot glue through placing generous amount around the circumference to prevent leakage during injecting the Ecoflex 00-50. To bond the main body of the actuator and the end closer a thin layer of Dregon Skin Silicones-10 is poured over the end closer. The thread in the container mold leave clockwise and counter-clockwise groves on the SPM surface which afford guide for the fiber thread. The fiber thread will restrict the radial inflation without changing the diameter of the SPM. Then, coating a layer of Ecoflex 00-50 over the outer surface of the SPM provide stress distribution over the whole body. Additionally, this thin layer will keep the fiber thread in its place and provide a smooth surface.

Figure 3. a) put hot glue on the holes, b) pneumatic template, and central channel template molds are placed on the base mold, and c) the threaded container, entire mold was assembled with hot glue.

3. RUNNING AND EXPERIMENT SETUP

3.1 SPM Control

To run this system electronics and other components like pressure pumps, solenoid valves and microcontrollers are utilized. According to the SPM design, the three pneumatic chambers are actuating separately. Therefore, the system was created with three pumps, three solenoid valves, load cell, and three pressure sensors. The microcontroller, Arduino MEGA 2560, controls the inflation and deflation of the SPM and read the load cell and pressure sensors signals. For inflation, a constant voltage were energized the pumps, and the valves were off.

3.2 Bending and Elongating Testing

The SPM performance was tested through measuring the amount of bending angle (β) at different frequencies. Kinovea is a software that has the capability of tracking motion from saved video. The tip of the SPM module can reach unlimited points on its workspace through implementing bending movements by three soft pneumatic chambers. The Kinovea provides a planar tracking for the actuator which requires careful setting for the bending orientations. Figure 4 shows the orientations of the SPM when actuating chamber 1, 2, or 3. The SPMs will be tested in three cases; a) bending when pumping one chamber, b) bending when pumping two chambers, and c) elongating when pumping three chambers. After placing the SPM in the right position, a camera is used to recorded videos for the SPM during performing bending or elongating. The camera provides 60 frames per second that guaranteed precise drawing for the tracking paths. The camera should be exactly perpendicular to

31st Florida Conference on Recent Advances in Robotics, May 10-11, 2018, University of Central Florida, Orlando, Florida

28

the bending axes to achieve accurate tracking measurements. Before taking the videos, a ruler was attached to the video wallpaper to calibrate the tracking workflow. Then the taken video was uploaded to the Kinovea software to measure the range of the bending in the SPM body.
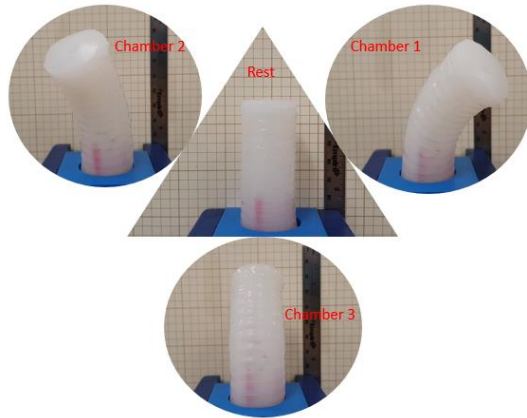

Figure 4. SPM orientations at rest and when actuating chamber 1, 2, or 3.
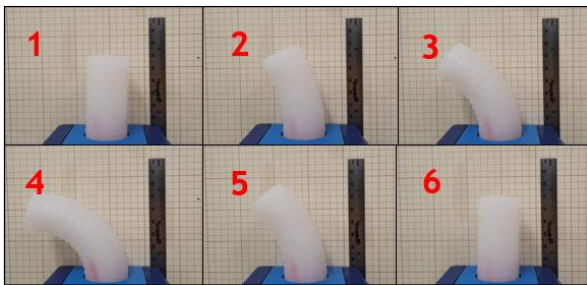

Figure 5. KINOVEA photo sequences for bending

4. RESULTS AND DISCUSSION

Tables 1 shows the bending angle (β) of the SPM at different frequencies, when one, two, and three chambers are actuated. Every single picture in the tables was calibrated, measured, and captured with the Kinovea software. It could be observed that the SPM perform wider bending when inflating two pneumatic chambers. Additionally, the bending angle increase as the frequency decrease because the actuator had more time to inflate. The forth column shows the elongating of the SPM at 1, 0.66, 0.5, 0.4, and 0.33 Hz. When the three chambers are actuated with the same rate, the SPM will expand vertically which cause the elongation. As expected, the SPM recorded higher elondation when actuate at lower frequency.

5. CONCLUSION

The soft pneumatic manipulators (SPM) was successfully designed, fabricated, and tested. The bending and elongating tests show that the SPM has high flexibility and dexterity which make it valuable for many applications.

Studies to develop performance and capabilities of soft pneumatic manipulators are vital for the future of soft robotics. With such researches, optimization of performance could be predicted and engineered to meet application demands

Table 1. Bending angle (β) of the SPM at 1, 0.66, 0.5, 0.4, and 0.33 Hz when one, two and three chambers were actuated.

6. REFERENCES

[1] Y. Sun, Y. S. Song, and J. Paik, "Characterization of silicone rubber based soft pneumatic actuators," in IEEE International Conference on Intelligent Robots and Systems, 2013, pp. 4446–4453.

[2] P. Polygerinos, Z. Wang, K. C. Galloway, R. J. Wood, and C. J. Walsh, "Soft robotic glove for combined assistance and at-home rehabilitation," in Robotics and Autonomous Systems, 2015, vol. 73, pp. 135–143.

[3] K. C. Galloway et al., "Soft Robotic Grippers for Biological Sampling on Deep Reefs," Soft Robot, vol. 3, no. 1, pp. 23–33, 2016.

[4] M. Cianchetti et al., "Soft Robotics Technologies to Address Shortcomings in Today's Minimally Invasive Surgery: The STIFF-FLOP Approach," Soft Robot., vol. 1, no. 2, pp. 122–131, 2014.

[5] M. Cianchetti, T. Ranzani, G. Gerboni, I. De Falco, C. Laschi, and A. Menciassi, "STIFF-FLOP surgical manipulator: Mechanical design and experimental characterization of the single module," in IEEE International Conference on Intelligent Robots and Systems, 2013, pp. 3576–3581.

[6] I. De Falco, A. Menciassi, and M. Cianchetti, "Stiff-flop surgical manipulator: design and preliminary motion evalutaion," 4th Jt. Work. New Technol. Comput. Assist. Surg., no. October 2014, pp. 131–134, 2014.

[7] I. De Falco, M. Cianchetti, and A. Menciassi, "A soft multi-module manipulator with variable stiffness for

31st Florida Conference on Recent Advances in Robotics, May 10-11, 2018, University of Central Florida, Orlando, Florida

29

minimally invasive surgery," Bioinspiration and Biomimetics, vol. 12, no. 5, 2017.

[8] D. Trivedi, A. Lotfi, and C. D. Rahn, "Geometrically exact dynamic models for soft robotic manipulators," in 2007 IEEE/RSJ International Conference on Intelligent Robots and Systems, 2007, vol. 24, no. 4, pp. 1497–1502.

[9] S. Kim, C. Laschi, and B. Trimmer, "Soft robotics: A bioinspired evolution in robotics," Trends in Biotechnology, vol. 31, no. 5. pp. 287–294, 2013.

[10] A. D. Marchese, C. D. Onal, and D. Rus, "Autonomous Soft Robotic Fish Capable of Escape Maneuvers Using Fluidic Elastomer Actuators," Soft Robot., vol. 1, no. 1, pp. 75–87, 2014.

[11] O. C. and E. D. E. Jennifer Frame, "Free-Swimming Soft Robotic Jellyfish," 29th Florida Conf. Recent Adv. Robot., 2016.

[12] R. V. Martinez et al., "Robotic tentacles with three-dimensional mobility based on flexible elastomers," Adv. Mater., vol. 25, no. 2, pp. 205–212, 2013.

[13] K. Jung, J. C. Koo, J. Do Nam, Y. K. Lee, and H. R. Choi, "Artificial annelid robot driven by soft actuators," Bioinspiration and Biomimetics, vol. 2, no. 2, 2007.

[14] F. Ilievski, A. D. Mazzeo, R. F. Shepherd, X. Chen, and G. M. Whitesides, "Soft robotics for chemists," Angew. Chemie - Int. Ed., vol. 50, no. 8, pp. 1890–1895, 2011.

[15] B. Mosadegh et al., "Pneumatic networks for soft robotics that actuate rapidly," Adv. Funct. Mater., vol. 24, no. 15, pp. 2163–2170, 2014.

[16] "Smooth-On Company." [Online]. Available: https://www.smooth-on.com/.

31st Florida Conference on Recent Advances in Robotics, May 10-11, 2018, University of Central Florida, Orlando, Florida

30

System Architecture of Medical Expertise Pooling Concept in terms of Potential Applications

Sakura Sikander, Sang-Eun Song

Department of Mechanical and Aerospace Engineering
University of Central Florida
Orlando, Florida

sakura@knights.ucf.edu, s.song@ucf.edu

ABSTRACT

Medical expertise pooling (MEP) is a concept to optimize the available physician resources and maximize the efficiency of the medical support system by matching the demand with the available expert physicians through a network of on-duty physician pool. The system to establish this concept, aims to utilize robotics, tele sensing and manipulation technologies to connect patients with physicians via network. The efficiency of this concept can be implemented in multiple potential applications. This paper describes enabling technologies and system architecture of the MEP concept in terms of possible applications.

Keywords

Telemedicine, Medical Expertise Pooling, Robotics, Network, Remote Healthcare, Remote Medical Devices.

1. INTRODUCTION

Medical expertise pooling (MEP) is a concept that proposes to utilize the total number of existing physicians and redistribute them all over the United States through network to overcome the physical limitation of the uneven ratio of physicians and patients across the nation [1]. The concept is to optimize the existing medical resources by matching the demand with the available physicians through a network of on-duty physician pool and to utilize robotics, tele sensing and manipulation technology to connect patients with physicians via internet.

Typical remote healthcare research applications are either focused on specific healthcare devices or systems with concentrated medical resources available in specific areas [2]–[7], whereas the proposed MEP focuses on distributing the medical expertise evenly across the nation on the basis of requirements [1].

For physicians to perform the first step toward treating a patient, they must start with some fundamental practices which are; checking vital signs, listening to the heart and body sounds with a stethoscope, and palpate to feel for any abnormalities. The most commonly used vital signs monitoring devices have the features of monitoring heart pulse rate, body temperature, and electrocardiography [2], [5], [6].

The proposed system can allow a physician to facilitate these fundamental steps as they would with an in-person patient at a long-distance for the fastest diagnosis. The enabling technologies include bioacoustics, haptics, and bi-directional control incorporated through robotics.

In this paper, we will discuss possible applications of MEP concept and related system design along with enabling technologies necessary to establish the concept.

2. POTENTIAL APPLICATIONS AND RELATED SYSTEM DESIGN

The proposed MEP [1] is vastly transformative and there are several cases where this paradigm can be implemented. Before going into the potential cases where this concept can be applied, let's look into the general system architecture which is designed to demonstrate the concept.

The system, divided into patient unit and provider unit as shown in Figure 1, involves three modules i.e. video and indicator module, bioacoustics module and haptic module. The patient unit and the provider unit will allow these modules to be used through a plug-and-play design simultaneously collecting medical data. The patient unit will be connected to the provider unit through network allowing virtual sensing capability to the physician. The provider unit is responsible for collecting, managing and demonstrating the tele sensing to the physicians so that physicians can diagnose the patient and provide necessary feedback.
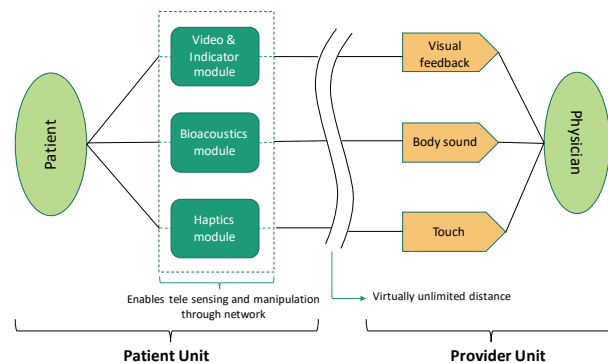

Figure 1. MEP concept: System Architecture [1]

31st Florida Conference on Recent Advances in Robotics, May 10-11, 2018, University of Central Florida, Orlando, Florida

31

The video and indicator module enables remotely and robotically controlled video camera and laser pointer for enhanced remote communication in which remote medical experts will be able to monitor the patients through video and point specific places on the patient body. The laser pointer mitigates the physical absence of medical experts as they can use it to explain and demonstrate the required action. The controllable laser pointer to localize a point of interest will be integrated with a small controllable camera attached to the ceiling of a transportation vehicle or a room. The system control will be attained by conventional visual servoing e.g. control joystick to move the pointer. In this system, a simple robotics technology is utilized in controlling video camera and pointer by enabling medical support using a bidirectional telemedicine unit that transmits critical medical information to the medical experts who can provide well-informed, life-saving decisions for the remote patients. Further, more complex robotics such as a robotic arm to provide physical support can easily be included to make it more automated.

In the bioacoustics module, a skin attached electronic stethoscope with multiple patches will be incorporated to process auscultation data from the body and provide continuous body sound monitoring. Electronic stethoscope technology enables sound magnification, noise canceling and data digitization. The feature of digital data processing helps to detect acoustic characteristics that human cannot hear.

The robotics enabled haptics module is to enable physical touch through the communication module directly to the physician to be able to feel for possible diseases like tumor or thyroid nodule in the patient's body. Enabling technologies i.e. haptics feedback, tactile technologies can be integrated to produce tactile imaging for palpation which is able to detect shape, size, and location [8], [9]. Further, to provide physician the actual texture, a surface can be created using soft robotics which will change its stiffness according to the input from the tactile image. As a result, when a physician sweeps his/her hand over the surface, he/she will be able to feel the stiffness to identify if there is any nodule.

Reliable and real-time delivery of medical data of patients to a distant medical facility is very important for the MEP system. In the system, the data will be sent wirelessly over long distances through the proposed advanced in wireless communication system [1]. In order to make the system efficient, as little information as
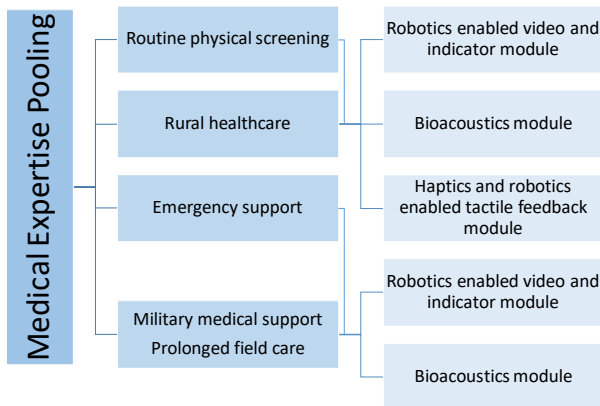
possible will be transmitted on the basis of importance without losing the accuracy of data. Since, wireless networks are likely to suffer from packet losses, a form of forward error correction (FEC mechanism) i.e. rateless coding [10] will be applied to recover the lost data and to ensure a fast and reliable communication over wireless networks.

Since, the MEP system has the features of providing robotically enabled visual, audio and tactile feedback remotely, it is vastly transformative, and it can have many potential applications in terms of remote healthcare. Possible applications include, general healthcare like routine physical screening, rural healthcare, emergency medical support, also this paradigm could be implemented for combat casualty care in military medicine (Figure 2).

In case of routine physical screening, the proposed MEP system could enhance quality of life and save time for both patient and physician. Patients will be able to maintain their routine physical screening staying at home.

With the use of MEP system in rural healthcare, people from rural areas will be able to get proper treatment since there will be no constraints of limited expert physicians. They will be able to get treatment from expert physicians through a network of on-duty physician pool regardless of their location.

In both cases i.e., routine physical screening and rural healthcare, three modules i.e., robotics enabled video and indicator module, bioacoustics module, haptics and robotics enabled tactile feedback module will be incorporated to provide diagnostics and treatment facilities using visual, audio and tactile feedback.

Now, if we consider mass casualty events or emergency medical situations, with the use of this MEP paradigm, early diagnosis is possible before hospital arrival, so patients do not have to undergo typical diagnostic procedures that need to be performed in the hospital. Once diagnosed using our proposed system, medical experts can provide assistance whether the patient needs to be admitted to a hospital or simple treatment can be done by local providers. Hence, the proposed system can save time and resources at hospital, which can be critical, especially in mass casualty events.

During combat casualty or prolonged field care (PFC), there is often a possibility that due to limited medical experts and lack of bidirectional communication, many soldiers cannot be survived. In such cases, MEP paradigm can be transformed in order to enable real-time remote medical support by off-site medical experts from
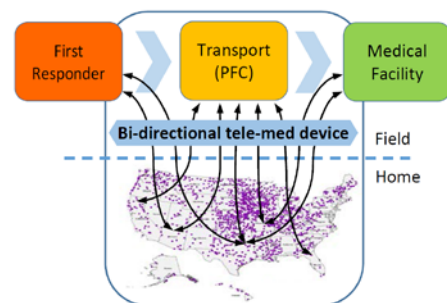

Figure 2. Potential applications of MEP concept

Figure 3. MEP concept: prolonged field care case

31st Florida Conference on Recent Advances in Robotics, May 10-11, 2018, University of Central Florida, Orlando, Florida

32

homeland who can provide critical support through secure network (Figure 3). The proposed system could provide advanced monitoring capability and deliver critical decisions during PFC, which can eventually increase survival rate.

Since, haptics enabled tactile feedback will not be necessary for mass casualty events, for such cases the system can be designed incorporating robotics enabled video and indicator module and bioacoustics module to maximize medical data acquisition and real-time communication for emergency situations.

3. DISCUSSION

The utilization of medical expertise pooling (MEP) saves hospital time and resources required during dire times. The system is critical to the enhancement of both hospitals and a patient's quality of life. MEP is able to distribute the medical experts throughout the nation regardless of their physical presence onsite. In the case of a mass casualty event, the use of the MEP will increase the hospital's efficiency and speed before the patient arrives at the hospital. This efficiency and speed will be possible due to the early diagnosis MEP will deliver to the physicians. The earlier a diagnosis can be determined, the quicker a patient can be treated. This would result in the decrease in total amount of examinations the patient has to typically undergo.

Development of MEP paradigm can revolutionize the medical support system by using physician resources all over the nation. This research can also be implemented for combat casualty care in military medicine, as well as the rural medical support in civilian healthcare. There are little to no alternative technologies that compares to this technology for both hospitals and the military. This research is important because implementing a MEP paradigm can lead to significant advancements in patient care.

4. REFERENCES

[1]   S. Sikander, P. Biswas, P. Kulkarni, H. Mansy, N. Rahnavard, and S.-E. Song, "A concept of medical expertise pooling by tele sensing and manipulation: Emergency medicine case," in *2017 IEEE Healthcare Innovations and Point of Care Technologies (HI-POCT)*, 2017, pp. 233–236.

[2]   A. Mehrotra, A. B. Jena, A. B. Busch, J. Souza, L. Uscher-Pines, and B. E. Landon, "Utilization of Telemedicine Among Rural Medicare Beneficiaries," *JAMA*, vol. 315, no. 18, p. 2015, May 2016.

[3]   G. Durner, J. Durner, H. Dunsche, E. Walle, R. Kurzreuther, and R. Handschu, "24/7 Live Stream Telemedicine Home Treatment Service for Parkinson's Disease Patients," *Mov. Disord. Clin. Pract.*, vol. 4, no. 3, pp. 368–373, 2017.

[4]   G. W. Muniz *et al.*, "Promoting early diagnosis of hemodynamic instability during simulated hemorrhage with the use of a real-time decision-assist algorithm," *J. Trauma Acute Care Surg.*, vol. 75, no. 2 Suppl 2, pp. S184-9, 2013.

[5]   N. N. Castellano, J. A. Gazquez, R. M. García Salvador, A. Gracia-Escudero, M. Fernandez-Ros, and F. Manzano-Agugliaro, "Design of a real-time emergency telemedicine system for remote medical diagnosis," *Biosyst. Eng.*, vol. 138, pp. 23–32, Oct. 2015.

[6]   M. Abo-Zahhad, S. M. Ahmed, and O. Elnahas, "A Wireless Emergency Telemedicine System for Patients Monitoring and Diagnosis," *Int. J. Telemed. Appl.*, vol. 2014, pp. 1–11, 2014.

[7]   A. Panayides, M. S. Pattichis, C. S. Pattichis, and A. Pitsillides, "A tutorial for emerging wireless medical video transmission systems [Wireless Corner]," *IEEE Antennas Propag. Mag.*, vol. 53, no. 2, pp. 202–213, 2011.

[8]   S.-Y. Kim, J.-H. Ryu, and W. Lee, "Palpation simulator with stable haptic feedback," *Minim. Invasive Ther. Allied Technol.*, vol. 24, no. 4, pp. 211–217, Jul. 2015.

[9]   C. Van Nguyen and R. F. Saraf, "Tactile Imaging of an Imbedded Palpable Structure for Breast Cancer Screening," *ACS Appl. Mater. Interfaces*, vol. 6, no. 18, pp. 16368–16374, Sep. 2014.

[10]   P. Maymounkov, "Online codes," *Secur. Comput. Syst. Gr.*, 2002.

31st Florida Conference on Recent Advances in Robotics, May 10-11, 2018, University of Central Florida, Orlando, Florida

33

A Sensor for Visibility Determination under Fog Conditions

Christina Drake, Harish Chintakunta, Christopher Coughlin, Ezequiel Garcia, Scott Hoos, Kristyn Ardrey, Paul Luckey and Aubury Erickson

Florida Polytechnic University
4700 Research Way
Lakeland, Florida 33805

cdrake@floridapoly.edu, hchintakunta@floridapoly.edu, ccoughlin@floridapoly.edu

ABSTRACT

In this paper, we describe a sensor approach utilizing commercial highway cameras for visibility determination under fog conditions. We achieved this by creating an engineered object in the field of view (FOV) of the camera that utilized two measurement approaches (contrast and light evaluation) via image processing. We employ the Koschmieder's law to estimate visibility conditions from fog measurements, and scattering profile to estimate visibility conditions from visible measurements of a modulated light. The contrast measurements are used during the daytime, and light evaluations during night. We discuss the merits and challenges of such an approach.

Keywords

Weather Sensor, Image Processing

1. INTRODUCTION

The onset of sudden fog or extremely dense fog is an issue that is critical to driver safety. Current State of the Art in real time fog detection is plagued by several false positive and false negative events due to the nature of fog formation, specifically when looking at low fog formation that would impact drivers. Both the thermodynamics and kinetics of fog formation make it difficult to evaluate over a small interrogation volume. Existing laser based sensors, such as the Vaisala PWD12, while excellent at close range measurement, are expensive, and are not able to get around the elusiveness of the type of fog that decreases driver visibility and detect with high confidence. Highway and other commercial cameras have the advantage of viewing a scene near a roadway and other areas of interest and typically have a large viewing area. We sought to take advantage of this by creating an object in the field of view of the camera and used it in conjunction with image processing for the purpose of visibility determination.

There are similar studies that utilize image processing on commercial cameras for either visibility or fog determination. The contrast of a "black" target is one established way of making visibility determinations that has been accepted and widely used since the 1920s. Hautiere et al. [1] demonstrated an onboard vehicle camera for fog detection. Similar to our approach, this group utilized a variation of contrast evaluation in the FOV based on the treatment by Koschmeider [2]. This technique provided only an estimation of visibility, and was inoperable at night. Tang et al [3] also sought to create a contrast sensor utilizing a camera. They compared a black target to the horizon. At reduced visibilities, their approach began to deviate and see decreased correlation. This is likely because they used the horizon as the contrast media to the black and was not controlled in the measurement.

In our approach, we also utilize Koschmieder's law as a basis of our contrast measurement but utilized against a tightly engineered contrast piece. We also utilized an LED light (650 nm) to monitor scattering with increased fog density.

2. SENSOR APPROACH

For the contrast portion of our initial sensor prototype, we utilized a high albedo, diffuse white surface with a near perfect black contrasting agent for visibility determination at varying fog densities. The departure from convention that makes our sensor unique is that a high albedo material (the front contrast pattern) is used in place of the sky or horizon as a proxy to ambient light or scene brightness, Figure 1.
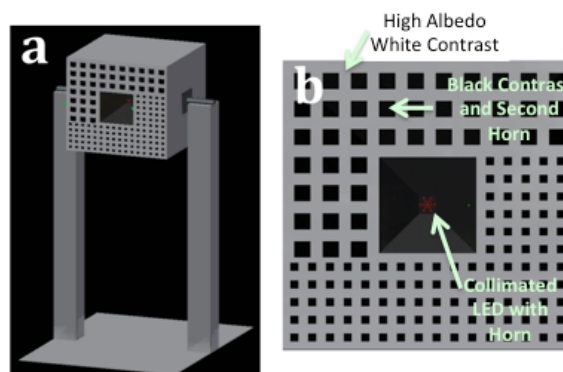

Figure 1. a) CAD of first sensor prototype and b) Sensor face and main components.

31st Florida Conference on Recent Advances in Robotics, May 10-11, 2018, University of Central Florida, Orlando, Florida

34

For our initial sensor prototype, a horn geometry was implemented behind the high albedo pattern, into the box, and utilized a highly absorbing, non reflective paint (black). The high albedo (white) front pattern utilized a paint and substrate that was highly diffuse and behaved as a lambertian surface. The difference in reflectivity between the dark and light portions of the contrast piece across visible wavelengths is close to 90%.

Figure 2. Prototype of sensor during a live field test in winter of 2017 along I-75 near Wildwood, FL.

For the light evaluation portion of our sensor, we utilized a modulated 650 nm collimated LED. We tested smaller versions of the prototype in an environmental chamber in the lab. These smaller sensor mock ups were the validation pieces used to validate the physics that lead up to the full sensor prototype shown in Figure 2. We describe the validation procedure below.

Using the treatment by Koschmeider, we can describe the following relation between the visual contrast $C_v(x)$ at a distance x with the extinction coefficient b_{ext} as,

$$C_v(x,b) = C_v(0)e^{-bx}; \qquad (1)$$

Assuming b to be zero under no fog conditions, $C_v(0)$ will be the measured contrast at the camera under these conditions. We use a laser – photodetector setup to estimate the true extinction coefficient using the following relationship,

$$P(b) = P(0)e^{-bd}; \qquad (2)$$

where P(0) is the power received at the photodetector under no fog conditions. From equations 1 and 2, we obtain

$$lnC_v(x;b) = [lnC_v(0)–(x/d)lnP(0)] + (x/d)ln[P(b)] \qquad (3)$$

This implies that the log-log plot of the contrast versus the power detected at the photodetector should be linear with a slope of x/d.

It was also necessary for us to create a table that related visibility back to our sensor scheme. We adopted a version of the International Visibility Code [4, 5] that ties visibility to contrast under differing fog conditions, Table 1. This is done by relating

	Weather Condition	Meteorological Range (m)	0.05 contrast	0.02 contrast
0	Dense Fog	<50	>59.9	>78.2
1	Thick Fog	50-200	59.9 - 15	78.2-19.6
2	Moderate Fog	200-500	15-5.99	19.6-7.82
3	Light Fog	500-1000	5.99-3	7.82-3.91
4	Thin Fog	1000-2000	3-1.5	3.91-1.96
5	Haze	2000-4000	1.5-0.749	1.96-0.954
6	Light Haze	4000-10000	0.749 - 0.3	0.954-0.391
7	Clear	10000-20000	0.3-0.15	0.391-0.196
8	Very Clear	20000-50000	0.15 - 0.06	0.196-0.078
9	Exceptionally Clear	>50000	<0.06	<0.078

3. SENSOR PERFORMANCE
3.1 Test set up
We created an environmental chamber for controlled fog density in our lab with the ability to directly control the amount of ambient light in the chamber. A typical test set up is shown in Figure 3. The contrast portion of the sensor, or LED, is typically set up at the back of the chamber. The desired ambient light conditions (direct visible light, diffuse visible light, or near infrared - NIR light) could be created depending on the intended outdoor conditions. A 635 nm laser is used to monitor the fog density in the box. A custom fog machine was utilized that outputs a persistent fog with a median particle size of 1 μm.

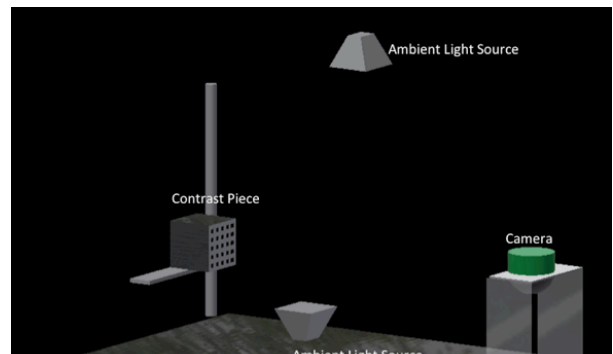

Figure 3. Placement of components within environmental chamber. Not shown are laser, photodetector and fog input.

31st Florida Conference on Recent Advances in Robotics, May 10-11, 2018, University of Central Florida, Orlando, Florida

35

Two different cameras were utilized during our experiments. A Bosch surveillance camera similar to those used on major interstates in Florida, and a Thorlabs 1.4 Megapixel Color Scientific CCD Camera. The scientific camera was utilized to help us understand and confirm the baseline physics of our approach. We also used it to better understand the compensation mechanisms, as well as camera response function, utilized in high-end surveillance cameras such as the Bosch, and their impact on utilizing visible cameras as measurement platform.

3.2 Verification of Sensor Behavior

We performed a series of experiments aimed at verifying that our engineered contrast approach obeyed Koschmieder's Law; that the contrast of an object decreases exponentially with extinction coefficient. We increased the fog density incrementally in our environmental fog chamber while measuring the contrast at each density. We placed a contrast pattern in the fog chamber (Figure 3), and recorded a video of the pattern under each fog density with the research grade camera. The frames from the video were used to measure the contrast at each fog density. The ground truth information for fog density was retrieved through retrieval of the extinction coefficient by means of a laser-photodetector setup.

In this experiment, we used 10 fog densities. To test the effect of ambient light on contrast measurements, we varied the ambient light intensity for each fog density in the fog chamber, and made contrast measurements for each ambient light intensity. This test was to make sure that we were successfully compensating for the camera response function in the pixel values. Successful compensation should be manifested by independence of the contrast measurements on the ambient light intensity. The ambient light intensities were measured using a Lux sensor connected to an Arduino. This measures the perceived light brightness to a human eye. For each fog density, we recorded the power of a laser beam measured at the photodetector.

To measure contrast, we computed the contrast every frame in each video and split the contrast measurements according to the different light intensity levels in the video. An average contrast and light intensity were computed for each light intensity, as well as for each fog density. As shown in Figure 4, the contrast measurement is almost invariant to the ambient light. We averaged contrast values over all ambient light levels in our verification of Koschmieder's law.

Ideally, the apparent contrast of an object should only depend on the extinction coefficient of the medium (fog or forming fog), and not on the ambient light intensity. However, due to various post processing and optical adjustments performed in commercial cameras, this is not the case in general. Figure 5 shows the change in contrast measured from our commercial camera with change in ambient light conditions. The x axis in Figure 5 corresponds to recorded ambient light using a lux meter, and the y axis corresponds to the measured contrast in the pattern. The figure on the right shows the contrast measurements after adjusting for the Camera Response Function (CRF) of the camera. As can be seen, accounting for CRF does not produce any appreciable improvement in the measured contrast. This indicated that adjustments to exposure and software adjustments play a dominant role in changing contrast with changes in ambient light.
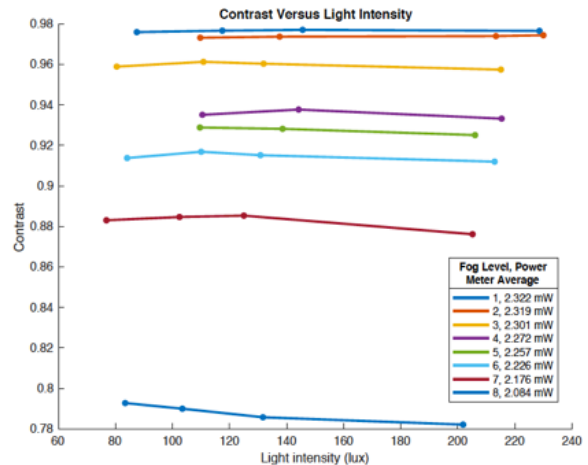

Figure 4. Change in contrast of engineered piece as a function of ambient light intensity

Therefore, for this preliminary proof of concept experiment, we used a research grade camera and shut off all the post processing. As expected, the contrast was then invariant to ambient light intensity. Figure 4 shows the contrast measurements with changing ambient light under various fog levels, and Figure 6 shows the average (over all light intensities) contrast for each fog level.
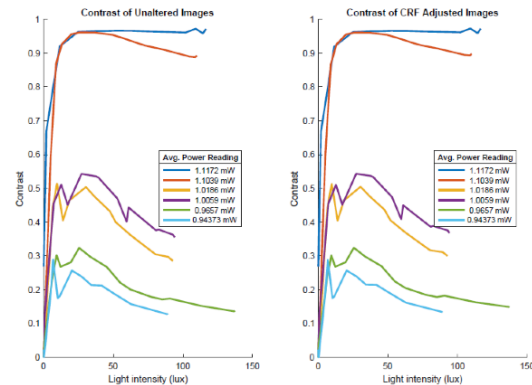

Figure 5. Contrast of unaltered commercial camera data (left) versus CRF adjusted data (right).

Using the average laser power and the average contrast measurement for each fog density, we were able to fit a regression line to the log(contrast) versus log(power level) curve. From Equation 3, we know that the slope of the log-log curve is equal to the ratio of the two distances: the distance from the contrast pattern to the camera and the distance from the laser collimator to the photodetector. The slope of the regression line in Figure 7 was 1.892 while the actual ratio (x/d) was 1.860, with an error of 1.6% in the slope. This is in very good agreement with theory and we feel confident that our contrast approach is appropriate to determining fog density.
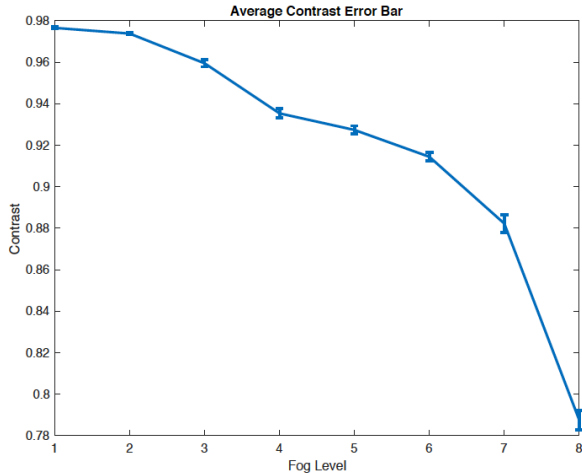
31st Florida Conference on Recent Advances in Robotics, May 10-11, 2018, University of Central Florida, Orlando, Florida

36

Figure 6. Average contrast measurement with standard deviation of the pattern, with increasing fog intensity
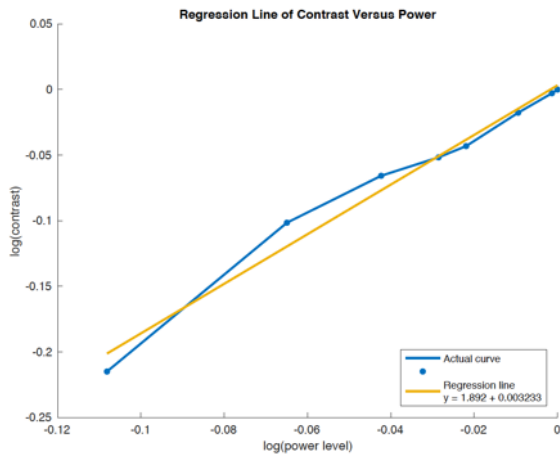

Figure 7. Regression line of the log-log curve of contrast and power level.

3.3 Live Test of Prototype Sensor

We ran a "live test" of our sensor prototype on I-75 near Wildwood, Florida. We placed 2 sensor boxes in the FOV of the cameras located at 167ft and 261ft from the camera post. These distances were chosen to have one sensor box in the depth of field of focus for the camera (167ft) and another just outside of the depth of field for focus (261ft) while maintaining a single scene for the test. Our test protocol was that the camera at that location is panned to a determined preset (with the focus conditions mentioned above) and is set there for 5 minutes while we acquire data. We were not able to utilize the cameras full time since they were in active use by the Orlando Regional Transportation and Management Center (ORTMC).

We utilized the following in evaluating our sensor:

1. When ambient light is available, we measure the contrast of the pattern on our sensor. The visibility is then estimated using Koschmieder's law.

2. During nighttime, we measure the scattering profile of our modulated light source, and estimate the visibility from this scattering profile. The camera records in the visible and NIR mode (gray scale) during nighttime. Here we present some of our preliminary findings from that test.

3.3.1 Visibility Estimation During Day

Figure 8 shows snapshots from 3 videos, one each under a) no-fog, b) low/medium fog and c) dense fog condition. We measured the contrast of the pattern on the sensor from each video. Table 1 summarizes the contrast measurements. Table 2 clearly indicate that at least as a first step, the contrast measurements provide a simple means for classifying the visibility into these 3 categories.
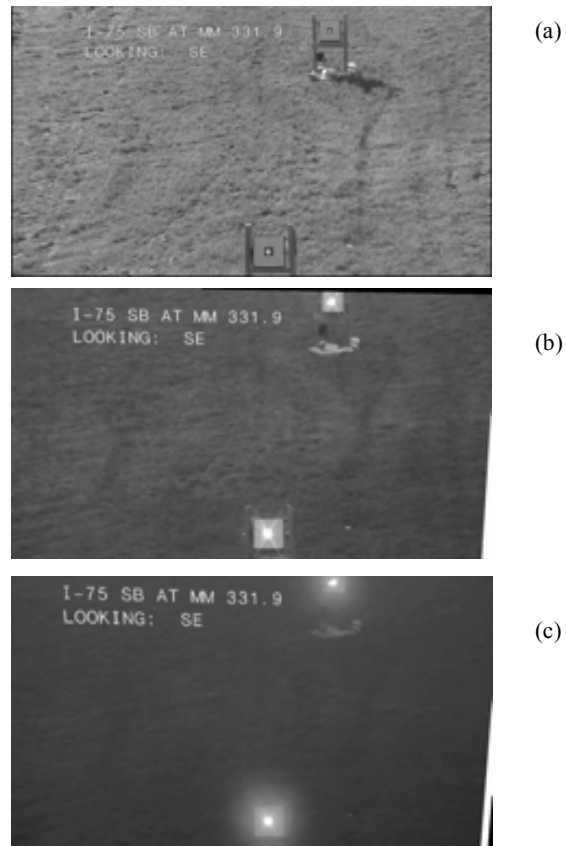

Figure 8. Snapshots from videos under (a) no-fog, (b) medium-fog, and (c) dense fog conditions.

Note that the contrast even under no fog conditions is rather low ($\approx 0{:}4$). There could be two reasons for such a low contrast, 1) the camera does not have sufficient resolution to clearly resolve the pattern, or 2) the recording method we used to record these videos causes loss of resolution. We are currently investigating which of these is the actual cause for low contrast under no fog conditions. We are also currently working on estimating the actual visibility (in meters) from the contrast measurements.

31st Florida Conference on Recent Advances in Robotics, May 10-11, 2018, University of Central Florida, Orlando, Florida

37

Table 2. Image luminance and contrast measurements from the images above. Ib is the background luminance, I is the black target luminance, and C is the contrast.

Frame	I_b	I	C
Nonfoggy	143.5748	89.3829	0.3774
Foggy	178.0281	156.6073	0.1203
Super-foggy	156.8281	154.7122	0.0135

3.3.2 Visibility Estimation During Night

The pattern on the sensor (being passive) is not visible during night. We are currently estimating visibility at night using the scattering profile of a modulated light source (preliminary results presented in this paper).

Under no fog conditions, the angle of incidence at the camera of light rays emanating from the light source will be very close to the direct line of sight. Under foggy conditions however, the scattering from the fog particles increases the range of the angle of incidence of these rays. We define the scattering profile to be function I(θ), where I is the irradiance of the modulated light incident on the camera at a 2-dimensional angle θ. Our objective is to classify the visibility conditions using I(θ).
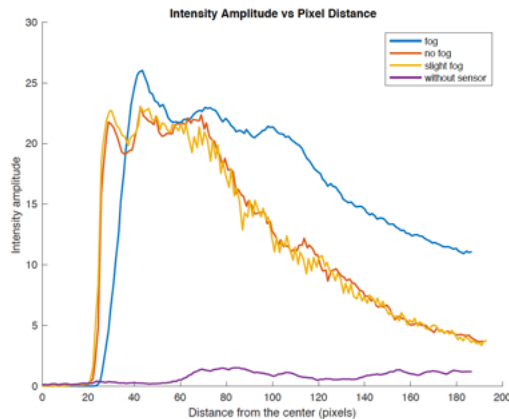

Figure 9. The scattering profiles extracted from videos taken at night under various visibility conditions.

.

Figure 9 shows the scattering profiles extracted from videos under different visibility conditions. For clarity of presentation, we restricted θ to a straight line. Note that in this case, the angle θ will be proportional to number of pixels from the center. We can make the following observations about the scattering profiles:

1. As Figure 9 shows, the scattering profile is much broader under foggy conditions when compared to no fog conditions. This shows that the scattering profiles can be used for classification between fog and no-fog conditions.

2. The scattering profile is almost flat (in fact, a random curve) when the camera is not focused on the sensor. This

indicates that the demodulation algorithm successfully removes background illumination.

3. The sensitivity of the scattering profile is not sufficient to distinguish between no fog and light fog conditions. We are currently working on improving the demodulation algorithm to improve this sensitivity. Our end goal will be to use the scattering profile to estimate scattering coefficient, and hence the visibility.

4. The scattering profiles are close to zero near the center because the pixels in the direction of the line of sight are saturated and hence all modulation information is lost. This cannot be avoided since the Bosch camera will adjust its aperture to compensate for the low ambient light conditions, thus saturating these pixels. This automatic adjustment also introduces inaccuracies in the demodulation algorithm.

4. CONCLUSION

We have demonstrated a viable sensor approach for visibility determination due to fog using an image processing approach for an engineered sensor piece, utilizing commercial road-side cameras. Both contrast and light evaluation are approaches that can be utilized. Challenges associated with this approach are compensation mechanisms in commercial cameras that make it challenging to determine true sensor conditions from a baseline. Future approaches will look at variants of our sensor approach that avoid triggering these conditions.

5. ACKNOWLEDGMENTS

6. REFERENCES

[1] Hautiére, Nicolas, et al. "Automatic fog detection and estimation of visibility distance through use of an onboard camera." Machine Vision and Applications 17.1 (2006): 8-20.

[2] Von Harald Koschmeider; Theorie der horizintalen Sichtweite II: Kontrast und Sitchweite; Beitr. z. Phys. d. fr. Atmosph. XII, S. 33-53, 1925

[3] Tang, Fanjie, et al. "A new visibility measurement system based on a black target and a comparative trial with visibility instruments." Atmospheric Environment 143 (2016): 229-236.

[4] Sabatini, Roberto, Alessandro Gardi, and M. Richardson. "LIDAR obstacle warning and avoidance system for unmanned aircraft." International Journal of Mechanical, Aerospace, Industrial and Mechatronics Engineering 8.4 (2014): 718-729.

[5] Zabidi, Suriza Ahmad, et al. "Investigating of rain attenuation impact on free space optics propagation in tropical region." Mechatronics (ICOM), 2011 4th International Conference On. IEEE, 2011.

31st Florida Conference on Recent Advances in Robotics, May 10-11, 2018, University of Central Florida, Orlando, Florida

38

Force and Pressure Control of Soft Robotic Actuators

Joseph Ingicco*, Mostapha AlSaidi*, Moed Abd, Craig Ades, Erik Engeberg

Ocean and Mechanical Engineering Department

College of Engineering and Computer Science

Florida Atlantic University

jingicco2013@fau.edu, malsaidi2015@fau.edu, mabd2015@fau.edu, cades@my.fau.edu, eengeberg@fau.edu

ABSTRACT

Soft Robotic Actuators (SRAs) have piqued the interest of researchers in recent years. SRAs are generally constructed of soft elastomers and use air or water as a mean of actuation. Due to the inherent properties of these actuators, they are ideal for Human-Robot Interactions (HRI), exoskeletons for rehabilitation and for grasping delicate objects. Since SRA's are actuated using a fluid, being able to effectively control the rate of actuation, pressure and the force applied is necessary so that the actuator and the object being grasped does not get damaged. This paper aims to evaluate three types of controllers, an open-loop controller, pressure-feedback controller, and a force-feedback controller, all used to control an SRA. A custom test stand was built to hold the SRA and test it with all three controllers. The pressure-feedback controller was set to limit the pressure to 8.9 kPa and the force was limited to 0.147 N in the force-feedback controller. Since the open-loop controller had no feedback, the SRA was actuated at a specified frequency while force and pressure measurements were taken. The force-feedback and the pressure-feedback controllers accurately controlled the actuators and the open loop-controller was able to actuate the SRA reliably.

Keywords
Soft robotic actuator, controller, force feedback, pressure feedback

1. INTRODUCTION

Soft Robotic Actuators are at the center of robotic innovation for their dexterity and low-cost manufacturability, since molds for SRAs can easily be made using 3D printers. SRAs are made from extremely elastic material such as Eco-Flex 30 [Smooth-On Inc] and other types of elastomers. Since there are no rigid links in SRAs, they are ideal for tasks involving HRI and for grasping delicate objects such as eggs or coral [1], [2]. Methods of actuation for these actuators vary depending on design and use, ranging from compressed fluids, chemical reactions and Shape Memory Alloys (SMA) [3], [4]. SRAs take on many bio-inspired designs with many stemming from octopus, fish and caterpillars; and can produce life-like motion [2], [4]–[6].

In a previous study that used an open loop controller to actuate SRA's, it was concluded that the frequency of actuation and the geometry of the actuator greatly effects the performance of a soft robotic actuator [7]. Furthermore, it was noted that a higher pressure built up inside the actuator and higher force exerted by the actuator were achieved at lower frequencies. With further testing it was determined that better control of SRAs was needed to reach peak performance.

The purpose of this study is to evaluate the performance of three different control methods for controlling a SRA. An open loop controller was used to control the frequency of actuation of the SRA. The closed loop pressure-feedback controller and the force-feedback controller were built off the open loop controller with the aim of accurately controlling the actuation of the SRA by limiting the force applied and the pressure inside the SRA.

The same actuator was used throughout this paper and the only parameter that changed was the method of control.
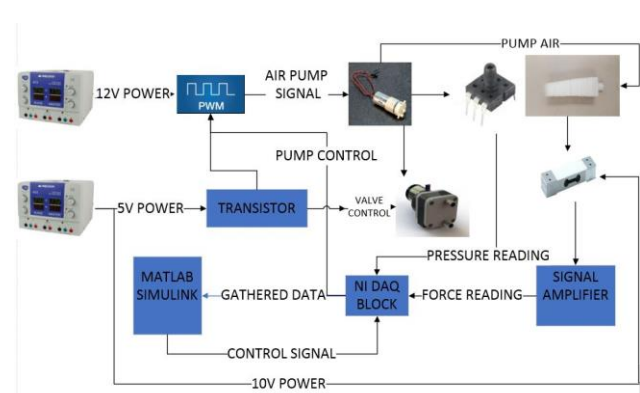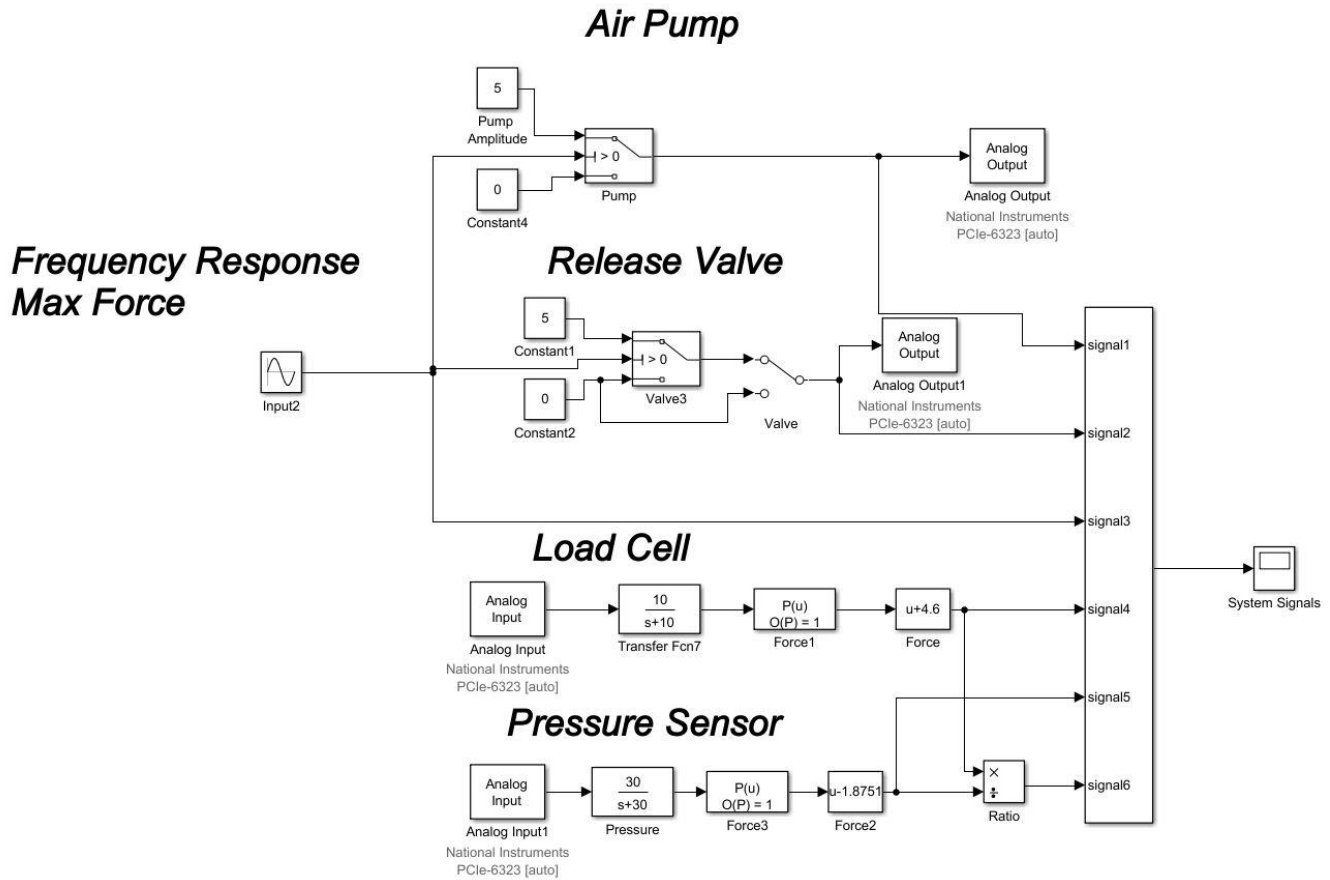

Figure 1: Test Station Setup

Figure 2: Open Loop Controller Layout

2. Experimental Setup

The test stand, shown in Figure 1, was comprised of a vertical aluminum plate that held the 3-D printed actuator mount and the 1kg load cell (LSP-1 by Transducer Techniques), which was used to monitor the force applied from the actuator. Off to the side of the stand was the SyRen 50 motor driver was used to send power to a generic 6V air pump. A 12V 2way solenoid valve was used to deflate the actuators. A Honeywell 0-15 psi pressure sensor was used to monitor the pressure of the actuator. Finally, a National Instruments DAQ block was used to allow the hardware to communicate back and forth with MATLAB/SIMULINK.

The actuator was fabricated using the same procedures as in [7]. A photo sequence of the actuator inflating is shown in Fig.3.

3. Controllers

3.1 Open Loop Controller

The open loop controller, shown in Fig. 2 used a sine wave as the input to the system. The frequency of the sine wave determined the rate of actuation for the SRA. For this controller the amplitude was set to 1. In this experiment, a frequency of 1 rad/sec was kept constant in all three controllers. The sine wave acts as a switch by activating the air pump and closing the valve when the amplitude is positive and opening the valve and turning off the pump when the value is negative. The force, pressure, error signal, and the input signal were recorded and saved to the MATLAB work space.
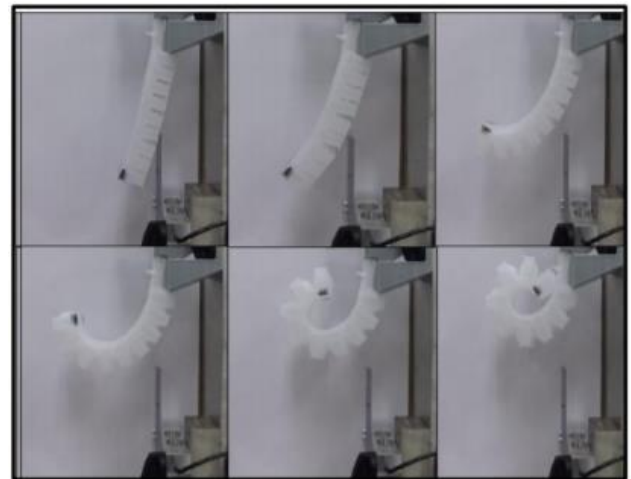
Figure 3: Photo Sequence of Actuator Inflating [7]

3.2 Force Feedback Controller

The force-feedback controller's sine input feeds into a gain block that is used to specify the force desire (F_D) (Fig. 4). For this experiment this gain was set to 15, which equates to .147 N (15 g) as the input force (F).

31st Florida Conference on Recent Advances in Robotics, May 10-11, 2018, University of Central Florida, Orlando, Florida

40

Force Feedback Control
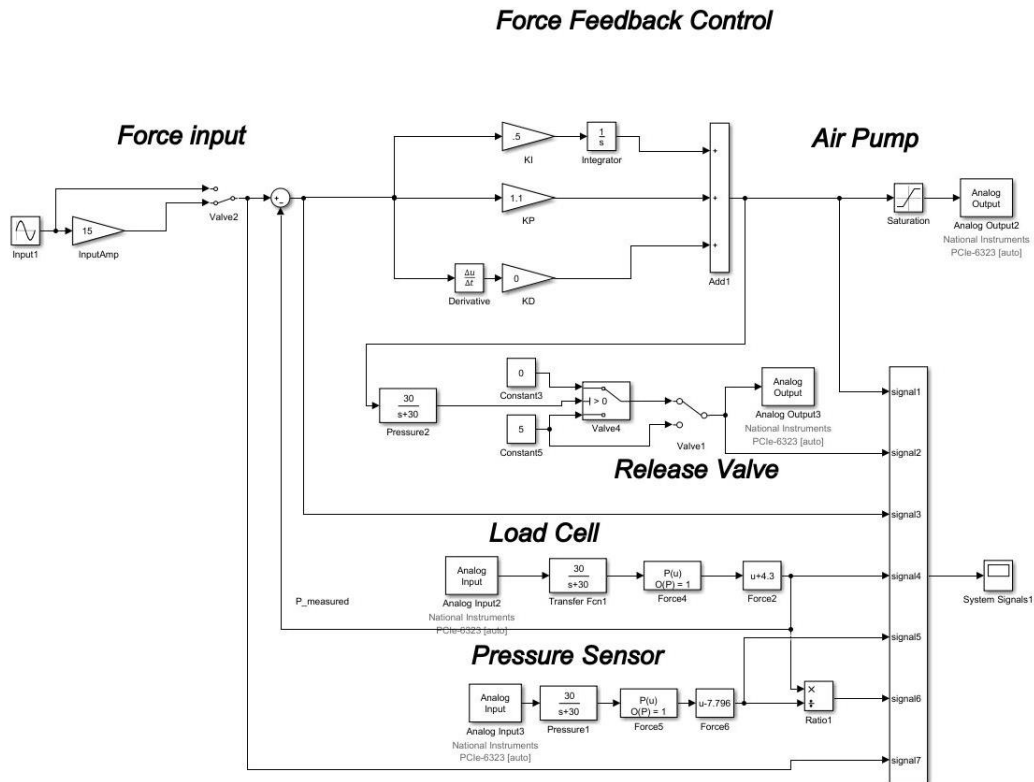
Figure 4: Force Feedback Controller Layout

Pressure Feedback Control
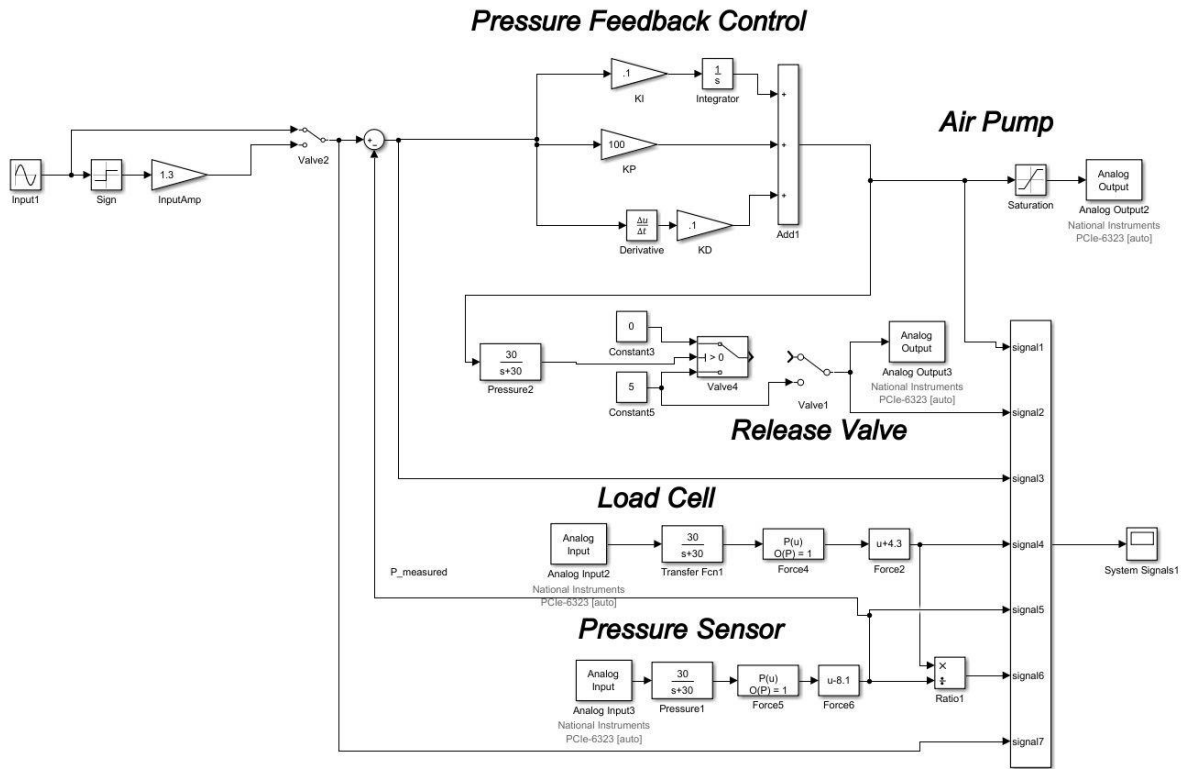
Figure 5: Pressure Feedback Controller Layout

31st Florida Conference on Recent Advances in Robotics, May 10-11, 2018, University of Central Florida, Orlando, Florida

41

The force tracked (F_T) was the force measured at the end effector of the actuator. As the SRA inflated, the end effector pushed on the plexiglass attached to the load cell which recorded the force applied by the actuator.

To optimize this control scheme was used. The value for the proportional and integral gain are:

$$K_P = 1.1 \text{ and } K_I = 0.5$$

3.3 Pressure Feedback Controller

The pressure-feedback controller (Fig. 5) has a sine wave that fed into a gain block set to 1.3, which limited the pressure desired (P_D) to 8.9 KPa (1.3 psi). The pressure tracked (P_T) was the recorded pressure inside the actuator during inflation and deflation. This controller used a PID control scheme with the following gains:

$$K_P = 100, K_I = 0.1 \text{ and } K_D = 100$$

4. Results and Discussion

Figure 6 shows a comparison of the force measured for the same actuator, at a frequency of 1rad/s, using the open loop and force feedback controllers.

As shown the force achieved using the closed loop controller with force feedback was consistent throughout the experiment and had a value of 0.15N. This value is greater than that achieved with an open loop controller that was consistent at a value of 0.12 N.

Moreover, the force controller achieved much better tracking of the input signal as shown in Figure 6, where the error is consistently less than 0.01 N. As shown in the figure the tracking is accurate and consistent with minimal amplitude noise. The noise did not noticeably affect the performance of the actuator.

An additional metric of performance of the controller is the mean and standard deviation of the error signal. The mean had a value of 0.00179 N and standard deviation equal to 0.0024 N. The value of the standard deviation is almost double that of the mean due to the noise in the signal being comparable to the amount of error. Though the variation in the amplitude of the noise is minimal, it was frequent, which resulted in a higher standard deviation.
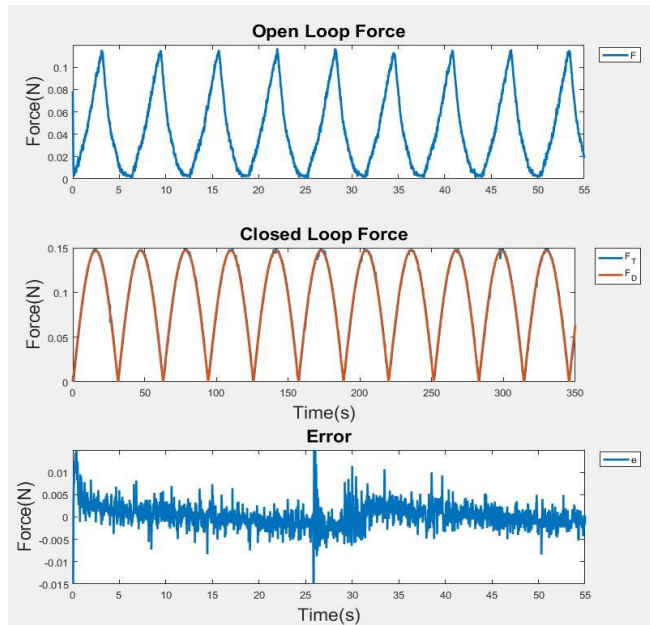

Figure 6: Open Loop Vs Force Feedback

Figure 7 shows a comparison of pressure measured inside the SRA at a frequency of 1rad/sec using the open loop and pressure feedback controller. The pressure is displayed in units of kPa and as shown the closed loop controller has a better performance in terms of pressure as it allowed pressure to build up to 8.5kPa while the open loop controller allowed pressure to build up to 5.5kPa.

The tracking of the pressure controller during the inflation of the actuator is very precise, however, the tracking lags in deflating the actuator. The reason for that is the valve that has an open/close control mechanism. Once the valve opens and the pressure is released, the pressure inside the actuator does not instantly release; rather, the elasticity of the SRA material constricts the air out of the actuator in a characteristic way based on inherent material properties.
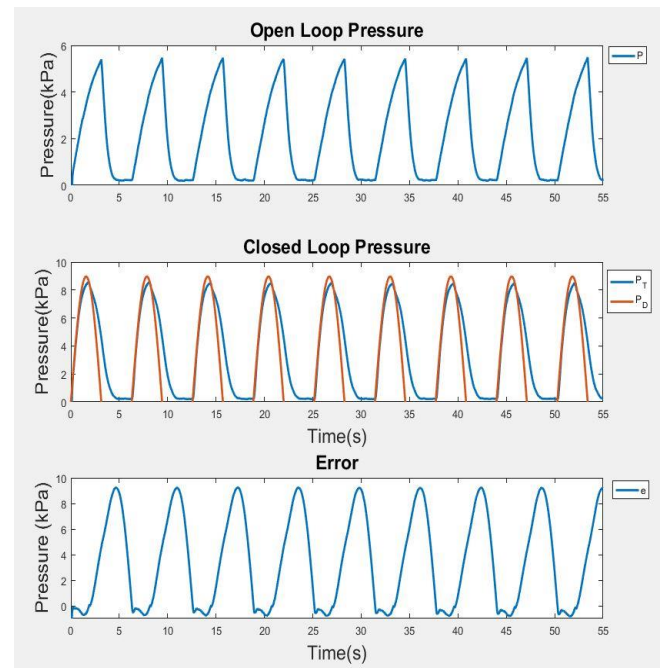

Figure 7: Open Loop Vs Pressure Feedback

Moreover, Figure 7 shows the P_T and P_D and the error signal. The error is almost zero for inflating the actuator and starts increasing for deflating the actuator. Even though the error signal looks cyclic with high amplitude, overall it does not substantially affect the performance of the actuator at low frequencies of operation. This impact would become significant at high frequencies.

Similarly to the analysis done on the force controller, the mean and standard deviation of the error signal were calculated for the pressure controller as well. The mean had a value of 5.045kPa and the standard deviation had a value of 5.21kPa. The high values of the mean and standard deviation are a result of the error achieved while deflating the actuator.

5. Conclusion

In conclusion the same actuator was tested at the same frequency by different controllers. The results between an open loop controller and a closed loop controller varied substantially and proved that a closed loop controller, either force or pressure feedback, could extract a higher performance from the SRA. Due

31st Florida Conference on Recent Advances in Robotics, May 10-11, 2018, University of Central Florida, Orlando, Florida

42

to the nature of the actuator and its behavior while inflating and deflating, the force feedback achieved better tracking for the signal and substantially less error. Finally, the type of controller to be used will depend on the application of the actuator. If it is handling of delicate objects perhaps a force feedback is more appreciated and a pressure feedback could be more sensible for the case of haptic feedback.

For future research into SRAs, studies on how long-term cyclical loading affects the performance of the actuator and the life cycle of the material use to create these actuators. SRAs are widely used in cases of HRI and with the handling of delicate objects, so benchmark studies can be performed to determine the appropriate force need to grasp the object as well as an acceptable error in the force applied. Since the amount of force needed to safely grasp a delicate object and the acceptable deviations in the applied force can vary depending on the object, a wide variety of objects should be tested.

Acknowledgment

6. REFERENCES

[1]   G. K. C. *et al.*, "Soft Robotic Grippers for Biological Sampling on Deep Reefs," *Soft Robot.*, vol. 3, no. 1, pp. 23–33, 2016.

[2]   D. Rus and M. T. Tolley, "Design, fabrication and control of soft robots," *Nature*, vol. 521, p. 467, May 2015.

[3]   R. Dylan, N. M. P., and S. A. A., "Controlling and Simulating Soft Robotic Systems: Insights from a Thermodynamic Perspective," *Soft Robot.*, vol. 3, no. 4, pp. 170–176, 2016.

[4]   C. Laschi, M. Cianchetti, B. Mazzolai, L. Margheri, M. Follador, and P. Dario, "Soft Robot Arm Inspired by the Octopus," *Adv. Robot.*, vol. 26, no. 7, pp. 709–727, 2012.

[5]   M. A. D., O. C. D., and R. Daniela, "Autonomous Soft Robotic Fish Capable of Escape Maneuvers Using Fluidic Elastomer Actuators," *Soft Robot.*, vol. 1, no. 1, pp. 75–87, 2014.

[6]   S. J. L. C., G. I. S., G. Phanideep, and W. I. D., "Soft Robots and Kangaroo Tails: Modulating Compliance in Continuum Structures Through Mechanical Layer Jamming," *Soft Robot.*, vol. 3, no. 2, pp. 54–63, 2016.

[7]   M. A. Abd *et al.*, "Impacts of Soft Robotic Actuator Geometry on End Effector Force and Displacement," in *FCRAR*, 2017, pp. 94–99.

31st Florida Conference on Recent Advances in Robotics, May 10-11, 2018, University of Central Florida, Orlando, Florida

43

Applications of Machine Learning to Virtual Reality

Jiri Kapralek and Nezamoddin N. Kachouie

Florida Institute of Technology
150 W. University Blvd.
Melbourne, Florida

jkapralek2013@my.fit.edu, nezamoddin@fit.edu

ABSTRACT

Delivering a high quality laboratory experience in the physical sciences outside of a real lab facility is difficult. Immersive virtual reality can provide such an experience. This will provide students in non-STEM majors a deeper understanding of and appreciation for the physical sciences than they would receive without performing any experiment. Moreover, realistic, immersive virtual reality experiments can be considered as a substitute for some real world lab experiments to provide long-term cost savings. The ultimate goal of this project is to create a virtual reality classroom or laboratory in which student-student, instructor-student, and student-instructor interactions are maintained. To achieve this, we develop a virtual lab that will observe how students practice the lab experiments in order to help them avoiding the previous mistakes and in turn improve their performance.

In this paper we develop a simple virtual reality experiment (Figure 1.) as proof of concept.

Figure 1. Virtual Reality Environment

Keywords
Virtual Reality, Machine Learning, Unity, Artificial Neural Networks.

1. INTRODUCTION

In this experiment, students are provided with eggs of different ages. The goal of this experiment is to determine the egg's age by submerging it in the water. To determine the density of an egg, students measure the egg's weight and the volume of displaced water when the egg is submerged in the water. Students will then calculate the density using a simple equation. We will run several simulations of this virtual experiment and data will be collected during each simulation. Collected data include questions asked by students, students' mistakes, unsafe approaches, etc. The collected data during these experiments will be used by a machine-learning algorithm to modify the simulation to better address the students' questions, help them to avoid unsafe approaches, etc. This experiment is proof of concept to demonstrate the value of virtual reality technologies in conjunction with machine learning algorithms in physical education.

This experiment suggests that we can take full advantage of the affordances offered by immersive VR, including the use of more innovative virtual experiences rather than normal lab experiments. Our future goal is to practice and extend the applications of VR and machine learning to other physical educations.

Preparing training datasets for a machine-learning algorithm is often time consuming or cost prohibitive. Therefore, a major advantage of merging a virtual reality engine such as Unity with a machine-learning algorithm is producing virtually unlimited training datasets. When using the physics engine in Unity, we can determine whether the simulation is a success or not. The physics engine's output will feed the machine learning algorithm to modify the simulation. This will be repeated until the desired outcome.

31st Florida Conference on Recent Advances in Robotics, May 10-11, 2018, University of Central Florida, Orlando, Florida

44

2. Machine Learning Approach: Artificial Neural Network

A machine learning algorithm is developed to train a model in virtual reality environment. Such trained model can be used individually or in conjunction with an electromechanical assembly for training purposes to perform a desired task. To train the model, some measurable criteria for success must be defined.

For the proposed task, i.e. a laboratory experiment, we have some predefined features to evaluate the experiments' success. There are several criteria to evaluate experiment's success such as how the procedure is performed by the student, whether the experiment's instructions have been followed, whether the student has safely performed all steps, and the accuracy of the outcomes. The algorithm will collect data for training purposes regarding successful trials, different approaches that are taken by students to perform the experiment, and potential patterns in different approaches. The algorithm will identify and use the correct procedures for activations of the neurons of an Artificial Neural Network (ANN). For example, when a student grabs a ruler, some neurons will be activated in a neural network layer based on how the student will use the ruler such as whether the ruler is in close proximity to the water surface, whether the ruler is perpendicular to the water surface, and whether the ruler is touching the surface of the table in order to measure the water displacement. In the second phase, after the algorithm is trained how to perform a successful experiment, new data sets will be used to evaluate the model. In the validation (test) phase, incomplete data sets are provided to the model. The goal of validation is whether the model can correctly predict the outcome of an experiment. It means whether the experiment is a success or failure. More specifically, the model monitors the student's performance and predicts whether the student will have correct outcomes (within some acceptable range). To determine how accurate, the prediction of egg's age is, we have defined a cost function that will be evaluated for each egg separately. With enough data collected through the backpropagation network, the algorithm will be optimized by minimizing the cost function. The third and last step in the machine learning algorithm training is to determine where exactly did the student deviated from a successful path in his/her approach and recommend one or more possible solutions in order to produce a successful result. For instance, in the collected data, there will be an indicator to show whether the student took the ruler, whether he/she touched the surface of the table while measuring, and how close the ruler was to a perpendicular position to the water surface. In this way, we can evaluate how accurate the measurements and in turn associated results (calculated density) will be. The algorithm can detect the wrong procedures and in turn the software would be able to generate a warning message and send to the student in real time. As a result, a customized model for each student can be developed to provide feedback to the students in real time. Depending on the experiment and its educational goals, the student might be notified either shortly after the mistake or after a lag-time which will be set to give the student a chance to correct his/her mistake. Once an adequate amount of data is obtained, an optimal time slot can be determined to provide the student with the feedback in order to minimize the interruption in the learning process. Although, the focus of this work is mainly to improve the success and productivity of education, it has a broad range of applications in the real world.

In order to activate a neuron, the weighted sum of inputs is:

$$weighted\ sum\ = w_1 a_1 + w_2 a_2 + \cdots + w_n a_n \tag{1}$$

where a_i is input i, w_i is the weight of input i, and n is the number of inputs. In the context of our experiment, the first layer of the neural network will receive multiple inputs associate with student's performance such as whether student picks up the ruler and how accurately he/she will measure the water volume displacement. Hence, a_i's & w_i's are input signals to the neuron layer and their associated weights respectively. This layer of neurons will assess the accuracy of water displacement measurement. For example, the angle of the ruler with perpendicular line to the water surface is an input associated with the accuracy of the measurement the water volume displacement. It means, if the angle to the water's surface is close to the perpendicular line, the weighted sum will obtain a large value and in turn will result in a high activation value for the neuron.

A sigmoid function

$$\sigma(x) = \frac{1}{1+e^{-x}} \tag{2}$$

is used in order to control the range of the weighted sum of input signals between 0 and 1. The sigmoid function will assign zero or small positive values to the negative values of the weighted sum. It assigns values close to one for large positive values of the weighted sum. The values monotonically increase between zero and one.

To activate the neuron based on the Hebbian theory, a bias is introduced in the weighted sum (Fig. 2):

$$a_o^{(1)} = \sigma(w_{0,0}\ a_o^{(0)} + w_{0,1} a_1^{(0)} + w_{0,2} a_2^{(0)} + w_{0,n} a_n^{(0)} +\ b_0) \tag{3}$$

31st Florida Conference on Recent Advances in Robotics, May 10-11, 2018, University of Central Florida, Orlando, Florida
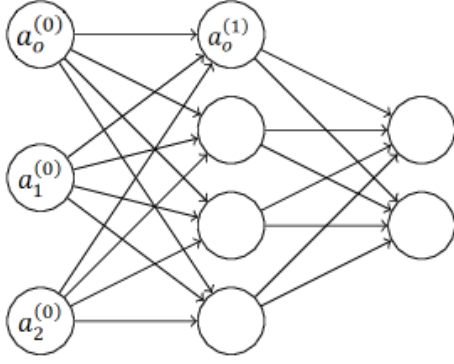
45

Figure 2. A typical neural networks with three layers

where b_0 is the bias. Bias determines how positive the relative weighted sum must be in order to activate the neuron. Therefore, the bias function acts as a threshold for the activation of the neuron. The neuron will not be activated until its activation weighted sum value reaches predefined positive value $|b_n|$ in Eq. 3. Eq. 3 can be written as

$$a^{(1)} = \sigma\left(\begin{bmatrix} w_{0,0} & \cdots & w_{0,n} \\ \vdots & \ddots & \vdots \\ w_{k,0} & \cdots & w_{k,n} \end{bmatrix}\begin{bmatrix} a_0^{(0)} \\ \vdots \\ a_n^{(0)} \end{bmatrix} + \begin{bmatrix} b_0 \\ \vdots \\ b_n \end{bmatrix}\right)$$

(4)

It can be simplified using vector notation to

$$a^{(1)} = \sigma(W a^{(0)} + b)$$ (5)

This simplified expression makes the computations faster by using matrix multiplication. An error term is calculated as the squared difference between desired value and the activation value. This error term will be evaluated for a back-propagation network in each iteration.

A cost function C is used to evaluate the accuracy of the machine-learning model. To maintain a time efficient method, in place of global minimum, a local minimum of the gradient of the cost function ∇C is identified. In each iteration, the error term will be computed and the average error for the whole training set (in virtual environment) will be calculated $(-\eta \nabla C(\vec{W}))$. The initial values are randomly generated, and in turn multiple local minima are identified. An absolute minimum among all minima will be determined. Since the optimization is performed in virtual reality, the input signals to neurons are coming from the physics engine. Hence, practically there is not any restriction regarding the number of iterations.

Our future work will be conducted to improve the machine learning algorithm and customize it further for the specific requirements of virtual reality environment. The eventual goal is to develop a sophisticated model, train it in

a virtual reality environment, and use it for a real world application.

3. Design Implementation

In order to train the ANN algorithm, for each parameter we generate independent random values within a specific range to simulate student's procedure. In the training phase, the ANN will be provided with the outcome of experiment based on the selected random set of values. It means whether or not the selected random set will produce correct results and if so, how accurate are the results. In this way, the output from the ANN will be compared with the ground truth values either using predefined values or provided values by the virtual reality environment. Through backpropagation, the cost function is going to be minimized and after convergence, ANN's activation values will be used in the test phase.

The trained ANN will receive input parameters from the virtual reality physics engine, (Fig. 3) such as coordinates, vectors, forces, distance, and Boolean operators.
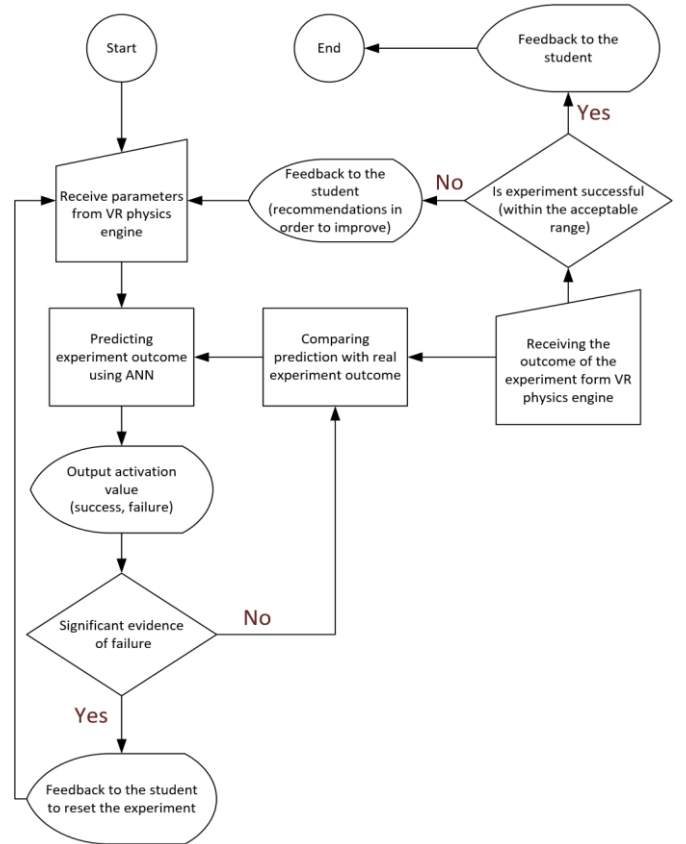

Figure 3. Implementation flow chart

31st Florida Conference on Recent Advances in Robotics, May 10-11, 2018, University of Central Florida, Orlando, Florida

46

The trained ANN will process the data generated by student's procedure to predict the outcome of the experiment and indicate whether or not the experiment is going to be successful. If there is strong evidence that the experiment is going to fail, the student will be notified by providing feedback in order to correct his/her mistakes. Once the experiment is complete, the accuracy of the prediction is going to be determined by comparing the predicted value (output activation value) with the actual value provided by the virtual reality physics engine. If the experiment outcome falls outside the acceptable range, the student will receive feedback to repeat the experiment along with recommended course of actions to improve his/her performance. If the experiment outcome falls within the acceptable range, the student will be provided with feedback regarding the accuracy of the results and potential ways to improve them.

4. RESULTS

In order to validate the proposed method, the ANN was trained using multiple sets of randomly generated vectors and the success rate was recorded. The validation is based on independently generated random vectors, therefore the validation and training are independent. Figure 4 shows proportion of successful trials. As we can see in the figure, the success rate depends on the tolerance considered to accept the procedure as a success. By increasing the acceptable range for the parameter the success rate increases accordingly. In this way we are able to adaptively set the acceptable accuracy based on the experiment at hand.
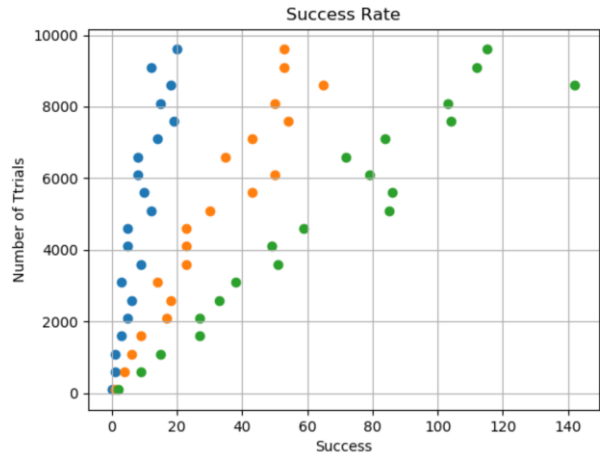

Figure 4. Success Rate of ANN

Future work will be conducted to further explore the impact of having multiple parameters on the training time of the ANN.

5. REFERENCES

[1] Johannes Fürnkranz, Tobias Scheffer, Myra Spiliopouou, "Learning Stochastic Tree Edit Distance" in *Machine Learning: ECML 2006*. Berlin, Germany, September 18-22, 2006

[2] Johannes Fürnkranz, Tobias Scheffer, Myra Spiliopouou, "A Selective Sampling Strategy for Label" in *Machine Learning: ECML 2006*. Berlin, Germany, September 18-22, 2006

31st Florida Conference on Recent Advances in Robotics, May 10-11, 2018, University of Central Florida, Orlando, Florida

47

Design, Development, and Evaluation of a Novel Device for Visualization of Volumetric Medical Images

Paria Alipour[1], Bryan Palogan[2], Leslie Simms[2], Sumit Laha[3], Ulas Bagci[3], and Sang-Eun Song[2]

Interventional Robotics Lab (IRL)
Department of Mechanical and Materials Engineering
University of Central Florida

(1) Department of Biology, University of Central Florida, Orlando, Florida
(2) Department of Mechanical and Materials Engineering, University of Central Florida, Orlando, Florida
(3) Department of Computer Science and Engineering, University of Central Florida, Orlando, Florida

paria@knights.ucf.edu, bryanpa@knights.ucf.edu, leslie.simms.44@Knights.ucf.edu, sumitlaha@Knights.ucf.edu, bagci@ucf.edu, s.song@ucf.edu

ABSTRACT

The proposed device offers virtual slicing of medical images with realistic spatial operation, boosts intuition and interaction, and enables users to view an anatomical target from any angle. The user holds the two handles of a monitor on each side and sweeps it through a virtual human body to view from the desired angle. The monitor is mounted on an encoded counter-balanced arm, which is movable with minimum effort through the human body volume. The encoders trace the position of the monitor which is used to compute the cross-sectional view. Our system generated cross-sectional views as the user moved the monitor within the defined workspace. The computed slices then are visualized on the Graphical User Interface. This device could enhance current digital education and radiology reading techniques by providing a practical and engaging tool to visualize the hidden features of a human body. Widespread adoption of 3D visualization techniques to observe medical images such as MRI scans will result in more accurate and detailed diagnosis techniques, as well as a more informative and resourceful academic environment.

INTRODUCTION

Medical imaging is ubiquitous in medical diagnosis, cancer detection, and pre- and intra-operative intervention planning. Whether the images come from Computed Tomography (CT) or Magnetic Resonance Imaging (MRI), visualization is the vital interface which reveals the internal structure of human body. Thus, visualization of medical images for end-users is of interest. To this end, various novel visualization techniques and new processing algorithms have been created.

The vision of this work is to develop an easy-to-use device for 3D visualization of volumetric medical images. Other devices for this purpose have been introduced but they mainly suffer from complexity such that even a trained user has difficulty to operate those devices. In addition to the complexity of the use, such systems are complicated in terms of design and development. Furthermore, they are not technologically mature enough to be employed in serious scenarios such as operation rooms or clinical settings. Moreover, most of the existing technologies are purely virtual, while an augmented system might outperform as it physically engages the user.

Related Work. The introduction of computed tomography has significantly impacted diagnostic radiology. Radiologists use X-ray, MRIs, and CT scans for diagnosis in emergencies (e.g. intracranial hemorrhage, etc.) as well as detecting and locating tumors in prostate [1], breast [2], colorectal [3], liver [4] and the brain [5]. In the US alone, over 70 millions CT scans are performed annually [6].

MRIs have especially gained popularity as they do not expose the subject to ionizing radiation as opposed to CT scans, while providing excellent soft-tissue contrast and resolution, allowing precise quantification of health and risk assessments [7]. To date, many studies have utilized medical imaging for noninvasive diagnosis, including but not limited to, investigation of gastrointestinal dysfunctions [8], transperineal prostate biopsy [9], evaluation of patients with suspected adnexal masses in ovarian cancer [10], ultrasound and magnetic resonance transient elastography for liver fibrosis [4]. Medical imaging is also used for surgical simulation and planning [11], [12].

Similarly, visualization of 3D medical images is prerequisite for many procedures. 3D Slicer (www.slicer.org), for instance, is an open-source platform that enables pre- and intra-procedural intervention planning. It is similar to a radiology workstation that enables versatile visualization [13] and it has been applied to image guided surgery, brain

mapping, and virtual colonoscopy [14]. Many studies have been devoted to software development of 3D Slicer including segmentation algorithm [15]–[18], surgical planning and navigation [19]–[22] and atlas generation [23].
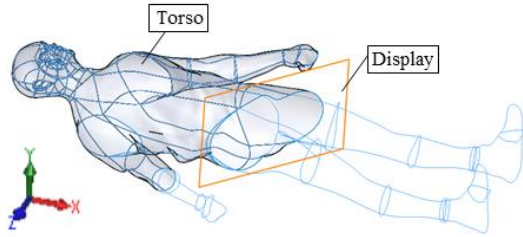

Fig. 1. The cross-section is visualized on the display. A virtual object (human body in this case) is arbitrarily sliced using a physical display

METHODS

A. Concept

The idea is to visualize a cutaway of a virtual object on a display (Fig. 1). That is, a virtual object is arbitrarily sliced using a physical display. Our system is different than previous approaches in terms of: 1) intuition: as opposed to 3D software, we believe moving the display while the object remains still matches the user's intuition; 2) simplicity of use: we believe the system is attractive to users as they can dissect the torso at any angles and go in and out at any directions; 3) generality: the virtual object can be replaced or scale down/up to satisfy the user needs; and 4) scalability: the open-source and simplicity of system integration allows the system to be assembled and used by potential users.

B. Mechanical Design

Design requirement. Key requirements and challenges are operational workspace, maneuverability, and localization.
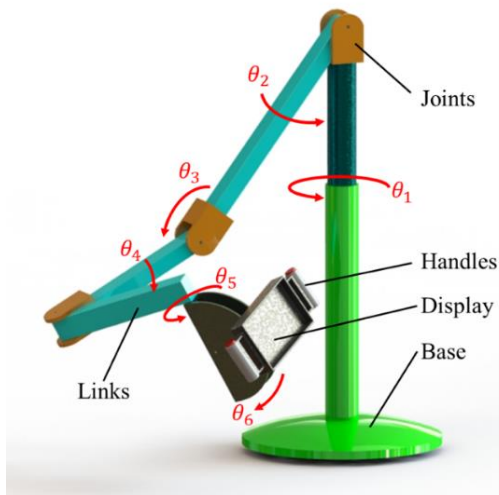
Maneuverability is the ability of accessing an arbitrary cross-section which is the display-body intersection shown in Fig. 1. This requires the display to be freely translated along and rotated about the global coordinate system axes. Localization is positioning an object within a known coordinate system. In this study, localization detects the display pose (the local coordinate system attached to the display's center of mass). Operational workspace is the volume that the display must be provided with full maneuverability and depends on the size of the virtual object.

Device Design. Shown in Fig. 1, this consists of a six-bar linkage, where the fixed link is the base and the five remaining links are free to rotate around their pivot points. The joint angular movements are measured by encoders which are installed at the joints. The position of the endpoint, where the tablet is mounted, is calculated by equations derived from forward kinematic analysis.

Device Optimization. The main structure of the device is designed to support a tablet with weight of up to 1 kg while it provides smooth movement when a user pushes/pulls the table. The length of the links is chosen to be sufficient to cover the required volume.

The arm has 6 DOF with maximum vertical and horizontal reach of 30 and 100 cm, respectively. The monitor tilts and rotates by 75 and 360 degrees, respectively. These dimensions provide sufficient workspace as a typical torso has the dimensions of 30x40x160 cm. Using Solidworks software, a CAD model of the arm was created. The arm has six DOFs to meet the design requirement for full dexterity of the tablet attached at the endpoint, as was needed.

Kinematic Analysis. Using MATLAB software, the kinematics of the arm was formulated by Eqs (1)-(5). The purpose of this analysis is to calculate the endpoint position given the measured joints angles. It should be noted that the joint angles are measured via optical encoders installed at joints.

For kinematic analysis, Denavit-Hartenberg (DH) parameters were used, which provide a series of transformation matrices from consecutive coordinate systems. The final transformation matrix is obtained as the product of

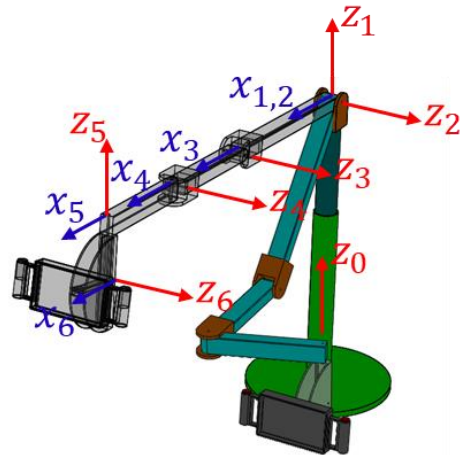
Fig. 2. CAD model of the arm and joint angles

Fig. 3. The assignment of the coordinate system

consecutive matrices. Figure 1 shows the coordinate systems attached to each joint. Eq (1) is a transformation matrix.

$$^{n-1}_nT = \begin{bmatrix} c\theta_n & -s\theta_n c\alpha_n & s\theta_n s\alpha_n & r_n c\theta_n \\ s\theta_n & c\theta_n c\alpha_n & -c\theta_n s\alpha_n & r_n s\theta_n \\ 0 & s\alpha_n & c\alpha_n & d_n \\ 0 & 0 & 0 & 1 \end{bmatrix} \quad (1)$$

where c and s denote sine and cosine, respectively. The DH parameters are d, θ, r, and α, where they are respectively represented as follows.
d: the offset along previous z to the common normal;
θ: angle about previous z, from old x to new x;
r: length of the common normal. Assuming a revolute joint, this is the radius about previous z;
α: angle about common normal, from old z axis to new z axis.
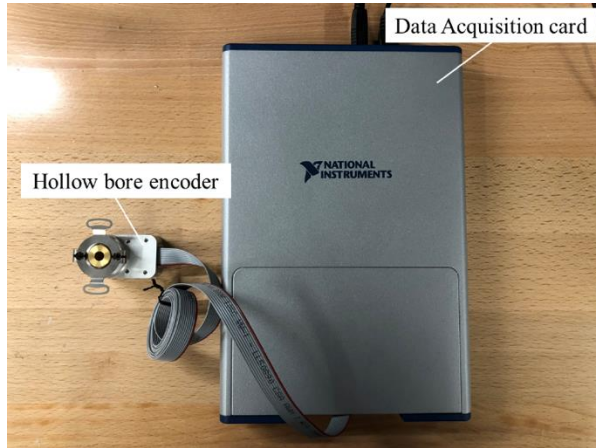

Fig.4. Electronic circuit for to read joint angles

C. Electrical Circuit

The electronic unit consists of a hollow bore optical encoder (US Digital HB5M) with bore diameter of ¼", a data acquisition card (National Instruments myDAQ PCI-6110), and power and connecting cable (USB A to B Cable).

A LabVIEW program was implemented to read the signals of the encoders and calibrate them by mapping the range of the analog voltage signals to range of motion of each joint.

D. Software

A visualization software is created using Qt 5.9.0 application framework. Since Qt is a cross-platform application framework, the software is portable to any operating systems (linux, windows, macOS). The following libraries have been used: a) Insight Segmentation and Registration Toolkit (ITK) 4.12.0, b) Visualization Toolkit (VTK) 8.0 and c) Grassroots DICOM (GDCM) 2.6.6.

The software architecture has three main layers – a) reading images using GDCM and ITK, b) data conversion from ITK to VTK and c) data visualization using VTK.

Since DICOM is the conventional and mostly used medical imaging format, we have designed our system to work on this format. In future versions, we intend to expand this feature to other medical image formats if necessary. The GDCM library handles the DICOM format. Note that both ITK and VTK can be used to read DICOM data, ITK helps processing algorithms while VTK provides visualization sources.
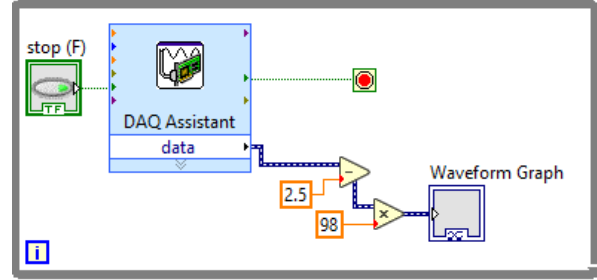

Fig. 5. LabVIEW circuit to read the encoder

In the next step, an image is displayed using VTK. From a single volumetric scan, three views (axial, coronal, and sagittal) are generated. A fourth view displays the cross-sections of the image when the display is placed parallel to any plane. To visualize the data at any plane other than the standard x-y, y-z, or z-x planes, the data is interpolated at that plane as illustrated in Fig. 5. The location information is fed to software continuously in real time from the Polaris system as the user moves the display along the virtual body.

E. Experimental Design

In order to test the simplicity of use of the proposed device, two survey-based experiments were designed. In both scenarios, 10 subjected were asked to conduct given tasks using a mouse and then repeat the same task with the proposed device.

In the first experiment, participants were asked to slice the torso such that the 2D image shown on the screen always remained perpendicular to the given path. In the end, subjects were asked to state which method they found easier.

In the second experiment, participants were requested to seek hidden objects in the torso using 3D slicer. The shape of the objects were unknown to them. They were measured for time taken until objects were successfully found. They were then asked to either draw the shape or choose from a multiple-choice quiz. Then they repeated the task with the proposed device

RESULTS

Device Prototype. At this stage of development, a simplified version of the device was prototyped. To prove the overall concept, a motion tracking system was used to trace the movement of the tablet. We used Microsoft Surface as a display. The Polaris read the pose of the tool from the markers, which were attached on the back side of the Surface (Fig. 6) and sent the results to the software. We initialized the system by specifying the center and dimension of the workspace prior to the test. Our system generated cross-sectional views as the user moved the Surface within the defined workspace. The

31st Florida Conference on Recent Advances in Robotics, May 10-11, 2018, University of Central Florida, Orlando, Florida

50

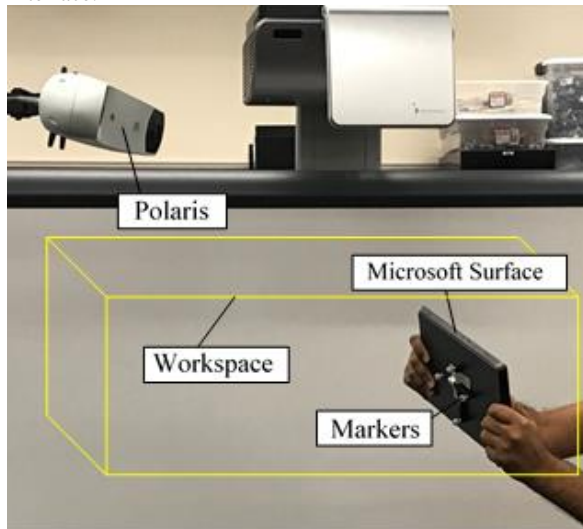computed slices were then visualized on the Graphical User Interface.

Fig. 6. Experiment

CONCLUSION

Over past decades, radiology reading has not been notably changed despite recent technological advancements. Radiologists read images for hours in front of monitors while they hold a microphone to annotate and record their vocal diagnoses. They constantly scroll back and forth across the images using standard computer input devices (i.e., mouse or keyboard) to visit different layers of images and try to visualize three-dimensional anatomy in their mind. Although recent technologies such as EchoPixel© and VisibleBody© have aimed to revolutionize visual anatomy education, these devices do not appear simple and intuitive enough to be used in pre- and intra-procedures. This study explores a novel, immersive, and interactive visualization of medical images.

Future work includes fabrication of the arm, CAD design refinement, and further software improvement. The arm can be assembled from off-the-shelf components. The length of arm's link can be optimized for an average human body.

REFERENCES

[1] P. Kozlowski, S. D. Chang, E. C. Jones, K. W. Berean, H. Chen, and S. L. Goldenberg, "Combined diffusion-weighted and dynamic contrast-enhanced MRI for prostate cancer diagnosis—Correlation with biopsy and histopathology," *J. Magn. Reson. Imaging*, vol. 24, no. 1, pp. 108–113, Jul. 2006.

[2] W. A. Berg *et al.*, "Detection of Breast Cancer With Addition of Annual Screening Ultrasound or a Single Screening MRI to Mammography in Women With Elevated Breast Cancer Risk," *JAMA*, vol. 307, no. 13, pp. 1394–1404, Apr. 2012.

[3] R. M. Paspulati, S. Partovi, K. A. Herrmann, S. Krishnamurthi, C. P. Delaney, and N. C. Nguyen, "Comparison of hybrid FDG PET/MRI compared with PET/CT in colorectal cancer staging and restaging: a pilot study," *Abdom. Imaging*, vol. 40, no. 6, pp. 1415–1425, Aug. 2015.

[4] A. E. Bohte *et al.*, "Non-invasive evaluation of liver fibrosis: a comparison of ultrasound-based transient elastography and MR elastography in patients with viral hepatitis B and C," *Eur. Radiol.*, vol. 24, no. 3, pp. 638–648, Mar. 2014.

[5] E.-S. A. El-Dahshan, H. M. Mohsen, K. Revett, and A.-B. M. Salem, "Computer-aided diagnosis of human brain tumor through MRI: A survey and a new algorithm," *Expert Syst. Appl.*, vol. 41, no. 11, pp. 5526–5545, Sep. 2014.

[6] A. B. de González *et al.*, "Projected Cancer Risks From Computed Tomographic Scans Performed in the United States in 2007," *Arch. Intern. Med.*, vol. 169, no. 22, pp. 2071–2077, Dec. 2009.

[7] H. Dehghani, S. Laha, P. Kulkarni, P. Biswas, U. Bagci, and S.-E. Song, "'Air Slicer' for Immersive Visualization of Medical Images," *Proc. 2018 Des. Med. Devices Conf.*, Apr. 2018.

[8] W. Schwizer, M. Fox, and A. Steingötter, "Non-invasive investigation of gastrointestinal functions with magnetic resonance imaging: towards an 'ideal' investigation of gastrointestinal function," *Gut*, vol. 52, no. suppl 4, pp. iv34-iv39, Jun. 2003.

[9] H. Dehghani, S. Zhang, P. Kulkarni, P. Biswas, L. Simms, and S.-E. Song, "Design and Simulation of Robotic Needle Guide for Transperineal Prostate Biopsy," *Proc. 2018 Des. Med. Devices Conf.*, Apr. 2018.

[10] K. Togashi, "Ovarian cancer: the clinical role of US, CT, and MRI," *Eur. Radiol.*, vol. 13, no. 6, pp. L87–L104, Dec. 2003.

[11] H. Dehghani Ashkezari, A. Mirbagheri, S. Behzadipour, and F. Farahmand, "A Mass-Spring-Damper Model for Real Time Simulation of the Frictional Grasping Interactions between Surgical Tools and Large Organs," *Sci. Iran. Int. J. Sci. Technol.*, vol. 22, no. 5, pp. 1833–1841, Feb. 2015.

[12] H. Dehghani Ashkezari, A. Mirbagheri, F. Farahmand, S. Behzadipour, and K. Firoozbakhsh, "Real time simulation of grasping procedure of large internal organs during laparoscopic surgery," in *2012 Annual International Conference of the IEEE Engineering in Medicine and Biology Society*, 2012, pp. 924–927.

[13] A. Fedorov *et al.*, "3D Slicer as an image computing platform for the Quantitative Imaging Network," *Magn. Reson. Imaging*, vol. 30, no. 9, pp. 1323–1341, Nov. 2012.

[14] S. Pieper, M. Halle, and R. Kikinis, "3D Slicer," in *2004 2nd IEEE International Symposium on Biomedical Imaging: Nano to Macro (IEEE Cat No. 04EX821)*, 2004, pp. 632–635 Vol. 1.

[15] R. Kikinis and S. Pieper, "3D Slicer as a tool for interactive brain tumor segmentation," in *2011 Annual International Conference of the IEEE Engineering in Medicine and Biology Society*, 2011, pp. 6982–6984.

[16] S. S. F. Yip *et al.*, "Application of the 3D slicer chest imaging platform segmentation algorithm for large lung nodule delineation," *PloS One*, vol. 12, no. 6, p. e0178944, 2017.

[17] J. Egger *et al.*, "GBM Volumetry using the 3D Slicer Medical Image Computing Platform," *Sci. Rep.*, vol. 3, Mar. 2013.

[18] E. R. Velazquez *et al.*, "Volumetric CT-based segmentation of NSCLC using 3D-Slicer," *Sci. Rep.*, vol. 3, p. srep03529, Dec. 2013.

[19] D. T. Gering *et al.*, "An Integrated Visualization System for Surgical Planning and Guidance Using Image Fusion and Interventional Imaging," in *Medical Image Computing*

31st Florida Conference on Recent Advances in Robotics, May 10-11, 2018, University of Central Florida, Orlando, Florida

51

and Computer-Assisted Intervention – MICCAI'99, 1999, pp. 809–819.

[20] N. Doba et al., "Usefulness of 3D slicer for the planning and monitoring of hepatocellular carcinoma treatment using FUS," *J. Ther. Ultrasound*, vol. 3, no. 1, p. O84, Jun. 2015.

[21] X. Chen, L. Xu, H. Wang, F. Wang, Q. Wang, and R. Kikinis, "Development of a surgical navigation system based on 3D Slicer for intraoperative implant placement surgery," *Med. Eng. Phys.*, vol. 41, pp. 81–89, Mar. 2017.

[22] S. Kim, Y. Tan, A. Deguet, and P. Kazanzides, "Real-Time Image-Guided Telerobotic System Integrating 3D Slicer and the Da Vinci Research Kit," in *2017 First IEEE International Conference on Robotic Computing (IRC)*, 2017, pp. 113–116.

[23] J. Rackerseder, A. M. L. González, C. Düwel, N. Navab, and B. Frisch, "Fully Automated Multi-Modal Anatomic Atlas Generation Using 3D-Slicer," in *Bildverarbeitung für die Medizin 2017*, Springer Vieweg, Berlin, Heidelberg, 2017, pp. 306–311.

31st Florida Conference on Recent Advances in Robotics, May 10-11, 2018, University of Central Florida, Orlando, Florida

52

An Overview of
Modeling and Control Techniques
for Soft Robots

Marilu Ortiz, Dr. Sang – Eun Song
University of Central Florida
Orlando, Florida
marilu.ortiz@knights.ucf.edu, s.song@ucf.edu

ABSTRACT

Soft Robotics' developments pose a promising advancement in key health care areas such as surgical interventions, medical therapies and rehabilitation. Some of the research work efforts are aimed to develop devices compliant to human, with a higher level of dexterity, autonomy and capable to reach complex body cavities and adapt to the environment, among other characteristics.

In order to be able to commercialize these devices for medical applications, a rigorous and comprehensive understanding of system behavior and performance, as well as an accurate design for controllability, is required to ensure that the devices will comply with the specified requirements and are safe to use.

Modeling and Control techniques capable of accurately describing the mechanical behavior of highly deformable devices (non-linear systems) that will operate iteratively with the environment is key to the successful realization of these devices.

This work presents an overview of recent research in modeling and control of Soft Robots, as well as a summary of main commonalities and challenges encountered.

Keywords

Modeling, Simulation, Control of Soft Robots. Soft Robotics in Medical Devices, Surgical Instruments.

1. INTRODUCTION

The field of robotics has emerged with new trends in the use of soft and compliance devices that utilize flexible or deformable materials and sources of power and sensing [5]. These devices pose higher dexterity levels, can reach complex areas of body [3] and are more compliant for human use. As stated by Duriez et al [2], the soft structures offer an infinite number of degrees of freedom (dof) and redundant actuation which provides additional benefits in maneuvering inside the body while interacting with soft organs and tissue, as is the case with medical and surgical robotics applications.

The motion of a soft robot is dependent on its deformation [6][2]. The modeling and control of a soft device or robot is complex because of the multiple degrees of freedom, highly deformable structure, non-linear behavior, redundant actuation and unpredictable interactions with the environment that will impose

additional deformations and changes in the systems' intended motion or dynamics, among other constraints [1][2].

Therefore, research work to develop new and robust techniques is key to be able to accurately model and control the robot. This paper presents an overview of recent research related to methods and techniques in modeling and control of soft robots.

2. MODELING OF SOFT ROBOTS

Conventional modeling, control techniques and kinematic equations used in rigid mechanisms does not directly apply to soft robots. Continuum mechanics methods have been used to formulate the dynamic description of a continuum, particularly it is being used to study deformations and behavior of elastic non-linear systems. [7][2]. The constitutive laws of a continuum system describe the relations between forces applied (e.g. stress) and resulting deformation (e.g. strain) of the system [7]. Selecting the optimum constitutive law is key to be able to obtain a realistic model and adequate solution. Assumptions are required to simplify the model and they need to be accurate enough to guarantee the quality of the model.

Some of the constitutive equations as discussed in Misra et al [9] for soft materials such as tissue are for example Hook's law, which applies to linear elastic materials,

$$\sigma = C : \varepsilon$$

which represents a simpler method to model elastic materials. Another approach presented is the use of non-liner elastic model such as hyperelasticity model. In this case, as stated in [9] strain energy density function (W(F)), it is used to obtain the stress in the material as a result of deformation:

$$P = \frac{\partial W(F)}{\partial F}$$

P is the First Piola – Kirchhoff stress tensor
F is the deformation gradient tensor.

Although simpler models like the ones governed by Hooke's law will increase computational efficiency, it will not accurately describe other more complex systems with non-linear behavior. Therefore, additional techniques are required for an accurate modeling of the system.

31st Florida Conference on Recent Advances in Robotics, May 10-11, 2018, University of Central Florida, Orlando, Florida

53

3. RECENT WORK

In recent works, different and combined techniques have been used to address some of these challenges.

In the work of Saunders et al [10], the locomotion of a highly deformable tobacco hornworm caterpillar, the Manduca Sexta, was modeled. The tobacco hornworm carterpillar can stretch and bend.

A reduced-order, planar, extensible-link model was utilized and various assumptions were made to simplify the model. One of the assumptions was that the caterpillar motion is quasi-static (inertial forces are negligible). Experimental data was acquired by the use of motion tracking systems and ground reaction forces were also measured. The motion tracking system was utilized to get the configuration parameters such as link length and orientation. To solve the sets of non-linear equations for the configuration parameters, an optimization method was used. Forces and torques on each link were computed by solving the 2D Newton Euler equations (inverse kinematics) and with the information obtained from the motion tracking system. A correlation coefficient was computed to compare ground reaction forces that were measured vs the ones computed with the model (91% correlation in the vertical direction and 76% in the horizontal direction).

Also, the quasi-static assumption was verified by taking into consideration the inertial forces in the model. It was confirmed that they were negligible in comparison with the external forces. The model can be utilized further to develop strategies for the locomotion control of soft robots similar to this model.

The model relies on obtaining experimental data to be able to solve for the inverse kinematic problem. Also, a quasi-static assumption is made, which limits the motion to low velocities.

A more general approach is described by Thieffry et al [6]. In this work, offline simulation of robot movement under various parametric conditions was done. A snapshot matrix ("Snapshot-Proper Orthogonal Decomposition (POD") was compiled with robot's accelerations that serve to reduce the dynamic model of the structure. Also, the modes were obtained from the snapshot space using a singular value decomposition. A significant number of simulations were required in order to obtain a snapshot matrix that makes the model as accurate as possible. In this work 3360 snapshots of accelerations were obtained.

The control laws were based on Linear Time Invariant (LTI) reduce order model. This model does not depend on geometrical conditions. As described by Thieffry et al [6], the challenge of this model is to get an accurate snapshot matrix that will entail multiple offline gathering of information of robot simulation. Also, the contacts were not included in the model, therefore, collisions with the environment are not taken into account.

The method works as long as the robot trajectory remains around a previously defined equilibrium point since the reduction matrix obtained using the POD method as well as the linearization of the compliance matrix was done around the equilibrium point. Therefore, a limited working area is part of the challenges discussed on this work. The reductions methods presented in this work will allow for the application of conventional rigid robotics control techniques to control the robot.

In the work of Duriez et al [1], the FEM simulation computes the non-linear deformation of the robot in real time at interactive rates

in the control algorithm. A soft silicone material is used to obtain experimentally the constitutive law of the silicone.

A reduced compliance matrix between actuators and end effector is obtained by the use of the FEM simulation and Lagrange multipliers. Constraints such as rigid or deformable obstacles were added and integrated in the control algorithm.

The final configuration of the soft robot, at the end of the time step, is corrected by using the value of the constraint response.

In their work, they found that more than one solution might exist due to actuator redundancy. Their method was validated on a real 3d soft robot made of silicone. As discussed in this work, one of the things that can be a future subject of study is to evaluate the quality of the solution obtained in the cases where several solutions were possible.

In the work of Lee et al [4], a more generic approach is presented, in which there is no need to obtain an analytical model for neither the system, nor the structural parameters, or understand in details the external environment of the robot. As discussed by Lee et al., [4] a generic control framework will learn the inverse model by utilizing a live motion tracking system to know where the state variable is at all times and this information is imputed into the control system to compute control commands based on real time information of the robot state space condition.

4. DISCUSSION

Soft structures mathematical models and resulting equations leads to complex numerical problems which are difficult to resolve.

The efforts in estimating the analytical model range from utilizing continuum mechanics approaches combined with the use of finite element analysis to estimate deformations and apply inverse modeling to get the internal forces required to achieve a desired deformation or movement.

In many of the research work reviewed, experimental studies were performed to gather information of structural parameters of the system, understand the kinematic behavior and being able to select the best constitutive laws. Also, experiments were conducted to compare the numerical solution to the experimental results and validate the accuracy of the model or obtain valuable information to adjust the model.

One of the common challenges in devices for medical applications such as those involved in surgical interventions is being able to account for unpredictable interactions with the environment (tissue and organs inside the body) which will impose additional deformations and deviations from the intended motion. These interactions with the external environment are difficult to model.

For this reason, the analytical model and/or control algorithms needs to account for these aspects in solving the inverse kinematic problem to obtain accurate solutions in which the required internal forces or commands necessary to control the performance of the device can be obtained.

Some of the approaches utilized interactive online Finite element modeling to be able to continuously iterate the modeling to accommodate the real-time changes and effects due to interactions within the device and the environment. Others rely on a nonparametric online learning framework with a motion tracking system to track the state variable and adjust the control system accordingly.

31st Florida Conference on Recent Advances in Robotics, May 10-11, 2018, University of Central Florida, Orlando, Florida

54

Also, some other challenges presented are around the use of optimization methods to get the best solution and managing actuators redundancy.

In the research work reviewed, the following common areas and related challenges were identified.

Table 1. Research Efforts Commonalities

Area	Challenges	Techniques
• Analytical Model – Constitutive laws	✓ Infinite Dofs ✓ Structural parameters of the system are not readily available ✓ Deformations are difficult to predict	✓ Experiment ✓ Finite Element Methods ✓ Optimize methods for model order reduction without sacrificing accuracy
• Global model • Robot Contact with environment (resulting in additional deformations or deviations from intended path)	✓ Structure geometry and parameters dependence	✓ Real time interactive model ✓ Non- parametric online modeling

5. CONCLUSION

As the Soft Robotics field continues to grow, advanced methods for modeling and control become important for the realization of these devices. In this review, different techniques are presented in which key research commonalties and challenges were identified as described in Table 1. Some of the commonalities in the research efforts are around methods to develop analytical model and accurately solve the inverse dynamic problem, the use of optimization methods to get the best solution, managing actuators redundancy, model reduction techniques and address the soft structure contacts with the environment.

Based on this review, some future efforts are aimed to being able to get global and accurate approaches that can simulate and control the locomotion of soft structures.

6. REFERENCES

[1] C. Duriez, "Control of Elastic Soft Robots based on Real-Time Finite Element Method," 2013 IEEE International Conference on Robotics and Automation, Karlsruhe, 2013, pp. 3782-3787. doi: 10.1107/ICRA.2013.6631138.

[2] C. Duriez *et al.*, "Framework for online simulation of soft robots with optimization-based inverse model," 2016 IEEE International Conference on Simulation, Modeling, and Programming for Autonomous Robots (SIMPAR*)*, San Francisco, CA, 2016, pp. 111-118.

[3] Cianchetti, M., et al. (2014). "Soft Robotics Technologies to Address Shortcomings in Today's Minimally Invasive Surgery: The STIFF-FLOP Approach." Soft Robotics 1(2): 122-131.

[4] Lee, K.-H., et al. (2017). "Nonparametric Online Learning Control for Soft Continuum Robot: An Enabling Technique for Effective Endoscopic Navigation." Soft Robotics 4(4): 324-337.

[5] M. Ortiz, "Soft Robotics Recent Developments in Minimally Invasive Surgery and Implantable Medical Devices", US-Korea Conference on Science, Technology and Entrepreneurship (UKC 2017), Washington DC, 2017, pp. 175.

[6] M. Thieffry, et al. "Dynamic Control of Soft Robots". IFAC World Congress, Jul 2017, Toulouse, France. 2017.

[7] Reddy, J. (2013). An Introduction to Continuum Mechanics. (2nd ed.) Cambridge: Cambridge University Press. doi:10.1017/CBO9781139178952.001

[8] Rus, D. et al. (2015). "Design, fabrication and control of soft robots". Nature 521, no. 7553.

[9] Sarthak Misra, et al. "Modeling of Tool-Tissue Interactions for Computer-Based Surgical Simulation: A Literature Review". Presence: Teleoperators and Virtual Environments 2008 17:5, 463-471.

[10] Saunders, F. (2010). "Modeling locomotion of a soft-bodied arthropod using inverse dynamics". Bioinspiration & biomimetics, 6(1), 016001.

31st Florida Conference on Recent Advances in Robotics, May 10-11, 2018, University of Central Florida, Orlando, Florida

55

Fast Robotic Soft Matter 3D Printing for Patient-specific Surgical Phantoms

Michael C. Chang[1], Sean R. Niemi[1], Christopher Kabb[2], Thomas E. Angelini[1], Frank J. Bova[3], Scott A. Banks[1]

(1) Department of Mechanical and Aerospace Engineering, University of Florida, Gainesville, FL 32611

(2) Department of Chemistry, University of Florida, Gainesville, FL 32611

(3) Department of Neurosurgery, University of Florida, Gainesville, FL 32611

Chtre12@ufl.edu, impstar@ufl.edu, cpkabb@chem.ufl.edu, t.e.angelini@ufl.edu, banks@ufl.edu

ABSTRACT

The recent introduction of three-dimensional (3D) printing (also known as additive manufacturing) techniques into the field of medicine and neurosurgery has provided methods for fabricating patient-specific models for neurosurgical training, teaching, simulation, and pre-surgical planning. Soft matter technology, using a granular gel as the supporting material for 3D printing photopolymer hydrogels, now permits printing of anatomically complex models with realistic textures and tactile properties.

However, there hasn't been a promising soft matter 3D printing system that could be used for fabricating neurosurgical patient-specific models. A major limitation is that current soft matter 3D printing technologies are unavailable to directly print these models with the same anatomical size in a timely fashion.

The aim of this project is to create a robotic soft matter 3D printing system using the soft matter 3D printing technology for fast fabrication of patient-specific models with anatomically realistic appearance and textures.

The prototype system consists of a SCARA (4-axis) robotic arm, a large-volume-closed-loop-pressure-controlled hydrogel dispensing pump, and a high-level controller for coordinating and synchronizing the robot and the pump. The method consists of path planning for 3D printing, fast motion control of the robotic arm, and precise hydrogel dispensing control. Models are directly fabricated from photopolymerizable hydrogel extruded into the granular gel. A 10-cubic-inch-sized model can be printed in 5 minutes. It significantly improves the time and cost for fabricating the same sized model, making it feasible to fabricate neurosurgical anatomical models for surgeons to practice/prepare in advance of surgical cases, or for realistic teaching exercises.

Keywords
Soft matter, 3D bioprinting, Robotics, Additive manufacturing

1. INTRODUCTION
Modern 3D printing technology, also known as additive manufacturing (AM), has been developed for decades, and has been rapidly improving because of advancing computer-aid design (CAD) software, decreased cost of materials and equipment, and more applications. The growth of 3D printing in manufacturing industry and consumer markets has been largely increasing because of the ability to fabricate arbitrary shapes. 3D printing has also been commonly applied in biomedical fields and modern research, for applications including scaffolds for tissue engineering, artificial human organs, and anatomical models for surgeries (a.k.a. surgical phantoms) [1]–[3].

Soft Matter 3D Printing

Because of the complex human anatomy and variations of each individual body, 3D printing technology is becoming an ideal tool for surgeons to use in preparing for difficult surgical procedures. There exists an increasing need to fabricate customized soft matter objects, such as human surgical anatomy (such as cardiovascular surgeries, neurosurgeries, etc.), for surgical training and pre-operational planning and training. In recent research, a modern 3D printing technology, soft matter 3D printing (a.k.a. 3D bioprinting), has utilized granular gel as supporting material in 3D printing for hydrogel polymer extrusion. Soft matter 3D printing provides not only the ability to fabricate models with soft-touch textures, but also provides great flexibility for fabricating complex-shaped models without huge waste of supporting materials [4].

Soft Matter Extrusion

Most of the current soft matter 3D printing systems and fused filament fabrication (FFF) systems share the standard 3D printing mechanism: a material extruder and a Cartesian motion platform. The main difference between them is the printing material and material extruder. Unlike FFF, soft matter 3D printing usually uses a soft matter extruder with liquid polymer, hydrogel, living cells, etc., while FFF uses a hot-end filament extruder with plastic filament. Soft matter extruders commonly consist of a syringe pump and a blunt-tip needle, and are built as a printhead assembly of the 3D printer, such as a modern bioprinter. Most of the soft matter extruders feature low-volume syringes and small-diameter nozzles/needles for printing small objects with high precision [5], [6]. There are two major limitations on this kind of syringe pump setup: one is the carriage payload of the soft matter extruder at the

end-effector of the 3d printer, and the other is the syringe volume. The carriage payload of the soft matter extruder at the printhead will determine the dynamic performance of the 3D printer motion. As the mass and moment of inertia of the printhead increases, it will result in unwanted vibration and impact on the accuracy of robotic motion repeatability for printing [7]. The syringe volume is usually limited by the syringe size (usually 10ml or smaller) on most bio-printers because of the need to reduce the carriage payload at the printhead for high-precision motion.

The New Robotic Soft Matter 3D Printing Platform

To achieve the goal of fast robotic soft matter 3D printing for fabricating patient-specific anatomical models in a timely manner, we require fast robotic motion of the printhead (i.e. the end effector of the 3d printer), using a soft matter extruder providing fast and accurate extrusion with a large-volume reservoir. A soft matter 3D printing system satisfying these requirements has not been reported.

In this article, we report a new robotic platform for soft matter 3D printing for fabricating soft-textured anatomical models, such as soft tissues, blood vessels, nerves, etc. It includes a 4-axis robotic arm, a large-volume-closed-loop-pressure-controlled hydrogel extruding system, and a high-level controller for coordinating and synchronizing the robot and the pump.

The purpose of our study was to test the hypothesis that the new robotic soft matter 3D printing platform would present fast printhead motion coordinating with the soft matter extruding system, while requiring less time for fabricating complex-shaped models at comparable resolution.

2. Methods and Materials

In this section, we provide a general description of the new robotic 3D printing platform for fast fabricating soft matter objects by the modern soft matter 3D printing technology, extruding liquid polymer in granular gel. To investigate the idea of fast printhead motion and soft matter extrusion, a 4-axis SCARA industrial robot and an "off-the-end-effector" (Bowden-style) soft matter extrusion system were utilized as the platform to fabricate soft-textured models.

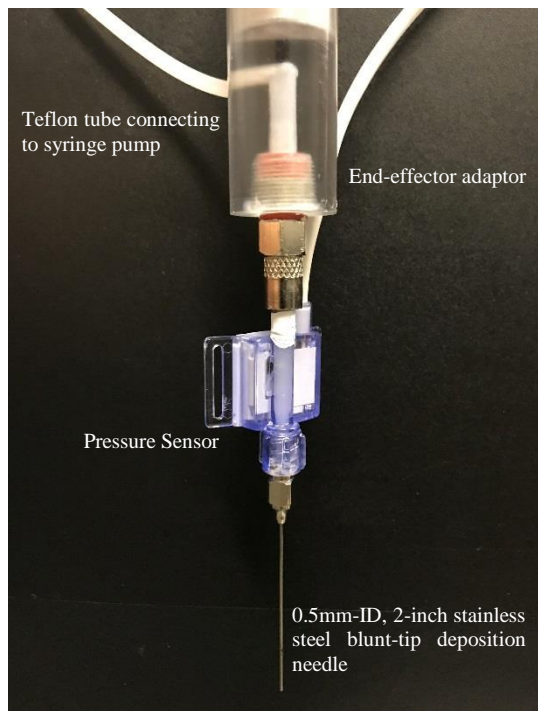**Figure 1. Robotic soft matter 3D printing system setup.**

Figure 2. An end-effector adaptor incorporating a pressure sensor and a blunt-tip needle, and a Teflon tube connecting the syringe pump.

2.1 Hardware

The new platform includes an Epson SCARA 4-axis robotic arm driven by Epson RC-700 controller, and a closed-loop-pressure-controlled hydrogel extrusion system (Figure 1). The hydrogel extrusion system consists of a custom stepper-motor-driven syringe pump, an end-effector adaptor incorporating a pressure sensor and a blunt-tip needle, and a Teflon tube connecting the syringe pump and the end-effector adaptor (Figure 2).

2.2 Software

The user interface and code for high-level coordination of robot and extrusion system were implemented in LabVIEW (National Instruments, Austin, TX). We use an open-source slicing engine (Slic3r) for 3D printing tool-path planning, and for setting parameters including layer thickness and material retraction on the hydrogel extrusion system.

2.3 Soft Matter Preparation

The supporting material and printing ink for soft matter 3d printing are prepared following the methods described in Bhattacharjee et al.[4], [8] To prepare the soft carbomer granular gel medium, the supporting material in soft matter 3d printing, 0.15 % (w/w) Ashland™ 980 Carbomer is suspended in ultrapure water and 0.01N NaOH. For the preparation of the printing ink, 25% (w/w) Polyethylene glycol 35000 is suspended in ultrapure water. Both of them were homogeneously mixed at 3500 rpm for 2 minutes in a FlackTek DAC 150 SpeedMixer before they were degassed.

2.4 Robotic Soft Matter 3D Printing Process

Complex-shaped models were used to demonstrate the system capability to fabricate complex anatomy and geometries. The 3D models were either designed and created using SolidWorks

31st Florida Conference on Recent Advances in Robotics, May 10-11, 2018, University of Central Florida, Orlando, Florida

57

(Dassault Systèmes), or segmented from medical imaging using ITK-Snap. All of the 3D models were exported in the STL file format, and were processed by Slic3r or CURA, open-source slicing engines, and sliced into layers with 0.25 mm thickness to generate G-code instructions for 3D printing. G-code files were then post-processed by MATLAB (MathWorks, Inc.), and sent to LabVIEW Interface for printing (Figure 3).

Hydrogel printing inks were first drawn into a 30-ml disposable syringe. The syringe was then connected with the Teflon luer-lock connecting tube to the end-effector adaptor, and mounted onto the stepper-motor-driven syringe pump. A container that used to hold the part to be printed was filled with the carbomer granular gel
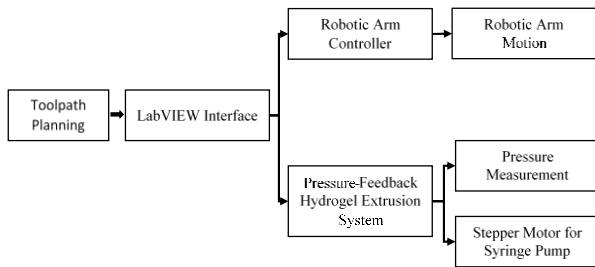

Figure 3. System process

supporting material, and manually placed on the build platform, which is a flat surface that is separated from the soft matter 3d printing platform. The needle tip of soft matter extruder was positioned at the center of the granular gel container in x and y and near the bottom of the container in z before printing.

2.5 Hydrogel Extrusion System

To achieve fast dynamic response and low vibration at the robotic arm end effector, an "off-the-end-effector" (Bowden-style)[9] soft matter extrusion system is served in the fast robotic soft matter 3d printing system. In order to resolve the hydraulic compliance due to the Teflon connecting tube and viscous hydrogel, and get high-quality soft matter 3D printing, closed-loop control of pressure feedback on syringe pump was implemented to eliminate general 3D printing issues, such as leaking nozzle/needle, stringing, and oozing[10].

A PID controller was employed as a highly responsive and stable pressure controller. The proportional, derivative and integral gains are tuned for particular setup (needle diameter, syringe size, hydrogel viscosity, length of the Teflon connecting tube, motor performance, etc.) for optimal performance. For characterizing the performance of the soft matter extrusion system, a well-characterized setup in TABLE 1 is used.

Table 1. Table captions should be placed above the table

Needle	a 2-inch blunt-tip needle with 0.5-mm-ID(inner diameter)
Syringe	30 ml disposable syringe
Connecting tube	2 feet
Hydrogel viscosity	~200 CP
Motor holding torque	22.6 N-cm / 32 oz-in

3. Result

The module-level performance of the Robotic Soft Matter 3D Printing system translates into the capability to fabricate soft matter objects significantly faster than current soft matter 3D printing systems that operate on a comparable resolution scale. To demonstrate the capability of fast soft matter 3d printing, a variety of test objects were printed using the platform.

We show a variety of test objects fabricated using PEG hydrogel, which include a CAD model of double-helical tubes, a CAD-generated blood-vessel model, and a segmented blood-vessel model. These models were printed using a 0.5-mm blunt-tip needle with a layer of 0.25mm, using settings chosen to compromise between build rate and overall quality.
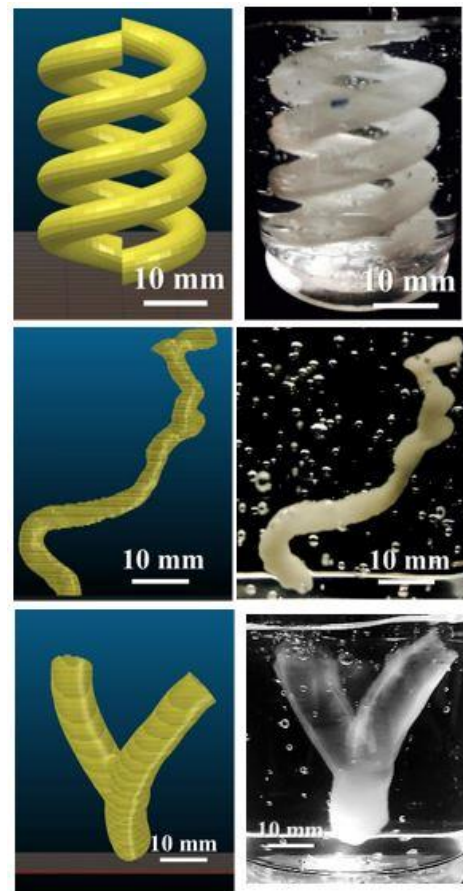

Figure 5. Printing result

4. Discussion

This study was designed to investigate the capability of the new robotic soft matter 3D printing system for fabricating complex-shaped models in a timely manner. We found the use of the new robotic soft matter 3D printing platform, which consists of a SCARA robot arm and a pressure-controlled hydrogel extrusion system, enhanced the current capability of printing soft-textured objects. By implementing fast robotic motion and pressure-controlled soft matter extrusion, complex-shaped 3D geometries are able to be fabricated faster than the standard 3d printing platform for soft matter. According to the result, we believe that the

31st Florida Conference on Recent Advances in Robotics, May 10-11, 2018, University of Central Florida, Orlando, Florida

58

new robotic soft matter 3D printing system has a great potential for fabricating patient-specific anatomical models in the future.

The major limitation for this study is the printing volume and resolution by the "off-the-end-effector" hydrogel extrusion system. The former depends on the syringe size used in the syringe pump, and the latter depends on the diameter of the needle for hydrogel deposition. Current syringe pump extruders for soft matter 3D printing are typically either large volume or high resolution, but not both. For printing higher resolution and fine-detailed objects, smaller diameter of needle should be used for material deposition. However, the backpressure in the syringe dramatically increases as the needle diameter decreases. The same situation happens when choosing a larger-volume syringe. The backpressure in the syringe dramatically increases as the inner-diameter of the syringe increases. According to Hagen-Poiseuille's equation[10], the force that is required to drive the syringe pump would dramatically increase as the needle diameter decreases and syringe diameter increases. This implies that either a higher torque of the stepper is needed to drive the syringe extrusion, or an advanced design for the soft matter extrusion system is needed for achieving both large-volume and high-resolution soft matter 3D Printing.

5. Conclusion

In summary, we have demonstrated a robotic soft matter 3D printing platform for fast fabricating soft-textured models using polymer hydrogel, achieving about 10-times faster build rate than standard 3d printing platform for soft matter. This system will serve as an example of how soft matter 3D printing may be improved by recognizing and overcome the limitation of the system performance. To achieve the true potential of fast soft matter 3D printing for large volume objects, it will be necessary to develop an advanced large-volume hydrogel dispensing system, multi-material printing capability, improved toolpath planning algorithms, and further evaluate the coupling between the dynamics of fast robotic motion and hydrogel extrusion. Nevertheless, the capability to fabricate soft-textured and complex-shaped objects in 5–10 minutes allows us to conceptualize the ideas for fast fabrication of patient-specific anatomical models, and motivates future work on adaptation of the technology to large-volume hydrogels dispensing, and multi-material extrusion.

6. ACKNOWLEDGMENTS

7. REFERENCES

[1] F. Rengier, A. Mehndiratta, H. Von Tengg-Kobligk, C. M. Zechmann, R. Unterhinninghofen, H. U. Kauczor, and F. L. Giesel, "3D printing based on imaging data: Review of medical applications," *Int. J. Comput. Assist. Radiol. Surg.*, vol. 5, no. 4, pp. 335–341, 2010.

[2] S. N. Kurenov, C. N. Ionita, D. Sammons, and T. L. Demmy, "Three-dimensional printing to facilitate anatomic study, device development, simulation, and planning in thoracic surgery," *J. Thorac. Cardiovasc. Surg.*, vol. 149, no. 4, p. 973–979.e1, 2015.

[3] G. T. Klein, Y. Lu, and M. Y. Wang, "3D printing and neurosurgery--ready for prime time?," *World Neurosurg.*, vol. 80, no. 3–4, pp. 233–5, 2013.

[4] T. Bhattacharjee, S. M. Zehnder, K. G. Rowe, S. Jain, R. M. Nixon, W. G. Sawyer, and T. E. Angelini, "Writing in the granular gel medium.," *Sci. Adv.*, vol. 1, no. 8, p. e1500655, 2015.

[5] R. L. Truby and J. A. Lewis, "Printing soft matter in three dimensions," *Nature*, vol. 540, no. 7633, pp. 371–378, 2016.

[6] C. Mandrycky, Z. Wang, K. Kim, and D. H. Kim, "3D bioprinting for engineering complex tissues," *Biotechnol. Adv.*, vol. 34, no. 4, pp. 422–434, 2016.

[7] K. L. Hillsley and S. Yurkovich, "Vibration control of a two-link flexible robot arm," *Proceedings. 1991 IEEE Int. Conf. Robot. Autom.*, vol. 3, no. 3, pp. 212–216, 1991.

[8] C. S. O'Bryan, T. Bhattacharjee, S. Hart, C. P. Kabb, K. D. Schulze, I. Chilakala, B. S. Sumerlin, W. G. Sawyer, and T. E. Angelini, "Self-assembled micro-organogels for 3D printing silicone structures," *Sci. Adv.*, vol. 3, no. 5, 2017.

[9] J. Griffey, "Chapter 2: The Types of 3-D Printing," *Libr. Technol. Rep.*, vol. 50, no. 5, pp. 8–12, 2014.

[10] K. T. Mcdonald, "Leaky Syringe," vol. 8544, pp. 1–4, 2014.

31st Florida Conference on Recent Advances in Robotics, May 10-11, 2018, University of Central Florida, Orlando, Florida

59

Robotic Finger Force Sensor Fabrication

and Evaluation Through a Glove

Craig Ades, Iker Gonzalez[(1)], Mostapha AlSaidi, Dr. Mehrdad Nojoumian[(2)], Dr. Ou Bai[(3)], Dr. Aparna Aravelli[(4)],
Dr. Leonel Lagos[(5)], Dr. Erik D. Engeberg

Ocean &Mechanical Engineering Department
College of Engineering and Computer Science.
Florida Atlantic University.
777 Glades RD EW 178, Boca Raton, FL

(1), (2) Electrical & Computer Engineering & Computer Science Department, Florida Atlantic University, Boca Raton, FL
(3) Electrical & Computer Engineering Department, Florida International University, Miami, FL
(4), (5) Applied Research Center, Florida International University, Miami, FL

cades@fau.edu, ikergonzalez2014@fau.edu, malsaidi2015@fau.edu, mnojoumian@fau.edu, obai@fiu.edu, aaravell@fiu.edu,
lagosl@fiu.edu, eengeberg@fau.edu

ABSTRACT

This force-feedback approach compares the effect on the sensing ability through a worn glove of the force application of an i-Limb Ultra robotic hand for several experimental scenarios. A Takktile sensor was integrated into a fabricated fingertip to measure the applied force of the i-Limb Ultra. A controller was then designed using MATLAB/Simulink to manipulate the finger motion of the i-Limb to apply force to an external load cell. Testing was performed to check the force measurements and sensing ability/quality for two cases: hand with no glove and hand with a nitrile glove. Each of these scenarios were tested by applying fingertip force in 3 different modes: open/close with no contact, continuous tapping and constant force.

Keywords

Force feedback, Powered prosthetic Hand, Robotics, Glovebox, Hotcell.

1. INTRODUCTION

The US Department of Energy's Office of Environmental Management oversees one of the largest environmental cleanup efforts in the world. The cleanup is a consequence of six decades of research/development and production of nuclear weapons in the US. Some of the current and future cleanup work presents real challenges to the workforce. The work is not only dangerous but also tedious and repetitive. One example is the use of gloveboxes and hotcells to process radioactive materials. This research will aid in the identification of better technologies to assist humans in these type of challenging tasks. Because gloveboxes and hotcells are designed to accommodate human workers, an anthropomorphic solution such as a prosthetic limb is required as a replacement to obviate expensive retrofitting requirements. Although prostheses have existed for centuries, the most extensive research and development of prosthetics occurred in the last few decades [1]. Many existing prosthetics have the ability to perform multi-finger dexterous movements to replace

human limbs [2]. Electromyogram (EMG), or myoelectric, control is one of the most common user interfaces for powered prostheses and generally is used when possible [3]. The reason for the widespread use of EMG control systems is the minimal effort required for operation due to the relatively small muscle signal needed [4]. The success of prosthetic hands hinges on the simplicity and reliability of the control system provided [5].

Moreover, in the recent years, the focus has been to provide force control to prosthetics [6], which provides an important form of communication between the user and the environment and an ease of control [7, 13]. As said by the hand surgeon Sterling Bunnell in 1944, "Without sensation, a worker can scarcely pick up a small object, and he constantly drops things from his grasp. The so-called eyes of his fingers are blind" (p. 222) [8]. Force control systems are becoming increasingly relevant in prosthetics as they restore some of the user ability to naturally control his hand. Without such systems, the user relies on visual feedback or control systems to operate the prosthetic limb in everyday applications [9]. However, with the use of embedded force control systems, prosthesis users will have the ability to perform delicate tasks that otherwise would be impossible.

The achievement of force sensing and measurement through a prosthesis is done by embedding a force sensor on the fingertip. Tactile force sensors are being used by researchers to examine their reliability and their performance in force control operations. Tactile sensors acquire information through physical touch [10]. In this paper, the TakkTile sensor by RightHand Robotics was used as it offers a reliable source of data at an inexpensive price. The sensor consists a MEMS barometric sensor embedded in a rubber material to not only protect the electronics but also to allow a wider area for sensing capabilities such as detecting subtle contact with objects [11].

Humans have the ability to sense the applied force on external objects despite the effects of wearing a glove. They are also able to adjust their

31st Florida Conference on Recent Advances in Robotics, May 10-11, 2018, University of Central Florida, Orlando, Florida
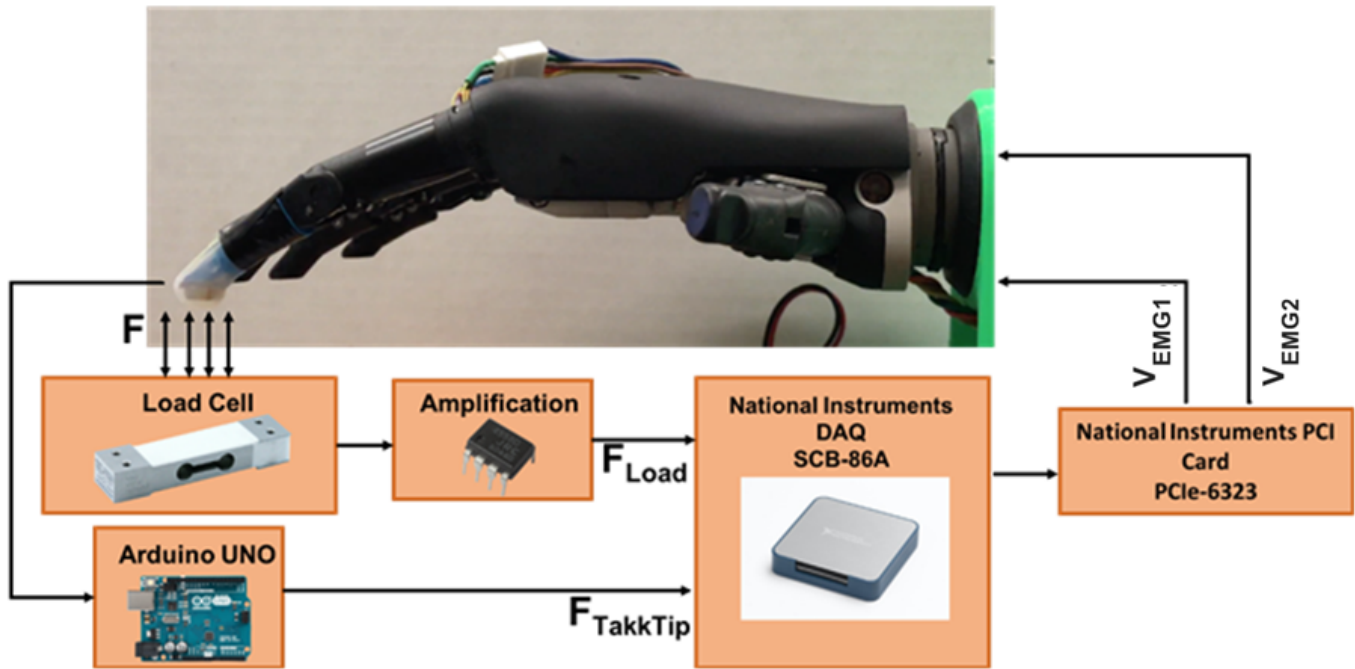
60

Figure 1 . System level diagram illustrating the experimental setup. Presented is the i-Limb Ultra with a TakkTip sensor mounted at the tip of the index finger. This sensor, the i-Limb and a load cell are connected to Simulink 2016b through a PCIe-6323 from National Instruments.

grip accordingly to perform various tasks with the ability to sense the applied force while wearing that glove, however, the effects of the glove on a robotic hand have not been examined as deeply yet.

This paper presents the effort taken to examine the effects of the glove on a robotic hand. This was done by designing a new force sensor geometry utilizing Takktile sensor and testing the sensor ability to detect force applied through various modes with and without gloves. An i-Limb Ultra Revolution prosthetic hand was used to perform the testing (Figure 1). A Takktile sensor from RightHand Robotics was embedded into a fingertip to be mounted onto the index finger of the i-Limb hand. This sensor was coined the TakkTip. The hand is inserted into the glove to compare the effect it has on the force. The experiment had three modes and each mode was tested with and without the glove.

2. TAKKTIP SENSOR FABRICATION

This new design, called the TakkTip, is comprised of a Takktile force sensor from RightHand Robotics (Figures 2, 3), and fabricated in three steps. The first step was modeling the desired geometry. The second focused on 3D printing the structure to support the sensor and the third was to embed the assembled sensor into a semi-soft rubber called DragonSkin 50.

Figure 2 . Fabricated TakkTip sensor for measuring the forces of all experiments in this paper.
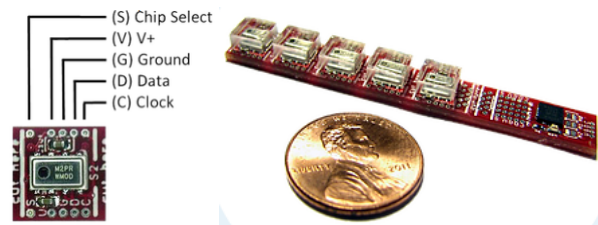
2.1 Takktile Force Sensor

Figure 3 – TakkTile sensor used to fabricate the TakkTip. On the left is and individual sensor and wiring diagram. On the right is the array or sensors the individual TakkTile sensor is separated from a Takkstrip [12].

31st Florida Conference on Recent Advances in Robotics, May 10-11, 2018, University of Central Florida, Orlando, Florida

61

2.2 Modeling and 3D Printing

Solidworks 2017 was used to create the CAD model for 3D printing (Figure 4). This was achieved by removing the preexisting fingertip on the i-Limb Ultra robotic hand. This exposed the mounting post which allows the fingertip to be removable with minimal effort. Multiple images were taken of the post to create a 3D model of the cavity needed for mounting. This design was printed using PLA filament (Figure 5).
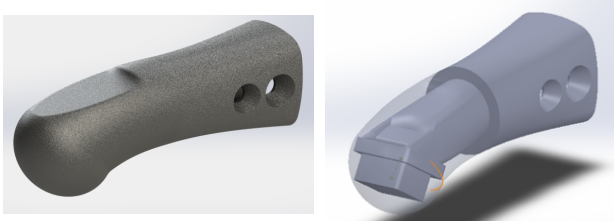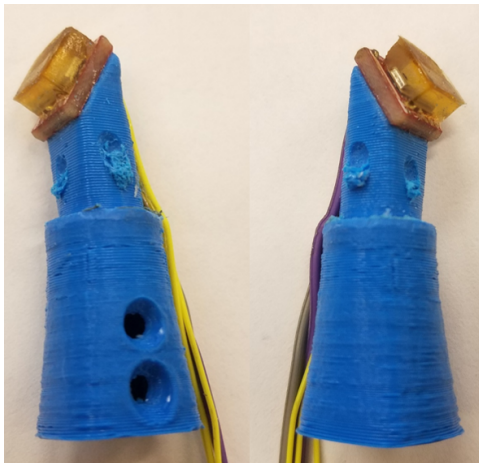

Figure 4 . CAD model in Solidworks 2017 of the TakkTip sensor.

Figure 5 . 3D printed structure used to mount the sensor to the i_Limb Ultra hand.

2.3 Molding

A 3D mold was created from the negative of the model described in the previous section (Figure 6). This was then 3D printed and prepped by sanding the edges smooth to achieve no visible gap between the two halves when clamped together. The supplies shown in Figure 6 were used to make Dragonskin 50 mix. The mix was prepared with a 1:1 ratio of Dragonskin A (yellow container) and Dragonskin B (blue container) using a digital scale and then the mixture stirred for one minute to completely combine the two parts of the mixture.
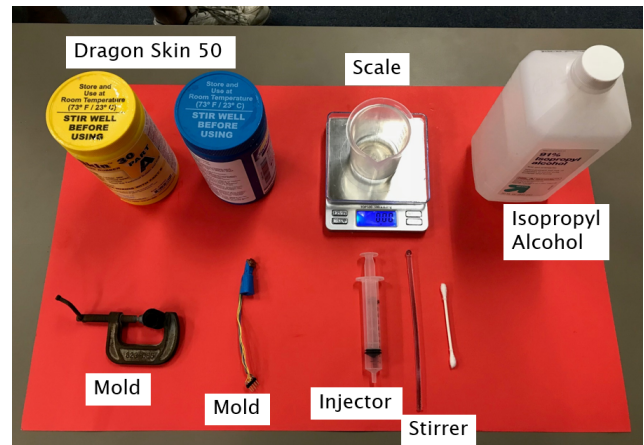

Figure 6. Supplies used to mold the soft tip of the TakkTip sensor in Dragonskin 50.

This was then placed into a vacuum chamber to degas until all of the bubbles stopped forming (Figure 7). Once this was complete the Dragonskin was poured into the mold using the injector to fill the mold to about 50%. The 3D printed structure (Figure 5) was inserted into the Dragonskin-filled mold and allowed to set overnight (Figure 7). This completed the fabrication of the TakkTip sensor.
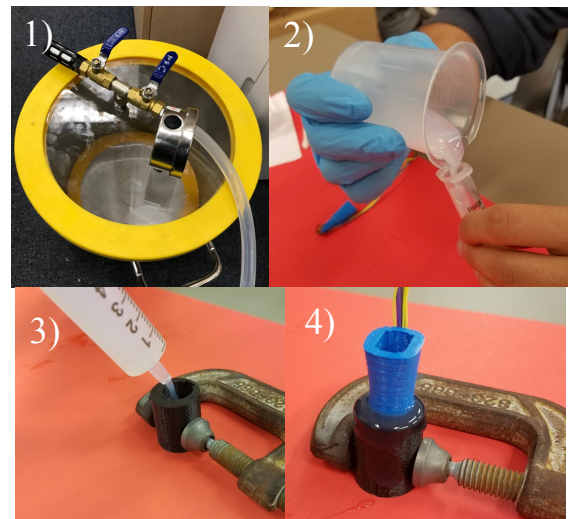

Figure 7. Molding the TakkTip into Dragonskin 50

2.4 Electronics

An Arduino Uno was used to connect the Takktile sensor and acquire the force data. This was output on one of the PWM channels and input into Simulink 2016b through a PCIe-6323 board from National Instruments with a SCB-68A data acquisition module attached. Additionally, a load cell (esp-35 from Transducer Techniques, Temecula, USA) was connected using an INA129p amplifier to amplify the signal and to provide analog low pass filtering.

The existing electromyogram signals used to control the movement of the i-Limb hand were measured during some testing cases to determine the signals needed to actuate the hand and replace the electromyogram sensors. This signal was found to be a square wave with a magnitude

31st Florida Conference on Recent Advances in Robotics, May 10-11, 2018, University of Central Florida, Orlando, Florida

62

of 4.7V. This allowed the creation of two control signals, V_{EMG1} and V_{EMG2}, as outputs from Simulink to provide the controllability to achieve the desired modes for testing.

2.5 Calibration

Both the load cell and the TakkTip needed to be calibrated to measure force accurately. This was done by placing known masses on the load cell and measuring the output voltage for a series of different weights. A linear fit was found using Microsoft Excel that related the force to the voltage. Once this was complete, the load cell was used to calibrate the TakkTip in the same manner.

3. EXPERIMENTAL METHODS

3.1 Donning and Doffing the Glove

This was very important in the analysis of whether there is an effect of wearing the glove on the force that can be sensed. To minimize the variability from test to test, all measurements were gathered during the same session and all mounting hardware was marked to easily perform testing in the same location after putting the glove on and taking it off, minimizing the possibility of error.

3.2 Measuring the Forces

The force measurements gathered during each test were made using the load cell, $F_{LoadCell}$, and TakkTip sensor, $F_{TakkTip}$. The TakkTip was connected to an Arduino Uno and a library found online was used to read data from the TakkTile sensor and send it out through one of the PWM pins. There were noticeable variations in force measurements due to the sensor being temperature sensitive. This was compensated for by calibrating the voltage of the sensor with the temperature and a correlation to map the two and compensate for temperature changes.

The load cell was connected to an amplification board prior to connecting to Simulink to both amplify and filter the signals.

3.3 Mode 1 – Open/Close

The open/close mode was tested by starting with the hand in the open position and continuously closing and then opening the hand at a rate of 9 rad/s (Figure. 8). The measurements were gathered with the glove on and the glove off.
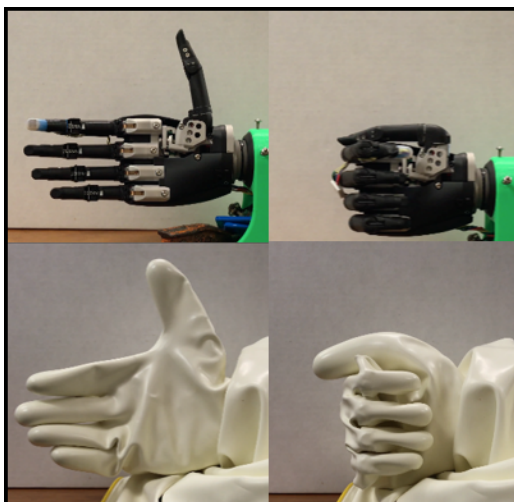

Figure 8. Mode 1 representing a fully opened hand posture cycling repeatedly to a closed posture and back.

Mode 2 – Tapping

The second mode, shown in Figure 9, measured the force applied by the i-Limb when intermittently in contact with an object. This formulated a tapping scenario. For consistency purposes, a load cell was utilized as the object in contact and also served as a way to confirm the measurements with an externally calibrated device. The reason for this is because a load cell offers a flat surface that helps with repeatability as well as a direct way of measuring the force being applied.
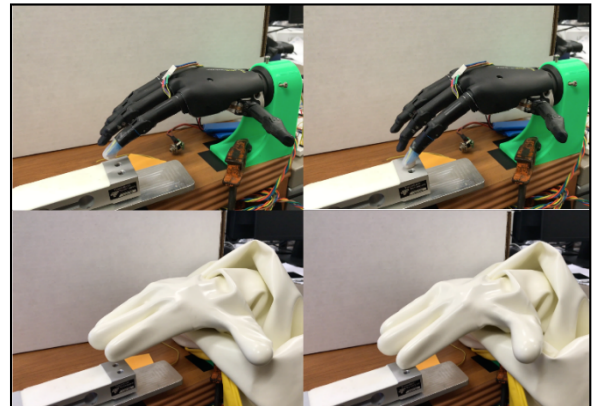

Figure 9. Mode 2 represents an intermittent tapping force to observe the effect that tapping has on the sensing ability through the glove.

3.4 Mode 3 Constant Force

The final mode (shown in Figure 10) tested the ability of the sensor to apply a constant load intermittently. Actuation was similar to the tapping mode but during contact with the load cell, the finger maintained contact and no additional movement commands were initiated until the sensor values reached steady state conditions. The finger was then extended to the fully opened position and the cycle repeated. This was performed with the glove and without the glove to observe the effect of the glove on the force measurement.
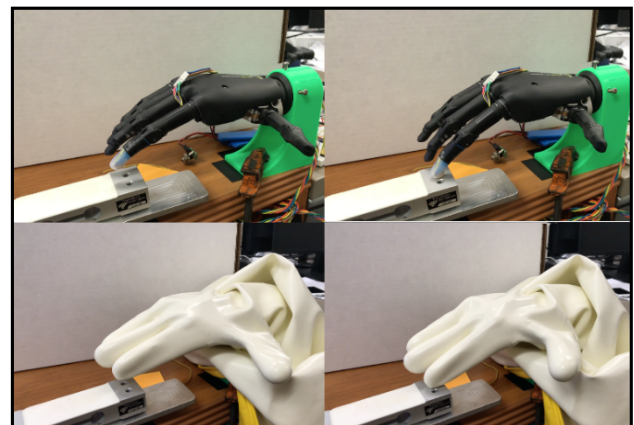

Figure 10. Mode 3 represents an intermittent constant force to observe the effect of the glove on a constantly applied load.

31st Florida Conference on Recent Advances in Robotics, May 10-11, 2018, University of Central Florida, Orlando, Florida

63

4. RESULTS

4.1 Mode 1 – Open/Close

The results for opening and closing the hand are presented below and show that there is a difference in the measured force when the hand operated with and without a glove (Fig. 11). Without a glove present the TakkTip had no observed force effects transferred from the motion of opening and closing the hand. When the glove is put onto the hand there is an inherent bias imposed on the force measurement through the TakkTip. This bias was consistently observed throughout many tests. Note that this bias varied in magnitude each time the glove was put on but once the glove was on the bias was consistent and discernable for force sensing capabilities through the glove during the opening and closing motions.
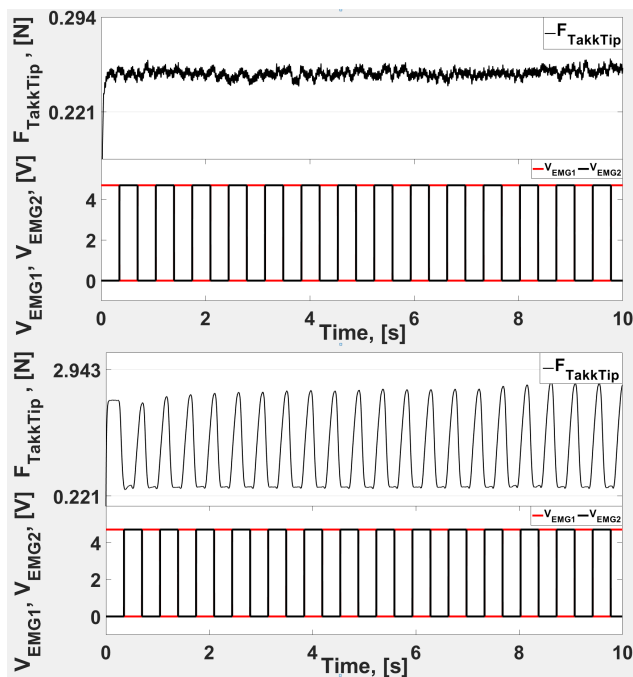

Figure 11. Results from opening and closing the i-Limb to the limits of its range for both no glove (top) and glove (bottom).

4.2 Mode 2 - Intermittent Tapping

Similar to the results from opening and closing the hand, there is an inherent bias when putting the glove on. In the case of intermittent tapping the force was discernable from test to test (Fig. 12). This justifies this sensor as able to detect an applied force through a glove for this mode. Note that the angle of contact between the TakkTip and the load cell remained consistent from test to test. This was important to obtain consistent results for determining the effect of the glove for this portion of the research. Future consideration will be discussed in the conclusion of this paper.
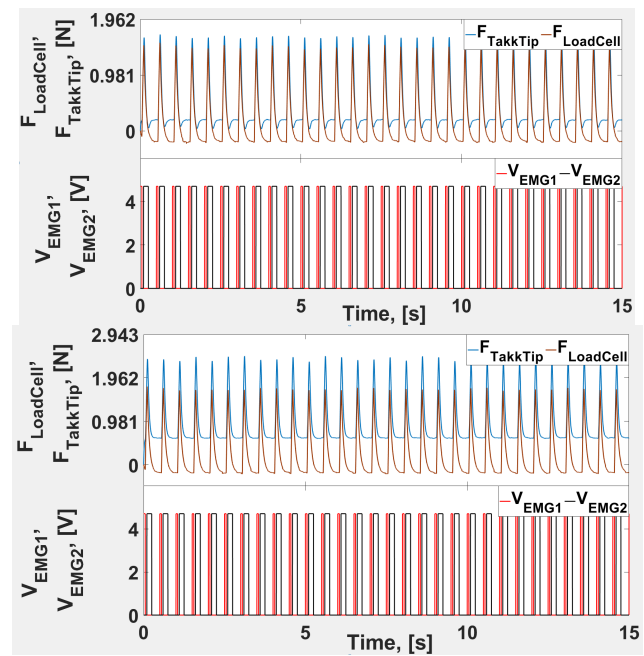

Figure 12. Results from intermittent tapping onto the load cell. This was done for both wearing a no glove (top) and glove (bottom)

4.3 Mode 3 – Intermittent Constant Force

The results for this mode have similar notes to mode 2. As illustrated in figure 13, all trials produced the same results and were consistent from test to test.
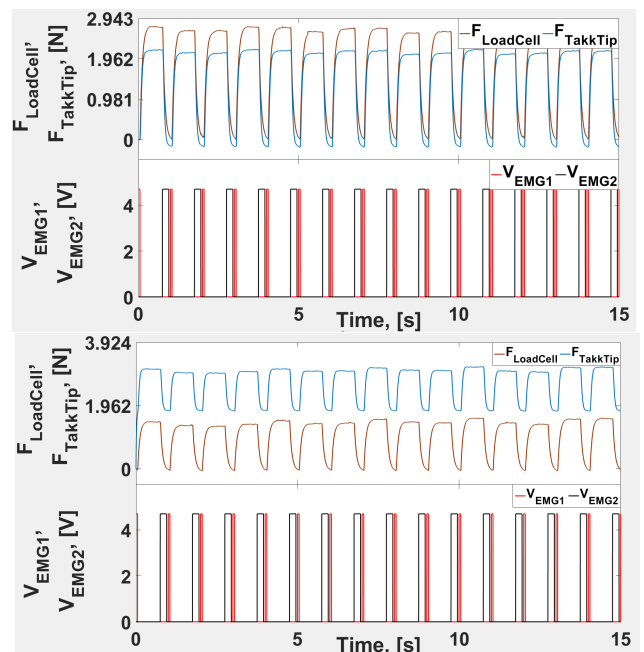

Figure 13. Results from intermittent constant force onto the load cell. This was done for both wearing a no glove (top) and glove (bottom)

31st Florida Conference on Recent Advances in Robotics, May 10-11, 2018, University of Central Florida, Orlando, Florida

64

5. CONCLUSION

This study found noticeable differences in tactile force sensor readings between the cases of a prosthetic hand wearing a glove and without the glove, however the force measurements from both cases were still recognizable and can be used to determine the force applied to an object. Note that an inherent bias was observed in the system when the glove was worn. Moreover, the sensing ability to the i-Limb was not substantially altered as the robotic hand performed the tasks for different modes with consistency throughout the experiment for the tested modes. The newly fabricated TakkTip sensor proved to detect contact with an object when compared to no object for the two studied modes, however, the sensor did not perform consistently if it was used at different contact angles. A future study can determine the characteristics of varied contact angles on the force sensing capabilities. Additionally, to address the inherent bias observed in all cases of force sensing through the glove, this can be compensated for by applying a zero-out calibration at the beginning of each test. Ultimately, these results suggest that the tested tactile sensor has potential to sense grasping forces in automated glovebox situations. The anthropomorphic solution afforded by a prosthetic hand offers direct application of electromyogram control methods [7], [13].

6. ACKNOWLEDGMENTS

7. REFERENCES

[1] Marshall, J. (2015, September 21). *The History of Prosthetics*. *http://unyq.com/the-history-of-prosthetics/*

[2] R. G. E. Clement, K. E. Bugler, and C. W. Oliver, "Bionic prosthetic hands: A review of present technology and future aspirations," *Surgeon*, vol. 9, no. 6. pp. 336–340, 2011.

[3] E. A. Corbett, E. J. Perreault, and T. A. Kuiken, "Comparison of electromyography and force as interfaces for prosthetic control," *J. Rehabil. Res. Dev.*, vol. 48, no. 6, pp. 629–641, 2011.

[4] Parker PA, Englehart KB, Hudgins BS. Control of powered upper limb prostheses. In: Merletti R, Parker P, editors. Electromyography: Physiology, engineering, and noninvasive applications. Hoboken (NJ): Wiley-Interscience; 2004.

[5] C. Cipriani, F. Zaccone, S. Micera, and M. C. Carrozza, "On the shared control of an EMG-controlled prosthetic hand: Analysis of user-prosthesis interaction," *IEEE Trans. Robot.*, vol. 24, no. 1, pp. 170–184, 2008.

[6] Q. Fu and M. Santello, "Improving fine control of grasping force during hand-object interactions for a soft synergy-inspired myoelectric prosthetic hand," *Front. Neurorobot.*, vol. 11, no. JAN, 2018.

[7] B. A Kent, N. Karnati, and E. D. Engeberg, "Electromyogram synergy control of a dexterous artificial hand to unscrew and screw objects.," *J Neuroengineering Rehabil*, vol. 11, no. 1, p. 41, 2014.

[8] R. Johansson and G. Westling, "Roles of glabrous skin receptors and sensorimotor memory in automatic control of precision grip when lifting rougher or more slippery objects," Exp. Brain Res., vol. 56, no. 3, pp. 550–564, 1984.

[9] C. Pylatiuk, A. Kargov, and S. Schulz, "Design and evaluation of a low-cost force feedback system for myoelectric prosthetic hands," in *Journal of Prosthetics and Orthotics*, 2006, vol. 18, no. 2, pp. 57–61.

[10] M. I. Tiwana, S. J. Redmond, and N. H. Lovell, "A review of tactile sensing technologies with applications in biomedical engineering," *Sensors Actuators, A Phys.*, vol. 179, pp. 17–31, 2012.

[11] https://www.righthandrobotics.com/

[12] (2012, Nov.). TakkTile project. [Online]. Available: http://www.takktile.com

[13] B. Kent, J. Lavery, and E. Engeberg, "Anthropomorphic Control of a Dexterous Artificial Hand via Task Dependent Temporally Synchronized Synergies," Journal of Bionic Engineering, vol. 11, p. 236-248, 2014, DOI: http://dx.doi.org/10.1016/S1672-6529(14)60044-5

31st Florida Conference on Recent Advances in Robotics, May 10-11, 2018, University of Central Florida, Orlando, Florida

65

Validation of Heterodyning Method Using Comsol Software

Shervin Tashakori, Ibrahim N. Tansel

Florida International University
Department of Mechanical and Materials Engineering
Miami, Florida 33174

ABSTRACT

Heterodyning effect has been used for many wireless communication, electronics and ultrasound applications. When two different frequencies are applied to proper nonlinear systems, new frequency components develop at the predictable frequencies. In the experimental studies, the perfect plates without any defects behaved like linear systems. Only the applied frequencies existed when the surface vibrations were monitored. However, once a defect like a crack or debonding started to develop the structure behaved like a nonlinear system. New frequencies and their harmonics developed at the difference and addition of the applied frequencies. In this study, COMSOL Multiphysics software was used to simulate the heterodyning effect. The response of two aluminum plates were studied when the upper face of one plate was excited at two different frequencies and the response of the bottom face of the second plate at the opposite side was simulated. Similar to the experimental studies, the monitored signal had only the excited frequencies when two plates were in contact. When the distance between the plates was increased to 0.012 µm, new frequencies were developed at the difference and addition of the excitation frequencies, and at their harmonics. The numerical results agreed with our expectations based on the experimental studies.

Keywords

Structural health monitoring, heterodyning effect, COMSOL Multiphysics software, Debonding, Delamination, crack

I. INTRODUCTION

Many structural health monitoring (SHM) techniques were introduced in the last few decades. Many of them needed a baseline or reference data which was collected when the structure was at the excellent condition. The defects were detected by monitoring the difference between the monitored signal and the baseline. Recently, nonlinear methods where developed to eliminate the need for the baseline data and the false alerts related to the change of the characteristics of the structure with time without any critical defects. Nonlinear methods relied on the change of the characteristics of the structure from linear to nonlinear.

Experimental studies proved that, cracks, lose bolts, debonding and delaminations make the structure behave like a nonlinear structure. These defects could be detected with the methods which can identify the change of the response characteristics from linear to nonlinear. Heterodyne method is one of these nonlinear methods. It was developed based on the detection of nonlinearity from the developing new frequencies without any restriction on the range of two or more excitation frequencies. The objective of this study was to validate the heterodyne method by using numerical methods. The study also investigated if the nonlinear characteristics of the structure could be simulated with the finite element analysis methods.

In the SHM studies, numerical methods need to calculate the response of the structure by considering that the experimental methods use piezoelectric (PZT) materials as sensors and actuators [1-6]. Since the thickness and complexity of the structures increase the computational cost, most of the works in this area used the finite element methods developed for thin plates and shells structures [7-11].

In this study, COMSOL Multi-physics software was used to represent a structure with two aluminum plate. Perfect contact of the plates and creating of an extremely small opening between them were considered.

II. MODELING PERFECT CONTACT AND MICRO SEPARATION WITH COMSOL

In this study, piezoelectric device module of COMSOL was used to simulate our piezoelectric transducers which were used as both sensor and actuator. Figure 1 shows the schematic of the simulated structure. The structure had two aluminum plates which have perfect contact. The structure had three cylindrical piezoelectric (PZT) transducers. In Figure 1 the top view of the plates is presented on the left. The plates were turned upside down, and their new view is presented on the right. Two PZTs were bonded on the top surface of the upper aluminum plate. These PZT transducers were excited at two different frequencies. Single PZT transducer was attached to the bottom surface of the second plate. This transducer was used as sensor. The simulations

31st Florida Conference on Recent Advances in Robotics, May 10-11, 2018, University of Central Florida, Orlando, Florida

66

were repeated when the contact between the plates were perfect. Later, the distance between the plates were increased to 0.12 µm. This micro separation simulated the debonding.
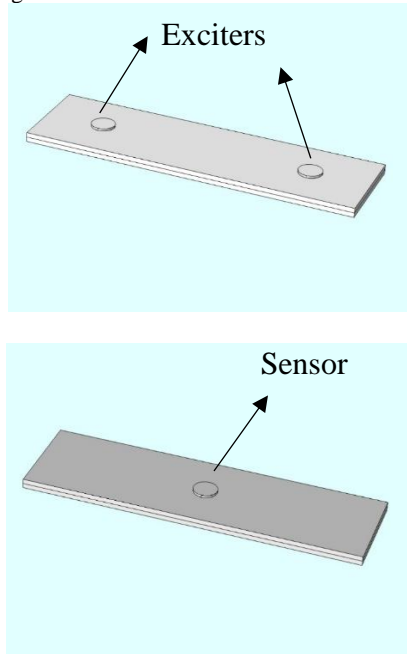

Fig. 1. Experimental setup. Two aluminum plates facing each other with 2 PZT exciters on the left and the view when the plates are turned upside down on the right.

Table 1. Dimensions of plates and PZTs

Name	Value
Length of plates	0.28 m
Width of plates	0.08 m
Height of plates	0.004 m
Radius of PZTs	.01 m
Height of PZTs	0.002 m
Voltage	100 V
First excitation freqency	1.7E5 Hz
Second excitation freqency	1.9E5 Hz
Distance between two plates	0-0.012 µm

The model was created with the COMSOL's piezoelectric device module. Time and frequency domain studies were performed. The simulated PZT transducers were made of Lead Zirconate Titanate (PZT-4) with density of 7500 kg/m3. The boundary condition of all four sides of the plates was defined with fixed constraints. The other sides were defined as free. The lower surfaces of PZTs which were attached to the plates were considered as ground with a zero charge. The upper surfaces of the exciters were charged with harmonic waves. The upper surface of the sensor was connected to the probe to be monitored. The solid model was meshed with free tetrahedral elements (Figure 2). The minimum and maximum mesh sizes were set to 450 µm and 10500 µm respectively.
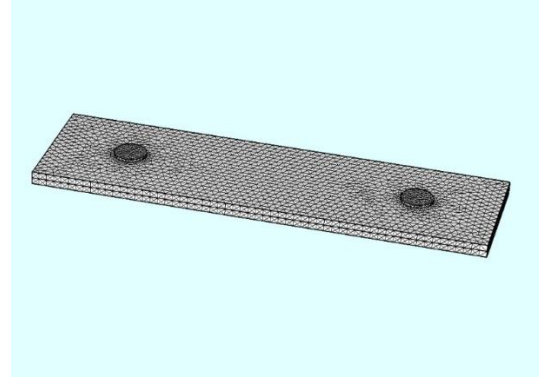

Fig. 2. Mesh structure of the finite element model.

To evaluate if the structure demonstrate the heterodyning effect, the structure was excited with two harmonic signals with different frequencies. Time domain response of the structure with two plates was captured from the PZT transducer at the bottom of the structure. The Fast Fourier Transform (FFT) of the response signal was calculated, plotted and studied. As you can see the propagation of the two harmonic signals with different frequencies was shown in figure 3.
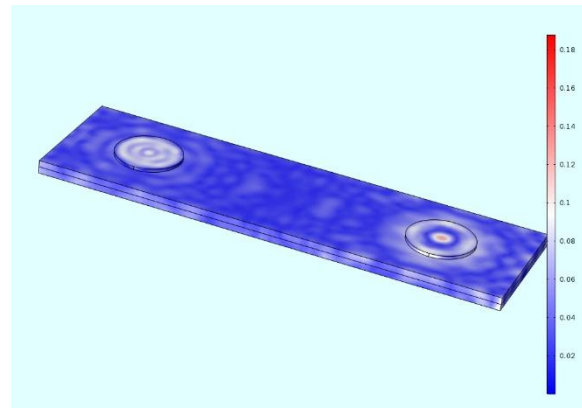

Fig. 3. Wave propagation of the two harmonic signals with different frequencies

31st Florida Conference on Recent Advances in Robotics, May 10-11, 2018, University of Central Florida, Orlando, Florida

67

I. SIMULATION RESULTS

In the simulations, aluminum plates with the density of 2700 kg/m3, modulus of elasticity of 70GPa, and Poisson's ratio of 0.33 were considered. Two PZT exciters at the top of the plates were excited with harmonic signals with the frequencies of 170 kHz and 190 kHz. The excitation signals had 100V peak to peak voltage. The simulate signal of the PZT attached to the bottom plate was sampled at 1MHz. First, the response of the structure was calculated when the plates had perfect contact with no separation distance between two plates. This corresponded to perfect bonding. The time and frequency domain plots of the simulated signals of the PZT transducer are presented in Fig. 4, 5.
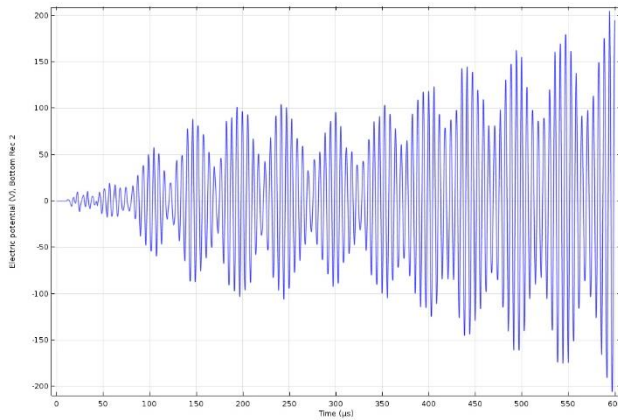

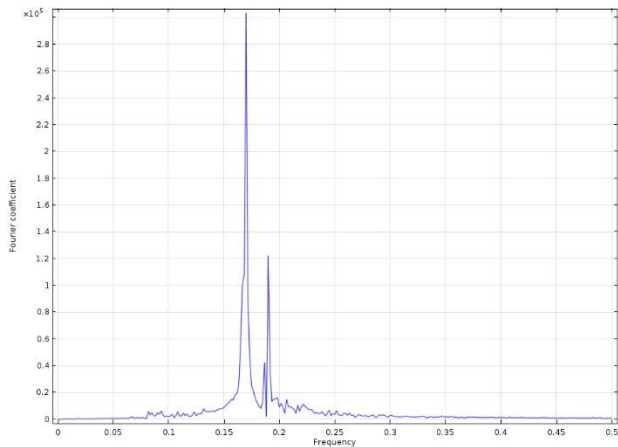**Fig4. Time domain response of the system when there is no debonding**

Fig4. Frequency domain response of the system when there is no debonding

The spectrum had two dominant frequencies at the excitation frequencies of 170 kHz and 190 kHz. The simulation was repeated when the distance between the aluminum plates was increased to 0.012 µm. The time domain response and FFT of the simulated sensor output is presented in Fig.6, 7.
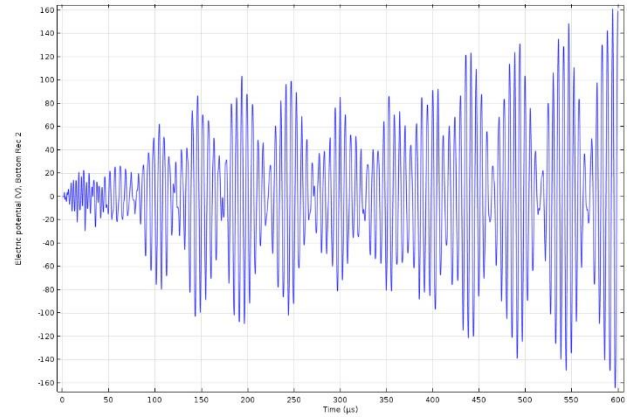
Fig. 6. Time response of the system for 0.012 µm distance between two plates
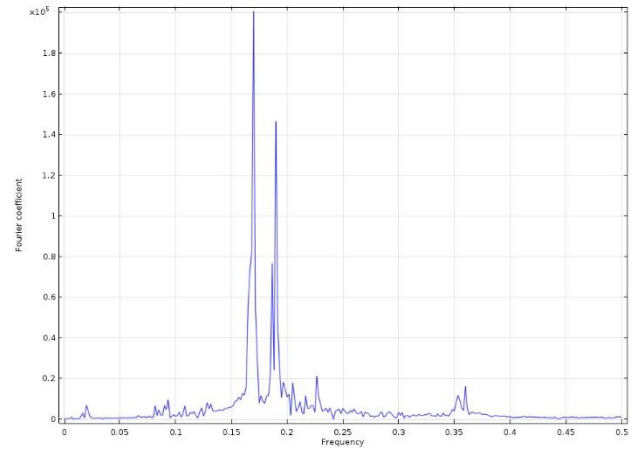
Fig. 7. Frequency response of the system for 0.012 µm distance between two plates

As it was expected, in the presence of micro separation (debonding), a small peak appeared at the difference of two excitation frequencies. The amplitude of the spike at the difference of the excitation frequencies is presented in Table 2.

Table 2. Comparing the amplitude of the peak at the difference of the excitation frequencies

Distance between two plates (µm)	Amplitude of the spike at the frequency of the difference
0	700
0.012	5600

31st Florida Conference on Recent Advances in Robotics, May 10-11, 2018, University of Central Florida, Orlando, Florida

68

I. CONCLUSION

Nonlinear SHM methods detect the defects from the characteristics of the monitored signal. According to the experimental studies, perfect structures behave as a linear system. Certain types of defects such as debonding, cracks, loose bolts and delaminations change the behavior of the system from linear to nonlinear.

In this study, perfect structure and debonding was simulated by using the COMSOL Multi-physics software. The FFT of the simulated sensor's data was investigated. The study indicated that two aluminum plates which are always in contact with behave like a linear system. When one of the plate is excited with two harmonic signals with two different excitation frequencies, the monitored signal of the simulated sensor which was attached to the other plate has two frequency components with the excitation frequencies.

Spikes showed up at the difference and sum of the excitation frequencies, and their harmonics as soon as the plates were separated. The spike at the difference of the excitation frequencies was very clear when the distance between the plates was 0.012 µm. The structure behaved as a nonlinear system as soon as the micro separation started. These results showed that the heterodyne method can be used for detection of debonding.

The results also confirmed that the COMSOL Multi-physics software is capable to simulate the response of the structures even if they have nonlinear behavior.

I. REFERENCES

[1] M. Sartorato, R. de Medeiros, D. Vandepitte, and V. Tita, "Computational model for supporting SHM systems design: Damage identification via numerical analyses," Mech. Syst. Signal Process., vol. 84, pp. 445–461, Feb. 2017.

[2] C. Yang and S. O. Oyadiji, "Damage detection using modal frequency curve and squared residual wavelet coefficients-based damage indicator," Mech. Syst. Signal Process., vol. 83, pp. 385–405, Jan. 2017.

[3] N. Grip, N. Sabourova, and Y. Tu, "Sensitivity-based model updating for structural damage identification using total variation regularization," Mech. Syst. Signal Process. vol. 84, pp. 365–383, Feb. 2017.

[4] R. de Medeiros, M. Sartorato, D. Vandepitte, and V. Tita, "A comparative assessment of different frequency based damage detection in unidirectional composite plates using MFC sensors," J. Sound Vib., vol. 383, pp. 171–190, Nov. 2016.

[5] M. Pedram, A. Esfandiari, and M. R. Khedmati, "Damage detection by a FE model updating method using power spectral density: Numerical and experimental investigation," J. Sound Vib., vol. 397, pp. 51–76, Jun. 2017.

[6] M. Sartorato, R. de Medeiros, D. Vandepitte, and V. Tita, "Computational model for supporting SHM systems design: Damage identification via numerical analyses," Mech. Syst. Signal Process., vol. 84, pp. 445–461, Feb. 2017.

[7] Y. Shen and V. Giurgiutiu, "Combined analytical FEM approach for efficient simulation of Lamb wave damage detection," Ultrasonics, vol. 69, pp. 116–128, Jul. 2016.

[8] A. S. Rizi, S. Hedayatrasa, X. Maldague, and T. Vukhanh, "FEM modeling of ultrasonic vibrothermography of a damaged plate and qualitative study of heating mechanisms," Infrared Phys. Technol., vol. 61, pp. 101–110, Nov. 2013.

[9] J. Xiang and M. Liang, "A two-step approach to multi-damage detection for plate structures," Eng. Fract. Mech., vol. 91, pp. 73–86, Sep. 2012.

[10] Y. Alkassar, V. K. Agarwal, and E. Alshrihi, "Simulation of Lamb Wave Modes Conversions in a Thin Plate for Damage Detection," Procedia Eng., vol. 173, pp. 948–955, Jan. 2017.

[11] A. H. Alavi, H. Hasni, N. Lajnef, and K. Chatti, "Damage growth detection in steel plates: Numerical and experimental studies," Eng. Struct., vol. 128, pp. 124–138, Dec. 2016.

31st Florida Conference on Recent Advances in Robotics, May 10-11, 2018, University of Central Florida, Orlando, Florida

69

Combat Coordination Using Peripheral Tactile Display

Christopher Clifford, Pradipta Biswas, Sang-Eun Song

University of Central Florida CECS
4266 West Plaza Drive PO #661248, Orlando, Florida 32816

Chris.e.clifford@knights.ucf.edu, pvbiswas@knights.ucf.edu, s.song@ucf.edu

ABSTRACT

The purpose of this paper is to perfect a wearable tactile display that can provide rapid response and group coordination for infantrymen-foot soldiers. Vibro-Tactile displays are devices that convey information to a person through the sensation of touch. This is achieved by using electromechanical actuators such as vibrators that are mounted in clothing or belts that hug the body. By activating the actuators in different patterns, the user can recognize these patterns as commands. This paper proposes an extremity worn tactile display concept that provides information regarding gunshot localization to the user in a prompt manner to enable rapid response to a threat.

Keywords

Tactile Display, Group Coordination, Gunshot Localization, Rapid Response

1. INTRODUCTION

Tactile displays are devices that convey information to a person using the sensation of touch. This can be achieved through vibrations, heat, or pressure. Vibrotactile actuators, similar to those used in cell phones, are commonly used for a variety of applications [1]. Tactile displays can help substitute primary senses such as sight with touch for intricate tasks such as navigation. Tactile displays may also be used in a peripheral sense where the tactile actuators provide hints or directions that do not require the wearer's complete attention to enacts an impulse reaction.
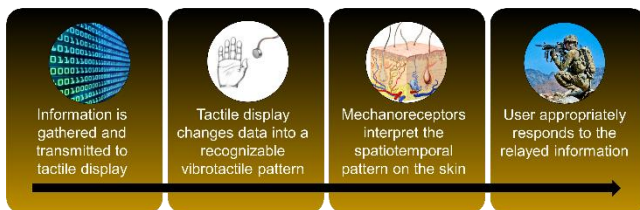

Figure 1. Data flow from raw information to tactile interpretation.

As shown in Figure 1, tactile displays translate raw data into a recognizable pattern on the skin for the wearer. Vibrotactile displays function by triggering the mechanoreceptors in the human skin by vibration. Depending on the application of the tactile display, some form of raw data will be transmitted to the tactile display by wired connection, wirelessly, or other means. The tactile display will then translate that data into a comprehendible pattern for the wearer. These patterns may change depending on the functionality of the display. An example of a spatiotemporal pattern is shown in Figure 2.
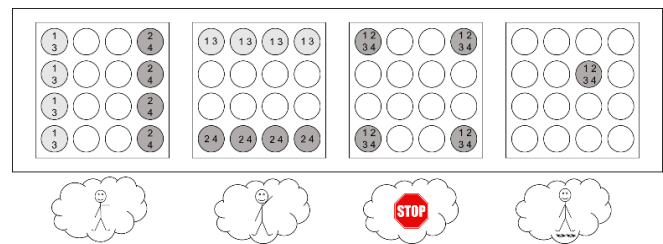

Figure 2. Example vibrotactile spatiotemporal pattern in a 4x4 array.

This represents patterns for a four-by-four tactile array. This kind of design has been used for many applications, including an MIT study where different spatiotemporal patterns like those above instructed the user to perform different navigational tasks [1]. The numbers in the tactors represent in what order the vibrations trigger as the time element in tactile displays is very important to how the wearer perceives the pattern. Some patterns may be much clearer or recognizable to the user if they pulsate left right such as in the first square, than if they were always both on.

Mechanoreceptors are sensory receptors embedded in the skin that give us the sensation of touch. Mechanoreceptors respond to mechanical pressure or distortions of these patterns on the skin. Certain areas of the body have a higher density of mechanoreceptors in the skin and are therefore more sensitive to smaller vibrations [2].

The more mechanoreceptors in a given area, the lower the two-point discrimination will be. Two-point discrimination is the minimum distance at which the body can identify two unique tactile stimuli. It is more difficult for the body to differentiate between two close stimuli in comparison to two spread apart stimuli [2]. Different parts of the body have different sensitivities to tactile

31st Florida Conference on Recent Advances in Robotics, May 10-11, 2018, University of Central Florida, Orlando, Florida

70

stimulation and therefore have different two-point discrimination thresholds. For example, two-point discrimination is much smaller in the fingertips than on the torso. This is intuitive because our fingertips have a smaller surface area and are used constantly to determine characteristics of objects through touch [2].
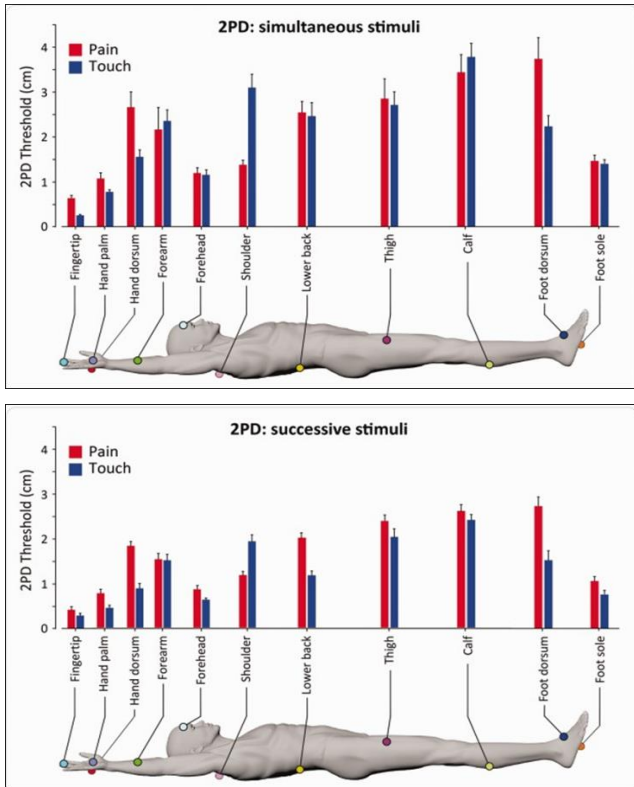

Figure 3. Two-point discrimination for successive vs. simultaneous stimuli in different regions of the body [2].

After the wearer of the tactile display feels the vibrotactile pattern on their skin, they will act accordingly depending on what the display is being used for. This result will vary greatly depending on application. For every tactile display however, the user must be trained to associate certain spatiotemporal patters with their respective commands. This can be seen in Figure 2 where the four corner tactors pulsating should indicate the wearer to stop moving.

Tactile displays must be in contact with the skin during data transmission for the wearer to receive the information; because of this limitation tactile displays are conventionally used in applications where the wearer is not drastically moving.

Tactile displays are used in many applications including assisting the blind and enhancing pilot's spatial awareness in limited visibility situations. The civilian use of tactile displays has shown that they can effectively supplement or partially replace another sense such as sight. Tactile displays have only been used in the military to assist pilots, however civilian uses are much more extensive. Furthermore, there are many areas of the body utilized by different tactile displays to achieve the same goals. Almost every area of the body has been used by tactile displays when guiding the blind including the fingers, torso, waist, feet and mouth. Below a few of these tactile display applications will be described.

Tang and Beebe used an oral mouthpiece tactile display to help the blind navigate outdoors. The device had an electro tactile display on the roof of the mouth and a tongue touch interface on the bottom for the user to operate. The tactile display could present four different arrow patterns representing left, right, forwards, or backwards [3].
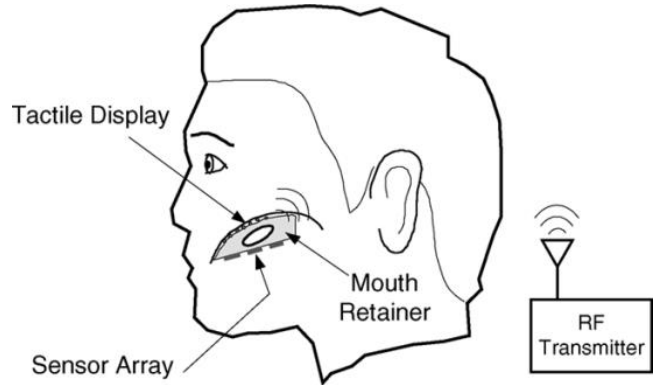

Figure 4. Tang and Beebe's oral microfabricated electro tactile display for the blind [3].

Velázquez et. al. designed a shoe integrated tactile display and evaluated the degree to which humans could interpret tactile information through this device [4]. The display consisted of a 16-point array of actuators on the bottom of the foot. The tactile display was integrated into the sole of a shoe. Some of the benefits of using the foot as the tactile receiver is the high density of mechanoreceptors and its continuous use by the body to maintain balance. The test subjects were successful at navigating the provided course given adequate time. These results were expected to improve were the subjects given more training with the device.
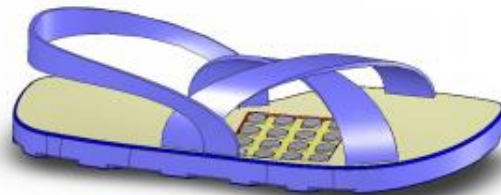
Figure 5. Velázquez 's Tactile display incorporated in a shoe [4].

The TNO Tactile Torso Display and the Naval Aeromedical Research Laboratory Tactile Situation Awareness System (TSAS), both provide intuitive three-dimensional spatial information [5].

The TNO Tactile Torso Display consists of small vibrating elements in array form. When activated they give a localized vibration that is similar to a tap on the shoulder. The TNO Tactile Torso Display is integrated into a vest. This display gives the pilot fast and intuitive spatial information. A tap on the left corresponds to an event on the pilot's left. The vest does not depend on visual information therefore giving the pilot redundancy when operating in IFR or limited visibility conditions [5].

31st Florida Conference on Recent Advances in Robotics, May 10-11, 2018, University of Central Florida, Orlando, Florida

71

Figure 6. A Helicopter Pilot Showing a TNO Tactile Torso Display (TTTD) [5].

The Tactile Situation Awareness System (TSAS1) is an advanced flight instrument that uses tactile displays integrated into the flight garments to provide situation awareness information to pilots. The TSAS system accepts data from various aircraft sensors and presents this information via tactors integrated into flight garments. TSAS has the capability of presenting a variety of flight parameter information, including attitude, altitude, velocity, navigation, acceleration, threat location, and/or target location [6].

The TSAS display uses an array of eight columns of two tactors to give spatial information to the pilot in 45° increments. This system, similar to the TNO display, supplements the pilot's other senses to add a layer of redundancy but does not replace them.
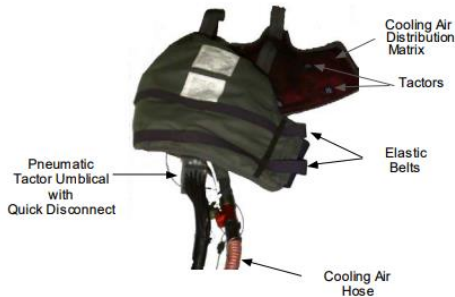

Figure 7. The Tactile Situation Awareness System (TSAS1) [6].

The benefits of tactile devices is that they reduce the risk of sensory overload in man-machine interfaces. Traditionally these activities addressed by the displays have a low demand on tactile information processing. In the pilot's scenario, it is extremely demanding on the pilot's sense of sight and hearing. By shifting some of the workload to the tactile sensory system, this device helps reduce the number of accidents due to a lack of spatial awareness resulting from sensory overload.

An important distinction to be made between the discussed tactile displays used for the blind and those used for the pilots is that the two displays designed for the blind completely substitute a lost sense whereas the two vests for military pilots give redundancy to the pilot's visual sensory system.

Current technology exists that can determine the origin of gunshots by analyzing soundwaves from the shot. One device that does this is the QinetiQ EARS Gunshot Localization System [7]. This device has been tested in Iraq and was popular with those soldiers that used it. The EARS system consistently and accurately determines the location of gunshots in a variety of environments. Another benefit of the EARS device is that it finds the location of the origin in under a quarter of a second.

Figure 8. QinetiQ EARS shoulder mounted sensor [7].

The EARS system comes in three variations: shoulder worn, fixed site, and vehicle mounted. When using the shoulder worn variation, which is what this proposal will pertain to, the user must carry the EARS sensor system as well as a separate display. The display gives the user audial and visual cues on an LCD screen regarding the location of the gunshot.

The disadvantages of this system are the extra equipment that must be managed in combat and the attention required from the overloaded audial and visual systems of the soldier. The display portion of the device does not quickly and concisely relay information to the soldier. This is because the device alerts the user through audial communication. It declares direction and distance of hostile gunfire through audio communication which could result in a couple second delay of information. In a battlefield environment one second can be the difference between life or death.

The objective of this paper is to adapt the tactile display as a peripheral device for soldiers and infantrymen to aid in gunshot localization in chaotic environments by assisting the wearer in taking cover and coordinating a retaliation. By doing so, military units would be more coordinated, and the chances of miscommunication would be greatly reduced by freeing their overloaded visual and audial senses. Tactile displays could provide soldiers with a wealth of information, including positions of allies and hostile gunfire.

When combined with a system such as the QinetiQ EARS shoulder mounted sensor, a tactile display could result in quicker response to hostile gunfire while simultaneously using a non-overloaded sensory system. The idea is that this system would enable split second decision making in critical situations for soldiers.

2. CONCEPT PROTOTYPE

To create a tactile display that can passively inform the wearer of a gunshot direction and to coordinate the group, the display must be supplementary to the wearer's other senses and not be a substitute

31st Florida Conference on Recent Advances in Robotics, May 10-11, 2018, University of Central Florida, Orlando, Florida

72

for a sense. Because it takes more attention from the wearer to differentiate between two nearby vibrations, it makes sense that the vibrotactile actuators should be spread across the body's extremities as to make that determination easier. By spreading the actuators across the extremities, the wearer does not have to dedicate much thought to understand the instructions given by the tactile display.

If a four by four matrix of actuators is used, the actuators are at the limits of the skin's two-point discrimination thresholds. When the actuators are spread across the body as in Figure 9, they reside on different regions of the skin and therefor do not confuse the wearer with the instructions being conveyed. An extremity display can be accomplished by placing individual actuators on the shoulders, wrists, and legs.
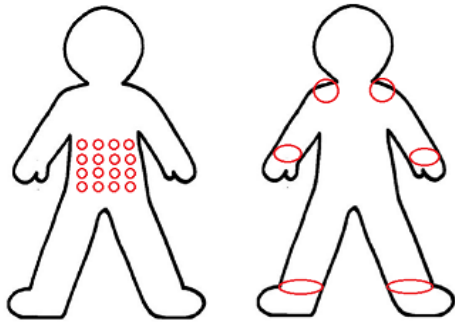

Figure 9. 4x4 matrix vs. extremity display

The benefit of this approach is that there is little chance the user will mistake a vibration on the left leg with, for example, a vibration on the right shoulder. By making the interpretation of the display more reliable and intuitive, information can be reacted to more naturally and as second nature to the wearer.

3. PROTOTYPE TESTING PLAN
To test the effectiveness of our tactile display, we would use a situation that could simulate a combat zone during hostile gunfire. The situation would represent a soldier in a hostile area who is approaching a barricade that provides cover when unexpectedly he is fired upon. The soldier must quickly decide which side of the barricade is opposite of the gunfire origination and get behind that side to avoid being injured.

To simulate gunfire, two speakers will be used; one speaker will be on the left of the barrier, and the other on the right. The speakers represent the origin of the gunshot, and one will be selected to play a gunshot sound to which the subject must react to.
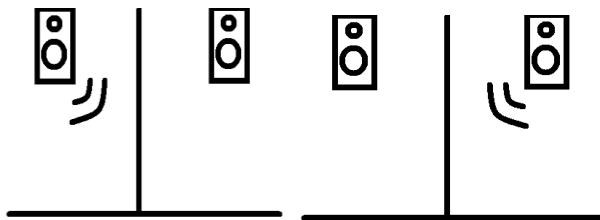

Figure 10. Test scenarios: left originating gunshot vs. right originating gunshot.

Two important factors in the results of these tests will be whether the subject chose the correct side for cover and how long the decision took to be made. The test subject's decisions will be compared to the true gunshot originations and the timer will begin as soon as the gunshot sound is played. By comparing control and test trials, we hope a trend can be discerned.

If no meaningful difference is found between the two methods, more speakers will be added in smaller radial intervals from the subject to test the limits of the human and device. For example, if results for the two-speaker test are identical, four speakers will be tested- two speakers on each side in 45 degree intervals.

3.1 Control Test
A control subject will react to the audial cues without the vest and decide to take cover on the side of the wall opposite to where they think the sound originated. Timing will begin as soon as the shot is fired.

3.2 Tactile Display Test
Similarly, the subject with the vest will make the same decision with the guidance of the tactile display. The tactile display will know the direction the gunshot originated and will try to convey this to the user using predetermined patterns that the subject will be trained to recognize. For these trials the subject should react based off the tactile cues and not the audial cues of the test.

By comparing the speed at which the subject takes cover, as well as how accurately they choose the safe position of cover, a relationship can be made to conclude whether an extremity tactile display could aid with supplementing decision making in critical situations.

4. CONCLUSION
In combat environments visual and auditory sensory systems are overloaded due to excessive stimulation. In civilian applications tactile displays have shown that they can transfer some of this bandwidth to the tactile sensory system which relieves stress on the overloaded systems. By making an intuitive tactile display that requires little attention in combat situations, military units can organically be coordinated to reduce casualties in hostile environments. Future work will include finding out the appropriate location of the display tactors on a soldier since they are heavily loaded with combat equipment which can compromise the sensation.

5. REFERENCES
[1]   L. A. Jones, B. Lockyer, and E. Piateski, "Tactile display and vibrotactile pattern recognition on the torso," *Adv. Robot.*, vol. 20, no. 12, pp. 1359–1374, Jan. 2006.

[2]   F. Mancini *et al.*, *Whole-Body Mapping of Spatial Acuity for Pain and Touch*, vol. 75. 2014.

[3]   H. Tang and D. J. Beebe, "An Oral Tactile Interface for Blind Navigation," *IEEE Trans. Neural Syst. Rehabil. Eng.*, vol. 14, no. 1, pp. 116–123, Mar. 2006.

[4]   R. Velazquez, O. Bazan, and M. Magana, "A shoe-integrated tactile display for directional navigation," in *2009 IEEE/RSJ International Conference on Intelligent Robots and Systems*, 2009, pp. 1235–1240.

[5]   J. B. F. van Erp and B. P. Self, "Introduction to tactile displays in military environments," *RTO-TR-HFM-122 Tactile Displays Orientation, Navig. Commun. Air, Sea L.*

31st Florida Conference on Recent Advances in Robotics, May 10-11, 2018, University of Central Florida, Orlando, Florida

73

Environ. chapter 1, 1/1 - 1/18, 2008.

[6]   B. McGrath, *TACTILE INSTRUMENT FOR AVIATION*. 2018.

[7]   QinetiQ North America, "Gunshot Detection System | QinetiQ North America." [Online]. Available: https://www.qinetiq-na.com/products/militaryprotection/ears/. [Accessed: 21-Mar-2018].

31st Florida Conference on Recent Advances in Robotics, May 10-11, 2018, University of Central Florida, Orlando, Florida

74

From Litigation Consulting to Research and Education

Oren Masory

Department of Ocean and Mechanical Engineering

Florida Atlantic University

777 Glades Rd., Boca Raton, FL 33431

masoryo@fau.edu

ABSTRACT

The responsibility of an Expert Witness is to provide the defending attorney or the prosecutor with technical information supporting their argument. In times it is as simple as measuring the temperature of an oven. In others it might involve the review of a design and the figuring out the cause of failure or reconstruction of vehicle accident and the determination of the cause of injuries by simulating the motion of the occupants inside the vehicle during the collision. This paper describes a few cases, in which the author served as an expert witness and how they evolve to research activities and eventually propagate to his classes.

Keywords

Education, Engineering Education, Senior project course.

1. INTRODUCTION

Most expert witness professionals are dealing with relatively small claims related to Personal Injuries (PI) due to slip and fall, product liability, vehicle accidents etc. The typical expert witness is, in many cases, a person who has extensive experience in a very particular area, for example, in the cases of vehicle's accident reconstruction, many of the experts are police officers who investigated accidents during their employment. These experts are either self-employed or working for small outfits and as a result they have no time nor resources to perform any kind of experimentation or research. Large cases, like train derailing or aircraft crash, are investigated by state/federal organization or large companies. Also, most common PI issues, like slip and fall, ladder and vehicle accidents, are also studied by large insurance company who eventually have a financial stake in understanding these issues.

There are less than a dozen Forensic Engineering programs in U.S. universities [1], none offering a doctoral degree. Due to lack of funding in this area limited or very little research is performed in academic institutions in particular on topics related to PI. Moreover, these issues do not attract the intension of faculty members due the requirement put in front him with regard to tenure and promotion. In most universities the topic is not even introduced, and thus new generation of engineers are not aware of this area as a career opportunity.

By providing Expert Witness services in the PI arena, one is exposed to problems that otherwise he would never be aware off.

Also, this hands on experience enhance his capacity to deal with issues such as the use of instrumentation in corrupted environment, improvisation to accommodate unexpected changes in the accident site, and other. From education point of view, many of these cases can be brought to class as examples or as a project in a design course. It is worth mentioning that usually students are interested in these examples since they are not textbook ones.

2. SLIP AND FALL ON WALKING SURFACES

The issue: Slip and Fall accidents are the leading cause of workers' compensation claims and medical costs, which amounts to approximately $70 billion annually [2]. A report by The Bureau of Labor Statistics [3] states "Together, falls, slips, or trips accounted for 35 percent of the injuries and illnesses to heavy and tractor-trailer truck drivers in 2014." In [4] it is reported "falls on the same level is the second highest category of compensable loss and cost $6.7 billion, according to the 2006 Liberty Mutual Workplace Safety Index". There are numerous reports on the subject but one that demonstrate the severity of this problem is reported in a study, performed by the National Floor Safety Institute (NFSI), that found that more than 3 million food service employees and over 1 million guests are injured annually as a result of restaurant Slips and Falls accidents. These injuries are increasing at a rate of about 10% annually [5]. As a result, one can realize that there numerous law suits related to slip and fall. The consultant responsibility, in these cases, is to determine the cause for the incidents. A major part of his investigation is to determine the Static Coefficient Of Friction (SCOF) of the surface on which the person slipped. Most of the time consultants are using off the shelf commercial slip-meters for this purpose.

All slip-meters are using, directly or indirectly, a simple test called "pull test" (see Figure 1). A foot, made of a standard material usually Neolite (material that imitates the characteristics of leather soles), is attached to the bottom of a block of weight W. The block is placed on the horizontal surface being tested, and a pulling force, F, is applied to the block. At any time the magnitude of the pulling force is equal to the friction force acting between the block and the surface. The pulling force is increased to the point that block starts to move (impending motion). At that instant the friction force assumes its maximum value and the SCOF, μ_s, is given by:

$$\mu_s = \frac{F_{max}}{N} \qquad (1)$$

Eq. 1 was established by Charles-Augustin de Coulomb (1785) who extensively study dry friction occurring between contacting surfaces in the absence of a lubricating fluid. However, Eq. 1 does not specifies any parameters needed to be satisfied while performing the test. These include: minimum contact pressure, contact area, contact surface shape and foot's surface texture (e.g. grooves. As a result, commercial slip meters differ one from the other with respect to these parameters.
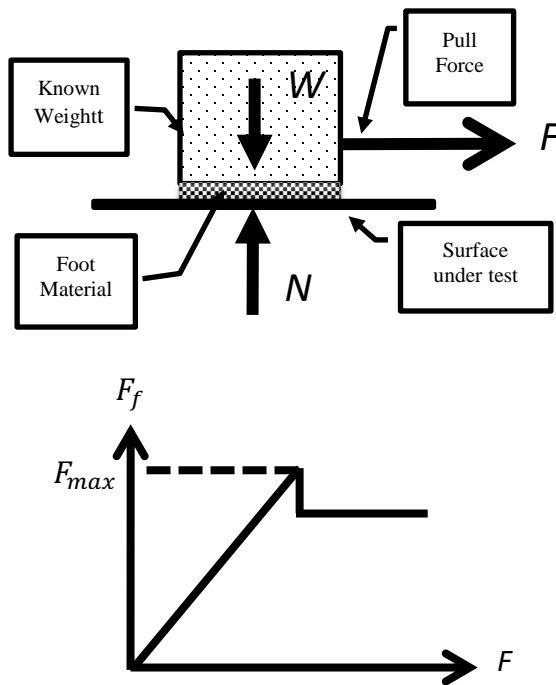

Figure 1: Pull test

Table 1: Circular versus Square feet.

Direction	North		South	
Shape	Square	Circle	Square	Circle
Mean	0.285	0.281	0.348	0.328
Variance *10^3	0.281	0.676	0.0621	0.897

Table 2: Tests' results for different contact areas.

	Contact area[sqin]	
	9	3
Contact Pressure [kPa]	28.828	27.918
Mean	0.386	0.387
Variance	0.000106	0.000186
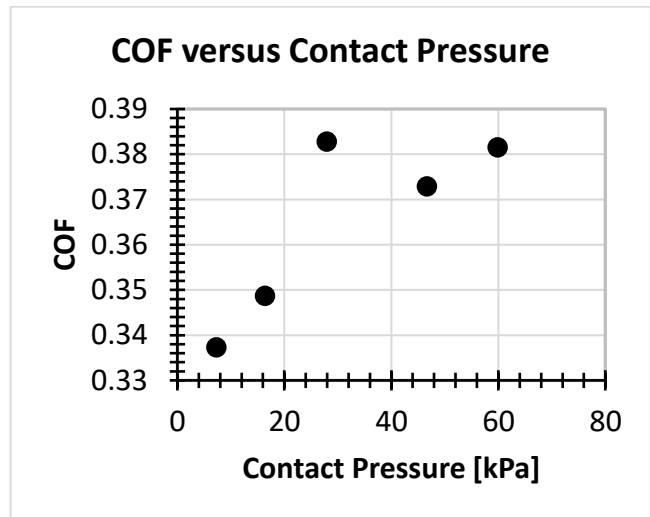
Figure 2: Effect of contact pressure on the value of SCOF.

Research: A small research work in which a small set of experiments were performed to determine the effect of these parameters on the value of the SCOF with the following results:

1. Figure 2 illustrates that a minimum contact pressure is required in order to have a reliable value of the SCOF.

2. Table 1 shows the values of the SCOF where circular and square feet, of the same contact area and under the same contact pressure, were used. It is clear that there is difference between the two SCOFs.

3. The effect of contact area on the value of the SCOF, as shown in Table 2, is minor.

4. The effect of grooves in the foot has a major effect on the SCOF as seen in Figure 3. Similar results were reported in a research related to traction capabilities of shoes' soles with different grooves [6].

The above issues will surface in court since commercial slip meters are different from each other with respect to the above parameters. An example for deviations in the readings of SCOF obtained by four different commercial slip meters, that were validated by ASTM F2508-13 standard [7], are shown in Figure 4. The dash line demonstrates a case classification of the surface slipperiness will vary from to another: from "very slippery" to "acceptable slippery" [8].

Education: This topic was discussed in Senior Design class and students were asked to suggest solutions. Variety of solutions, in which the test is executed fully automatically, using a microcontroller, which also control the pulling speed, sample and record the pulling force, were proposed:

1) A simple linear pull using square foot (Figure 6a).
2) A rotational "pull test", where the rotational speed and torque are measured, and the foot is has shape of a disk (Figure 6b). The idea was to measure the average SCOF in all possible pulling direction (rather 4 direction as specified in ASTM F2506-13).

31st Florida Conference on Recent Advances in Robotics, May 10-11, 2018, University of Central Florida, Orlando, Florida

76

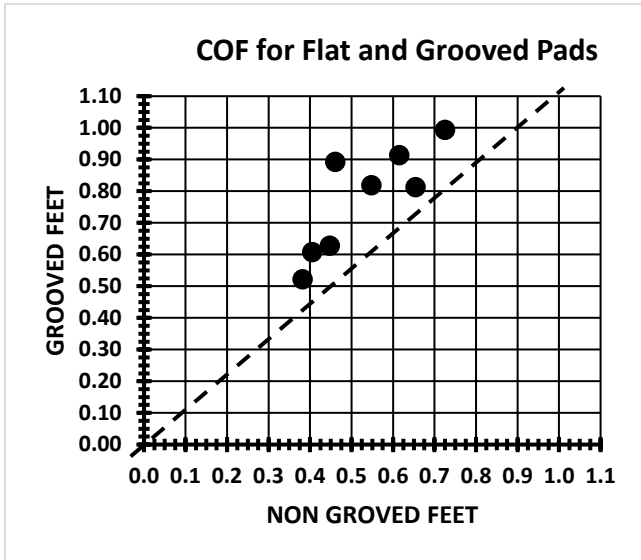3) A rotational arm with an interchangeable foot. (Figure 6c).

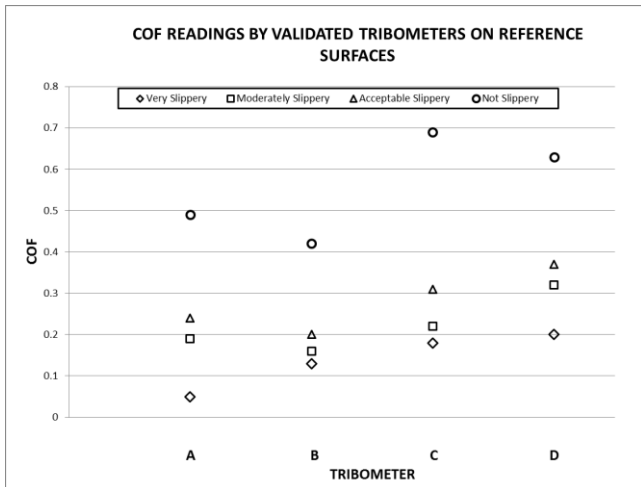**Figure 3: The effect of grooves on the SCOF value.**

Figure 5: COF measurements of the reference surfaces by the 4 validated tribometers.

3. GOLF CART EJECTION ACCIDENTS

The issue: The state of Florida is blessed with 1534 golf courses [9] and probably over 250,000 golf cart (extrapolating from the fact that only The Villages there are more than 50,000 golf carts [10-11]). Top speed of a golf cart is 15[mph] while for Low Speed Vehicles (LSV), which, in many communities allowed to share city streets of speed limit of 35[mph], is 25[mph]. It was estimated that there were approximately 48,255 golf cart related injuries during the years 2002-2005 [666]. The Consumer Product Safety
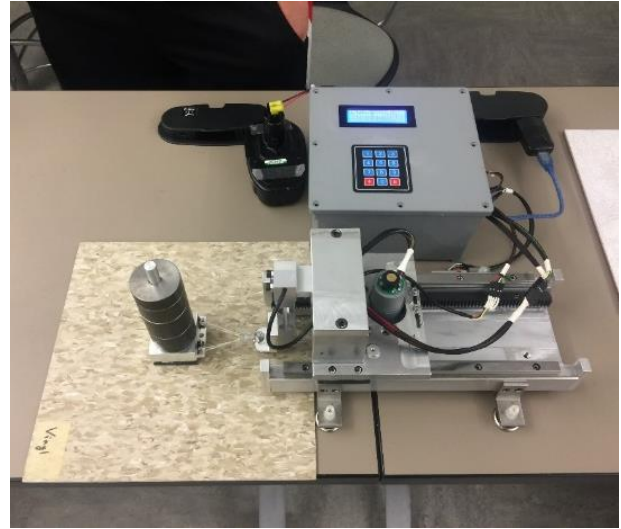
(a)
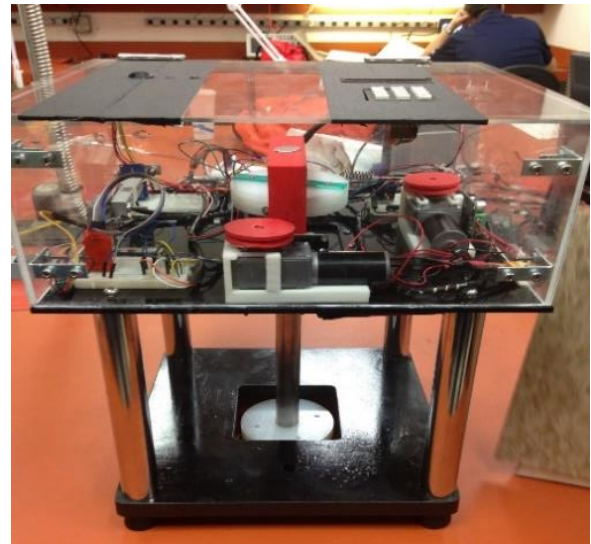
(b)
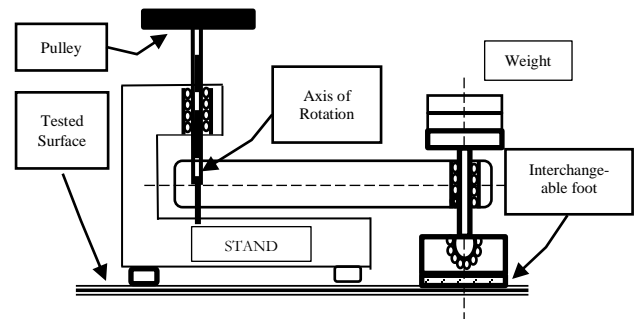
(c)

Figure 6: Students' projects.

31st Florida Conference on Recent Advances in Robotics, May 10-11, 2018, University of Central Florida, Orlando, Florida

77

Commission (CPSC) estimated that between the years 2002 and 2011 an annual average of 13,740 were injured severely enough to be sent to the hospital while using golf carts [12]. Overwhelming majority, (38.3%) of these injuries are due to passenger ejection, and more than twice as likely to result in head or neck injury, and more than six times as likely to result in concussion [13]

Research: Being involved in the investigation of ejection accidents, in particular of rear facing passengers, a limited research program was initiated. A commercial golf cart was instrumented with accelerometers, mounted at the front and rear passengers' seats, and a set of runs with different driving speed and turning radii was performed. The acceleration signals were sampled at 100[Hz] and recorded. The cart geometry, in particular the dimension and the location of the hip restraints, was model using Articulated Total Body (ATB) simulation tool. The passenger was modeled by GBOD [14] and was incorporate into the ATB simulation. At this point, the acceleration signals, obtained by the actual driving, were used to "Drive" the simulated cart and the motion of the passenger was observed. Analyzing the cases where the passengers were ejected (see Figure 7), provide the maximum allowed acceleration given the geometry of the hip restraint [15]. In addition, modifications to the restraint provided at the rear of the cart were proposed.

Education: In this study one senior student was involved. He was supported by the university Undergraduate Research Program. In the Mechanical Engineering Las course there was an opportunity to engage students in these kind of measurements. In one lab assignment students were asked quantify the comfort level of a passenger as the vehicle crosses a standard street bump at different speeds. They had to measure and record the three acceleration components using their smart phones and find correlation with comfort level expressed by the driver in scale 1 to 5.

4. EVENT DATA RECORDER AND COLLISION ANALYSIS

The issue: In the past the impact force and the energy absorbed by the vehicle during collision were estimated by measuring the actual deformation of the crush and using experimental stiffness coefficients. It is obvious that these measurements are not accurate and their accuracy, in spite of a standard procedure, depends on the person who took them. Therefore the estimation of the impact force and the absorbed energy, which are indicators for the severity of the accident and the inflected injuries, will different from one expert to the other.

Once airbags are installed, the airbag control module serves as an Event Data Recorder (EDR). The module includes an accelerometer, sampled at 100[Hz], and the reading are used to determine whether or not to deploy the airbag. If the airbag was deployed, the acceleration readings are recorded and can be retrieved later for the reconstruction of the accident.

Although there is a large volume of publications related to this topic, there are still unresolved issues that need clarification, for example:

1. Statistically quantify the errors in the crush measurements
2. The airbag module records the acceleration only if the airbag is deployed. Therefore, collision at low speed, usually below 30[mph], has to be analyzed in different way.

3. Which of the two methods is more reliable
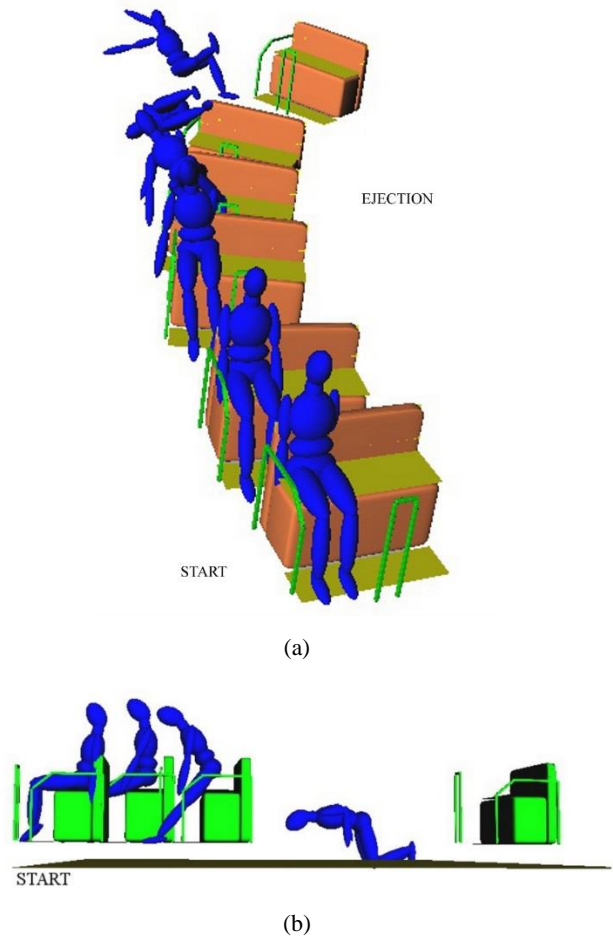4. Any other analysis method will provide more accurate results

(a)

(b)

Figure 7: Ejection from golf cart. (a) Sharp turn; (b) High acceleration

Research: The opportunity to determine the uncertainty in variety of measurements, performed during accident reconstruction, presented itself in WREX 2000 conference that took place in Texas A&M University. Attendees, professional accident reconstructionists, were asked to measure skid marks length, drag coefficient, yaw marks, residual crush of a vehicle that was involved in frontal collision. Figure 8 [16]. illustrates the crush measurement obtained by 17 attendees. The average crush depth recorded by the participants ranged from 11.0" to 34" with an average of 19.4" and standard deviation of 5.2". The reported length of the damaged area ranged from 48" to 78" with an average of 62.4" and standard deviation of 9.9". The results, with the uncertainty of the stiffness coefficient, make this method very unreliable and any expert testimony will be questioned and might be dismissed.

A different approach was proposed in [17] in which a special network called "Abductive Network" (AIM) which in a way similar to Neural Networks but the function implemented at each node is a

31st Florida Conference on Recent Advances in Robotics, May 10-11, 2018, University of Central Florida, Orlando, Florida

78

polynomial where the coefficients are found during the training. Using crush depth results from 50 crush tests the impact force and the crush energy were calculated using CRASH 3 (commercial software package) and compared with the results obtained by the AIM (see Figure 9). As shown the network solution is by far more conservative.
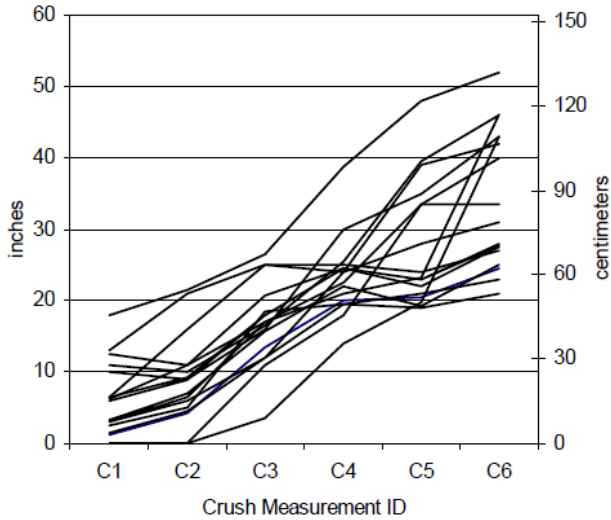

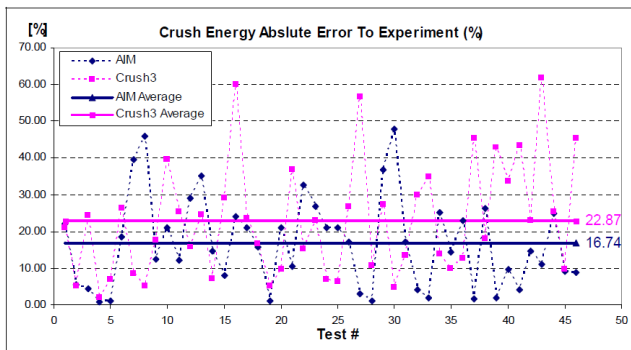**Figure 8: Residual crush measurements profiles**.

Figure 9: Crush energy absolute error.

Education: First, the work with Abductive Networks was partially performed by French undergraduate students who come to FAU for a period of 4-6 months as required by their degree program. In Numerical Methods class, students are asked to down load acceleration measurements from crash test that were performed by the National Highway Transportation Safety Administration (NHTSA). Then they have filter the signal using low pass and moving average filters. Then they integrate the signal, using any of the numerical integration methods cover in class, to find the velocity and to determine the coefficient of restitution. With one more integration the displacement of is found and compared to the actual crush depth given in the same database. Deviation between the two should be explained.

5. CONCLUSIONS

Expert witness subject includes a wide spectrum of topics from biology, fire investigations, patent infringement to computer science. It is perceived that PI investigations are very limited in scope which is far away from reality. A good expert witness in this area should master engineering concept from many disciplines mechanical, Electrical, Material, Biomechanics and others. At times it is very challenging problem that requires some experimentation, research or at least to find relevant information. Almost in all cases the investigation is taking place at the accident site which present many difficulties, due time delay and contamination, which do not exist in laboratory environment.

At the completion of the accident the expert is facing other challenges: 1) Present his finding to a jury who are nor familiar with issue; and 2) Defend his position in cross examination that might become very intimidated. Most important, working for the plaintiff, one should remember that the opinions expressed by the Expert Witness determine the financial outcome of the law suites effecting the plaintiff's future quality of life.

Whatever the reason is, real or perception, the profession does not attract engineering students, as reflected by the number of programs offered in the US. This might be due to lack of interest or the credit hour availability, the result is the same.

6. REFERENCES

[1]   http://study.com/articles/Schools_with_Forensic_Engineering_Programs_How_to_Choose.html
[2]   National Floor Safety Institute, https://nfsi.org/
[3]   BLS News Letter USDL 15-2205, November 19, 2015
[4]   Liberty Mutual Research Institute for Safety, Vol. 10, No. 3,
[5]   Slips and Falls Study: Objective Auditing Techniques to Control Slips and Falls in Restaurants, CNA June 2007. Autumn 2007.
[6]   Kai Way Li, Chin Jung Chen, "Effects of tread groove orientation and width of the footwear pads on measured friction coefficients", Safety Science, Vol 43, 2005.
[7]   ASTM 2508 "Standard Practice for validation, calibration, and certification of walkway slip meters using reference surface".
[8]   Comment on
[9]   https://www.golflink.com/golf-courses/state.aspx?state=fl
[10]   www.insidethebubble.co/82-cool-facts-the-villages/
[11]   Mcgwin G. et. al, "Incidence of golf cart related injuries in the US", The Journal of TRAUMA, Infection and Critical Care, Vol 64, June 2008.
[12]   CPSC- National Electronic Injury Surveillance System, 2011, www,cpsc.gov/Neiss/oracle.html
[13]   Watson, D. Mehan, T., Smith, G, "Golf cart-related injuries in the U.S.", American Journal of Preventive Medicine, Vol 35, July 2008.
[14]   Articulated Total Body Model Version V; User's Manual, https://www.researchgate.net/publication/235173886_Articulated_Total_Body_Model_Version_V_User's_Manual.
[15]   K. Schau, O. Masory, "Ejection of a Rear Facing, Golf Cart Passenger", Journal of Accident Analysis and Prevention, Vol. 59, October 2013, pp. 574-579.Kyle

31st Florida Conference on Recent Advances in Robotics, May 10-11, 2018, University of Central Florida, Orlando, Florida

79

[16] Wade Bartlett, William Wright, Oren Masory, Raymond Brach, Al Baxter, Frank Navin, Bruno Schmidt, "Evaluating the Uncertainty in Various Measurement Tasks Common to Accident Reconstruction", SAE Technical paper 2002-01-0546

[17] O. Masory, N. Putod, "Determination of Impact Force and Crush Energy Using Abductive Networks", Proc. 20th Florida Conference on Recent Advances in Robotics, May 31-June 1, 2007.

31st Florida Conference on Recent Advances in Robotics, May 10-11, 2018, University of Central Florida, Orlando, Florida

80

Collecting Image Datasets with a Quadcopter

Saif Alabachi, Gita Sukthankar

Department of Electrical and Computer Engineering
University of Central Florida; Orlando, Florida

s.mohammed@knights.ucf.edu, gitars@eecs.ucf.edu

ABSTRACT

Although generic object detection models exist, it is important to train mobile robots to detect and recognize specific objects that are unique to an environment. Transfer learning can be used to reduce the number of new images required to learn the new object instances by leveraging more general existing models. This paper describes our user interface for collecting custom image datasets with a quadcopter and performing object instance labeling and annotation semi-autonomously. Collecting images with marked objects is a time-consuming process and usually done under heavy human supervision. We evaluated our dataset by detecting the annotated objects in the real-time quadcopter video feed.

Keywords

Image Dataset Construction, Transfer Learning, Human Robot Interaction, Semi-autonomous agent, Quadcopter.

1. INTRODUCTION

Convolutional neural networks have achieved outstanding performance on object detection methods but depend on the existence of large datasets with millions of annotated images [1]. However, image dataset construction remains a time-consuming task that requires substantial effort even with the availability of helpful tools. Our work addresses the problem of collecting and annotating a dataset of object images using a quadcopter. We demonstrate that we can use the collected images to create customized object detectors for important landmarks in our indoor environment. The quadcopter serves a dual purpose: not only is it used during the image collection process but also it can utilize the customized object detectors.

Customized object detectors can be trained with fewer images using transfer learning. Transferring image representations reduces the time and data needed for training, because the models leverage features learned from the original dataset. It is possible to fine tune or transfer a pre-trained model and still obtain satisfying detection results without the need to relearn the entire network. For instance, Oquab et al. addressed this problem in object and action classification using a transfer learning model trained on different datasets [2].

However, dataset construction and annotation require major manual effort even with the availability of helpful tools. Our aim is to automate this process and reduce the need for human monitoring. For this project we developed a sketch based user interface system to guide the quadcopter. The user simply sketches a bounding box around the object of interest, and the quadcopter collects images semi-autonomously with minimal guidance from the human. To add variance to the dataset while reducing the flight time, we added image filtering capabilities to the user interface to augment the dataset with additional synthetic images with changes to brightness, contrast, zooming, and rotation. For transfer learning, we selected a state of the art object detection model: the SSD [3] MobileNet [4] architecture for compute constrained devices (built on VGG-16 [5]).

2. RELATED WORK

The availability of large image datasets has yielded dramatic improvements in image classification. Important datasets include: CIFAR-10 with 6000 examples of 10 classes, CIFAR100 with 600 examples of 100 non-overlapping classes [6], the Lotus Hill [7] dataset with 50,000 images, and ImageNet [8] with almost 15 million high-resolution images in 22,000 categories. In ImageNet, the images are collected from the web and labeled using Amazon's Mechanical Turk [1]. However these datasets typically lack bounding boxes localizing the object instances, and the ones that contain bounding boxes are usually human-annotated. Examples include COCO [9] which has about 80 object categories with over 1.5 million object instances, and PascalVOC [10] with 20 classes and 27,450 annotated objects.

Some tools have been created to help researchers label images into segments. LabelMe [11] is a web-based tool that allows easy image annotation and instant sharing. One collection strategy is to gather natural samples from the Internet using query patterns to generate the desired image dataset [12]. It is also possible to analyze the image and its text-annotation in order to select a ground-figure segmentation and to use this information to classify segments into visual categories [13].
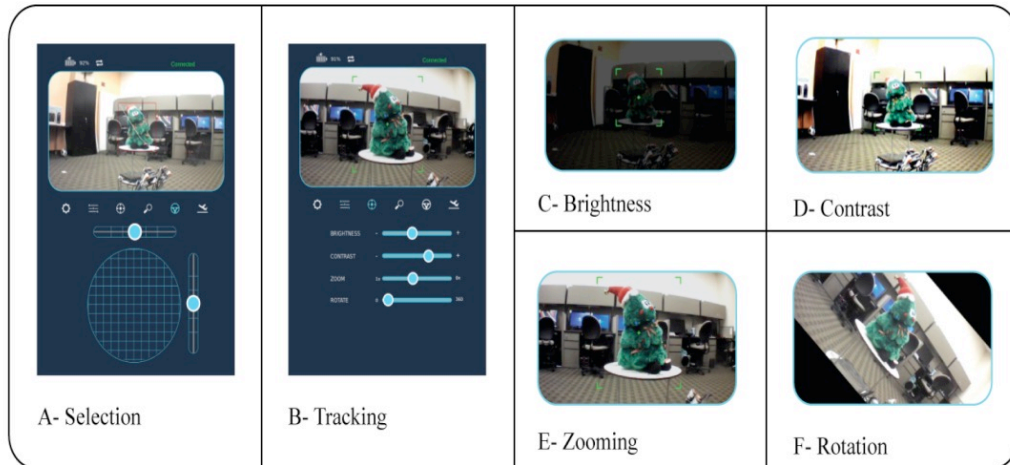
Fig. 1. A. The user selects the object after quadcopter take off. B. The tracking process starts and the quadcopter flies autonomously to free the user's attention. C. The brightness filter is applied before saving the candidate image. D. Contrast filter application. E. Zooming filter application. F. Rotation filter application.

The COCO challenge [9] was created to advance the state of the art in object recognition by making it advantageous to combine object recognition with scene understanding. For precise object localization, COCO objects are labeled using per-instance segmentations; the dataset contains photos of 91 objects with crowdsourced annotations labeled using a novel user interface for category detection [2]. Our research improves on existing tools by using a quadcopter for image collection and adding functions to the flight interface to synthetically augment the dataset.

3. METHOD

In this section, we describe the procedure used to collect our customizable annotated-object image dataset. Our experiments were performed on the commercially available Parrot Augmented Reality (AR) Drone Version 2. This drone has two cameras: one front-mounted HD camera and a downward facing QVGA camera. For our experiments, we extended an early version of our user interface described in [14]; a video demo of the original system can be viewed at: https://youtu.be/ErA2111xjzMl.

3.1 Dataset Construction

First the human manually flies the quadcopter to the object of interest and then sketches a circle around the object to initialize the four coordinates of the bounding box (x min, y min x max , y max). The selection should only include a single object to match the original training COCO dataset (see Figure 1 A).

The bounding box is sent to our system to initialize autonomous navigation. An object tracker is used to calculate the bounding box in subsequent frames which are saved to the image dataset.

Sometimes, due to the network delay, undesired annotations may occur that need to be eliminated from the dataset before the

learning process. The system collects one candidate image each second to allow enough time for the filtering operation to be applied before storing the resultant frame. We believe that our platform can also be used to create action image datasets following the same procedure.

3.2 Tracking

For tracking, we evaluated several online trackers available within openCV and one hybrid tracker (combining offline and online tracking). Some of the trackers failed since they were not designed for a moving camera, and others had problems achieving real-time performance on a mobile computer. However, the adaptive correlation filter, MOSSE [15], was found to be stable and capable of handling the 30 frames per second generated by the Parrot ARDrone 2.0 camera.

3.3 Image Filters

Before storing the candidate sample, the annotated frames can be processed using image filtering operations in order to create more variation in the dataset. These filters are accessed directly through the user interface and include brightness, contrast, rotation, and zooming. Rotation is useful as it is not possible to hover with a tilt orientation while capturing high quality images, and artificially zooming preserves the battery life by reducing the quadcopter movement. Figure 1 B, C, D, E, and F show examples of images captured with these filters.

3.4 Semi-autonomous Navigation

After the initial bounding box is drawn, the quadcopter starts flying autonomously, and the system enters a visual dataset collection mode, acquiring data at a rate of 1 fps. The quadcopter

31st Florida Conference on Recent Advances in Robotics, May 10-11, 2018, University of Central Florida, Orlando, Florida
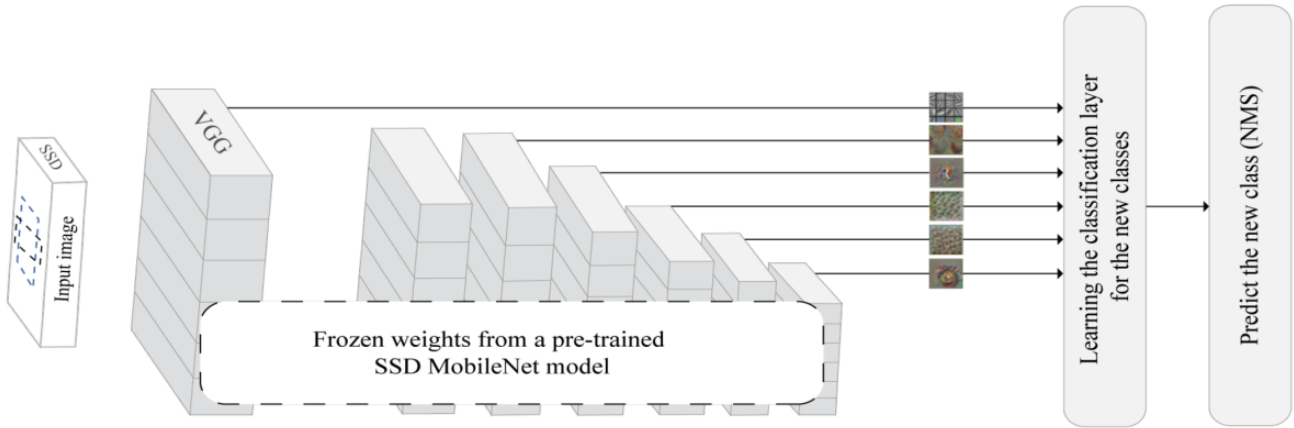
82

Fig. 2. Transfer learning from the SSD MobileNet architecture

modifies its yaw angle and altitude to track the object designated by the user. The x-axis error between the object centroid and canvas center is used to estimate the orientation angle, and the y-axis error is used to estimate the quadcopter's altitude.
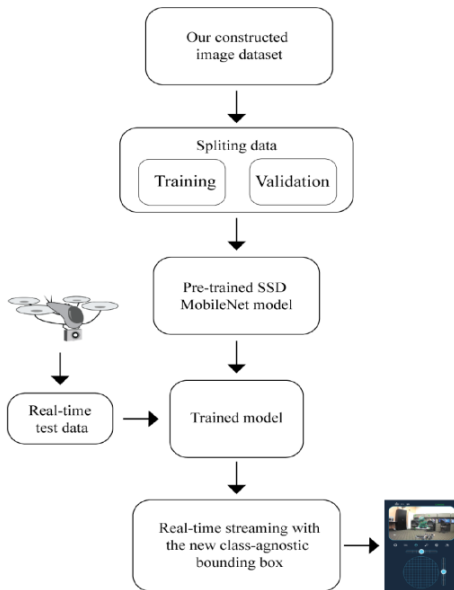
Fig. 3. Flowchart illustrates the transfer learning phase on the new constructed dataset and the testing phase using the video streaming from the quadcopter.

The errors are transmitted to a PD (proportional-derivative) controller with gains K_p and K_d set to 0.25. The quadcopter uses its inertial sensors to monitor roll Φ, pitch Θ, yaw ψ, rotational speed Ψ and the vertical velocity ζ; controls are issued using a series of ROS Twist commands $u = (\Phi, \Theta, \zeta, \Psi)$ $[-1, 1]^4$ at a frequency of 100Hz. Our interface is capable of eliminating

		84%
	Christmas toy	53%
	potted plant	81%
	tissue box	98%

31st Florida Conference on Recent Advances in Robotics, May 10-11, 2018, University of Central Florida, Orlando, Florida

83

Fig. 4. a. Classification Loss. b. Localization Loss. c. Total Loss = (Confidence Loss + $\alpha *$ Localization Loss)

4. RESULTS

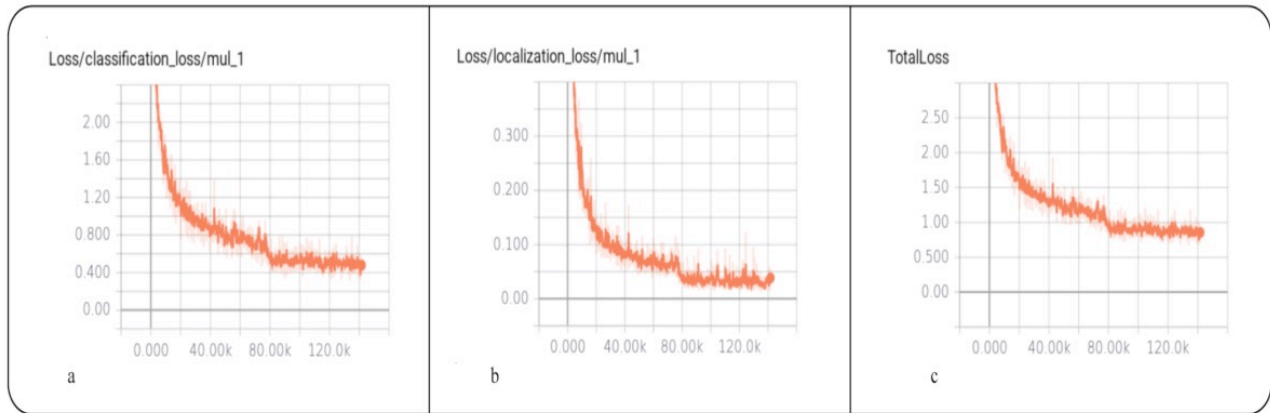For our experiments, we collected a dataset with images for four classes of which three are new and one already existed in the COCO dataset. The classes are: 1) coffee machine 2) Xmas toy 3) potted plant and 4) tissue box. Our image dataset contains 270 bounding box annotated images for each class with one class per image. The examples always have the object located near the center of the frame. Our test samples consist of 640×360 frames gathered from the real-time video streaming of the quadcopter frontal camera. The transfer learning process required two days to reach an average total loss (Confidence Loss + α Location Loss) < 0.9. α is a parameter reducing the location loss function by bringing the predictions closer to the ground truth. Our training configuration is batch size = 60, learning rate = 0.004 with 0.95 decay factor. Figure 4 shows the loss functions in the graphs a, b, and c.

The architecture is SSD MobileNet, and the object detection API provided by the Tensorflow community is used to detect the new classes. We used weights extracted from a network trained on the COCO dataset before the classification layer. The new classifier is trained on the constructed dataset. Figure 5 shows the object detection model after applying transfer learning on the constructed dataset. As shown in the left figure, the potted plant is an existing class, but the model can't detect it with confidence > 50%, whereas the trained model is able to detect all the new classes after one day of transfer learning.

In the testing phase, we evaluate our dataset annotation accuracy by obtained the classifier performance on predicting the class of the objects appearing in the test data. The classifier predictions are shown in Table I. Figure 3 illustrates our experiment. The bounding box surrounding the objects in the live stream indicates successful real-time object detection.

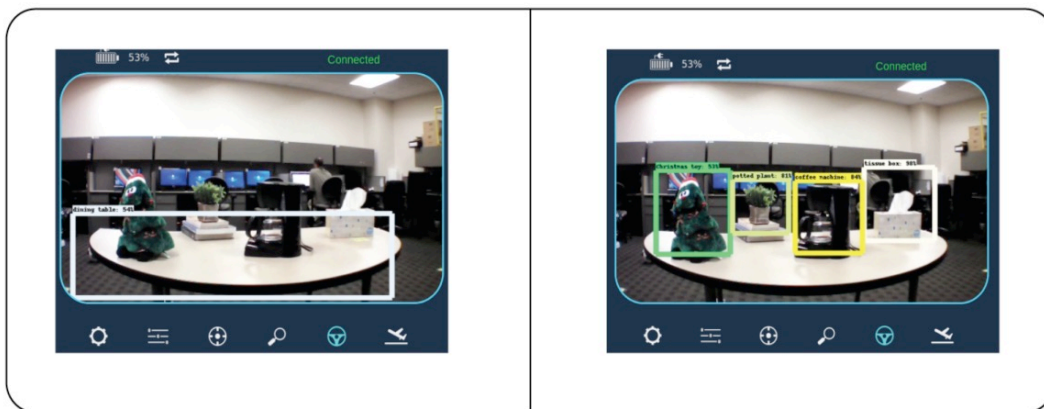Fig. 5. To the left is the object detection model trained on the COCO dataset. Christmas toy, tissue box, and coffee machine are new classes whereas potted plant is an existent class. The picture to the right is the detection result after the completion of transfer learning.

31st Florida Conference on Recent Advances in Robotics, May 10-11, 2018, University of Central Florida, Orlando, Florida

CONCLUSION

This paper presents a novel approach to constructing an annotated object image dataset using a semi-autonomous quadcopter that gathers multiple viewpoints of a target object and applies image filters to create a synthetically augmented dataset for training customized object detectors using transfer learning on a CNN model. Our platform is capable of capturing high quality images of a fixed or moving object using a friendly user interface that can be launched from a mobile device. We demonstrate that the customized object detectors trained with the semi-autonomously constructed dataset perform well at detecting objects viewed through the quadcopter video feed in real time.

5. REFERENCES

[1] A. Krizhevsky, I. Sutskever, and G. E. Hinton, "ImageNet classifica-tion with deep convolutional neural networks," in Advances in Neural Information Processing Systems, 2012, pp. 1097–1105.

[2] M. Oquab, L. Bottou, I. Laptev, and J. Sivic, "Learning and transferring mid-level image representations using convolutional neural networks," in Proceedings of the IEEE Conference on Computer Vision and Pattern Recognition, 2014, pp. 1717–1724.

[3] W. Liu, D. Anguelov, D. Erhan, C. Szegedy, S. Reed, C.-Y. Fu, and A. C. Berg, "SSD: Single shot multibox detector," in European Conference on Computer Vision. Springer, 2016, pp. 21–37.

[4] A. G. Howard, M. Zhu, B. Chen, D. Kalenichenko, W. Wang, T. Weyand, M. Andreetto, and H. Adam, "MobileNets: Efficient convolutional neural networks for mobile vision applications," arXiv preprint arXiv: 1704.04861, 2017.

[5] K. Simonyan and A. Zisserman, "Very deep convolutional networks for large-scale image recognition," arXiv preprint arXiv:1409.1556, 2014.

[6] A. Krizhevsky and G. Hinton, "Learning multiple layers of features from tiny images," University of Toronto, Tech. Rep., 2009.

[7] B. Yao, X. Yang, and S.-C. Zhu, "Introduction to a large-scale general purpose ground truth database: methodology, annotation tool and benchmarks," in International Workshop on Energy Minimization Methods in Computer Vision and Pattern Recognition. Springer, 2007, pp. 169–183.

[8] J. Deng, W. Dong, R. Socher, L.-J. Li, K. Li, and L. Fei-Fei, "ImageNet: A large-scale hierarchical image database," in IEEE Conference on Computer Vision and Pattern Recognition, 2009, pp. 248–255.

[9] T.-Y. Lin, M. Maire, S. Belongie, J. Hays, P. Perona, D. Ramanan, P. Doll´ar, and C. L. Zitnick, "Microsoft COCO: Common objects in context," in European Conference on Computer Vision. Springer, 2014, pp. 740–755.

[10] A. S. Razavian, H. Azizpour, J. Sullivan, and S. Carlsson, "CNN features off-the-shelf: an astounding baseline for recognition," in IEEE Conference on Computer Vision and Pattern Recognition Workshops (CVPRW), 2014, pp. 512–519.

[11] B. C. Russell, A. Torralba, K. P. Murphy, and W. T. Freeman, "LabelMe: a database and web-based tool for image annotation," International Journal of Computer Vision, vol. 77, no. 1, pp. 157–173, 2008.

[12] Y. Yao, J. Zhang, F. Shen, X. Hua, J. Xu, and Z. Tang, "A new web-supervised method for image dataset constructions," Neurocomputing, vol. 236, pp. 23–31, 2017.

[13] A. Tegen, R. Weegar, L. Hammarlund, M. Oskarsson, F. Jiang, ˚om, "Image segmentation and D. Medved, P. Nugues, and K. Astr¨ labeling using free-form semantic annotation," in IEEE International Conference on Pattern Recognition, 2014, pp. 2281–2286.

[14] S. Alabachi and G. Sukthankar, "Intelligently assisting human-guided quadcopter photography," in Proceedings of Florida Artificial Intelligence Research Society, Melbourne, FL, May 2018.

[15] D. S. Bolme, J. R. Beveridge, B. A. Draper, and Y. M. Lui, "Visual object tracking using adaptive correlation filters," in IEEE Conference on Computer Vision and Pattern Recognition, 2010, pp. 2544–2550.

31st Florida Conference on Recent Advances in Robotics, May 10-11, 2018, University of Central Florida, Orlando, Florida

85

MHopCAV: Multi-Hop Clustering for Autonomous Vehicle Networks

Christopher Medrano-Berumen, Mustafa Ilhan Akbas

Department of Computer Science
Florida Polytechnic University
4700 Research Way; Lakeland, Florida

cmedranoberumen2844@floridapoly.edu, makbas@floridapoly.edu

ABSTRACT

Autonomous vehicle (AV) technology will have a massive impact on the transportation infrastructure [1]. Intelligent transportation systems are going to be available as vehicle (V2V) and vehicle to infrastructure (V2I) communication become available together with AV technology.

In the intelligent transportation systems, the communication among AVs and between AV networks and the infrastructure will be critical. Therefore, clustering solutions must be developed for AV fleets. In this paper, we present the clustering protocol, MHopCAV, the Multi-Hop Clustering Algorithm for Autonomous Vehicle Networks. MHopCAV uses the k-hop clustering algorithm [2], which is designed for dynamic, wireless networks, and adapts it for the clustering of nodes in ACV networks.

The k-hop Clustering Algorithm uses a set of four rules to distribute a cluster based on weights. There is a minimum and maximum weight that are defined, "MIN" and "MAX" respectively, as well as the weight of each node, "w_n". The cluster head is the node with the MAX weight. The cluster heads also have the network of nodes surrounding them, "N(n)".

The set of rules are as follows:

Rule 1: This rule creates the basis for the hierarchical structure of each cluster, where each node will adopt a weight one less than whatever the greatest weight in its network is.

$\quad$ if $\max(W(N(n))) > w_n$, $\ w_n = \max(W(N(n))) - 1$

Rule 2: Whenever all nodes in a network have the minimum weight, the node will declare itself the cluster head.

$\quad$ if $\max(W(N(n))) ==$ MIN && $w_n ==$ MIN, $\ w_n =$ MAX;

Rule 3: In order to avoid fragmentation, when none of the nodes are the cluster head, the node will lower its weight by one.

$\quad$ if $\max(W(N(n))) <= w_n$ && $w_n \ != $ MAX, $\quad w_n = w_n - 1$;

Rule 4: When there are multiple cluster heads, some other criteria can be used to decide which node will remain cluster head.

$\quad$ if $\max(W(N(n))) ==$ MAX && $w_n ==$ MAX,

$w_n =$ apply criterion to select a node from set$(\max(W(N(n))), w_n)$;

$w_n = w_n - 1$;

MHopCAV adapts k-hop clustering algorithms for AV networks. In these networks, the members of a cluster are defined within a predefined communication range and the maximum weight found in that network, "W(N(n))". AVs use their communication capabilities to announce their properties to other AVs around them periodically, and from the information gathered, calculate their own weight in the network.

Each node has its own update interval at which it sends out the information including its address, weight and energy. The energy is important in this update since for rule four, the node with the most battery left is used as the cluster head. Each node stores every one of these packets as a neighbor ("N(n)") and uses the timestamp given in it to check if it hasn't been updated for mobility purposes.

As a results of the highly mobile nature of AV network, MHopCAV ensures that nodes that are not within range of any other node adopt the minimum weight. Additionally, the neighbors are traversed to remove any node that has not been heard from for a preset time interval.

OMNeT++ [3] is used for the simulation study of MHopCAV. OMNeT++ allows realistic simulation of the mobility and wireless networking features of AV networks.

Keywords
Autonomous Vehicles, Connected Vehicles, Clustering, KHOPCA

REFERENCES
[1] D. J. Fagnant and K. Kockelman. "Preparing a nation for autonomous vehicles: opportunities, barriers and policy recommendations". Transportation Research Part A: Policy and Practice, 77, pp.167-181, 2015.

[2] M. R. Brust, H. Frey, S. Rothkugel. "Adaptive Multi-hop Clustering in Mobile Networks". Proceedings of the International Conference on Mobile Technology, Applications, and Systems and the International Symposium on Computer Human Interaction in Mobile Technology, NY, ACM: 132–138, 2007.

[3] A. Varga, and R. Hornig. "An overview of the OMNeT++ simulation environment." In Proceedings of the international conference on Simulation tools and techniques for communications, networks and systems & workshops, p. 60. ICST, 2008.

31st Florida Conference on Recent Advances in Robotics, May 10-11, 2018, University of Central Florida, Orlando, Florida

86

Real Time Road Lane Segmentation and Tracking System

Michael Person, Mathew Jensen, Anthony O. Smith, Nezamoddin Nezamoddini-Kachouie, Marius Silaghi

IGVC Spec 2 Team

College of Engineering and Computing

(1)College of Science

Florida Institute of Technology, Melbourne, Florida 32901

mperson2016@my.fit.edu, mjensen@fit.edu, anthonysmith@fit.edu, nezamoddin@fit.edu, msilaghi@fit.edu

ABSTRACT

Robust, low latency road lane detection is essential to the safe operation of an autonomous vehicle. Lane detection is performed by searching an image for lane markers in order to form a model of the lane that the vehicle can follow. Deep Learning CNNs are able to form robust lane models that are able to operate in poor conditions when classical computer vision algorithms will fail. However CNNs are computationally expensive models that are not yet able to detect lanes at the the necessary speed on a desktop machine let alone an embedded device. The concept being explored is how to leverage the visual power of CNNs but be able to obtain information at close to real time speeds. The proposed system is a segmentation CNN and a Bayesian tracking algorithm that is able to achieve the necessary speed but with no loss of information so that an autonomous vehicle can still safely drive within the lane. A segmentation CNN, trained on the KITTI autonomous driving dataset, outputs a dense pixelwise prediction of where the lane is. Blob detection is then performed to extract the most likely set of connected pixels. These predicted lane pixels are used to compute the lane state, which we define as the lane's inverse radius of curvature and is analogous to the lanes centerline. Since the state variable is continuous, it is nonlinearly discretized and then tracked with a particle filter on a GPU. The particle filter's output is available even when no image data has been processed by the CNN to provide information about where the lane is currently.

Keywords: Autonomous Vehicle Perception, Embedded GPU Computing, Convolutional Neural Networks, Particle Filtering

1. INTRODUCTION

For an autonomous vehicle to function safely and effectively, it must have precise knowledge about about it's surroundings. This encompasses but is not limited to detection of all other vehicles, pedestrians, cyclists, stop lights, road signs, and lastly the road itself. Before complex reasoning about the environment can be made, an autonomous vehicle's first task is to be able to identify and safely drive within the current lane. Lane detection by itself is a challenging problem with many different scenarios; there are combinations of solid, striped and white, yellow lines and sometimes there are no lane lines at all. To complicate things further, lane lines can be occluded by other vehicles, glare from the Sun can obscure the lines, or shadows on the road can provide false detections. Given how many possible situations an autonomous vehicle may encounter, it is advantageous to pursue the use of

Figure 1. Stanely, winner of the DARPA Grand Challenge in 2005 [1]

machine learning algorithms because of their power to accurately generalize to many different inputs.

Once the lane the vehicle is traveling in, or travel lane, has been identified, the lane information must be mapped into a value which can be passed to the steering controller to keep the vehicle in the lane. Some such values are the Cross Track Error (CTE) in Frenet Coordinates or the lane's radius of curvature. The steering controller must be supplied with a Process Variable, the current state, and Set Point, the desired state, at a high rate of speed in order for the vehicle to be able to respond in it's dynamic environment. The controller's time restraint requires the perception system to identify the travel lane at higher rates of speed than are generally achievable by computer vision algorithms.

In this research the development of a real time lane tracking algorithm is proposed. In the algorithm, the travel lane is first segmented from the current time step's image using a high latency convolutional neural network (CNN) which is used to form the travel lane's current radius of curvature. The radius of curvature is then supplied as evidence to a particle filter which provides a Markovian prediction for the travel lane's radius of curvature at the desired speed. Finally, future works of completing the development of the lane tracking algorithm is proposed.

2. LITERATURE REVIEW

Ever since AlexNet in 2012, CNNs have become popular computer vision algorithms for a variety of tasks [2]. The first semantic segmentation, or pixelwise class labeling, network called Fully Convolutional Network was introduced in 2014 [3]. Since then CNN models have been developed specifically tailored for autonomous driving applications [4][5]. A computationally efficient

Figure 2. Cityscapes Test Set Input

Figure 3. Cityscapes Segmentation using ported PSPNet

Figure 4. KITTI Test Set Input

Figure 5. Original Pyramid Pooling Module Output

Figure 6. Lane Pyramid Pooling Module Output

CNN that is able to be deployed in real time called Efficient Neural Network (ENet) was able to achieve 58.3 class Intersection over Union (IoU) on the Cityscapes autonomous driving segmentation dataset [6]. In comparison Pyramid Scene Parsing Network (PSP-Net) was able to achieve 80.2 class IoU but is not able to provide segmentation in real time. PSPNet utilizes a 101 convolutional layer Residual Network (ResNet101) to perform feature extraction which are then passed into a Pyramid Pooling Module. The Pyramid Pooling Module performs segmentation with the extracted features. ResNet101 has been extremely successful at image classification so it is known to provide representationaly powerful features [7]. The Pyramid Pooling Module takes the extracted feature maps from ResNet101 and uses a billinear interpolartion to resize them spatially to the the same size as the input image. A series of bottleneck convolutions, average pooling operations, and concatenation are then applied to the resized feature maps to create the final segmentation.

3. METHODOLOGY

In this section, the segmentation CNN and particle filter development is described. The algorithm is currently under development so it will be explicitly stated whether or not each section has been constructed or still needs to be built.

3.1 PSPNet Augmentation

PSPNet was first ported from its native Caffe implementation trained on Cityscapes to a Tensorflow implementation [8]. This included a trained weight conversion and also a network implementation.

After PSPNet was converted, a second Pyramid Pooling Module was added branching off from the ResNet101 output and initialized with the originally trained weights. All convolutional weights, biases, batch normalization reparameterization weights, and moving mean and variances were frozen to their original values in
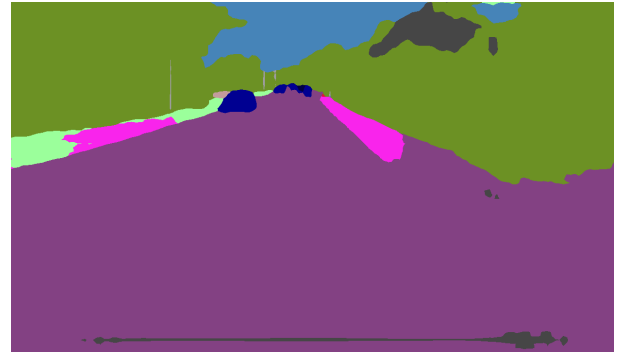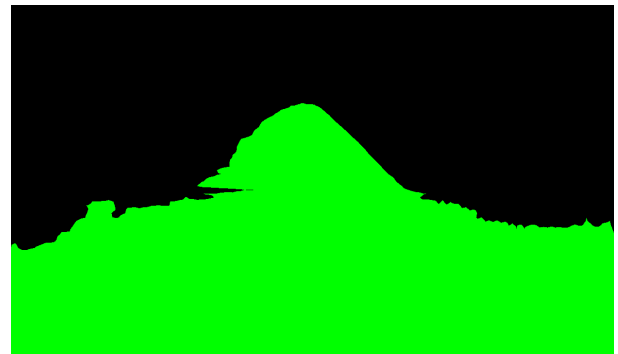
ResNet101 and the original Pyramid Pooling Module while the added Pyramid Pooling Module values were left as trainable variables. The KITTI urban marked subsection of the lane detection dataset was used to train the added Pyramid Pooling Module parameters which consists of 94 labeled instances, the same data augmentation as the original PSPNet training was performed. The loss function that was optimized was the average pixel wise cross entropy and added l2 normalized weight regularization with decay value of 0.001. Training was performed for 30 epochs with a batch size of 3. The Yellowfin optimizer was used due to it's efficiency at optimizing residual-like connections [9]. After the trained model was obtained, the model was frozen and then kernel fusion was performed to create the deployment ready model for an embedded Nvidia Tegra system. All of the above mentioned pieces have been completed.

3.2 Segmentation Post Processing

After the lane had been segmented out, Gaussian Blur kernel is applied and then a connected component clustering search was performed [10]. The clustering algorithm searches for groups of spatially connected pixels. The group with the largest number of pixels was selected to be the most probable group of lane pixels.
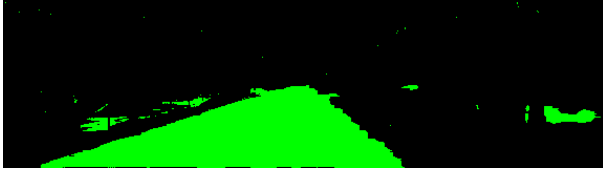
31st Florida Conference on Recent Advances in Robotics, May 10-11, 2018, University of Central Florida, Orlando, Florida

88

Figure 7. Example of a Poorly Segmented Lane

Figure 8. Outputted Connected Components

Figure 9. Selected Lane Pixel Grouping

Figure 10. First Order Markov Chain

Figure 11. Separation of Discrete State Values
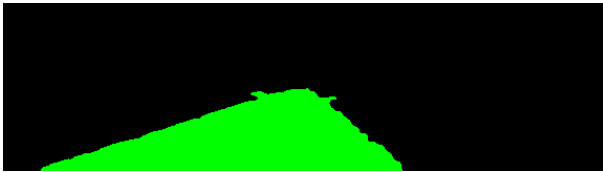
The poorly segmented lane can be seen in Figure 7, the output of the Gaussian Blur and connected component search can been seen in Figure 8, and the final selected lane grouping can be seen in Figure 9. All of the above mentioned functions have been implemented.

After the grouping of lane pixels has been selected, a second order polynomial will be fit using least squares to the height and width of each pixel location. The radius of curvature of the travel lane is then computed using Equation 1 [11]. The radius of curvature's sign determines whether the lane is curving left or right and an infinite radius of curvature indicates a straight travel lane. The polynomial and curve fitting has not been implemented yet.

$$R = \frac{\left(1 + \left(\frac{dx}{dy}\right)^2\right)^{\frac{3}{2}}}{\frac{d^2x}{d^2y}} \qquad (1)$$

3.3 State Formulation

The radius of curvature of the travel lane is modeled to be a continuous random variable, ranging from negative to positive infinity, with evidence not available at every time step in a typical first order Markov Chain, seen in Figure 10. In order to ease the computational complexity of this problem the state variable is discretized with an absolute range of 10m to 10,000m. This range was chosen because an average car is not able to follow a sharper curve and above 10,000m is a large enough value to approximate a straight line. However there are two sets of these ranges; one from -10,000m to -10m and 10m to 10,000m. These ranges oppose one another because -10,000m and 10,000 meters both represent going straight and -10m and 10m both represent turning away from one another. In order to solve this, the inverse radius of curvature is used as the state variable instead [12]. The range then becomes -.1 to .1 where 0 represents going straight.

The separation between the discretized values became a challenge. If one assumed a 0.1m separation between states to allow
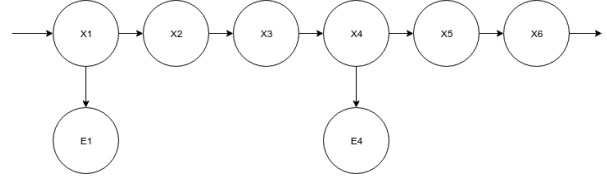
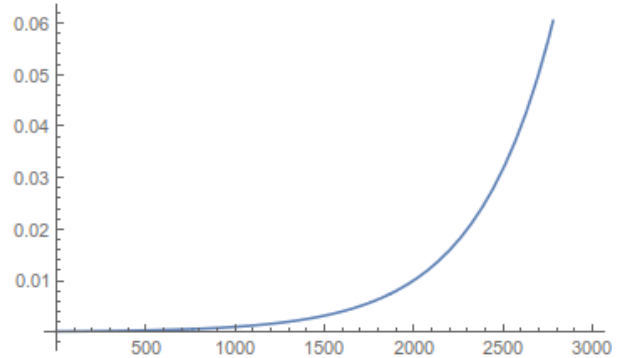for fine control for sharper curves then roughly 200,000 different values would need to be included in each state. Instead it was noted that closer to the -10m and 10m values a a fine level of resolution is needed but at -10,000m and 10,000m a lower resolution is acceptable. Therefore an exponentially growing separation between states was used, seen in Equation 2 and Figure 11. A was determined to be $\frac{1}{10,000}$, B was determined to be 6.90776, and n is the number of values in the discretization. These values were determined by enforcing the boundary conditions of a 0.1m separation at -.1 and .1 and 150m separation at 0. Equation 2 allows for an arbitrary large discretization while providing finer resolution where is is needed and coarser resolution where it is not. The state formulation is not yet complete.

$$s(x) = Ae^{\frac{Bx}{n}} \qquad (2)$$

3.4 Transition and Sensor Model Formulation

In order to form the transition model, the way the state of the travel lane evolves of time needed to be determined. Qualitatively it was determined that the lane will most likely stay at it's current state and will, with decreasing probability, deviate to the left or right. The probability for one state to transition to another state is set to be a Gaussian distribution with the mean centered at each state. This means that each state is most likely to transition to the same state in the next time step and with ever decreasing probability transition to a state to either the left or right. Since a Gaussian is a continuous distribution that ranges between $-\inf$ and $\inf$, a maximum transition range of 10% of the total states are populated with non-zero probabilities. After these probabilities are assigned, each row is normalized. An example transition matrix with 10 states can be seen in Equation 3.

31st Florida Conference on Recent Advances in Robotics, May 10-11, 2018, University of Central Florida, Orlando, Florida

89

$$
\begin{bmatrix}
0.9 & 0.1 & 0 & 0 & 0 & 0 & 0 & 0 & 0 & 0 \\
0.1 & 0.8 & 0.1 & 0 & 0 & 0 & 0 & 0 & 0 & 0 \\
0 & 0.1 & 0.8 & 0.1 & 0 & 0 & 0 & 0 & 0 & 0 \\
0 & 0 & 0.1 & 0.8 & 0.1 & 0 & 0 & 0 & 0 & 0 \\
0 & 0 & 0 & 0.1 & 0.8 & 0.1 & 0 & 0 & 0 & 0 \\
0 & 0 & 0 & 0 & 0.1 & 0.8 & 0.1 & 0 & 0 & 0 \\
0 & 0 & 0 & 0 & 0 & 0.1 & 0.8 & 0.1 & 0 & 0 \\
0 & 0 & 0 & 0 & 0 & 0 & 0.1 & 0.8 & 0.1 & 0 \\
0 & 0 & 0 & 0 & 0 & 0 & 0 & 0.1 & 0.8 & 0.1 \\
0 & 0 & 0 & 0 & 0 & 0 & 0 & 0 & 0.1 & 0.9
\end{bmatrix}
\tag{3}
$$

The sensor model is implemented in much the same way as the transition model. The found state from the image segmentation is associated with the nearest state. Then a Gaussian centered at that state's index is used to create a vector of probabilities for each state assuming only 10% of the states get a non-zero value. After the Gaussian is applied, the vector is normalized. An example sensor model vector with 10 states and found evidence at index 3 can be seen in Equation 4.

$$
\begin{bmatrix}
0 \\ 0 \\ 0.1 \\ 0.8 \\ 0.1 \\ 0 \\ 0 \\ 0 \\ 0 \\ 0
\end{bmatrix}
\tag{4}
$$

3.5 Particle Filter Implementation

It is qualitatively assumed that to accurately predict the state of the lane, a discretization of 3,000 values is needed. It is also qualitatively assumed that for an accurate approximation of the posterior, 3,000 particles is needed. Even simply an application of the transition model with a 3,000 by 3,000 matrix is not able to be done at 30Hz on a desktop CPU, let alone the CPU of a Nvidia Tegra embedded system. To solve this problem, a GPU implementation of the particle filter is developed that exploits the natural parallelization of matrix operations and the particle filtering algorithm.

The first major development is that the transition model must be applied to the ith particle at time step $t-1$ to propagate it forward one unit in time, seen in Equation 5. However, this is inefficient because it requires each particle to be done in series. In order to parallelize this operation, a particle matrix is formed, seen in Equations 6 and 7. This matrix operation now computes the transition of every particle simultaneously. This matrix multiplication is still slow using a CPU though. A speed test was performed using the Eigen library in C++, the Numpy library in Python, and the cuBLAS library in CUDA. Both CPU implementations took over 4 seconds while the cuBLAS version took less than 0.1 seconds. TODO: POPULATE W/ REAL NUMBERS

$$
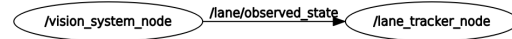\vec{\mathbf{p}}_t^{(i)} = \mathbf{T}\vec{\mathbf{p}}_{t-1}^{(i)}
\tag{5}
$$

Figure 12. ROS Compute Graph

$$
\mathbf{P}_t = \begin{bmatrix} \vec{\mathbf{p}}_t^{(0)} & \vec{\mathbf{p}}_t^{(1)} & \dots & \vec{\mathbf{p}}_t^{(N-1)} \end{bmatrix}
\tag{6}
$$

$$
\mathbf{P}_t = \mathbf{P}_{t-1}\mathbf{T}
\tag{7}
$$

Another challenge that was overcome was the inefficiency of normalizing the particle matrix. In order to efficiently normalize each particle stored within the particle matrix, a vector of ones is generated and the vectorized summation is performed using Equation 8 using the cuBLAS library. After the summation $\vec{\alpha}_t$ is found, a CUDA kernel was written to divide each element in every column of $\mathbf{P}_t$ to perform the normalization. This GPU implementation allows for quick normalization even with large matrices.

$$
\vec{\alpha}_t = \vec{1}\mathbf{P}_t
\tag{8}
$$

The library cuRAND is used to randomly initialize the prior distribution of the particle matrix. The last implemented function is to find the most probable state of the lane. In order to do this, the sum over all particle's states is formed in the same manner as Equation 8 and then that column sum is summed to normalize the final particle. After the normalized, average particle is found the maximum index is found and mapped back to a given radius of curvature of the travel lane.

The entire system is implemented in the Robotic Operating System (ROS) [13]. The ROS framework was chosen in order to be able to deploy this lane tracking system in real world applications. There are two ROS nodes in the system, one Python node to compute image segmentation and form the evidence and a second C++ and CUDA node to perform the particle filtering, seen in Figure 12. Currently, the particle filter publishes a predicted state at it's maximum rate and updates the particle matrix whenever evidence is computed from the segmentation process. The segmentation process occurs as fast as possible and when it is done, publishes a single floating point value of the computed state.

4. FUTURE WORK

This research project is only in it's infancy with many improvements to be made and many steps still to be completed. To complete the system, the particle filter likelihood weighting needs to be implemented as does the particle resampling. Once these are completed, an analysis of the convergence rate of the particle filter needs to be performed. The proposed method to do so is by generating artificial evidence of a straight lane with added Gaussian noise and the number of steps to convergence to the correct state will be counted. This process will also be performed with left and right curving lanes. The results of these three analyses will influence the search for the initialization of the particle matrix.

Accuracy results for the travel lane segmentation needs to be performed as well. The proposed method for this is to form separate the initial 94 labeled instances into a training and test set, retrain the

31st Florida Conference on Recent Advances in Robotics, May 10-11, 2018, University of Central Florida, Orlando, Florida

model using the new training set, and form the RMSE of the radius of curvature of the segmented lane versus the provided label in the test set.

Lastly the overall accuracy of the tracker needs to be determined. Since the KITTI dataset does not include sequences of images, a unique dataset collected at 30Hz will need to be collected including both straight and curved lanes. After which the segmentation will be performed on each image and stored. Next the images will be published at 30Hz and the output of the particle filter using evidence from the segmentation whenever possible will be be stored as well. Finally the image segmentation radius of curvature and the output of the particle filter will be used to form a single RMSE value.

5. ACKNOWLEDGMENTS

6. REFERENCES

References

[1] Sebastian Thrun, Mike Montemerlo, Hendrik Dahlkamp, David Stavens, Andrei Aron, James Diebel, Philip Fong, John Gale, Morgan Halpenny, Gabriel Hoffmann, Kenny Lau, Celia Oakley, Mark Palatucci, Vaughan Pratt, Pascal Stang, Sven Strohband, Cedric Dupont, Lars-Erik Jendrossek, Christian Koelen, Charles Markey, Carlo Rummel, Joe van Niekerk, Eric Jensen, Philippe Alessandrini, Gary Bradski, Bob Davies, Scott Ettinger, Adrian Kaehler, Ara Nefian, and Pamela Mahoney. Stanley: The robot that won the darpa grand challenge: Research articles. *J. Robot. Syst.*, 23(9):661–692, September 2006.

[2] Alex Krizhevsky, Ilya Sutskever, and Geoffrey E Hinton. Imagenet classification with deep convolutional neural networks. In F. Pereira, C. J. C. Burges, L. Bottou, and K. Q. Weinberger, editors, *Advances in Neural Information Processing Systems 25*, pages 1097–1105. Curran Associates, Inc., 2012.

[3] Jonathan Long, Evan Shelhamer, and Trevor Darrell. Fully convolutional networks for semantic segmentation. *CoRR*, abs/1411.4038, 2014.

[4] Hengshuang Zhao, Jianping Shi, Xiaojuan Qi, Xiaogang Wang, and Jiaya Jia. Pyramid scene parsing network. *CoRR*, abs/1612.01105, 2016.

[5] Adam Paszke, Abhishek Chaurasia, Sangpil Kim, and Eugenio Culurciello. Enet: A deep neural network architecture for real-time semantic segmentation. *CoRR*, abs/1606.02147, 2016.

[6] Marius Cordts, Mohamed Omran Sebastian Ramos, Markus Enzweiler, Rodrigo Benenson, Uwe Franke, Stefan Roth, Bernt Schiele, Daimler Ag R, Tu Darmstadt, Mpi Informatics, and Tu Dresden. The cityscapes dataset.

[7] Kaiming He, Xiangyu Zhang, Shaoqing Ren, and Jian Sun. Deep residual learning for image recognition. *CoRR*, abs/1512.03385, 2015.

[8] Martín Abadi, Ashish Agarwal, Paul Barham, Eugene Brevdo, Zhifeng Chen, Craig Citro, Greg S. Corrado, Andy Davis, Jeffrey Dean, Matthieu Devin, Sanjay Ghemawat, Ian Goodfellow, Andrew Harp, Geoffrey Irving, Michael Isard, Yangqing Jia, Rafal Jozefowicz, Lukasz Kaiser, Manjunath Kudlur, Josh Levenberg, Dan Mané, Rajat Monga, Sherry Moore, Derek Murray, Chris Olah, Mike Schuster, Jonathon Shlens, Benoit Steiner, Ilya Sutskever, Kunal Talwar, Paul Tucker, Vincent Vanhoucke, Vijay Vasudevan, Fernanda Viégas, Oriol Vinyals, Pete Warden, Martin Wattenberg, Martin Wicke, Yuan Yu, and Xiaoqiang Zheng. TensorFlow: Large-scale machine learning on heterogeneous systems, 2015. Software available from tensorflow.org.

[9] Jian Zhang, Ioannis Mitliagkas, and Christopher Ré. Yellowfin and the art of momentum tuning. *arXiv preprint arXiv:1706.03471*, 2017.

[10] Andreas Bieniek and A Moga. An efficient watershed algorithm based on connected components. 33:907–916, 06 2000.

[11] M. Bourne. Radius of curvature, March 2018.

[12] Mariusz Bojarski, Davide Del Testa, Daniel Dworakowski, Bernhard Firner, Beat Flepp, Prasoon Goyal, Lawrence D. Jackel, Mathew Monfort, Urs Muller, Jiakai Zhang, Xin Zhang, Jake Zhao, and Karol Zieba. End to end learning for self-driving cars. *CoRR*, abs/1604.07316, 2016.

[13] Morgan Quigley, Ken Conley, Brian P. Gerkey, Josh Faust, Tully Foote, Jeremy Leibs, Rob Wheeler, and Andrew Y. Ng. Ros: an open-source robot operating system. In *ICRA Workshop on Open Source Software*, 2009.

[14] Muhammad Aizzat Zakaria, Hairi Zamzuri, and Saiful Amri Mazlan. Dynamic curvature steering control for autonomous vehicle: Performance analysis. *IOP Conference Series: Materials Science and Engineering*, 114(1):012149, 2016.

[15] Christian Rathgeber, Franz Winkler, Xiaoyu Kang, and Steffen MÃijller. Optimal trajectories for highly automated driving. 9(6):696, 2015.

[16] Diederik P. Kingma and Jimmy Ba. Adam: A method for stochastic optimization. *CoRR*, abs/1412.6980, 2014.

[17] A Geiger, P Lenz, C Stiller, and R Urtasun. Vision meets robotics: The kitti dataset. *Int. J. Rob. Res.*, 32(11):1231–1237, September 2013.

[18] J. Deng, W. Dong, R. Socher, L.-J. Li, K. Li, and L. Fei-Fei. ImageNet: A Large-Scale Hierarchical Image Database. In *CVPR09*, 2009.

[19] Guoliang Liu, Florentin WÃűrgÃűtter, and I MarkeliÄĞ. Combining statistical hough transform and particle filter for robust lane detection and tracking, 07 2010.

[20] Marcos Nieto, Andoni Cortés, Oihana Otaegui, Jon Arróspide, and Luis Salgado. Real-time lane tracking using rao-blackwellized particle filter. *Journal of Real-Time Image Processing*, 11(1):179–191, Jan 2016.

[21] ZuWhan Kim. Robust lane detection and tracking in challenging scenarios. 9:16 – 26, 04 2008.

[22] N Apostoloff and A Zelinsky. Robust vision based lane tracking using multiple cues and particle filtering. pages 558 – 563, 07 2003.

[23] Heidi Loose, Uwe Franke, and Christoph Stiller. Kalman particle filter for lane recognition on rural roads, 07 2009.

31st Florida Conference on Recent Advances in Robotics, May 10-11, 2018, University of Central Florida, Orlando, Florida

91

Real-time policy generation and its application to robot grasping

Masoud Baghbahari, Neda Hajiakhoond, Aman Behal

Department of Electrical and Computer Science and NanoScience Technology Center
University of Central Florida
Orlando, FL32816 USA

bahari@knights.ucf.edu, hajiakhoond@knights.ucf.edu, abehal@ucf.edu

ABSTRACT

Real time applications such as robotic require real time actions based on the immediate available data. Machine learning and artificial intelligence rely on high volume of training informative data set to propose a comprehensive and useful model for later real time action. Our goal in this paper is to provide a solution for robot grasping as a real time application without the time and memory consuming pertaining phase. Grasping as one of the most important ability of human being is defined as a suitable configuration which depends on the perceived information from the object. For human being, the best results obtain when one incorporates the vision data such as the extracted edges and shape from the object into grasping task. Nevertheless, in robotics, vision will not suite for every situation. Another possibility to grasping is using the object shape information from its vicinity. Based on these Haptic information, similar to human being, one can propose different approaches to grasping which are called grasping policies. In this work, we are trying to introduce a real time policy which aims at keeping contact with the object during movement and alignment on it. First we state problem by system dynamic equation incorporated by the object constraint surface into dynamic equation. In next step, the suggested policy to accomplish the task in real time based on the available sensor information will be presented. The effectiveness of proposed approach will be evaluated by demonstration results.

Keywords

Real time, Policy generation, Dynamic equation, Grasping.

1. INTRODUCTION

In the era of mining and interpreting data, machine learning and artificial intelligence have demonstrated their abilities in this regard. A lot of works and attempts reported in literatures specifically during recent years provide better insight about the efficacy of the mentioned fields [2]. In fact, the pursued goal behind all of these recent valuable researches is to present a simplified, comprehensive parametric or non-parametric representation for modeling, decoding and extracting the informative features underneath the provided data set. The obtained outcome will be utilized to predict an output corresponding to new input data [3].

An essential assumption which highly determines the quality of prediction is the informativeness of data set itself. A machine learning algorithm always works based on previous observed and known data as the main source to understand the underlying unknown structure. Having access to more volume and a rich data set certainly helps the algorithm to differentiate between various of

future unknown input data and interpolate better to provide more accurate results [1].

When it comes to the realm of real time applications more considerations will be required. Real time applications are always facing with possible new different data at each instance of the time. The time-dependent nature of these data gives a dynamic behavior to the data set. For example, an autonomous vehicle moving in surrounding with other vehicles, pedestrians and under traffic restrictions needs to react immediately according to the received real time data from its sensors, camera or remote information. As another example consider a networks of connected sensor nodes transferring data between themselves or a master node. Different routes for this purpose are available between them and selection of best one needs a real time analyzing process [5]-[4]-[11].

A robot as an agent dealing with real time unknown environment and structure needs to adjust its behavior dynamically with such time and structure dependent changes. For instance, a robot aims at grasping an unknown object. The expected shape of real objects ranges from the simplest form to the most complex one. To grasp a target object a robot has to adapt the limb and end-effector configuration. The configuration depends on the object shape feature which is the edges of the object. For human being, the information of edges can be achieved by vision inspection easily. Recent years of research have been conducted using the same idea and ability by a camera in robotic [7] – [8]. Nonetheless, despite enhancement, vision algorithm in robotic domain still suffers from several weakness. High time computational and memory usage for a light, low specifications and remote control robot analyzing several other sensor information at the same time are the expense of advanced vision algorithm implementation [8].

Meanwhile, another feasible option is to precept the object through touching and sensing the surface. This Haptic strategy has been addressed in several references promising to perform better under the explained limitations in robotics. Fortunately, new manufactured robot has been equipped with sensors which gives the contact force torque information at each instant of the time. One can gather such kind of information from the object as the input data set to feed them to machine learning algorithms for structure identification, classification, modeling or shape reconstruction. Certainly previous similar diverse circumstances learning are needed to deal with novel and unknown objects. Moreover, the trained model which can be very complex should be stored in robot internal memory for real time implementation [8].

In this paper we will propose the solution for such machine learning shortages by directly implementing a policy for grasping by the robot. In other words, the idea would be eliminating the learning and exploring process as the intermediate level, proposing an immediate policy in real time to accomplish the grasping task as the robot keeps touching the object. The paper will be organized as different sections. Section 2 describes the system dynamic behavior and object force torque generating model, in section 3 the unified real time policy will be presented. The demonstrations of work are provided in section 4 and section 5 summarizes the paper.

2. SYSTEM DESCRIPTION
In this section, the required mathematical relationship of system in real time and the model of interaction surface are investigated. The provided mathematical relationships are useful for next sections algorithm.

2.1 System Real Time Dynamic Equation
To derive a real time policy, a time-dependent model of system is required. Such model is so called dynamic equation in robotic expressing the relationship between target variables and the input commanded signal. The target variables are either joint velocities $\dot{q}$ or the end-effector velocity $\dot{x}$ respect to a specific frame. The end-effector position and orientation is a twist vector of size of (6×1) denoted by $x \in \mathbb{R}^6$. The time derivative of these variables so called linear and angular velocity is related to joint velocities by Jacobian matrix $J(q)$:

$$J(q)\dot{q} = \dot{x} \tag{1}$$

On the other hand, grasping is a kind of robot environment interaction. As a consequence, it is essential to evaluate the effect of this interaction on the robot dynamic equation. Keep in mind this fact, the dynamic equation of robot in joint space is described by:

$$M(q)\ddot{q} + C(q, \dot{q}) + g(q) = \tau - J^T F \tag{2}$$

τ is the joint torques vector, F representing the interaction force-moment between the robot end-effector and the object. The inserted force and moment by end-effector to object form the components of wrench F:

$$F = \begin{bmatrix} f_e \\ m_e \end{bmatrix} \tag{3}$$

Inertia matrix $M(q)$ which is dependent on the joint angles is a bounded positive definite matrix, the Centrifugal and Coriolis forces $C\dot{q}$ and $g(q)$ gravitational forces are both bounded as well. The skew-symmetricity is one of the most important feature of robot [12].

Depend on the number of joints, redundancy in robot kinematics is possible. An immediate consequence of redundancy is smaller dimensionality of Cartesian space than joint space. Assuming that $J(q)$ is a full row rank matrix, further decomposition of joint velocity vector achieves by [12]:

$$\dot{q} = J^+ J\dot{q} + J^- \dot{q} \tag{4}$$

Where $J^+ = J^T(JJ^T)^{-1}$ and $J^- = I - (J^+J)$.

To have more control over the end-effector situation over time, it is more convenient to consider the Cartesian space dynamic equation. To do that, we can transform the joint space dynamic equation to Cartesian space by taking derivative of (1) and express the joint acceleration according to end-effector acceleration as follow:

$$\ddot{x} = J\ddot{q} + \dot{J}\dot{q} \tag{5}$$

$$\ddot{q} = J^+(\ddot{x} - \dot{J}\dot{q}) + J^-\ddot{q} \tag{6}$$

Replacing into (2), the final dynamic equation would be:

$$MJ^+ \ddot{x} + MJ^- \ddot{q} + g + d(t) = \tau - J^T F \tag{7}$$

In which the $d(t) = -MJ^+\dot{J}\dot{q} + C\dot{q}$ is a very small magnitude term and will be considered as disturbance. To create a better relationship between the end-effector and interacting force moment, following torque signal τ is presented as the first step of policy generation:

$$\tau = MJ^+(\ddot{x}_d - M_d^{-1}(B_d(\dot{x} - \dot{x}_d) - (F - F_d))) + J^T F \tag{8}$$

This torque signal simply imply the cancellation of force-moment effect via jacobian matrix on the joint torque and brings the desired force regulation inside a decoupled dynamic equation. By this way the force-moment effect in each direction can be handled much more easily.

For grasping the target end-effector velocity variable respect to end-effector itself provides more freedom to manipulate and guide the end-effector during alignment and movement on the object. To achieve this goal, the acceleration signal designs base on the relationship between the end-effector velocity in base frame and the end-effector velocity in end-effector frame:

$$\dot{x} = R_e \dot{x}_e \tag{9}$$

$$\ddot{x} = \bar{R}_e \ddot{x}_e^e + \dot{\bar{R}}_e \dot{x}_e^e \tag{10}$$

In which we have:

$$\bar{R}_e = \begin{bmatrix} R_e & 0 \\ 0 & R_e \end{bmatrix} \tag{11}$$

Now it is enough to have a choice for acceleration as:

$$a = \bar{R}_e a^e + \dot{\bar{R}}_e \dot{x}_e^e \tag{12}$$

Such selection simply provides:

31st Florida Conference on Recent Advances in Robotics, May 10-11, 2018, University of Central Florida, Orlando, Florida

93

$$\ddot{x}_e^e = a^e \quad (13)$$

a is the acceleration referred to the end-effector frame.

This equation simply means that to change the system behavior at each instant of the time, suitable acceleration signal as a good policy has to be generated. The best policy obtains when we incorporate feedback from the action into the policy. The reason behind that is because any degradation from the desired policy has to be compensated in a closed loop manner. To reach to this goal, we propose following policy for acceleration:

$$a^e = M_d^{-1}\ (v_d^e + B_d(v_e^e - v_{de}^e) - B_f(F_e - F_{de})) \quad (14)$$

Based on this expression, the robot configuration can alter according to any terms in right hand side of equation. To put in to perspective, the result from inserting this policy into robot dynamic equation (7), finally one can reach to the following dynamic equation known as error dynamic:

$$M_d\ (\dot{v}_e^e - \dot{v}_{de}^e) + B_d(v_e - v_{de}^e) = B_f(F_e^e) \quad (15)$$

Because the coefficients of this dynamic error are positive, starting from any initial conditions for the velocity, the error signal for each term will be vanished over time. Using appropriate coefficients for M_d, B_d the rate of convergence to zero can be adjusted easily.

As it is also shown in experimental results section, some recent advanced manufactured robots have provided a velocity mode control in which the robot can be easily commanded in desired direction of movement by a velocity command. Such mode of control automatically will compensate the effect of external force torque on the joints, a direct dynamic equation of the robot velocity would be accessible without need of inertia and Coriolis terms parameters involved in mathematical equations.

2.2 Interacting Force Moment Modeling

To introduce a model for interacting force-moment between the object and end-effector, similar to [12] we assume that the object 3D surface geometry can be stated as a 3-dimensional constraint manifold by:

$$\phi(X, \theta) = 0 \quad (16)$$

During the contact with the object the end-effector Cartesian position satisfies the above equation. The θ is a vector including the object-related parameters and determines the shape of the object or constrained surface.

Using partial derivative and chain role taking time derivative of (16) yields following equation:

$$J(X, \theta)\dot{X} = 0 \quad (17)$$

In which $J(X, \theta)$ is the so called constraint Jacobian matrix defined as:

$$J(X, \theta)\ = \frac{\partial \phi(X, \theta)}{\partial X} \quad (18)$$

This relationship indicates that the velocity of end-effector movement on the surface is always perpendicular to the surface gradient vector. Actually, the velocity of end-effector belongs to the null space of constraint jacobian matrix. This matrix is very useful in modeling of moment inserted from the surface to the end-effector. The moment generates under the end-effector attached sensor from the misalignment situation between the sensor plate with the surface. Having access to the surface gradient vector and the end-effector direction, one can determine the resulting moment. The interaction force between the end-effector and the surface directly depends on the amount of elasticity of the contacted object, Fig. 1.
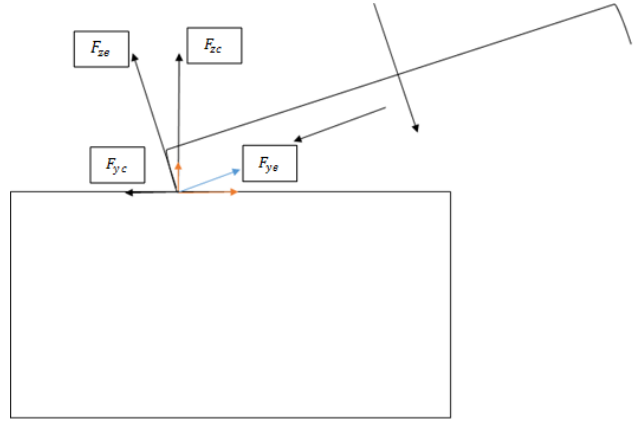

Figure 1. Decomposition of contact force during grasping

Assuming the elasticity of K, interaction force is also related to the amount of surface deformation from the equilibrium point of contact X_0:

$$F_e = K|X - X_0| \quad (19)$$

The force is always in the end-effector z direction or end-effector approaching direction.

To formulate the moment, let to assume that the wrist has a circle shape with radios equal r. The resulting moment sensing under the sensor plate would be:

$$m_e = r(z_e \times J_e f_e) \quad (20)$$

This relationship indicates that the cross product of end-effector approaching direction and surface normal vector, is a measure of misalignment between the end-effector and the object surface.

Where z_e is the unit vector of end-effector approaching direction is expressed in end-effector frame and J_e is the surface gradient vector f_e is the force vector capturing the end-effector z direction inserted force by (20) defined as follow:

31st Florida Conference on Recent Advances in Robotics, May 10-11, 2018, University of Central Florida, Orlando, Florida

94

$$f_e = \begin{bmatrix} 0 \\ 0 \\ F_e \end{bmatrix} \quad (21)$$

In next section, using the proposed model for force and moment modeling, we aim to generate required force moment term inserted in right hand side of (15) to guide the end-effector to move on the object surface. This movement finally reaches the end-effector to a suitable configuration for grasping the target object.

3. UNIFIED REAL TIME POLICY GENERATION

Grasping is a task of combination of movement and alignment around the object. Depend on the rate of mixture of movement and alignment, the object will be grasped first either by movement or alignment. Naturally this process can be done sequentially or continuously. Sequentially means first completely alignment with the object and then move on the object and vise-versa. As these two distinguishable phases be accomplished at the same time the process is called continuously. Our goal is to provide a smooth combined version of mixture of both of them. All these explanation reveals this fact that grasping task is required a kind of policy definition for the task at each instant of time. In other words, a real time on line version of policy generation is required.

Aiming to this purpose, the following definition for F_e^e in (15) is presented:

$$F_e^e = \begin{bmatrix} 0 \\ (1 - \alpha(\tanh(F_{ye})))(F_{ye} - F_{dye}) \\ F_{ze} - F_{dze} \\ \tau_{xe} \\ \tau_{ye} \\ 0 \end{bmatrix} \quad (22)$$

All the terms inside the vector is the sensor provided information. The role of $(1 - \alpha(\tanh(F_{ye})))$ is crucial. As long as the force in movement direction or y direction is near zero, the whole coefficient vanishing and the commanded force in y direction guides the end-effector on the surface. Also, if it is far from zero, it is an indicator of misalignment with the object. In such case, alignment has more priority over movement. So the whole term is around zero which means ineffective commanded force in y direction.

More precisely, the term in end-effector y direction can move the end-effector as long as the force in opposite direction be less than predefined desired force. This situation certainly cannot happen when the end-effector is not aligned with the surface. Here is where the moment on the end-effector due to misalignment isn't zero. As a consequence of commanding the robot with this measured moment from the sensor, the robot starts to become aligned with the object as much as it can to reduce the level of opposite force and create freedom for end-effector to move on the object in desired direction.

4. Experimental Results

To demonstrate the proposed real time policy, we use the Mico Kinova robot. It is a six degree of freedom light assistive robot supported by ROS package. The robot has velocity mode control in which one can command the robot end-effector with desired velocity. Based on (9) using the rotation matrix between the end-

effector and base frame, one can easily compute the end-effector velocity in end-effector frame and also send the desired velocity in end-effector frame to the robot. To identify the dynamic equation governs the system, we can command the system by just step function in each direction of end-effector. The error between the command and the end-effector velocity is in Figure.2. Since the data received form the robot is very noisy, we just pass them through a low pass filter.

The target object for grasping is a bottle of water. We select α the coefficient of $tanh$ function in (20) equal zero. In such case, the grasping task will be done purely as an alignment before complete grasping. As the uploaded video in (https://www.youtube.com/watch?v=Y19Zw3-3VDY) confirms, the grasping by proposed policy is done successfully. The Figure.3 shows the profile of end-effector force and moment during making contact with the object. The force in approaching direction is set on a constant value while the end-effector has contact with the object during grasping process. It is worth noting that the force for x and y direction are due to this fact that the gripper fingers have no equal contact with the object. The alignment is done by the information provided by the torque around end-effector y axis denoted by τ_y. All the force torque sensor data converge to a steady state after a period of alignment. During this time the torque results from misalignment is bigger that it's steady state situation.
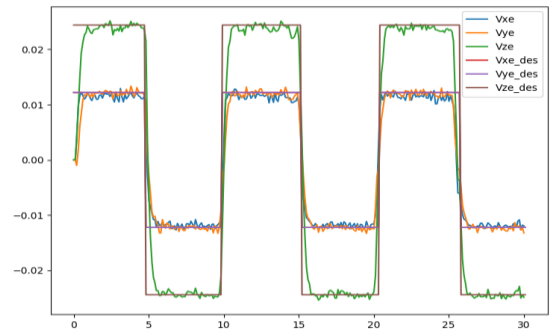

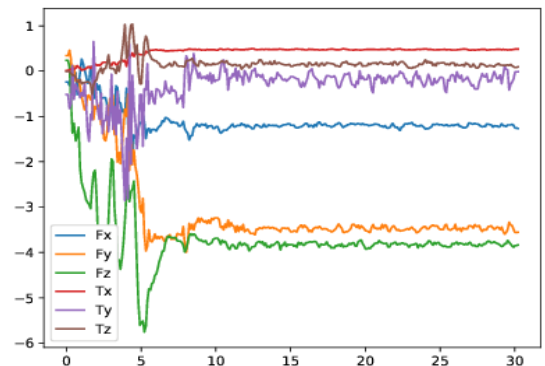**Figure 2. End-Effector Frame Velocity and Desired Values**

Figure 3. The force moment profile during alignment and grasping the object

31st Florida Conference on Recent Advances in Robotics, May 10-11, 2018, University of Central Florida, Orlando, Florida

95

5. CONCLUSIONS

In this paper we proposed a real time policy generation algorithm based on the real time data. The approach is smooth in implementation. Robot grasping as a good example demonstrates the performance of suggested solution. The provided figures of work indicate that the robot can align itself with object during grasping process.

6. REFERENCES

[1] Robert, C. (2014). Machine learning, a probabilistic perspective.

[2] N. H. Bidoki, M. B. Baghdadabad, "A glance at structural classifiers and their applications," 2nd National Conference on New Approaches in Computer Engineering Islamic Azad University, Roudsar-Branch.

[3] Alpaydin, Ethem, "Introduction to machine learning," MIT press, 2014.

[4] N. H. Bidoki, M. B. Baghdadabad, G. R. Sukthankar, and D. Turgut,"Joint Value of Information and Energy Aware Sleep Scheduling in Wireless Sensor Networks: A Linear Programming Approach," In Accepted to appear in IEEE ICC'18, May 2018.

[5] Nishihara, Robert, et al, "Real-time machine learning: The missing pieces.," Proceedings of the 16th Workshop on Hot Topics in Operating Systems. ACM, 2017.

[6] N. H. Bidoki and M. D. T. Fooladi, "Linear programming-based model for joint routing and sleep scheduling in data-centric wireless sensor networks," Information and Knowledge Technology (IKT), 2014.

[7] Levine, Sergey, et al. "Learning hand-eye coordination for robotic grasping with large-scale data collection," International Symposium on Experimental Robotics. Springer, Cham, 2016.

[8] Bohg, Jeannette, et al. "Data-driven grasp synthesisa survey " IEEE Transactions on Robotics 30.2 (2014): 289-309.

[9] A. Mayle, N. H. Bidoki, S. S. Bacanli, L. Blni, and D. Turgut, "Investigating the Value of Privacy within the Internet of Things," In Proceedings of IEEE GLOBECOM'17, December 2017.

[10] D. Turgut, L. Massi, N. H. Bidoki, and S. S. Bacanli "Multidisciplinary Undergraduate Research Experience in the Internet of Things: Student Outcomes, Faculty Perceptions, and Lessons Learned," 2017 ASEE Annual Conference Exposition Conference, June 2017. National Conference, 2016.

[11] M. Baghbahari, N. Hajiakhoond "Evaluation of estimation approaches on the quality and robustness of collision warning systems," IEEE SoutheastCon, April 2018.

[12] Namvar, Mehrzad, and Farhad Aghili "Adaptive force-motion control of coordinated robots interacting with geometrically unknown environments, " IEEE Transactions on Robotics 21.4 (2005): 678-694.

31st Florida Conference on Recent Advances in Robotics, May 10-11, 2018, University of Central Florida, Orlando, Florida

96

Design of a Bio-Inspired Crawler for Autonomous Pipe Inspection and Repair Using High Pressure Cold Spray

Hadi Fekrmandi, John Hillard, William Staib [(1)]

Department of Mechanical Engineering, South Dakota School of Mines and Technology
South Dakota School of Mines and Technology
501 E. St. Joseph Street, Rapid City, SD

Hadi.Fekrmandi@sdsmt.edu, John.Hillard@mines.sdsmt.edu, William.Staib@mines.fiu.edu

ABSTRACT

In this paper, we describe design of a robotic pipe crawler for inspection and repair of remote to access internal piping systems. Current snake robots for pipe are primarily designed for inspection purposes and unreliable for conducting further operations including repair. This shortcoming is due to the limited load carrying capacity that impedes them from offering a holistic and viable inspection and repair approach. Towards achieving this goal, a collaborative effort has been formed among Advanced Intelligent Mechatronics Systems (AIMS) research laboratory and Advanced Materials Processing Technology Transition and Training Center (AMPTECH) of South Dakota School of Mines and Technology (SDSM&T). The objective is to design and develop a long-range tethered modular pipe crawler with high load capacity carrying capable of identifying and localizing the pipe damages using Non-Destructive Evaluation (NDE) and conducting repair through coating defected pipe areas via high pressure particle deposition also known as cold spray process.

A modular design concept is adopted in the design of crawler with four modules using a bio-inspired peristaltic movement for locomotion. Adoption of modular design concept along with high load carrying capacity allows the integration of two additional modules for carrying NDE and cold spray equipment, respectively. The current design allows navigation through 4 inch and above pipe diameters. To provides access for remote areas of piping system all modules are designed to satisfy dimensional requirement to pass 45 and 90-deg bends. Also, in order to maximize the pull force available for carrying the inspection and repair equipment, a self-locking mechanism is used in the design of the grippers. This paper describes the design considerations for maximum load carrying capacity and initial design efforts for the pipe robot. It highlights the break through innovations in the design of gripper mechanism using four-follower face cam mechanism and other novel features especially within NDE inspection and cold spray repair modules.

Keywords

Pipe Inspection, Robotic Crawler, Modular Design, Peristaltic Locomotion, Non-Destructive Evaluation, High Pressure Cold Spray, Visual Inspection.

1. INTRODUCTION

Research trends indicate that autonomous bio-inspired robotic systems are emerging in our daily lives as well as industrial applications [1-4]. The possibilities of bio-inspired robots are virtually endless for commercial entities and government agencies [5]. Snake robots are a subset of bio-inspired systems that are a class of hyper-redundant mechanisms that move by replicating interval shape-changes inspired by snakes and worms [6]. The narrow cross-section area of a snake robot and the extreme range-of-motion of the joints allow it to navigate many diverse environments, including pipes, channels, uneven ground, and internal hard-to-access areas [7]. This makes them applicable in a wide range of diverse operations, such as urban search-and-rescue in unknown and unstructured terrains of collapsed mines and disaster zones. For example, the use of inspection and rescue robots played an important role in emergency-response to the nuclear accident at Fukushima Daiichi nuclear power plant [8, 9]. Particularly, the harsh environments of nuclear applications demand a reliable and resilient robot. Snake robots are well-suited to pipe inspection applications due to their ability to actively locomote in a wide range of pipe diameters and configurations with a single mechanism. Due to these advantages, snake robots have a wide range of applications including pipe inspection [10]; automated search and rescue operations [11, 12]; visual and nondestructive inspections of city gas [13] and water mains [14], monitoring of power plants [15], nuclear facilities [16], and onshore oil and gas industries [17, 18].

South Dakota is ideally located, neighboring of some of the nation's most oil and gas reach states including North Dakota, Wyoming, and Colorado, where pipelines are in widespread usage and pipe-inspection and repair is important. To establish pipe inspection and repair capabilities at the Advanced Intelligent Mechatronic Systems (AIMS) research laboratory of the South Dakota School of Mines and Technology (SDSM&T), several design challenges must be addressed particularly in pull force capacity. The same redundancy that provides snake robots with superior dexterity also poses significant challenges, particularly due to the limited load-carrying capability [19]. Two of these limitations that this current research is targeting to overcome are: a.) a lack of sufficient payload-carrying capability for repair equipment in long piping with multiple bending and variations in dimension and b.) an inability of nondestructive evaluation

31st Florida Conference on Recent Advances in Robotics, May 10-11, 2018, University of Central Florida, Orlando, Florida

97

algorithms to cope with in-field inaccuracies of measurements and strict field deployment regulations. Specifically, the current research objectives are aimed to: 1.) develop and implement a novel bio-inspired mechanism for locomotion of robots to significantly increase the payload-carrying capacity, allowing it to carry equipment and conduct damage identification and mitigation and 2.) develop and implement state-of-the-art nondestructive evaluation algorithms for reliable autonomous in-pipe damage characterization.

2. ANALYSIS

2.1 Dimensional Requirement of Modules

The maximum length and width of an individual module to move around bending segments of piping are related to each other. To find theses values first the maximum possible length of a rod L such that it could move around a corner with entrance diameter of A and exit diameter of B (shown in the Figure 1) is calculated. The length L should be minimized with in terms of the angle θ.
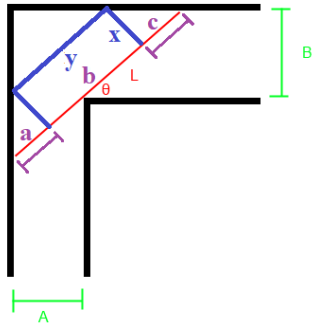

Figure 1. Maximum dimension of module feasible moving around a bending with variable corridor diameters

The length L could be formulated by being expressed in terms of the angle θ formed between the wall and the rod:

$$L = \min_{0 \le \theta \le \frac{\pi}{2}} \left(\frac{A}{\cos\theta} + \frac{B}{\sin\theta} \right)$$

To minimize the length L in terms of the angle θ, the derivate $\frac{dL}{d\theta}$ is calculated and set equal by zero:

$$\frac{dL}{d\theta} = \frac{A\,\sin\theta}{\cos^2\theta} - \frac{B\,\cos\theta}{\sin^2\theta} = 0$$

By doing so the angle θ is found as:

$$\theta = \arctan\left(\frac{B}{A}\right)^{\frac{1}{3}}$$

By substituting θ back into the original equation for maximum length L will be obtained as follows:

$$L = \left(A^{2/3} + B^{2/3} \right)^{3/2}$$

According to the geometry shown in the Figure 1 the dimensional requirement of a cylindrical module in terms of its diameter x and length y is found as:

$$L = x \tan\theta + y + \frac{x}{\tan\theta}$$

This concludes that dimensions of the modules are related to each other and choosing one will dictate the other.

2.2 Cam Profile in Four-Follower Face Cam Mechanism

Inside the instrumentation module, a four-follower face cam mechanism is used to convert the rotational motion of stepper motor to translational motion of followers in the radial direction. This way, the NDE sensors that could be installed at the end of followers, will extend radially and contact internal surface of the pipe to engage in proper NDE operation. Design constraints for cams are [20]:

- The cam function must be continuous through the first and second derivatives of displacement across the entire interval of 360°.

- The jerk must be finite across the entire interval.

The simple harmonic cam profiles cause discontinuous acceleration and infinite jerks at the follower and therefore are considered bad cam design choices. In this study, the cycloidal cam profile is selected for as the cam profile and implemented for the grooves that guide the slider. The equation for a cycloidal cam has a cycloidal displacement as follows:

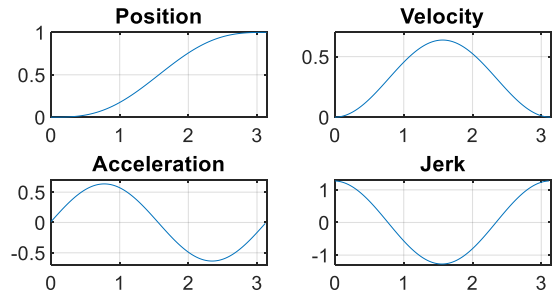$$s = \frac{h}{\beta}\theta - \frac{h}{2\pi}\sin\frac{2\pi\theta}{\beta}$$

Figure 2. Cycloidal cam profile and motion parameters

The dynamic motion parameters of the follower for a cycloidal cam are shown in the Figure 2. The choice of this cam is a valid design decision since there are no discontinuity or infinite values observed in the acceleration and jerk diagrams.

2.3 Actuating force and gripping forces

In the design of the crawler, a stepping motor with an integrated threaded rod is used as a linear actuator. The lead screw with a traveling nut converts the rotational motion to linear motion and transmit the actuating force. The claws of gripper have the structure of slider-crank mechanisms with traveling nut as common slider. Although due to frictional losses the lead screws don't have a very high efficiency but generally they are self-locking. This feature is employed to hold loads in the modules and grippers and allows to release the motors. For this design, the

31st Florida Conference on Recent Advances in Robotics, May 10-11, 2018, University of Central Florida, Orlando, Florida

98

NEMA 17-size hybrid bipolar stepping motor with a built-in lead screw in place of the normal output is used. The specifications of the stepper motor with the lead screw is give in Table 1.

Table 1. Specifications of stepper motor with the lead screw

Stepper Motor	**Type**	NEMA 17-size
	Dimensions	42.3 mm square × 38 mm
	Steps per revolution	200 (1.8° step angle)
	Linear step size	40 µm (1.6 mil) per full step
	Current rating	1.68 A per coil
	Voltage rating	2.8 V
	Holding torque	3.7 kg-cm (51 oz-in)
Leadscrew	**ISO**	Tr 8 × 8 (P2)
	Shaft type	threaded rod
	Number of leads	4
	Original length	18 cm
	Acme thread form	trapezoidal
	Diameter (d)	8 mm
	Lead (l)	8 mm
	Pitch (p)	2 mm

The linear actuating force could be found from the formula for torque T required to lift or lower a load F. This calculation can be conducted by knowing the parameters of lead screw:

$$T_{L/R} = \frac{F\, d_m}{2} \left(\frac{\mp l + \pi f\, d_m \sec(\alpha_n)}{\pi\, d_m - f\, l \sec(\alpha_n)} \right) + T_c$$

Where indeces L and R indicate lowering and raising torques, respectively. f is coefficient of friction between stainless steel threaded rod and copper alloy travelling nut and is equal to 0.15. The mean diameter d_m and the normal pressure angle are found as:

$$d_m = d - \frac{p}{2} = 7mm$$

$$\alpha_n = tan^{-1}(tan(\alpha) * cos(\theta))$$

Where α is the half of the thread angle considering that the Acme type has a 29° thread angle. The lead angle θ is found from:

$$\tan(\theta) = \frac{l}{p\, d_m}$$

Knowing the maximum torque provided by the stepper motor being 37 kg-mm, a total actuating force of 188.94 Newtons (19.26 kg) is attained from the above formula. To find the overall pull force of the robot, a static analysis needs to be conducted to obtain the reaction force at the contact point of each claw with the pipe:

$$\sum M_O = 0$$

$$F = \frac{B\, b \sin(\alpha + \beta)}{L\, (\sin(\beta) + \mu \cos(\beta))}$$

Where α and β depend on the geometry (see Figure 3) and could be calculated from:

$$r2 + L \cos(\beta) = R$$

$$r1 + a \cos(\alpha) + c\, \cos(\beta) = R$$

B is the portion of the actuating force transmitted to each claw and depends on the number of claw:
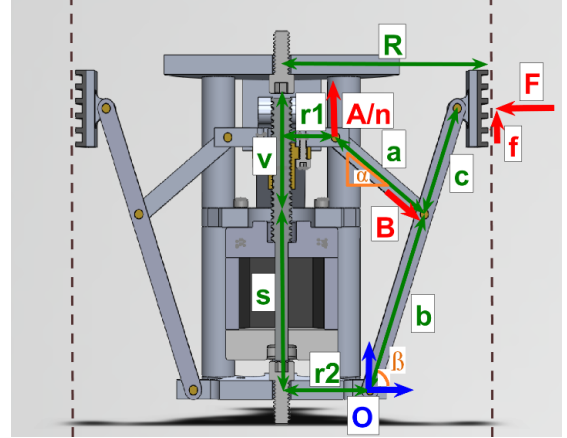
$$B = \frac{F/n}{\sin(\alpha)}$$

Figure 3. Pull force analysis based on the actuating force

The overall pull force is generated from effects of friction forces at the contact pads and depend on the coefficient of friction (Figure 4).
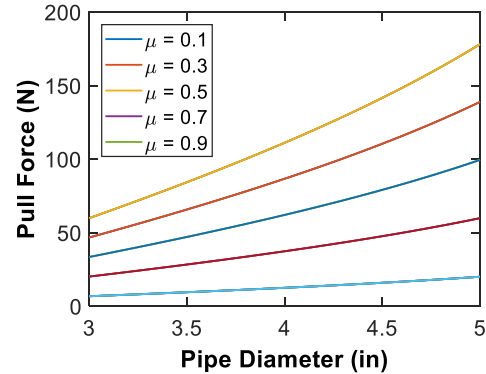

Figure 4. Pull force versus pipe diameter for various coefficient of friction between the pipe and claws

3. DESIGN

This research is comprised of three distinct yet complementing tasks each defined within development of certain modules of the pipe crawler.

3.1 Bio-Inspired Locomotion

First task is to develop and implement a novel bio-inspired mechanism for the locomotion of a robot and to significantly

31st Florida Conference on Recent Advances in Robotics, May 10-11, 2018, University of Central Florida, Orlando, Florida

99

increase the payload-carrying capacity, allowing it to carry and conduct damage identification and mitigation equipment; The objective of this study is to develop a robotic field deployable inspection and repair crawler with nondestructive evaluation capability. Sure method adopted from structural health monitoring community [21-26] will be deployed for addressing primarily pipe inspection needs. The bio-inspired peristaltic locomotion previously has been effectively utilized in developing customized robotic crawlers for hazardous and remote areas of nuclear waste storage piping and tanks at the DOE-EM Hanford Site [27-29].

To provide collaborative robotic support for human personnel performing inaccessible inspection and repair tasks from internal pipe and tank areas, there is a need for inspection robotic tools that can identify the location, type, and extent of internal defects. The crawler will perform both inspection and repair of pipes and identify the defective location. For this inspection, SDSM&T will be designing a pipe crawler, a bio-inspired snake robot that uses the peristaltic movement for locomotion. A preliminary design of locomotion module that has been developed using the lead screw stepper motors in shown in Figure 5.

Figure 5. Preliminary design of pipe crawler for locomotion modules and grippers

3.2 Non-Destructive Evaluation and instrumentation module

Second task is to implement state-of-the-art nondestructive evaluation algorithms for reliable autonomous in-pipe damage detection and characterization. The new robot will have a modular design with the use of interchangeable cylindrical modules connected with a pair of universal joints. The forward motion of the robot is generated by using peristaltic movements via compact cylindrical linear actuators and two gripping mechanisms. A front camera module will provide a live video feedback. In addition, a separate instrumentation module will conduct NDE inspection of the internal circumferential surface of the piping. The team is considering deploying a four-follower face cam mechanism shown in Figure 6 to convert the rotational motion of a motor to linear motion of followers.
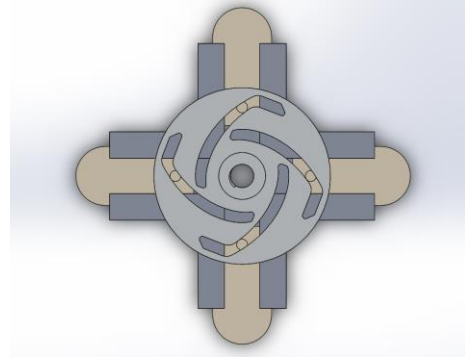

Figure 6. Four-follower face cam mechanism, the NDE transducers will be installed at the end of followers

Therefore, by extending NDE transducers to contact the 4. inch diameter pipe and conduct thickness and corrosion measurements. Integration of additional sensors including radiation motioning is also be possible, allowing conduct required measurements according to inspection mission. The nondestructive evaluation process is fully automated, and a tether will enclose the communication and power lines. The instrumentation module will be compatible with the requirements of nuclear environment inspection procedures and may include NDE capabilities such as visual, ultrasound, EMAT, laser-depth, or non-contact thickness measurements. A rendering graph of the instrumentation module is shown in Figure 7.
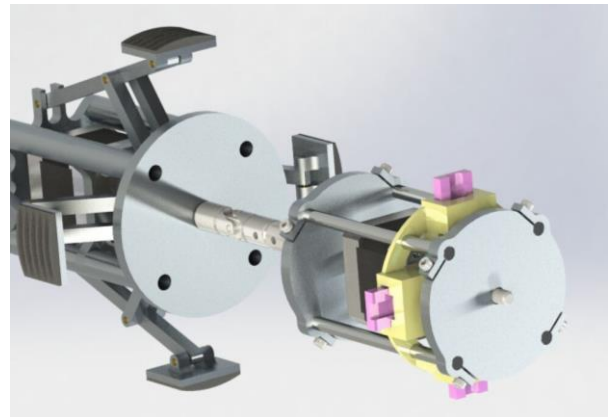

Figure 7. Four bar face-cam mechanism integrated to the instrumentation module

3.3 Maintenance and Damage Mitigation using Cold Spray

Third task is to deploy the cold spray process which is schematically shown in Figure 8. This process, also known to as supersonic particle deposition, is a high-energy solid-state coating and powder consolidation process. Cold spray uses an electrically heated high-pressure carrier gas, such as nitrogen or helium, to accelerate metal powders through a supersonic nozzle above a critical velocity for particle adhesion. The bonding occurs when a combination of mechanical interlocking and metallurgical bonding from re-crystallization at highly strained particle interfaces. Cold Spray can create mixtures of metallic and nonmetallic particulates to form a coating or free-standing structure by means of ballistic impingement upon a substrate. The

31st Florida Conference on Recent Advances in Robotics, May 10-11, 2018, University of Central Florida, Orlando, Florida

100

Cold Spray process is applicable to corrosion-resistant coatings, dimensional restoration and repair, wear-resistant coatings, and electromagnetic interference (EMI) shielding.
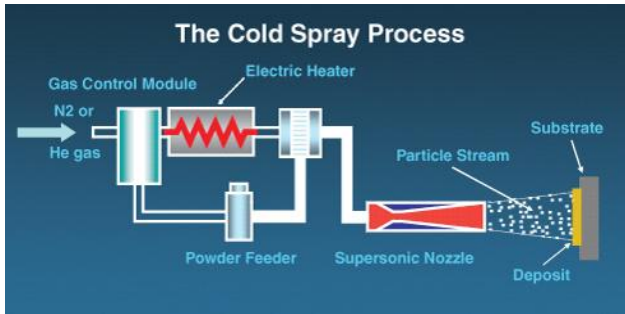

Figure 8. Schematic of the Cold Spray Process [30]

Cold Spray is in the family of thermal spray processes; however, it has the lowest overall temperatures and highest velocities of the thermal spray family. As a result, cold spray coatings are deposited in the solid state and possess the highest strengths of any thermal spray process. Cold spray coatings cause almost no microstructural changes in the powder materials deposited except for extreme plastic deformation, and it does not increase the oxide content in the coating over the base oxygen level present in the starting powder. The modular design approach, along with improved load-carrying capacity, will allow incorporating additional additive repair technologies. Upon diagnosis of pipe damage by instrumentation module the repair module will deploy a coating using cold spray material deposition process [30] compatible with the requirements of nuclear environments. The repair module will integrate the high-pressure metal deposition applicator for temporary-damage mitigation developed by collaborating research partner. A cold spray applicator installed on a robotic arm at AMP center of SDSM&T is shown in Figure 9.
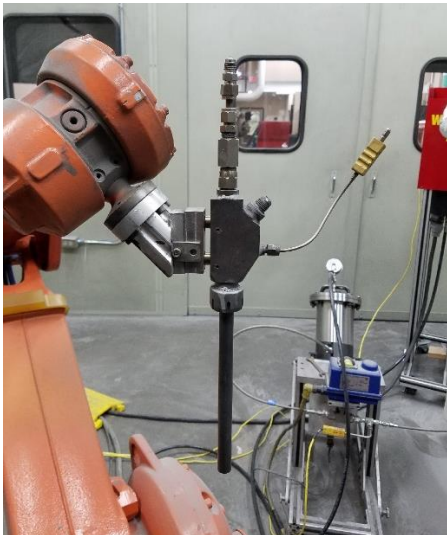

Figure 9. High pressure metal deposition applicator on a robotic manipulator at AMP lab of SDSM&T

The robotic inspection tools will be connected to the user through a tether comprised of power and control lines; a cable management system will automatically supply and retrieve the tether. The system will also be able to help with localizing the robot and identifying the extent of damage inside pipes and tanks with the desired accuracy and conduct the repair process accordingly. During the design and development process, the team will communicate with research partner to effectively establish the components of design according to government Technology Readiness Levels (TRL) and nuclear deployment requirements. A full assembly rendering of the robot is show in Figure 10.
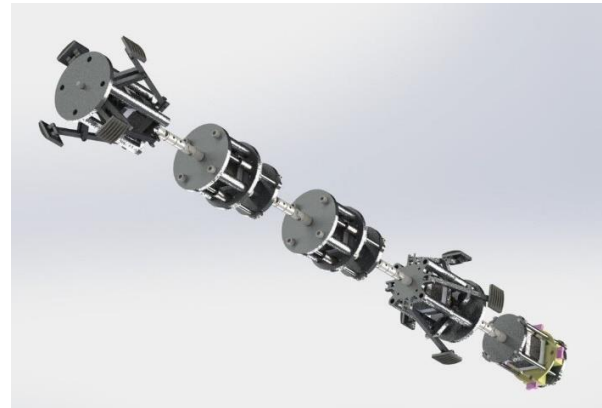

Figure 10. Assembly rendering of current design of robot

4. Conclusion and Future Work

The design and architecture of a novel modular pipe inspection and repair robot is presented. In the process of designing of the pipe crawler influential parameters for maximizing pull force and functionality were considered including torque, module size and NDE sensor requirements. The results are a design with high pull force output yet small module dimension and weight. In addition, integration of a four-follower face cam mechanism in the instrumentation module allows the NDE sensors to make contact between with the internal pipe wall and measure the characteristics of the pipe interior surface condition. We believe that the current modular design will lead to a robust inspection robot and as the next step the design team will be building and testing a prototype of robot were several areas for improvement areas will be identified and implemented.

The repair module will be designed and incorporated to the robot via close communication with our collaborating research team who are specialized at additive repair processes. This collaboration will be significantly facilitated through our access to high pressure cold sprayed deposition facilities of AMP center at SDSM&T. The instrumentation module has space for several additional sensors among which the radiation sensor has already been build and tested. Finally, the integration of a module for a visual inspection and measuring pull force are being evaluated.

5. ACKNOWLEDGMENTS

31st Florida Conference on Recent Advances in Robotics, May 10-11, 2018, University of Central Florida, Orlando, Florida

101

6. REFERENCES

1. Kim, S., C. Laschi, and B. Trimmer, *Soft robotics: a bioinspired evolution in robotics.* Trends in biotechnology, 2013. **31**(5): p. 287-294.
2. Liu, Y. and D. Sun, *Biologically inspired robotics.* 2017: CRC Press.
3. Mattar, E., *A survey of bio-inspired robotics hands implementation: New directions in dexterous manipulation.* Robotics and Autonomous Systems, 2013. **61**(5): p. 517-544.
4. Pfeifer, R., M. Lungarella, and F. Iida, *Self-organization, embodiment, and biologically inspired robotics.* science, 2007. **318**(5853): p. 1088-1093.
5. *National Robotics Initiative 2.0: Ubiquitous Collaborative Robots (NRI-2.0)*
6. Hopkins, J.K., B.W. Spranklin, and S.K. Gupta, *A survey of snake-inspired robot designs.* Bioinspiration & biomimetics, 2009. **4**(2): p. 021001.
7. Wright, C., et al. *Design and architecture of the unified modular snake robot.* in *Robotics and Automation (ICRA), 2012 IEEE International Conference on.* 2012. IEEE.
8. Nagatani, K., et al., *Emergency response to the nuclear accident at the Fukushima Daiichi Nuclear Power Plants using mobile rescue robots.* Journal of Field Robotics, 2013. **30**(1): p. 44-63.
9. Kawatsuma, S., M. Fukushima, and T. Okada, *Emergency response by robots to Fukushima-Daiichi accident: summary and lessons learned.* Industrial Robot: An International Journal, 2012. **39**(5): p. 428-435.
10. Ogai, H. and B. Bhattacharya, *Pipe Inspection Robots for Structural Health and Condition Monitoring.* 2018: Springer.
11. Wolf, A., et al. *A mobile hyper redundant mechanism for search and rescue tasks.* in *Intelligent Robots and Systems, 2003.(IROS 2003). Proceedings. 2003 IEEE/RSJ International Conference on.* 2003. IEEE.
12. Bai, Y. and Y. Hou, *Research of Pose Control Algorithm of Coal Mine Rescue Snake Robot.* Mathematical Problems in Engineering, 2018. **2018**.
13. Schempf, H., et al., *Visual and nondestructive evaluation inspection of live gas mains using the Explorer™ family of pipe robots.* Journal of Field Robotics, 2010. **27**(3): p. 217-249.
14. Mirats Tur, J.M. and W. Garthwaite, *Robotic devices for water main in-pipe inspection: A survey.* Journal of Field Robotics, 2010. **27**(4): p. 491-508.
15. Tâche, F., et al., *Magnebike: A magnetic wheeled robot with high mobility for inspecting complex-shaped structures.* Journal of Field Robotics, 2009. **26**(5): p. 453-476.
16. Yamamoto, T., et al., *A Flexible In-Pipe Robot Capable of Moving in Open Spaces via a Pneumatic Rotary Mechanism.* IFAC-PapersOnLine, 2017. **50**(1): p. 1050-1055.
17. Shukla, A. and H. Karki, *Application of robotics in onshore oil and gas industry—A review Part I.* Robotics and Autonomous Systems, 2016. **75**: p. 490-507.
18. Shukla, A. and H. Karki, *Application of robotics in offshore oil and gas industry—A review Part II.* Robotics and Autonomous Systems, 2016. **75**: p. 508-524.
19. Rollinson, D. and H. Choset, *Pipe network locomotion with a snake robot.* Journal of Field Robotics, 2016. **33**(3): p. 322-336.
20. Norton, R.L., *Design of machinery: an introduction to the synthesis and analysis of mechanisms and machines.* 2004: McGraw-Hill Professional.
21. Fekrmandi, H., *Development of new structural health monitoring techniques.* 2015.
22. Fekrmandi, H., et al., *Inspection of the integrity of a multi-bolt robotic arm using a scanning laser vibrometer and implementing the surface response to excitation method (SuRE).* International Journal of Prognostics and Health Management, 2014. **5**(1): p. 1-10.
23. Fekrmandi, H., et al., *Investigation of the computational efficiency and validity of the surface response to excitation method.* Measurement, 2015. **62**: p. 33-40.
24. Fekrmandi, H., et al., *A novel approach for classification of loads on plate structures using artificial neural networks.* Measurement, 2016. **82**: p. 37-45.
25. Baghalian, A., et al., *Non-contact quantification of longitudinal and circumferential defects in pipes using the surface response to excitation (sure) method.* J. Prognostics Health Manage, 2017. **8**: p. 1-8.
26. Fekrmandi, H. and Y. Gwon. *Reliability of surface response to excitation method for data-driven prognostics using Gaussian process regression.* in *Health Monitoring of Structural and Biological Systems XII.* 2018. International Society for Optics and Photonics.
27. Abrahao, A., et al., *Development of Inspection Tools for the AY-102 Double-Shell Tank at the Hanford DOE Site-16383.*
28. Dwayne McDaniel, L.L., Hadi Fekrmandi, Anthony Abrahao, Ryan Sheffield & Erim Gokce. *Robotic Technology Research at Florida International University for the Department of Energy Environmental Management.* in *National Institute of Standards and Technology.* 2016.
29. Hadi Fekrmandi, R.S., Dwayne McDaniel. *Validation of the Miniature Inspection Tool for the AY-102 Double-Shell Tank at the Hanford DOE Site.* in *29th Florida Conference on Recent Advances in Robotics (FCRAR).* 2016. Miami.
30. Champagne, V.K., *The cold spray materials deposition process: fundamentals and applications.* 2007: Elsevier.

31st Florida Conference on Recent Advances in Robotics, May 10-11, 2018, University of Central Florida, Orlando, Florida

102

Application of a Single Actuator Multiple Manipulation (SAMM) Mechanism

Christopher Rose, Jonathan McConnell, Sang-Eun Song

University of Central Florida
4000 Central Florida Blvd
Orlando, FL

christopher.rose@knights.ucf.edu, jonathan.mcconnell@knights.ucf.edu, s.song@ucf.edu

ABSTRACT

Multi-Degree-Of-Freedom (MDOF) motion in a system normally requires one actuator per Degree-Of-Freedom (DOF) for position control. With the use of a Single Actuator Multiple Manipulation (SAMM) mechanism, it is possible to centralize the control of an entire MDOF system to a single actuator.

For slow systems that allocate a low duty cycle to multiple actuators, a SAMM mechanism can yield a cheaper, more efficient design as it utilizes more of an actuator's potential over the lifetime of the system. As the number of DOFs increases, a SAMM mechanism can also significantly reduce the total actuator weight of a system.

A SAMM mechanism can be created by designing individual modules to transfer the bidirectional rotation of an actuator to each DOF. By arranging these modules around an actuator, each can be activated and controlled. The prototype described in this paper uses an oscillating ratchet mechanism to facilitate this activation.

Keywords

Actuation, Efficiency, Design, Multi-degree-of-freedom

1. INTRODUCTION

In the wake of a growing interest in centralizing control and minimizing actuator size, there have been many valid proposed approaches for achieving MDOF motion from a lower amount of actuators [1]. It has been previously shown that, with the use of clutches, a "Uni-drive modular robot" can be created to drive many DOFs from one central rotating axis [2]. It has also been shown that with a vibrating transducer exciting the natural frequencies of resonators, many DOFs can be simultaneously activated [3]. With these examples, MDOF motion was achieved, but at the cost of some added complexity. In the case of the Uni-drive solution, secondary actuation was needed to activate each DOF in the form of a clutch mechanism. In the case of the vibrating transducer, the constant connection of the channels to the central vibrating actuator raises the possibility of cross-talk amongst the DOFs. The simplicity of a SAMM mechanism's selective activation of modules allows it to adequately mimic MDOF motion through the use of only gear trains and an oscillating ratchet mechanism.

In order to prove the viability of the SAMM concept, it is necessary to design a working prototype to transfer the motion of a single motor to multiple output shafts. Such a prototype provides insight into the Size, Weight, and Power (SWaP) savings of a SAMM mechanism in comparison with traditional DOF manipulation mechanisms.

2. PROTOTYPE DESIGN OVERVIEW

2.1 General Design

For simplicity, a 4 DOF prototype was developed with a ratchet as the power transmission mechanism and a worm gear as a locking mechanism for each module as shown in Figure 1.
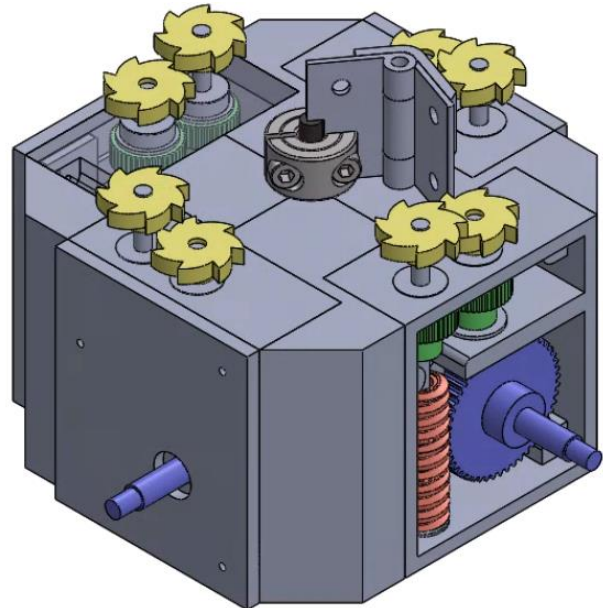

Figure 1. A full assembly CAD model of the 4 DOF prototype SAMM mechanism. The four modules exhibit rotational symmetry with respect to the motor shaft. The cover of one module has been removed for better visibility.

31st Florida Conference on Recent Advances in Robotics, May 10-11, 2018, University of Central Florida, Orlando, Florida

103

2.1.1 Stepper motor

To control a MDOF system with one actuator, a simple solution is to actuate each DOF one at a time in rapid succession. The prototype configuration seen in Figure 1 was chosen as a proof of concept for the SAMM design. For this chosen prototype, a motor must rapidly turn on and off in a controlled and accurate manner. The motor starting torque required for this process suggests that a stepper motor should be chosen as the input actuator over an AC motor, DC motor, or another rotational actuator.

2.1.2 Ratchet/Gear Interfacing

The chosen mechanism for power transmission relies on a ratchet shaft to activate the desired DOF while rotating in the clockwise direction, and leave input gears undisturbed while traveling in the counterclockwise direction. This ratchet is a simple, lightweight option for the power transmission; it also presents the advantage of low cost for replacement of the interfacing components.

2.1.3 Circular Module Arrangement

Individual modules for each DOF facilitate the translation of the motor's oscillations into rotations in the output shafts. These modules are arranged in a circle around the motor to create a sturdy design that can be scaled to control a different number of DOFs.

2.2 Ratchet Design

2.2.1 Hinge Design

The physical ratchet in the prototype shown previously in Figure 1 consists of a spring-loaded hinge that favors an open configuration. This hinge is attached to the motor shaft. Its angle is restricted by a plate. By adjusting the angle of the restricting plate, the radius of the ratchet arm can be adjusted.

2.2.2 Input Gear Design

The contour of the input gear teeth is flat to catch the ratchet arm while it rotates in the clockwise direction. When the ratchet traverses in the counterclockwise direction, it meets with the smooth contour on the back of the teeth. This helps the hinge to depress and pass over the gear without rotating it.
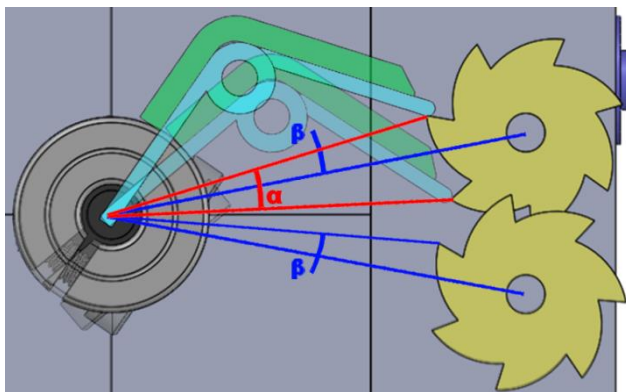

Figure 2. A top view of the angle of rotation provided by the motor to move one tooth of the input gear. This 14.93 degree rotation in the motor shaft (denoted by angle α) produces approximately 1.29 degrees of rotation in the output shaft. The angle β is the dephase angle of the two input gears.

2.2.3 Avoiding Interference

As shown in Figure 2, the number of teeth on the input gear has been optimized so that the adjacent tooth is left past the interference point after each oscillation of the ratchet. This is important to avoid possible locking of the mechanism. All input gears have the same angle relative to a radial line from the motor shaft to the outside diameter of the input gears. This means there will be a small dephase of the position of the input gears for the same DOF module. If more DOF's are added, the ratchet arm length will have to be increased and the mentioned dephase angle, β, seen in Figure 2, will have to be adjusted.

2.3 General Module Design

For actuation of each DOF, there is a module which consists of 2 spur gears, 4 bearings, 3 shafts, and a worm gear coupling. This module design is shown in Figure 3.
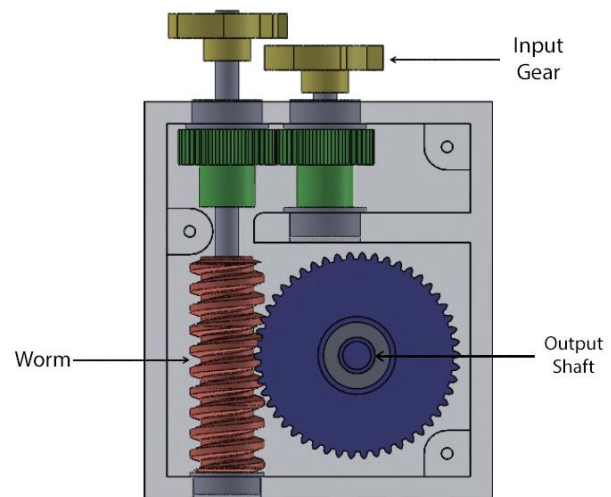

Figure 3. A front view of a prototype module showing the input gears, gear train, and output shaft. This module is used to convert the rotation of a motor into rotation in the output shaft.

The modularity of the mechanism allows for easy adjustments to the number of DOFs needing control. Each module must be controllable in both direction and non-back-drivable when not being activated. The non-back-drivable nature of the modules removes the need for clutches or secondary actuators seen in other architectures [4].

2.3.1 Bidirectional Design

Due to the use of a ratchet mechanism for module activation, it is necessary to have an input gear for each direction of rotation. The first of the two gears applies its rotation directly to the rest of the gear train. The second input gear first applies rotation to a gear coupling which rotates the rest of the gear train in the opposite direction.

2.3.2 Non-back-drivable Design

For the prototype module shown in Figure 3, the problem of non-back-drivability is solved by a worm-gear coupling. The threads of the worm can drive the gear when rotated, producing a rotation in the output shaft. When a rotation is instead applied to the output shaft, the threads of the worm hold the gear in place.

31st Florida Conference on Recent Advances in Robotics, May 10-11, 2018, University of Central Florida, Orlando, Florida

104

2.3.3 Prototype Capabilities

In the current configuration of the prototype module, the output ratio of the gear train is 40:1. With the seven teeth of the input gears, one full rotation of the output shaft is produced with 280 oscillations of the ratchet mechanism. The current design favors high torque output and high resolution of rotation for precise control as opposed to increasing the speed of output rotation. This lowers the size of the motor needed to move large systems.

3. DISCUSSION

The state of current technology provides an inherent limitation in the number of applications available for a SAMM mechanism. The prototype design has also taken on additional limitations in the realms of part selection and ease of design in an attempt to make a fully functional prototype that is both easy to assemble and appealing to potential markets. In future research, the miniaturization of a SAMM mechanism can introduce potential microelectromechanical systems (MEMS) applications.

3.1 Improvement of Design

The modularity of the prototype design implies an inherent scalability to different numbers of DOFs. It is important to explore the compaction ratio in comparison with multiple actuators as well as the maximum torque, speed, and efficiency that can be achieved. Other areas of improvement are the housing design and the power transmission mechanism.

3.1.1 Part Selection and Housing Design

This initial prototype is based on 3D printable and market-available parts. 3D printing has become an attractive option in combination with topology optimization to maximize structure stiffness while minimizing weight, which is attractive for the aerospace industry. The optimized structure may contain complex contours which are unachievable or cost prohibitive for traditional subtractive manufacturing and injection molding. For the purpose of showing the mechanism, topology optimization has not been applied to the structure. For a more compact and lightweight design, smaller components could be specially fabricated, but this will significantly increase the price unless mass production is organized. For the purposes of mass production, depending on the application, it is important to compare other methods of manufacturing such as injection molding and subtractive manufacturing to investigate which method is optimal.

As a fast prototype, the frame of the mechanisms was developed using additive manufacturing, which gives a low prototype cost, but increases the overall volume compared with other material alternatives. The use of 3D printing technology also allows the development of a variety of support structure configurations.

The components chosen to build the prototype were selected as a function of size, price, and availability in the future to create a scalable, cheap, and simple design that can be easily adopted in several markets where speed is not a priority. Among these markets are closed-circuit television cameras, domotics, robotics, toys, advertisement, space, research, and others.

The efficiency and weight of the system could be improved by the use of a DC Motor with a more sophisticated control system; the only setback would be the increase of price. The use of a stepper motor, depending on the given speed and torque values,

may present the problem of resonance if the speed is coincident with the motor's natural frequency.

3.1.2 Introduction of a Cam Interface

As previously mentioned, the interface between the motor shaft and the gearbox input shaft is a ratchet mechanism, in which the tip of the ratchet relies on friction to slide over the tailored, 3D printed gears. The interface for this configuration has the advantage of fewer components, less weight, and easy assembly, but has a diminished lifespan due to abrasion of the interfacing components. The abrasion problem can be overcome with a low friction interfacing surface, the use of lubrication, or a material resistant to abrasion like a magnesium alloy. An alternative to the current interface can rely on a small bearing to roll over a modified gear contour that accounts for the bearing radius instead of the tip of the ratchet. This is an option that will increase the lifespan of the critical component, but will be directly affecting weight, recurrent fabrication costs, and will increase the inertia the shaft has to overcome each time there is a change in direction. The latter will minimally affect the motor life and the energy consumption of the mechanism.

3.2 Design Disadvantages

The compactness can decrease the total actuator volume and mass in a MDOF system, but the conversion to a SAMM mechanism introduces the main drawbacks of low speeds and non-simultaneous DOF actuation in applications. These drawbacks can be neglected for applications in slow, low duty cycle environments, as the delayed in DOF response would be outweighed by the extended wait time between actuations.

4. CONCLUSION

The created CAD model has shown that the prototype is a viable design for a SAMM mechanism. It has been shown with this prototype that a SAMM mechanism can be compact, cheap, and easy to assemble. The prototype presented provides a scalable design that can be easily adapted to accommodate extra DOF manipulation modules. In the ratchet mechanism it has been found that specific geometric conditions must be present to achieve an effective power transmission from the motor to the input shaft. Further research is being conducted to quantify the prototype limitations and capabilities.

5. REFERENCE

[1]   P. Bolognesi, O. Bruno, A. Landi, L. Sani, and L. Taponecco, "Electromagnetic Actuators Featuring Multiple Degrees of Freedom : a Survey," *ICEM Conf. Proc.*, no. February 2014, pp. 1–6, 2004.

[2]   H. Karbasi, J. P. Huissoon, and A. Khajepour, "Uni-drive modular robots: Theory, design, and experiments," *Mech. Mach. Theory*, vol. 39, no. 2, pp. 183–200, 2004.

[3]   J. D. Penn, "A Multiple Degree of Freedom Actuator Using a Single Vibrating Transducer," Massachusetts Institute of Technology, 2012.

[4]   N. Tirasuntarakul and A. Dheeravongkit, "Design and Analysis of Micro Actuating Mechanism Driving Multi-Degree of Freedom," *Appl. Mech. Mater.*, vol. 851, pp. 464–469, 2016.

31st Florida Conference on Recent Advances in Robotics, May 10-11, 2018, University of Central Florida, Orlando, Florida

105

Target Identification and Retrieval Integration with Swarm Robotics

Kumar Yogesh Shah, Naadir Kirlew, Daniel Klumpp, Jose Tormo, Grant Wilcox, Carlos Celemin,
Abdulaziz Alenezy, Pietro Dimitri, Ibrahim Tansel

Florida International University
Department of Mechanical and Materials Engineering
Miami, Florida 33174

ABSTRACT

The research presented within the following paper was developed in conjunction with the goal of participating in the 2018 NASA Swarmathon Competition, an In situ resource utilization type challenge. FIU's motivation for participation was the advancement of research with a purpose of developing integrated robotic platforms through means of swarm robotics. The FIU project team conducted research via a variety of scientific papers and research on swarm robotics and behaviors, as well as various search algorithms and their performance to ultimately develop a search algorithm code to complete the desired search and retrieval task within the confines of resource availability and time constraints. The search algorithm was implemented with identification and retrieval operations, then tested against a base code offering limited functionality. The two variations were tested via the NASA provided virtual platform, Gazebo. The results of the two simulations were used as comparison to gauge the margin of improvement achieved by the developed search and retrieve algorithm code over the provided base code. Results are outlined below.

I. INTRODUCTION

The motivation for the research conducted and described below is the Third Annual NASA Swarmathon Competition held annually at the Kennedy Space Center in Florida. Florida International University's (FIU) objective was to develop an integrated robotic platform capable of improving the resource retrieval rate by upgrading the base code and search algorithm used in the swarm robot rovers provided by NASA. The reason for the development of these robotic platforms is resource location, identification, and collection, also known as ISRU (In-situ resource utilization) in extraterrestrial type missions. Using the NASA provided robotic rovers, dubbed Swarmies, the team aimed to develop an efficient search and retrieve algorithm to autonomously collect the available "planetary resources" which are represented by AprilCubes in the Swarmathon competition. FIU was motivated to participate in the Swarmathon to contribute to the collective cause of revolutionizing extraterrestrial exploration via implementation of swarm based robotic systems through research, innovation, and teamwork.

The study had two components: coding and enhancement of it with by reviewing previously published studies. The basic code was prepared by dissecting the base code provided by NASA, provide a basic understand "as-provided" functionality, as well as exploitation possibilities regarding the modification of the provided base code. At the same time existing publications related to swarm functions including algorithms, effective ways of communication between rovers, as well as optimization algorithms were reviewed. From the publications and research, a series of possible search and retrieval behaviors were designed and studied to understand its functionality on the Swarmies platform. The final code was prepared by integrating the parallel studies. Testing was then performed, and the results of virtual simulations were compared to analyze the outcomes.

II. LITERATURE SURVEY

2.1 Swarm Robotics

The term swarm robotics is based on multi-robot systems referring to multiple robots cooperating to perform a complex set of tasks. Swarm robotics is an approach to multi-robot systems in which multiple robots are involved, taking biological behaviors of swarm like creatures, such as ants, as inspiration to accomplish search, identification, and collection. Swarm robotics dates back nearly 40 years, to the 1980's [2], having had major strides as research provides new solutions for complex tasks in a broad field of possibilities, yet swarm-like technology is still considered to be in its infancy stages.

Due to the availability of the multiple agents, the swarm itself may be far more simplistic than a centralized single robot performing complex tasks, therefore, the behavior of the swarm would be considered a complex combination of many simple individual robots. Swarm robotics allows for multiple agents to take on complex tasks, allowing for a simplification of each unit rather than a single, far more intricate robot. The decentralization and autonomy into local communication through distributed intelligence between each swarm robot allows for a greater overall grasp of the complex task at hand, leading to an increased robustness and reliability regarding the task at hand [9].

Based on the task and its complexity, sheer numbers alone do not necessarily produce the best possible outcome according to insight gleaned from preliminary research. Swarm robots need an efficient way of communication with a certain level of intelligence to reliably cooperate as a whole. Multi-agent robot systems, such as swarms, are intrinsically advantageous over the single robot system

solution [1]. Advantages such as parallelism allow for simplification of a larger single task into subtasks for increased speed and or efficiency, as confirmed by related research and applications. The robustness of the solution is increased due to the introduction of redundancy by essentially eliminating single failure points. Adding to the advantages of swarm technology, adaptability and flexibility allows for tasks to not be exclusive to anyone agent in case of unexpected failures. Lastly, the scalability of swarm robots is desirable as tasks assigned to multi-robot systems become far more complex, thus the high capacity for scalability becomes increasingly relevant.

2.2 Robot Operating System (ROS)

The Robotic Operating System (ROS) is a flexible platform to implement coding for robots that can be shared and communicated as needed across multiple platforms in the robotic swarm. The ROS includes libraries, tools, and convention that aims to assist in creating complex robot behavior [9]. The ROS is an integral piece of the swarm technology necessary to facilitate autonomy of the search and retrieve competition goal. As the Swarmies navigate the competition course, communication related to obstacles and resources can be passed between the individual rovers via the ROS. While the communication capabilities were not utilized within the subject experimentation, the ROS provides the possibility to expand the search and retrieval capabilities of the robotic swarm.

2.3 AprilTags

The AprilTag system is a printable code style tag that is used in computer based visual detection systems. Edwin Olsen at the University of Michigan founded and pioneered the AprilTag system. The tags are 2D barcodes that were developed to aid in the visual capabilities of the robots as they perform robotic functions. See the figure below.
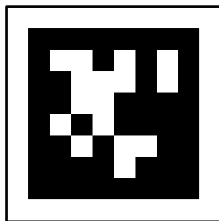

Figure 1 – AprilTag 2D barcode

The tags provide a unique fiduciary marker for the robot's camera that facilitates the tag's identification and determination of the distance to the location in the image. It is advisable that the user calibrates the camera and pre-determines the physical size of the tag in use. The tags are made in a normal printer while the detection software is used to calculate the approximate location based on the known size of the unique code arrangement. Java or C applications are used with AprilTags; however, the C implementation is recommended since it requires no external application [4].

2.4 Search Algorithms [8]

The following represents search algorithm techniques researched by the FIU team as code design alternatives for implementation into the ROS on-board the robotic rovers. Each algorithm was studied to assess feasibility regarding the ease of implementation

considering time constraints faced by the team in order to develop a working algorithm necessary to compete. The algorithms that offer advantages over alternatives are favorable but require further resource input to achieve successful coding. FIU identified the following algorithms as possible candidates for implementation.

Path finding algorithms display maps as nodes with each node having a movement price associated with the potential movement. This price represents the value tied to the cost of moving to a specific tile while calculating the path. While calculating a path, these algorithms take into account the local and global price to make sure the path chosen is the most optimal. Local price is the price of associated with movement to each of the tiles available around the current position or source tile. Global price is the total price associated with traversing each path to the intended goal. Analyzing both permits the code find the most optimal path to the targeted goal.

2.4.1 Greedy Search Algorithm

The Greedy code takes into account the local costs while moving to the goal hoping it would lead to the cheapest global cost. This as shown in the image below does not take into account for objects in the way and makes the path route sometimes more expensive than other route plotting algorithms.
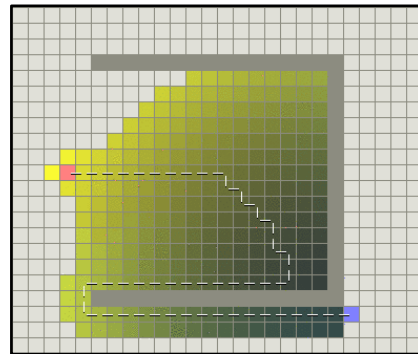

Figure 2 – The Greedy path plotting algorithm movement from the source tile (pink) to the goal tile (purple). Note that obstacle avoidance was not considered during early movements [8]

2.4.2 Dijkstra Search Algorithm

The Dijkstra algorithm analyzes all possible paths to the goal and will choose the path with the lowest global cost, but the most notable compromise is the Dijkstra search process uses a significant amount of time relative to alternatives. As shown in the image below, the Dijkstra algorithm searched for a path at the top of the map when the goal was at the bottom of the map. Crucial time and resources are spent accomplishing the intended goal and evidently this process is inherently inefficient on its own.

31st Florida Conference on Recent Advances in Robotics, May 10-11, 2018, University of Central Florida, Orlando, Florida
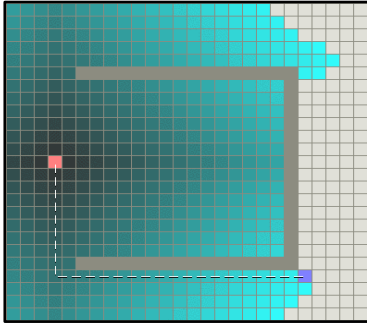
107

Figure 3 – The Dijkstra path plotting algorithm movement from the source tile (pink) to the goal tile (purple). Note the large number of tiles searched at the top of the grid that were ultimately insignificant to reaching the goal [8]

2.4.3 A Star (A*) Search Algorithm

A star (A*) is a path plotting algorithm that plots a path the shortest distance from point A to point B. This code considers the cheapest possible and most direct route while attempting to avoid obstacles. The A* code was created by combining the Greedy Best-First-Search and Dijkstra's Algorithms, both discussed above. The Greedy code works fast to arrive to the goal but is not always efficient. The Dijkstra algorithm calculates numerous alternate paths, ultimately making it choose a better path, but at the cost of time.

The combination of both Dijkstra and Greedy algorithm gave birth to A* and as shown in the map below it combines the search method of both to make a more efficient code. A*, like Greedy, tends to search for a path in the direction of the goal, but does not move according to local cost. A* looks for the most inexpensive path to the goal like Dijkstra, but unlike Dijkstra, this code does not spend time analyzing paths unnecessary path to the goal.
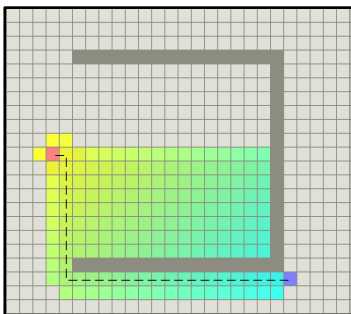

Figure 4 – A* path plotting algorithm movement from the source tile (pink) to the goal tile (purple) [8]

A* is the best combination of both of algorithms deriving its abilities form the strengths of both methods and calculates the most efficient path in the direction of the goal. A more familiar application of the A* path plotting algorithm is the implementation of A* that is used by our GPS and other path calculator programs like Google Maps and Waze. These systems rely on the A* path algorithm to plot the best routes to distant places.

2.4.4 Particle Swarm Drone Search Algorithm

The particle swarm drone search algorithm was recommended to the FIU team as a feasible search method for implementation by on-campus faculty at FIU. The particle swarm drone search algorithm searches for items in an artificial map using particle swarm methods. Since it searches in an artificial environment, special consideration will be needed to ensure the search algorithm would be functional with the competition robots. Particularly, focus would need to be placed on the considerations for upgrading the movement system away from that of a particle as our terrestrial drone moves differently than that of the particle. The particle swarm drone search algorithm implements nine different search algorithms into one, namely; Sphere, Rosen, Easom, Michalewics, Rastrigin, HolderTable, Ackley, Shubert and Rosenbrock. While the article swarm drone search algorithm exhibits potential for successful search capabilities, time constraints surrounding development of related code directed the FIU team away from utilizing the discussed method.

2.4.5 Coordinate-Based Search Algorithm

The coordinate-based search algorithm design consists of a custom algorithm derived by the FIU coding team and uses the location of the drone to search the field for retrieval targets, goals, and obstacles. The algorithm divides the field into designated search quadrants, then breaks down each quadrant into rows on which the rover is intended to move and search. The number of rows is dependent on the size of the search field. When the drone finds a resource, it would save the current position of resource identification in its memory and proceed to return the procured resource to the designated collection zone. The drone would then return to the point it left off before returning to search the field. The coordinate-based search algorithm showed significant potential for implementation in conjunction with additional functionalities necessary to perform the desired tasks of search and retrieval. Consequently, the coordinate-based method was the focus of FIU's proceeding with code development.

2.4.6 Proposed Search Algorithm

The FIU team developed its own search algorithm. The search algorithm is a univariate linearized search algorithm that was structured using the position of the Swarmie within the expected competition area to search the field and use its location to direct it in the desired linearized pattern. The algorithm allows for linearized searches of the field to retrieve as many cubes as possible before the time limit is reached. The FIU team did not designate a scouting Swarmie to find all cube while the others pick up. Instead, all Swarmies are coded to pick up AprilCubes when identified. The algorithm has a built-in avoidance system making the robot move left or right within a row until the obstacle has been bypassed. The Swarmie will then return to the active row.

A flowchart explanation and a corresponding description of the main functions of the search and retrieve algorithm can be viewed in the Appendix of the paper.

31st Florida Conference on Recent Advances in Robotics, May 10-11, 2018, University of Central Florida, Orlando, Florida

108

III. ALGORITHM PERFORMANCE IN SIMULATED ENVIRONMENT

3.1 Gazebo Virtual Testing Platform [6]

The FIU team tested the chosen search algorithm with a computer-based simulation environment named Gazebo. Gazebo is a 3D dynamic simulator with the ability to accurately and efficiently simulate populations of robots in complex environments [6]. These characteristics, as described by *gazeboism.org*, allows Gazebo to be the ideal environment to test and optimize complex algorithms that are based in ROS, C++, and even python. The basic requirements of Gazebo are Ubuntu, a variation of Linux, as well as Nvidia video card and an Intel I5 processor. This allows the trials done to be replicated by anyone if the computer has the proper hardware.

Furthermore, with Gazebo it is possible to run virtual simulations of robots or physical robots. This allows the users to create code that can be first tested on the virtual simulation then incorporated into a physical robot to test for applications with real world stimuli. More information regarding the Gazebo virtual simulation platform can be found on Gazebo's website listed in the reference section at the end of this report.
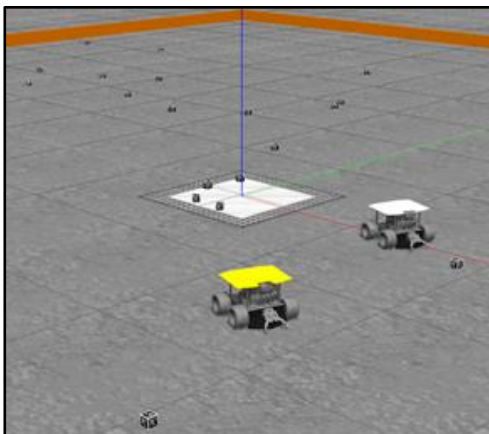

Figure 5 – FIU's Gazebo virtual simulation environment depicting two rovers, a collection zone at the center, and AprilCubes scattered throughout the simulated competition environment

3.2 Simulations

The search algorithm chosen and implemented by the FIU team was initially identified as the most effective and simplest to translate given resource and time constraints. The final code developed is categorized as a univariate linearized search algorithm. The performance of this algorithm was tested against the NASA provided base code that resembles a random search pattern algorithm. The base code was found composed of a random number generator commanding the Swarmie robot to move in a randomized pattern with no goal or aim of sweeping a distinct area or path.

Virtual testing and simulations were set up in the Gazebo environment discussed above. Conducting testing in the virtual platform would provide a reliable environment capable of simulating the Swarmies at Kennedy Space Center competition

field. The largest consideration regarding the subject virtual simulations are that any simulations conducted in Gazebo represent optimal conditions compared to testing perform on the physical rovers.

Optimal considerations include that the onboard instrumentation is performing as expected and no anomalies are encountered in the virtual environment. Comparing the two codes and search algorithms in this manner would allow for assessment of the performance gained over the base code without the need to consider physical robotic hardware performance at the simulation phase of the code development. In order to analyze the performance of the chosen search algorithm, the algorithm was translated into C-plus-plus (C++ or Cpp) code in the search controller behaviors, and then tested against the random search algorithm provided by NASA as a starting point.

The testing parameters were as follow: 10-minute simulations were run with three virtual rovers on a 15-meter by 15-meter field. Uniform and clustered configurations of AprilCube placement were utilized with the number of cubes increased over three runs. The testing was done with 32 and 64 resources as this proved to be the best number of AprilCubes allowed for the simulation to run without errors. The rovers started from the same position with each new trial and the cubes were placed in the exact same locations for every consecutive trial run to maintain comparable consistency. Using the plotted data from the GPS and odometer on the rqt-interface, the total area covered by each rover was summed and recorded. Since the goal of the algorithm is to identify and retrieve, and each rover is capable of recognizing multiple cubes and tagging their location, the greater the amount area covered in the allotted time yielded better algorithm performance.

3.3 Simulation Results

Through multiple runs on the Gazebo virtual simulation environment, including the variations of multiple setups discussed above which include the random search algorithm and the univariate linearized search algorithm, the performance of FIU's developed algorithm over the provided random search algorithm became evident. The more linearized search algorithm developed was capable of searched a wider area in the trial defined amount of time, when compared to the random search algorithm that provided by NASA, in all but one instance. The results of the field area covered by three Swarmie robots with two types of arrangements for the cube position, and a varying number of cubes are presented in Table 1. The below table represents the four scenarios set up that performed in the simulation.

Table 1 – Search algorithm performance outcomes

	Uniform – 32	Uniform – 64	Clustered – 32	Clustered – 64
Random Search	5.85 m^2	16.23m^2	8.24m^2	12.16m^2
Univariate Linear Search	8.33m^2	17.08m^2	7.86m^2	19.48m^2

According to the outcomes represented in Table 1, the univariate linearized algorithm allowed for the rovers to each cover a higher amount of area in the allotted 10 minutes in all virtual simulations excerpt for the Clustered-32 trial. Based on the virtual simulations, the FIU team choose to utilize the univariate search algorithm developed. This algorithm showed the most promise considering additional functionality operations in need of development for

31st Florida Conference on Recent Advances in Robotics, May 10-11, 2018, University of Central Florida, Orlando, Florida

109

successful physical testing. Of the additional operations, the pickup controller function is among the most pertinent for successful retrieval of identified resources.

IV. ROBOTIC INTEGRATION

4.1 The NASA Swarm Robot – "Swarmie"

The first task regarding integration to the physical platform undertaken was analyzing the provided Swarmie. Gaining a foundational understanding of how the individual components of the robot are laid out and function aided in code development and ensured the provided on-board equipment of the robotic system was undamaged and would function properly. Each Swarmie is equipped with ultrasonic sensors, a live-feed camera, a GPS, a compass, wheel encoders, a gripper claw assembly, and an inertial measurement unit. The Swarmie was assembled according the instructions provided by NASA and available on the competition website.
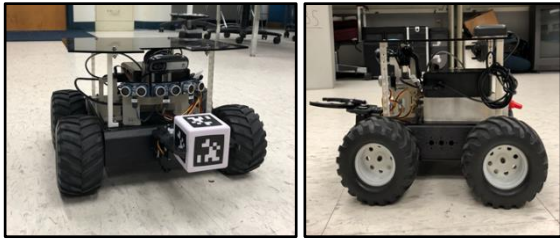
Figure 6 – Front and left side views of the assembled Swarmie provided by NASA

4.2 Computer Vision and Open CV

Computer vision is a multidisciplinary field pertaining to computer capabilities for developing a powerful level of understanding from images and videos. OpenCV is an open source computer vision library equipped with hundreds of functions and algorithms for processing images and videos with support in C++ [5]. The OpenCV platform is utilized in the Swarmathon as means of recognizing the AprilTags on the AprilCubes and the collection zone or home base. OpenCV functions and algorithms use the live feed from the Logitech C170 camera mounted on each Swarmie. The camera feed is dependent on the limitations of this specific camera, as well as outside variables such as lighting and stability while the rover is in motion. The FIU team focused on exploitation of the provided code to merge an efficient algorithm with the OpenCV capabilities.

The on-board camera is the eye of the robot and it is used to detect and recognize objects, specifically AprilTags and subsequently AprilCubes. The camera used in the Swarmie is pointing towards the ground at a 30-degrees from horizontal and works with internal software to detect and identify the AprilTags. This software was coded to detect a target at 0.65-meters in front of the robot's gripper assembly. The figure above shows the relationships between the AprilCube and the Swarmie, and how the distance values to each were calculated. This calculation is based on measurements of the hypotenuse and adjacent, using the distance of target the camera detects as the hypotenuse and the adjacent is known as it is a physically measurable distance. The system works with OpenCV

and Computer Vision to identify the AprilCubes and is an integral portion of the overall success related to resource retrieval performance.
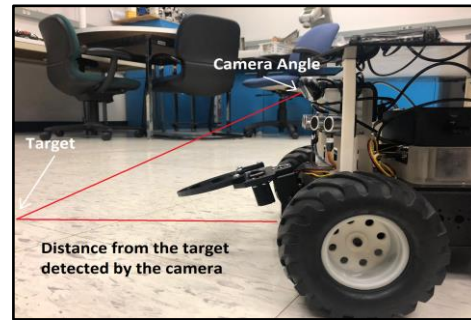

Figure 7: Camera and target identification with reference geometry depicted as red lines

4.3 GPS - Global Positioning System

A low-power consumption GPS chip can be found on board of each Swarmie. NASA has equipped them with the LEA-6 modules, capable of high performance per the u-blox 6-position engine. The GPS utilizes the doppler shift in radio frequencies in determining lines of both position and location. Using triangulation from the information of at least 3 satellites, signals with time stamps are collected by the GPS and compared to the time it arrived in order to produce longitude and latitude coordinates. GPS bias is usually remedied by allowing clock errors as a variable, allowing the receiver to successfully locate the Swarmies position on Earth.

4.4 Inertial Measurement Unit (IMU)

The IMU unit on each Swarmie reports x, y, and z acceleration of the robot, as well as orientation using the magnetic north as reference. Exploitation of the onboard IMU will produce data that can be checked against other instrumentation data. The IMU data will also help limit the Swarmies' speeds to values within the competition rules.

4.5 Kalman Filters

The collected data is checked through offset calibrations, which were physical values that can be double checked with the code for accuracy, and through the use of Kalman Filters. Kalman Filters are an optimal recursive data processing algorithm pertinent to continued function of the algorithm. The filter is capable of analyzing all the provided input from different sensors and returns optimized data that parallels the system's needs. A graphical representation of the application for a Kalman Filter is as per the figure below.
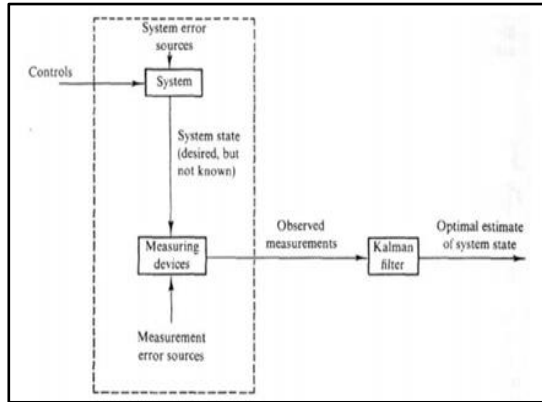
31st Florida Conference on Recent Advances in Robotics, May 10-11, 2018, University of Central Florida, Orlando, Florida

110

Figure 8 - Common Kalman Filter Application

V. METHODS

5.1 Global Positioning System (GPS)

The GPS was given extensive consideration while developing the Swarmies' code. The location reference the GPS provided was essential in the design of the pattern the Swarmies will be taking. The GPS must take into account the location of the Swarmies to accurately map the patterns in which the other Swarmies move and where obstacles and cubes are located. The GPS is primarily utilized by calling a specified function to execute do-while loops that allows the Swarmie to move to locations using its GPS data.

5.2 Encoders

The FIU team implemented minimal changes to the provided wheel encoder program. Past FIU's teams performed in-depth evaluation of the encoders related to the same design goals and provided information stating that the encoders were not an accurate information source. Reliance on the encoders made the robot perform incorrectly and produced excessive error when relying on the wheel encoder sensors for navigation.

5.3 Compass

The compass was implemented to work with the GPS and the search algorithm to calculate the current direction the robot is moving. The compass proved a vital tool for establishing pertinent information related to the Swarmie's heading data.

5.4 AprilCube Pickup and Drop Off

The FIU team changed the pickup and drop-off code to work on a distance-based calculation and continuously used the GPS and odometer to calculate the rover's current position while the camera was used to update the AprilCube position. The original pickup and drop-off sequence installed on the robot relied on a time-based countdown and control sequence where it would perform different actions based on how much time had passed. This method proved ineffective and failed during initial testing and was quickly abandoned for the method described above.

The new method ensured the Swarmie was able to correctly identify and collect the targeted resource, and then not drop or lose control of the AprilCube on its way back to the collection zone. If dropped,

the robotic code was constructed to tell the Swarmie to move back and search for the AprilCube in a 160- degree range from the last known location.

VI. PHYSICAL TESTING

6.1. Initial Configuration and Testing

Testing was conducted to establish and understand the Swarmies' capabilities and functionality after the search algorithm was developed and tested on the virtual platform. The testing of the Swarmies was conducted in FIU's robotics lab in both the provided simulated environment using Gazebo as discussed above, and a mock course built in the robotics lab to execute physical tests and evaluate the results as discrepancies were anticipated between the virtual and physical simulations.

The model course included the NASA specified home base, and replicas of the competition AprilCubes that featured printed AprilTags on six sides of the cube. Initial configuration of the Swarmie contained parameters that were interfering with other operations during the starting procedures. To resolve this, the FIU team conducted individual component tests or evaluations to check how sensitive each component was. The observable data was compared with the output data displayed on the rover rqt-interface. The rqt interface proved to be a crucial tool for evaluating physical performance. See the Figure 9 depicting a screenshot of the rqt-interface.
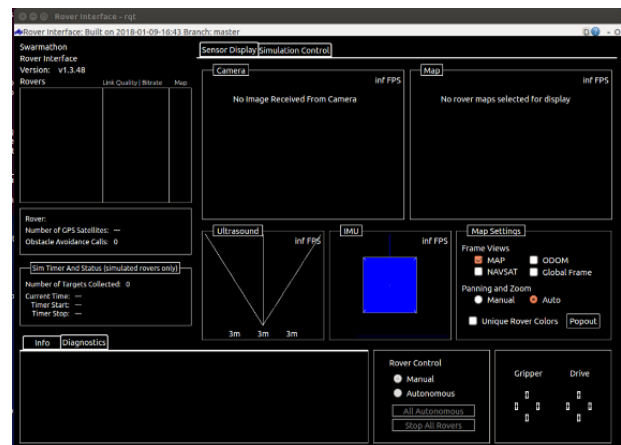

Figure 9 – Rqt-interface or rover interface

6.2 Calibration

Calibrations were performed for each component to increase accuracy. The calibration was done initially by testing the rover's functions related to the onboard camera, GPS, and gripper functionality. To specifically determine the offset of the actual Swarmie, the distance was measured from the chassis to various points of the gripper, the chassis to the camera, the camera to the grippers and ground, various range of angles the camera could function, as well as the actual velocities that the Swarmie travelled. Appropriate comparisons were made between physical and code produced data. The FIU team placed AprilCubes at various distances and angles away from the rover. Camera and ultrasound

31st Florida Conference on Recent Advances in Robotics, May 10-11, 2018, University of Central Florida, Orlando, Florida

111

sensors stated values were recorded and compared to the actual known distances to determine at what values the camera and ultrasound should respond to and operate based on.

6.3 GPS

GPS testing was done by taking screenshots of the Rover interface (rqt-interface) displaying NAVSAT, ODOM, and position data produced by the physical rover during simulations. The position of the Swarmie was then changed after each trial and the testing was repeated. The results of all tests were compared to assess the accuracy and reliance of the GPS. While testing the GPS, the FIU team noticed that the rover's reported location was not as accurate as initially anticipated. Further investigation led to the conclusion that the GPS hardware and software the robotic rovers utilize can produce up to a 5-foot margin of error.

6.4 Compass

Testing the compass was conducted by rotating the Swarmie while comparing the direction the Swarmie was reporting though the rqt-interface with an actual compass in hand inside the robotics lab. The complete testing was done using 20-degree directional change increments and the results were compared. No significant discrepancies worth offsetting was noted during the compass evaluation.

6.5 Wheel Encoders

The wheel encoders were tested by measuring and marking the wheels of the Swarmies, then commanding it to move in a desired direction. Through the rqt-interface, the information provided by the operating Swarmie was noted and then compared with the known physical data information.

6.6 Ultrasound Sensors

Testing for the ultrasound sensors was done by placing an object in front of the Swarmies within recognizable distance to the sensor's mounted location. A measurement was taken by hand to compare with the produced data representing the distance between the sensor and the object.
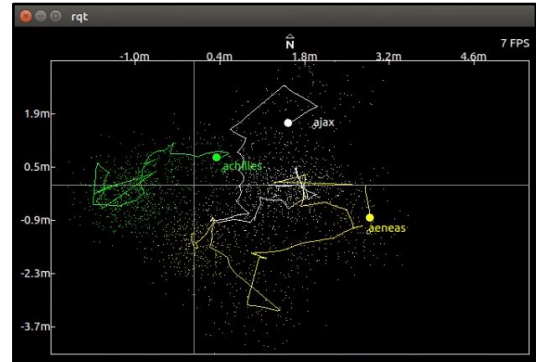
VII. RESULTS

7.1 GPS

The position data taken by the algorithm is usually error prone, as each iteration of the GPS would locate the Swarmie at different positions within a specific range as the data is converted to x and y-coordinates on the world map coordinate. This can be appreciated by the rqt GUI interface map display as per the Figure 10, where the dots are GPS x and y-coordinates, and they propagate at a certain distance from the IMU and wheel encoders data.

Figure 10 - IMU and GPS Graphical Data

7.2 Ultrasound Sensors

While testing the ultrasound sensors, The FIU team observed the calibration of the sensor was initially too sensitive and was finding objects from 5-feet away. The increased sensitivity caused the Swarmie to enter an evade mode as though it encountered an obstacle to avoid even though no obstacle existed.

The ultrasound sensors were adjusted to a lower sensitivity that resulted in the Swarmie operating more predictably and as coded. The Swarmie no longer entered the evade mode after the adjustments were made. The adjustments subsequently allowed the Swarmie to identify and pickup AprilCubes as intended. The ultrasound sensitivity adjustment enabled proper function of the Swarmie and behavior as intended by the FIU coding team.

7.3 Wheel Encoders

It was concluded that noise picked up by the IMU and GPS, and an amount drift accumulated by the wheel encoders, facilitated unpredictable divergence from the intended path and caused the Swarmie to become lost or simply have inaccurate position data. The noise captured can be appreciated in the following figure, part of the rqt and GUI interface. The amount of noise and drift is displayed while running simulations and running code on the physical test Swarmies.

Figure 11 - GPS and IMU GUI offset data

The data gathered by the GPS, IMU, and Wheel Encoders was checked against each other and through the EKF (Extended Kalman Filter) and results showed that after filtering the data nearly represented the correct position of the Swarmie. The Extended Kalman Filter is a built-in option that FIU implemented at discretion. The FIU team decided to apply this utilized Kalman Filter due to its capacity to linearize.

31st Florida Conference on Recent Advances in Robotics, May 10-11, 2018, University of Central Florida, Orlando, Florida

112

7.4 Camera

Although the image quality of the camera was an initial concern while the Swarmie was in motion, laboratory testing concluded this did not impede the Swarmie's search and retrieve process. The FIU team was satisfied with the camera's functionality after sufficient testing proved the images produced during slower movements were reliable and allowed for proper identification of AprilTags.

7.5 AprilCube Pickup and Drop Off

The adjustment from a time-based pickup to a distance-based pickup was an invaluable change implemented by the FIU team. When the Swarmie positively identified an AprilCube, it successfully completed the pickup function approximately 70% of the time on its first attempt and was observed to take a maximum of three attempts to retrieve the AprilCube as intended. Adjustments to the pickup and drop-off function over the provided base code resulted in better overall Swarmie performance.
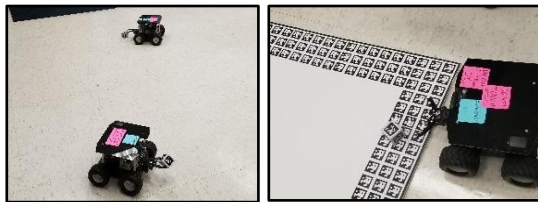
Figure 12 – Swarmies executing pickup and drop off functions during laboratory testing

VIII. CONCLUSION

The development of FIU's implemented algorithm was a direct outcome of the physical constraints found through multiple testing iterations and time allowance. The team observed that the calibration of the rovers' sensors was extremely important in the physical test as the results from the performance of the virtual simulations varied from the real-world testing of the rovers, as expected, as the Gazebo platform offers ideal testing conditions. Ultimately, the comparison of the base code provided by NASA and FIU's univariate linearized search algorithm revealed improvements were made over the base code. The outcomes were sufficient to move forward with code development.

FIU's final approach to the search algorithm drew inspiration from two main sources, a biological approach derived from ant colonies' behaviors and the linear motion of chess pieces on the game board. Using linearity, the rovers are coded to search all sections of a determined area as they attempt to move in straight patterns to cover the entire developed grid. This search algorithm was tuned through the rqt-interface as the rovers searched for the AprilTag resources in the laboratory test environment.

Obstacle avoidance allows for the rovers to cover the entire grid and camera vision differentiates between an obstacle or AprilTag.

The GPS and odometry package played an important role in improving the ability to retrieve AprilCubes and successfully place them in the home base. The Kalman Filters allowed for more reliable data from the GPS. The use of better performing hardware could increase the efficiency of the algorithm's performance. FIU's algorithm and improvements on the pickup control may be used in later editions of FIU teams participating in the NASA competition.

A flowchart explanation and a corresponding description of the main functions of the search and retrieve algorithm developed can be viewed in the Appendix.
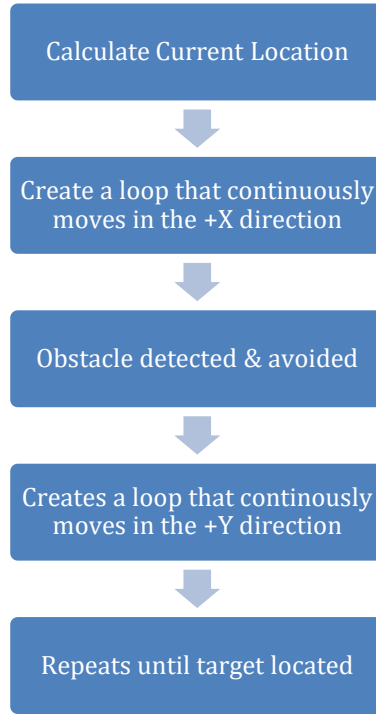
IX. ACKNOWLEDGMENTS

X. REFERENCES

[1] Altshuler, Yaniv, et al. "Swarm Intelligence — Searchers, Cleaners and Hunters." Unknown Publisher and Date.

[2] Mohan, Yogeswaran, and S.G. Ponnambalam. "An Extensive Review of Research in Swarm Robotics." ResearchGate, Jan. 2010.

[3] Moore, Thomas, and Daniel Stouch. "A Generalized Extended Kalman Filter Implementation for the Robot Operating System." SpringerLink, Springer, Cham, 3 Sept. 2015.

[4] Olson, Edwin. "AprilTag: A Robust and Flexible Visual Fiducial System." April Robotics Laboratory, 2011

[5] "OpenCV Library." OpenCV Library, OpenCV Team, 2018 [Online]. http://opencv.org/. [Accessed Jan-Mar 2018].

[6] Osrf. "Beginner: Overview." Gazebo, Open Source Robotics Foundation, 2014, gazebosim.org/tutorials?tut=guided_ b1&cat

[7] Parker, Lynne E. "Distributed Intelligence: Overview of the Field and Its Application in Multi-Robot Systems." Association for the Advancement of Artificial Intelligence, 2007.

[8] Patel, Amit. "Introduction to A-Star (A*)." Introduction to A*,1997,theory.stanford.edu/~amitp/GameProgramming/A StarComparison.html

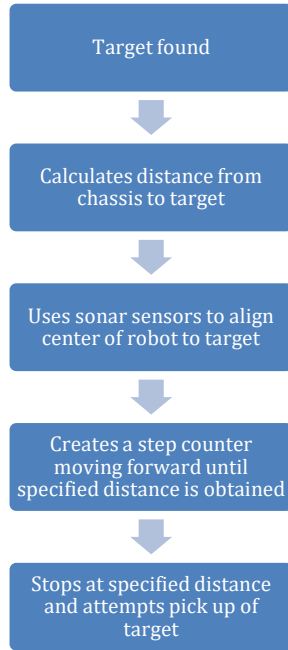[9] ROS Wiki, "ROS/Introduction," Wiki.ros.org, 2018. [Online]. http://wiki.ros.org/ROS/Introduction. [Accessed Jan-Mar 2018].

31st Florida Conference on Recent Advances in Robotics, May 10-11, 2018, University of Central Florida, Orlando, Florida

113

APPENDIX: FINAL CODE EXCERPTS AND DESCRIPTIONS

<u>Search Controller Flowchart:</u>

```
┌─────────────────────────────┐
│  Calculate Current Location │
└─────────────────────────────┘
              ↓
┌─────────────────────────────┐
│  Create a loop that continuously │
│   moves in the +X direction │
└─────────────────────────────┘
              ↓
┌─────────────────────────────┐
│  Obstacle detected & avoided │
└─────────────────────────────┘
              ↓
┌─────────────────────────────┐
│  Creates a loop that continously │
│   moves in the +Y direction │
└─────────────────────────────┘
              ↓
┌─────────────────────────────┐
│   Repeats until target located │
└─────────────────────────────┘
```

The flowchart representation of the FIU code shown above depicts the search algorithm. The concept behind the search algorithm was derived from the game of chess. The code programs the robots to create a grid based on search area. In the scenarios that were tested, the robots were already programmed to know what the grid size was and coincided with the competition grid. The robots were then able to move in a linear pattern that, between three rovers, would ensure the majority of the terrain was searched at least once. As such, the robot would first use the GPS to understand what it's current location was and break the coordinates down into x and y values. The robot then was programed to move in the positive x-direction by creating a loop that would continuously move forward until an obstacle is detected and then would change directions and move in the positive y-direction. This process was repeated and tested numerous times and was determined that the robots were able to search the majority of the terrain as intended.

31st Florida Conference on Recent Advances in Robotics, May 10-11, 2018, University of Central Florida, Orlando, Florida

114

Pickup Controller Flowchart:

```
┌─────────────────────────────┐
│         Target found         │
└─────────────────────────────┘
              │
              ▼
┌─────────────────────────────┐
│  Calculates distance from    │
│      chassis to target       │
└─────────────────────────────┘
              │
              ▼
┌─────────────────────────────┐
│   Uses sonar sensors to align │
│    center of robot to target  │
└─────────────────────────────┘
              │
              ▼
┌─────────────────────────────┐
│     Creates a step counter    │
│      moving forward until     │
│  specified distance is obtained│
└─────────────────────────────┘
              │
              ▼
┌─────────────────────────────┐
│  Stops at specified distance  │
│   and attempts pick up of     │
│           target              │
└─────────────────────────────┘
```

Above, the flowchart represents the FIU code used to retrieve a cube as shown. There were numerous methods tested including time-dependent, position-dependent, sonar-dependent, and camera dependent. Ultimately, the code that worked the best and was used in the final application was one that combined position, sonar and camera to ensure successful retrieval. Once a cube or resource was identified, the robot would calculate the position of the cube using the hypotonus from the camera and the center of the chassis. Then the rover would create a loop recalculating the distance of the cube from the robot until a predetermined distance was reached. In this scenario, that distance was approximately 3.75-inches, which was the ideal location of the gripper to successfully retrieve the cube. In order to ensure the robot stayed perfectly aligned to the cube, ultrasound was incorporated. Three sonar sensors were mounted above the gripper and below the camera allowing for the rover to detect objects to its left, center, and right. As such, the code was made so that once a cube was identified the robot would rotate either left or right so that the center sonar was the only one "blocked" indicating that the cube was directly in front of it.

31st Florida Conference on Recent Advances in Robotics, May 10-11, 2018, University of Central Florida, Orlando, Florida

115

Obstacle Avoidance Flowchart:
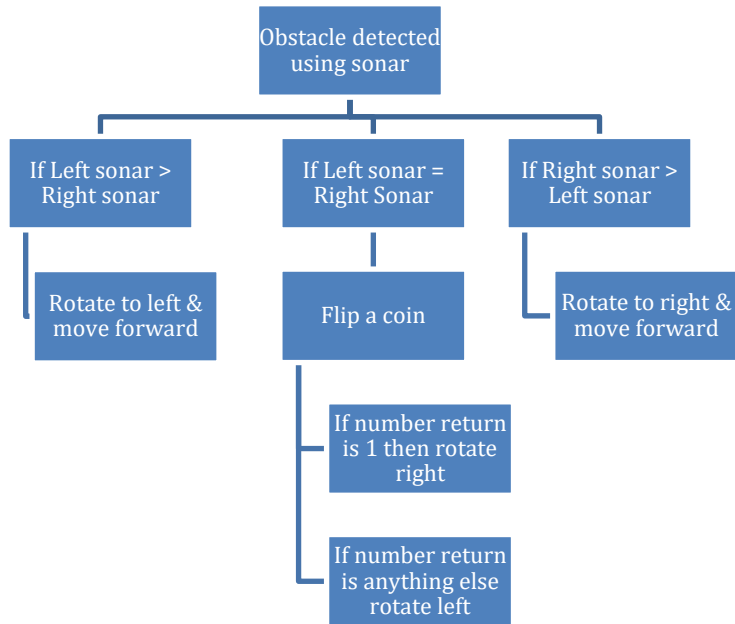
The flowchart shown above represents the FIU code implemented for obstacle avoidance. In order to ensure the robots were capable of successfully navigating terrain that included obstacles, an algorithm was written named Obstacle avoidance. The algorithm was based primarily on the sonar sensors. The sonar sensors were capable of detecting objects farther away than the camera's visibility could discern. In addition, since three sonar sensors were used the robots were also able to detect which direction the obstacle was located at and more accordingly. For example, if an obstacle was detected in the left and center sonar while the right sensor was clear, then the robot would rotate towards the right allowing the robot to clear the obstacle without difficulty. Similarly, the robot would rotate to the left if the opposite scenario was presented. In the event that both the right, left, and center sensor detected an obstacle, the robot would "flip a coin" and then assign a value to heads and tail and move either right or left depend on the result.

31st Florida Conference on Recent Advances in Robotics, May 10-11, 2018, University of Central Florida, Orlando, Florida

116

Design, Fabrication, and Preliminary Testing of Air-Bearing Test Vehicles for the Study of Autonomous Satellite Maneuvers

S. Kwok-Choon, K. Buchala, B. Blackwell, S. Lopresti, M. Wilde, T. Go

Florida Institute of Technology
150 West University Boulevard
Melbourne, Florida, 32901

skwokcho2006@my.fit.edu, kbuchala2011@my.fit.edu, blackwellb2010@my.fit.edu, stuart@lopresti.org,
mwilde@fit.edu, tgo@fit.edu

ABSTRACT

This paper explores the design, fabrication, and preliminary testing of two air-bearing vehicles to serve as the core of a satellite maneuvering testbed. The two air-bearing vehicles are a platform for the development and testing of formation flight, autonomous docking and capture control systems, different types of capture mechanisms, relative navigation sensors, and on-orbit servicing verification experiments.

The air-bearing vehicles produce a thin film of nitrogen between microporous carbon air-bearings and a 1.8 m by 3.6 m glass plate on top of a vibration-insulated optical bench, resulting in virtually frictionless planar motion. Systems testing on an air-bearing table is a cost-effective method for experimental validation of guidance, navigation, and control systems. The air-bearing vehicles are equipped with cameras, Microsoft Kinect sensors, accelerometers, an eight-thruster reaction control system, a reaction wheel, and various grippers and grasping features. The motion of the two vehicles is continuously tracked by an OptiTrack motion capture system, permitting a wide range of autonomous and tele-operated control approaches.

With a focus on the lessons learned during the design, fabrication, integration, and testing of the air-bearing test vehicles. Preliminary testing explored open loop control to perform linear, and rotation maneuvers. Outlined are the main steps required to build this pair of air-bearing test vehicles. First, the design and parts fabrication. Second, the assembly and testing of subsystems. Third, a discussion of the communication relay with a series of dynamic experiments, that allowed for calculation of the average force and associated error exerted from each solenoid thruster if operating at full capacity.

Keywords

Robotics, Air-Bearing Vehicles, Air-Bearing Table Testing, Preliminary Open Loop Testing, Thruster Force Estimation Method

1. INTRODUCTION

The observation, recognition, and capture of malfunctioning satellites and orbital debris is a growing concern [1,4,6–8,10,13]. Linked to this is the study of different methods to enable rendezvous and capture for small satellite swarming, space debris removal, as well as on-orbit servicing [3,5,9]. NORAD is tracking the orbital debris in Low Earth and Geo-Synchronous Orbit (see Figure 1)
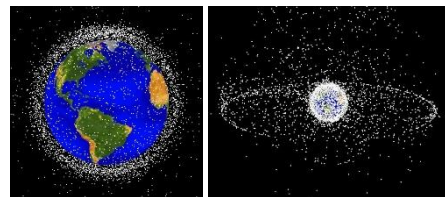

Figure 1: Orbital Debris in Leo [15] and Geo. [16]

Ground testing is a cost effective solution that allows for simulation and testing of simulated satellites, satellite capture methods, rendezvous and docking with uncooperative targets. Various research groups and entities have built ground test facilities in order to verify and refine different experiments and controllers [2,11,12,14]. The air-bearing vehicles described were developed as a platform for the testing of formation flight, autonomous docking and capture control systems, relative navigation sensors, and capture mechanisms.

The paper first describes the design and fabrication of the air-bearing vehicles. It then provides an overview of the communication relay developed to relay commands between the vehicles and control station using User Datagram Protocol (UDP) over Wi-Fi and Ethernet. The tests and main assembly were done at the Orbital Robotic Interaction, On-orbit servicing, and Navigation (ORION) laboratory at Florida Institute of Technology. The results section, describes the open loop translation and rotation tests performed and the preliminary calculation of the Force exerted by the on board thrusters and the associated error based on measurements taken.

31st Florida Conference on Recent Advances in Robotics, May 10-11, 2018, University of Central Florida, Orlando, Florida

117

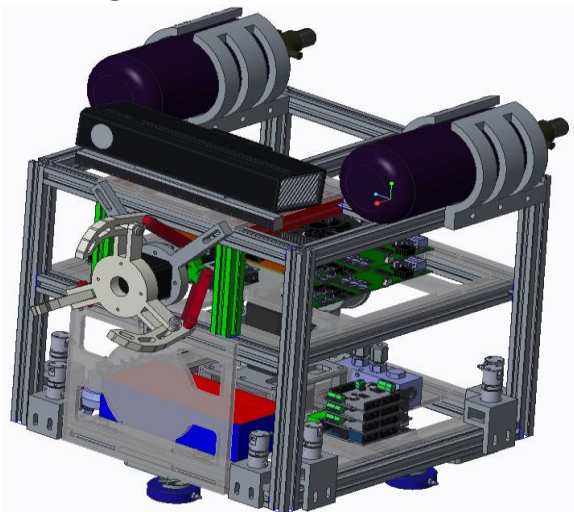## 2. DESIGN AND FABRICATION
2.1. Design

Figure 2: CAD Design

The air-bearing vehicles (ABVs) are designed with the intent of studying planar satellite capture and docking (See Figure 2) are modular; therefore, future improvements are possible based on the test and experimental requirements.
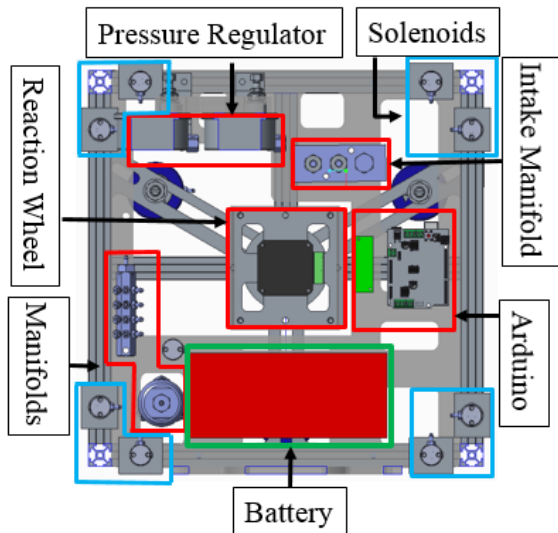

Figure 3: Air Bearing and Pneumatic Systems

The ABVs move on a flat floor with three degrees of freedom (DOF) : translation in the horizontal XY-plane with rotation about the vertical Z-axis. This was possible by using air-bearing pads for floatation, compressed-nitrogen thrusters and an onboard reaction wheel (See Figure 3 and Figure 4). Both the chaser and target ABV have the same propulsion system. Each solenoid provided thrust by actuating open and allowing compressed-nitrogen air to pass through. Initial testing did not use the on board reaction wheel in conjunction with the solenoids.

Located on the upper deck: is the onboard computer, voltage regulators, and the air-bearing chaser vehicle is equipped with a rapid-prototyped three-fingered grasping mechanism with a

Kinect V2 sensor system (See in Figure 5). One of the eventual goals is to have a Kinect V2 sensor system installed on board the chaser vehicle used for on-board distance and object recognition with image processing.
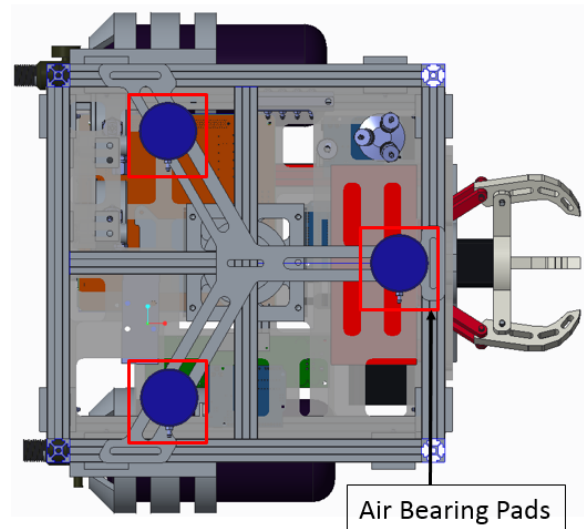
Figure 4: Air Bearing Pads
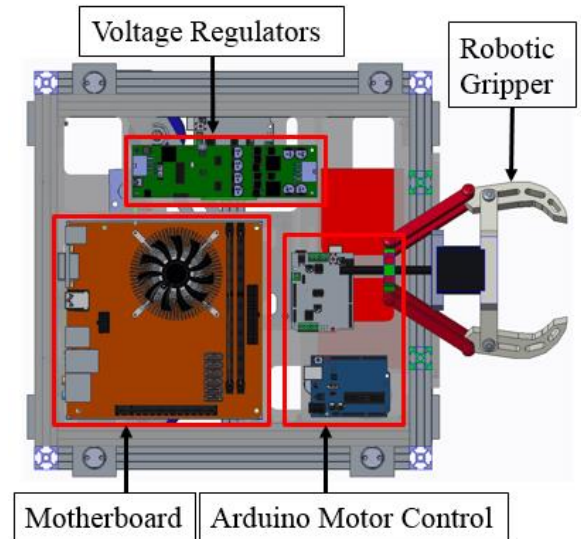
Figure 5: Upper Deck Design

2.2. Fabrication

First the frame was assembled, with the lower layer installed. This included the laser cut acrylic mount surfaces as well as the pressure regulator and pneumatic systems (see Figure 6, 7). With the completion of the CAD and frame design, Fabrication and assembly of the air-bearing vehicles commenced.

Manifold A connected to the air-bearing pads located in the base, with manifold B splitting the air to the solenoids (see Figure 7).

31st Florida Conference on Recent Advances in Robotics, May 10-11, 2018, University of Central Florida, Orlando, Florida

118

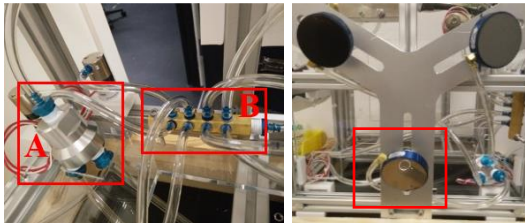**Figure 6: Frame Construction and Pneumatic system**

Figure 7: Pressure Manifolds and Air Bearing Pads

The upper deck components (computer, voltage regulators, and microcontrollers) installed and tested after the pneumatic sub-systems (See Figure 5,Figure 8).
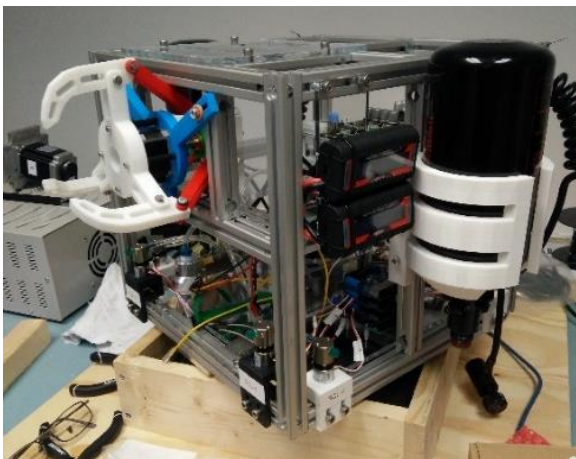

Figure 8: Install Power Regulators: Initial Installation of voltage regulators and wattmeter.

The full assembly of both the chaser and target vehicles shown in Figure 9. In order to help reduce mass. The air tanks' location changed from the sides to on top of the vehicles, with a bumper installed at the base in order to protect the electronic components and reduce the possibility of damage caused by inadvertent collision. The completed chaser and target vehicles are shown (see Figure 9), where the chaser (Right) will now be called Bob, and the target vehicle (Left) called Charlie.
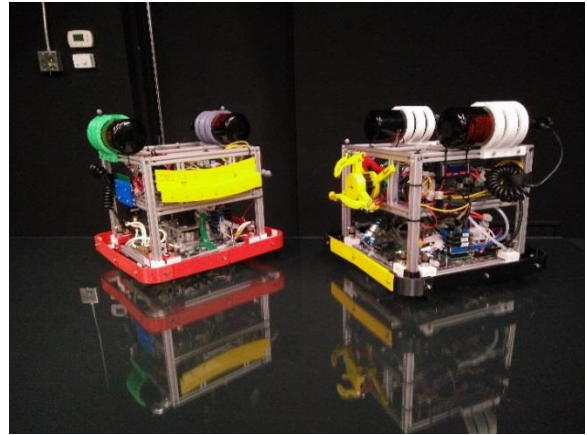
Figure 9: Vehicles fully assembled. Chaser (Bob Right) Target (Charlie Left)

3. COMMUNICATION RELAY

The communication relay infrastructure necessary to send and receive commands between the ABVs and the remote PC control station is illustrated in Figure 10.
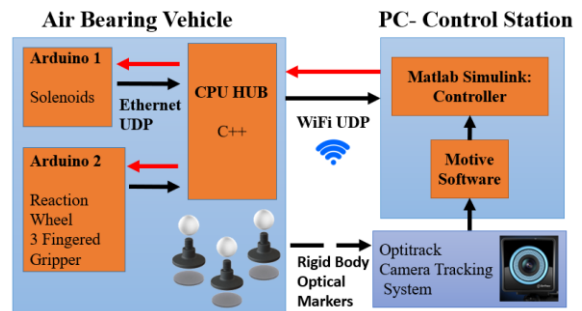

Figure 10: Communication Relay Infrastructure

There are four main segments integrated to work in-sync with one another: Wi-Fi UDP communication between Arduino IDE, C++ HUB on the vehicle using UDP sockets, Matlab Simulink, and Optitrack Motive Software. The communication relay infrastructure provides flexibility and modular growth based on the type of experiment and sensors used.

The major functions of each segment of the communication relay are described in the following sections.

3.1. PC Control Station

The Optitrack Camera System records the global relative position and orientation of the air-bearing vehicle. Motive Software obtains the current position of the defined rigid bodies from the Optitrack Camera System. Matlab Simulink receives and records the broadcasted information over UDP Multicast from the Motive Software. After receiving the broadcasted Optitrack position information, the Matlab-Simulink Controller then sends the control signal to the air-bearing vehicle.

31st Florida Conference on Recent Advances in Robotics, May 10-11, 2018, University of Central Florida, Orlando, Florida

119

3.2. Air-Bearing Vehicle:

The onboard CPU receives the command from the PC Control Station. With both Arduino 1 and 2 are in communication with the CPU Hub with Ethernet UDP. The CPU sends the appropriate command to the different on board microcontroller. Arduino 1 controls the solenoids used for vehicle planar thruster maneuvering. Arduino 2 controls the gripper as well as the on-board reaction wheel.

4. TESTING SET UP

The ORION laboratory is located at Florida Institute of Technology. The Air-Bearing table with vibration damping is shown at the North side of the ORION Lab near the experiment preparation room (see Figure 11).
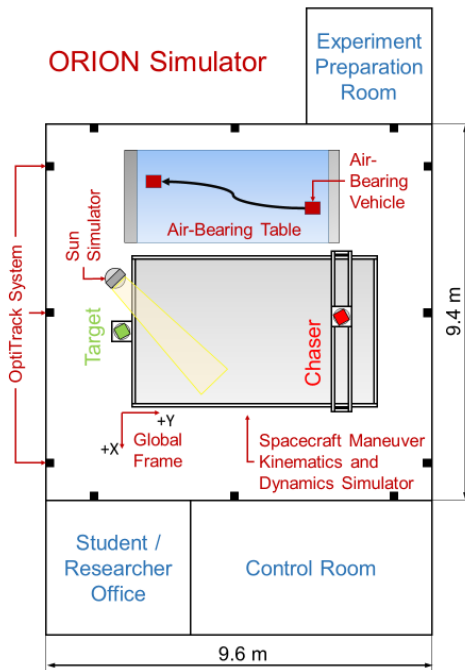
Figure 11: ORION Lab Space

4.1. Test Facility / Test Apparatus

The ORION laboratory features an Optitrack Prime 17W optical tracking system [17,18] that is able to provide position information. The external sensors are used in conjunction, thereby providing real-time system positional awareness, enabling the study of planar orbital object maneuvers between the chaser and target systems.
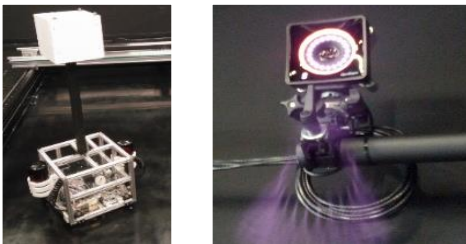

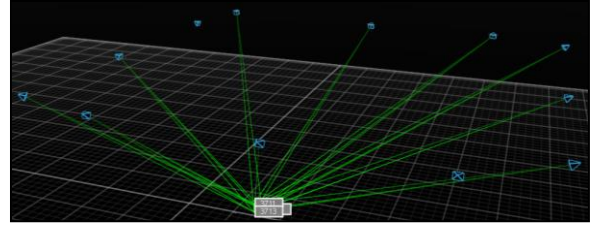**Figure 12: Leak Test (left) and Optitrack Camera (right)**

Figure 13: Optitrack Camera Array

The left image of Figure 12 is one of the ABVs at the leak check and pneumatic systems phase done to ensure that there were no air leaks. The right image of Figure 12 shows one of the Optitrack cameras used to track assigned objects (see Figure 12). After initial calibration and 3-dimensional mapping, rigid body objects are defined using Optitrack markers as (see Figure 13). The local body frame of the vehicle shown in Figure 14. The Optitrack system, once set up, is able to track an object as a rigid body, where the [X, Y, Z] are with respect to the global relative frame, and the [θ, ψ, φ] angles are with respect to the global coordinate axis frame.

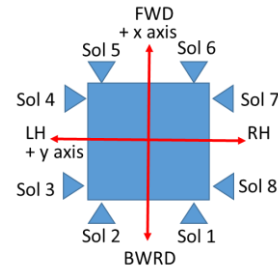**Figure 14: Local Body Frame of the Air-Bearing Vehicle**

5. RESULTS
5.1. Open Loop Control: Translation Test
5.1.1. Translation Description of Solenoid Firing

The first series of tests performed was to calculate the force exerted from the solenoid thrusters during an open-loop maneuver as well as the associated error from the measurements recorded. Each air-bearing vehicle has eight solenoid thrusters located around its body (see Figure 15). In order to perform a linear translation maneuver in the +x-axis direction and measure the exerted force on the vehicle. Solenoids 1 and 2 were commanded open with the other solenoids kept in the off position.
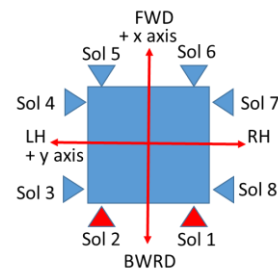

Figure 15: Solenoids turned on for Translation
5.1.2. Air-Bearing Translation Example

The time stamped images of the air-bearing vehicle displayed below (see Figure 16) show the translation command given versus

31st Florida Conference on Recent Advances in Robotics, May 10-11, 2018, University of Central Florida, Orlando, Florida

120

the distance travelled with time. Possible sources of error for the linear translation experiment include:

1) The solenoids on the vehicle may have been misaligned and not parallel to the x-axis on the body frame
2) The vehicle may not have been exactly level leading to a mass bias on one side of the vehicle versus the other
3) The amount of thrust produced by each thruster may have not been identical.

Figure 16 shows the time-lapse progression of the vehicle as it moves from one side of the air-bearing table to other side from the start to end of a particular run of the experiment.
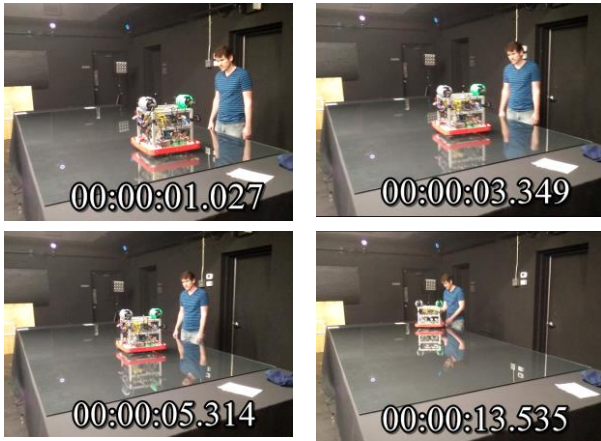

Figure 16: Translation Example

5.1.3. PWM Solenoid Command

A Pulse Width Modulated (PWM) signal of 100% duty cycle was sent to solenoids 1 and 2, with all other solenoids not engaged. The signal sent to the on-board CPU commanded Sol1 and Sol2 were commanded to be open from 2 seconds to 17 seconds (see Figure 17, Figure 18) with all other solenoids not activated.
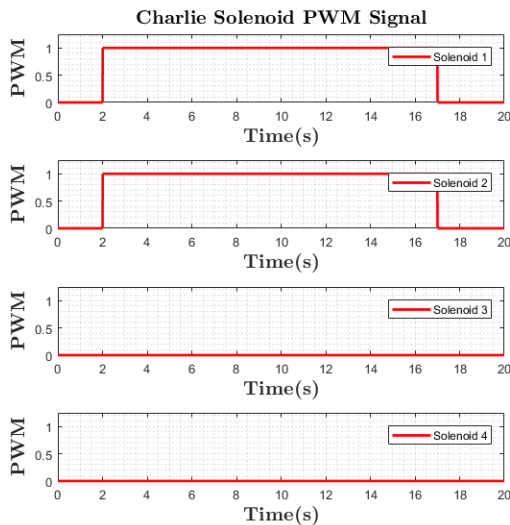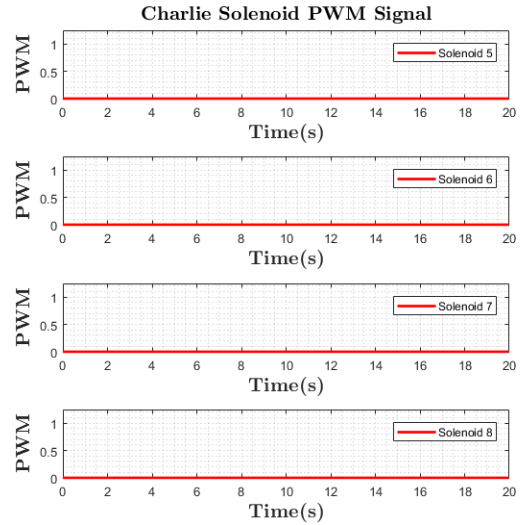

Figure 17: PWM signal Solenoid 1234

Figure 18: PWM signal Solenoid 5678

5.1.4. Translation Data Collection

Five experimental runs performed to compare the thrust provided versus time and command sent (see Figure 19). Charlie was released from the same relative position in the Global Coordinate Frame of the laboratory. As the vehicle travelled across the optical table, the position was logged for further analysis. The translation of the vehicles X, Y, and θ position shown in Figure 19. There appears to be a larger translation in the Y direction with a relatively small amount of drift in the X direction, and θ heading.
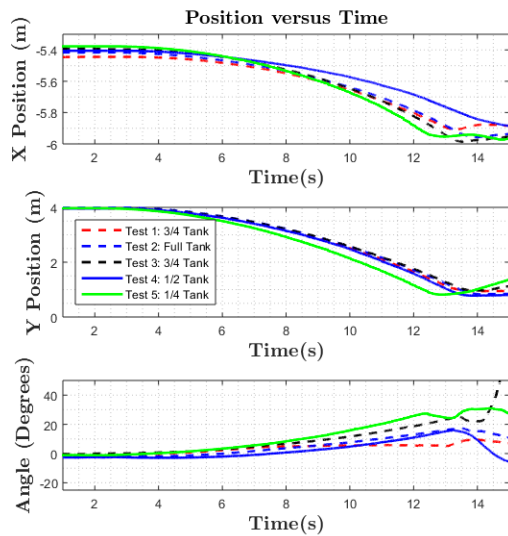

Figure 19: Optitrack Position Tracking of Test Vehicle

31st Florida Conference on Recent Advances in Robotics, May 10-11, 2018, University of Central Florida, Orlando, Florida
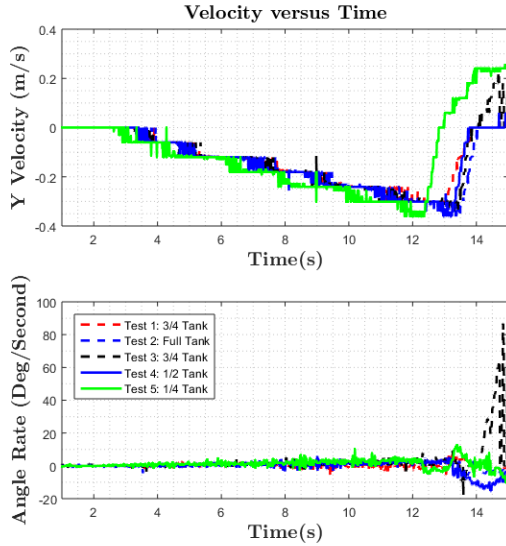
121

Figure 20: Optitrack Velocity Tracking of Test Vehicle

Figure 20 shows the Optitrack $\dot{Y}, \dot{\theta}$ velocity tracking data for the air-bearing test vehicle. The vehicle is caught at the end of the table is shown when $\dot{Y}$ velocity changes direction at the 12 second mark. During normal operation, AVB is not expected to move at a very fast rate (>5 m/s) across the glass plate surface. Therefore, the current position and filtered velocity data of the rigid body can be used in the future development of a closed loop controller within Matlab-Simulink.

5.1.5. Example data collected from Test 1

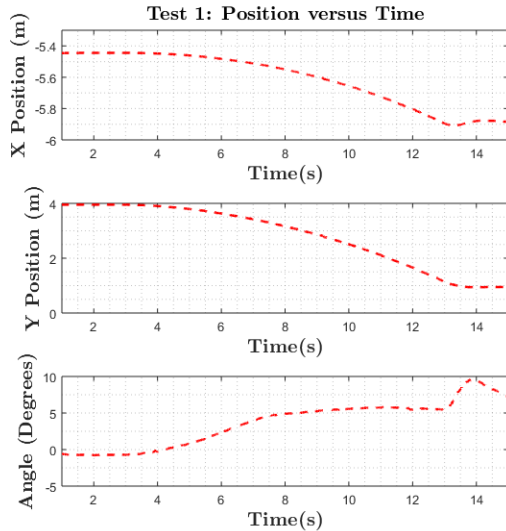This section discusses example data collected during a single experiment run

Figure 21: Optitrack Position Tracking Test 1

Figure 21 shows the change in X, Y, and angle θ of the vehicle as it was released from its start position and the linear translation maneuver was performed.
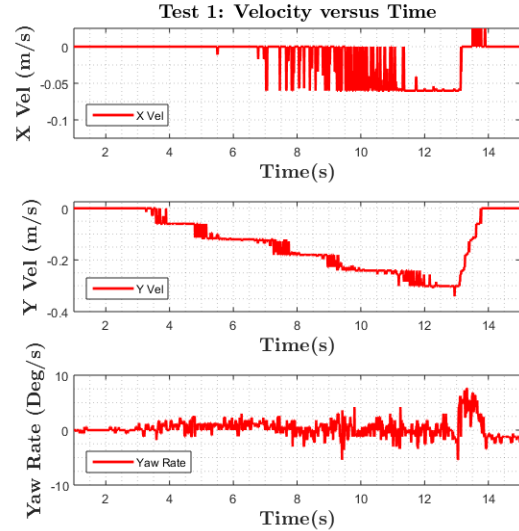

Figure 22: Optitrack Velocity Tracking Test 1

Figure 22 shows the rates of change $\dot{X}, \dot{Y}, \dot{\theta}$ of the vehicle. The point of capture can be seen where the vehicle is stopped, approximately at 12 seconds where the $\dot{Y}$ rate changes direction, to prevent the vehicle from falling off the air-bearing table.

5.1.6. Calculations to determine average force exerted by each thruster during translation

To perform calculations to find the approximate force from the thrusters on the air-bearing vehicle, the boundary conditions outlined in

Table *1* apply, with the mass and time measurements in Table 2. The initial velocity of the ABV is zero with the friction forces from the glass surface considered negligible. Error calculations done using Root Mean Square (RMS) approach.

Table 1: Boundary conditions for calculations

$Velocity_{initial}$	$U_i = 0 \; m/s$
$Time_{initial}$	$T_i = 2.0 \; seconds$
$Time_{final}$	$T_f = 10.0 \; seconds$
$Time_{difference}$	$\Delta T = 8.0 \; seconds$
Friction Effects	Considered Negligible

Table 2: Mass and Time Measurements

M_A = mass Charlie with no tanks	12.050 kg ± 0.050 kg
M_B = mass of 1 tank full	1.447 kg ± 0.001 kg
M_C = mass of 1 tank empty :	1.364 kg ± 0.001 kg
$M_\Delta = M_B - M_C$ (Mass difference of full versus empty.)	0.083 kg ± 0.001 kg
Ratio of tank$_1$, tank$_2$ filled	R_1, R_2
Measurement error in time, $\frac{\partial \Delta T}{\partial \varepsilon}$	$\pm 0.005 \; seconds$
Distance error in the x-direction and y-direction.	$\frac{\partial \Delta x}{\partial \varepsilon}, \frac{\partial \Delta y}{\partial \varepsilon} = \pm 0.5 mm$

31st Florida Conference on Recent Advances in Robotics, May 10-11, 2018, University of Central Florida, Orlando, Florida

122

Calculation for mass of the air-bearing vehicle M_{tot}, was defined as the mass of the tank changes based on the fuel consumed.

$$M_{tot} = M_A + 2M_C + (R_1 + R_2)M_\Delta \qquad (1)$$

The mass measurement error was defined:

$$\frac{\partial M_{tot}}{\partial \varepsilon} = \sqrt{\left(\frac{\partial M_{tot}}{\partial M_A}\frac{\partial M_A}{\partial \varepsilon}\right)^2 + \left(\frac{\partial M_{tot}}{\partial M_C}\frac{\partial M_C}{\partial \varepsilon}\right)^2 + \left(\frac{\partial M_{tot}}{\partial M_\Delta}\frac{\partial M_\Delta}{\partial \varepsilon}\right)^2} \qquad (2)$$

When performing the series of experiments, the observation was that one test consumed approximately ¼ of the total air capacity of the on board air-tanks, an illustration shown (see Figure 23). One full tank of air had a pressure of 2600 psi. There are two air tanks located on each air-bearing vehicle. An approach to consider is that the mass of the air tanks would vary with time as the propellant was consumed to provide thrust. However to get an approximate of the force provided by the thrusters, the initial mass at the start of each test was considered.
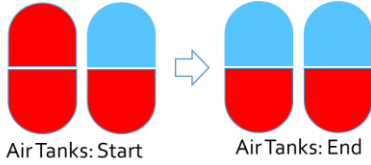

Figure 23: Illustration for Air Tank capacity.

The distance travelled for the air-bearing vehicle, ΔS, with the error in x-direction $\frac{\partial \Delta S}{\partial x}$, and y-direction, $\frac{\partial \Delta S}{\partial y}$:

$$\Delta S = \sqrt{\left(x_f - x_i\right)^2 + \left(y_f - y_i\right)^2} = \sqrt{(\Delta x)^2 + (\Delta y)^2} \qquad (3)$$

With the error in x and y distance expressed respectively as:

$$\frac{\partial \Delta S}{\partial x} = \frac{1}{2}(\Delta x^2 + \Delta y^2)^{-\frac{1}{2}}(2\Delta x) \qquad (4)$$

$$\frac{\partial \Delta S}{\partial y} = \frac{1}{2}(\Delta x^2 + \Delta y^2)^{-\frac{1}{2}}(2\Delta y) \qquad (5)$$

The full expression for the error in displacement is expressed as:

$$\frac{\partial \Delta S}{\partial \varepsilon} = \sqrt{\left(\frac{\partial \Delta S}{\partial \Delta x}\frac{\partial \Delta x}{\partial \varepsilon}\right)^2 + \left(\frac{\partial \Delta S}{\partial \Delta y}\frac{\partial \Delta y}{\partial \varepsilon}\right)^2} \qquad (6)$$

Using the kinematic motion equation:

$$\Delta S = U_i \Delta T + \frac{1}{2}a\Delta T^2$$

After rearranging the acceleration of the vehicle, a, is found:

$$a = \frac{2 * \Delta S}{\Delta T^2}$$

With the error in acceleration of the vehicle:

$$\frac{\partial a}{\partial \varepsilon} = \sqrt{\left(\frac{\partial a}{\partial \Delta S}\frac{\partial \Delta S}{\partial \varepsilon}\right)^2 + \left(\frac{\partial a}{\partial \Delta T}\frac{\partial \Delta T}{\partial \varepsilon}\right)^2}$$
$$= \sqrt{\left(\frac{2}{\Delta T^2}\frac{\partial \Delta S}{\partial \varepsilon}\right)^2 + \left(\frac{-4\Delta S}{\Delta T^3}\frac{\partial \Delta T}{\partial \varepsilon}\right)^2} \qquad (7)$$

With the equation for Force and Force measurement error defined:

$$F = M_{tot}a,$$

$$\frac{\partial F}{\partial \varepsilon} = \sqrt{\left(\frac{\partial F}{\partial M_{tot}}\frac{\partial M_{tot}}{\partial \varepsilon}\right)^2 + \left(\frac{\partial F}{\partial a}\frac{\partial a}{\partial \varepsilon}\right)^2}$$
$$= \sqrt{\left(a\frac{\partial M_{tot}}{\partial \varepsilon}\right)^2 + \left(M_{tot}\frac{\partial a}{\partial \varepsilon}\right)^2} \qquad (8)$$

The amount of air in the tank with the initial and final position listed in

Table 3. The calculated acceleration and mass approximations listed in Table 4. The calculated force exerted by both solenoids as well as the force exerted by one thruster are shown in Table 5.

Table 3: Test Condition, Initial and Final Recorded Position

Test	Air in the tanks at start	$[X \quad Y]_{initial}$ (m)	$[X \quad Y]_{final}$ (m)
1	$\frac{3}{4}$ tanks full	[-5.444 3.953]	[-5.656 2.506]
2	$\frac{4}{4}$ tanks full	[-5.416 3.988]	[-5.638 2.562]
3	$\frac{3}{4}$ tanks full	[-5.393 3.958]	[-5.645 2.581]
4	$\frac{1}{2}$ tanks full	[-5.405 3.957]	[-5.573 2.484]
5	$\frac{1}{4}$ tanks full	[-5.377 3.968]	[-5.671 2.14]

Table 4: Calculated Acceleration and Mass Approximation

Test	$[\ddot{X} \quad \ddot{Y}]$ (m/s^2)	Mass Approximation.
1	[-0.0066 -0.0452]	14.903 kg $\pm$ 0.0501kg
2	[-0.0069 -0.0446]	14.944 kg $\pm$ 0.0501kg
3	[-0.0079 -0.0430]	14.903 kg $\pm$ 0.0501kg
4	[-0.0053 -0.0460]	14.861 kg $\pm$ 0.0500kg
5	[-0.0092 -0.0571]	14.820 kg $\pm$ 0.0500kg

Table 5: Calculated Force Exerted by Solenoid Thrust

Test	$Force_{12}$ Force exerted by both thrusters	$Force_1$ Force exerted by one thruster
1	0.6811 N $\pm$ 0.0025N	0.3405 N $\pm$ 0.0025N
2	0.674 N $\pm$ 0.0024N	0.3370 N $\pm$ 0.0024N
3	0.6519 N $\pm$ 0.0017N	0.3260 N $\pm$ 0.0017N
4	0.6885 N $\pm$ 0.0025N	0.3443 N $\pm$ 0.0025N
5	0.8574 N $\pm$ 0.0031N	0.4287 N $\pm$ 0.0031N

From Table 5, the average force exerted by each of the solenoids on the ABV during the linear translation maneuver can be denoted using the following equation expression:

$$Avg\, F_1 = \frac{\left(\sum_{i=1}^{n=5} F_1(i)\right)}{n} \pm \max\frac{\partial F_1(i)}{\partial \varepsilon}error \qquad (9)$$

$$Avg\, F_1 = 0.3553\, N \pm 0.0031\, N$$

31st Florida Conference on Recent Advances in Robotics, May 10-11, 2018, University of Central Florida, Orlando, Florida

123

5.2. Rotation Test

5.2.1. Rotation Description of Thruster Firing

An open loop command for counter clockwise rotation was performed as a validation experiment to demonstrate that rotation is possible by using solenoids 1,3,5,7 in conjunction with each other. An illustration of which solenoids were commanded to activate can be seen Figure 24.
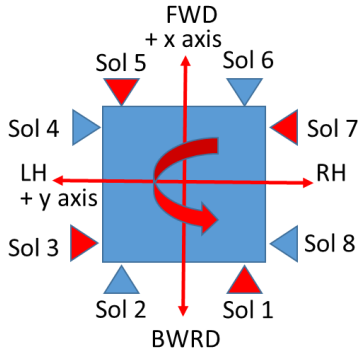

Figure 24: Illustration of Solenoids Turned on for Rotation

The time stamped images obtained from a video recording show the vehicle perform a counter clockwise rotation sequence that was commanded (see Figure 25).

Figure 25: Rotation Command Example

5.2.2. PWM Solenoid Command

The rotation experiment was performed using a PWM duty cycle signal of 80% (see Figure 26 and Figure 27). Where Solenoid

Thrusters: Sol1, Sol3, Sol5, Sol7 were commanded to pulse with Sol2, Sol4, Sol6, Sol8 not activated.
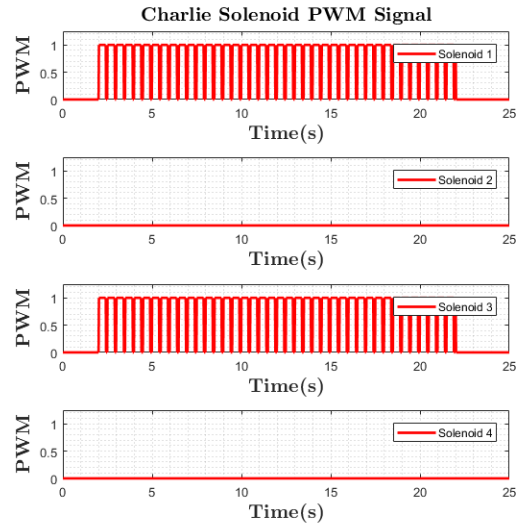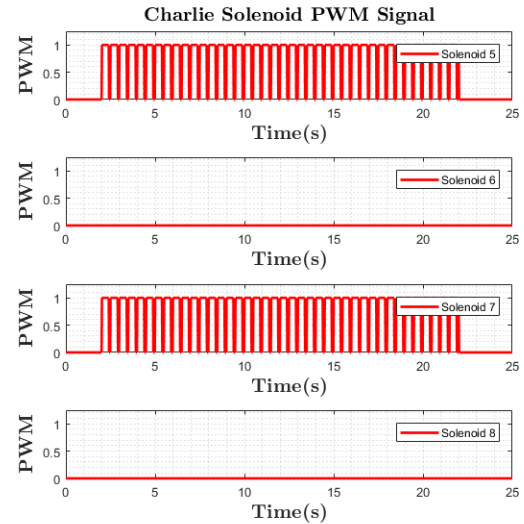

Figure 26: PWM Signal Solenoid 1-2-3-4

Figure 27: PWM Signal Solenoid 5-6-7-8

5.2.3. Data Collected from Rotation Experiment

The Optitrack system recorded the translation and rotation information of the air-bearing vehicle as shown in the below figure (see Figure 28). The data shows the rotation of the vehicle being tracked by Optitrack in the angle θ, as well as the global position X and Y. There does appear to be some noise in the signal recorded by Optitrack, this is shown in the fluctuation of the angle, θ, data.
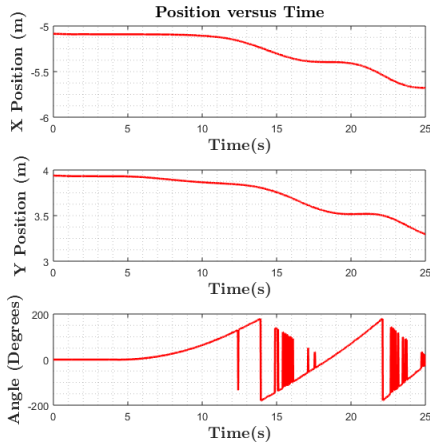
31st Florida Conference on Recent Advances in Robotics, May 10-11, 2018, University of Central Florida, Orlando, Florida

124

Figure 28: Rotation Position Tracking

6. CONCLUSION

Covered is the design, fabrication, and communication relay created for the ABVs. The first series of experiments included open loop command to perform linear translation and a rotation experiments. Calculations were made to gain an estimation for the thrust exerted from each solenoid. In conclusion, the main objectives of preliminary testing were met; however, future work includes the creation of a closed loop controller in order to perform trajectory and position control in 3-DOF. With the additional testing of both the chaser and target air-bearing vehicles together in order to achieve rendezvous and docking.

The model and theory equations are extendable to the 3D motions. However, to have the capability of orbital 6-DOF motion would require a re-design and following a similar path to the SPHERES program for MIT that performs testing on the ISS station or parabolic flight experiments. While possible, undertaking such a task would present its own set of technical and logistic complexities.

7. ACKNOWLEDGEMENTS

Acknowledgements include Stuart LoPresti with assistance in the fabrication, assembly, and testing process of the air-bearing vehicle. Kendrick Buchala and Branden Blackwell for assistance with experimental testing and vehicle tracking. As well as assistance provided by the Florida Tech Makerspace, Machine Shop, and MAE faculty.

8. REFERENCES

[1] F Aghili. 2008. Optimal control for robotic capturing and passivation of a tumbling satellite with unknown dynamics. *AIAA Guid. Navig. Control Conf.* August (2008). Retrieved from http://arc.aiaa.org/doi/pdf/10.2514/6.2008-7274

[2] Farhad Aghili and Kourosh Parsa. 2008. An adaptive vision system for guidance of a robotic manipulator to capture a tumbling satellite with unknown dynamics. *2008 IEEE/RSJ Int. Conf. Intell. Robot. Syst. IROS* (2008), 3064–3071. DOI:https://doi.org/10.1109/IROS.2008.4650758

[3] Angel Flores-Abad and Ou Ma. 2012. Control of a space robot for minimal attitude disturbance to the base satellite for capturing a tumbling satellite. *SPIE Defense,*

Secur. Sens. 8385, (2012), 83850J–83850J–12. DOI:https://doi.org/10.1117/12.918523

[4] Marshall H Kaplan and D Ph. 2009. Survey of Space Debris Reduction Methods. September (2009), 1–11.

[5] Shuichi Matsumoto, Steven Dubowsky, Stephen Jacobsen, and Yoshiaki Ohkami. 2003. Fly-By Approach and Guidance for Uncontrolled Rotating Satelite Capture. August (2003), 5745.

[6] Shin-Ichiro Nishida, Satomi Kawamoto, Yasushi Okawa, Fuyuto Terui, and Shoji Kitamura. 2009. Space debris removal system using a small satellite. *Acta Astronaut.* 65, (2009), 95–102. DOI:https://doi.org/10.1016/j.actaastro.2009.01.041

[7] Shin Ichiro Nishida and Satomi Kawamoto. 2011. Strategy for capturing of a tumbling space debris. *Acta Astronaut.* 68, 1–2 (2011), 113–120. DOI:https://doi.org/10.1016/j.actaastro.2010.06.045

[8] Carmen Pardini and Luciano Anselmo. 2014. Acta Astronautica Review of past on-orbit collisions among cataloged objects and examination of the catastrophic fragmentation concept $. *Acta Astronaut.* 100, (2014), 30–39. DOI:https://doi.org/10.1016/j.actaastro.2014.03.013

[9] Ary Pizarro-Chong and Arun K. Misra. 2008. Dynamics of multi-tethered satellite formations containing a parent body. *Acta Astronaut.* 63, (2008), 1188–1202. DOI:https://doi.org/10.1016/j.actaastro.2008.06.021

[10] Richard Rembala, Frank Teti, and Patrice Couzin. 2012. Operations concept for the robotic capture of large orbital debris. *Adv. Astronaut. Sci.* 144, (2012), 111–120.

[11] Marco Sabatini, Giovanni B Palmerini, and Paolo Gasbarri. 2015. Acta Astronautica A testbed for visual based navigation and control during space rendezvous operations $. *Acta Astronaut.* 117, (2015), 184–196. DOI:https://doi.org/10.1016/j.actaastro.2015.07.026

[12] Jana L Schwartz and Christopher D Hall. 2003. Historical Review of Air-Bearing Spacecraft Simulators Introduction. 26, 4 (2003). DOI:https://doi.org/10.2514/2.5085

[13] G. Tommei, a. Milani, and a. Rossi. 2007. Orbit determination of space debris: Admissible regions. *Celest. Mech. Dyn. Astron.* 97, (2007), 289–304. DOI:https://doi.org/10.1007/s10569-007-9065-x

[14] Wenfu Xu, Bin Liang, and Yangsheng Xu. 2011. Acta Astronautica Survey of modeling , planning , and ground verification of space robotic systems. *Acta Astronaut.* 68, 11–12 (2011), 1629–1649. DOI:https://doi.org/10.1016/j.actaastro.2010.12.004

[15] leo640.jpg (JPEG Image, 640×640 pixels). Retrieved April 12, 2018 from https://www.orbitaldebris.jsc.nasa.gov/images/beehives/leo640.jpg

[16] geo640.jpg (JPEG Image, 640×512 pixels). Retrieved April 12, 2018 from https://www.orbitaldebris.jsc.nasa.gov/images/beehives/geo640.jpg

[17] OptiTrack - Motion Capture Systems. Retrieved April 11, 2018 from https://optitrack.com/

[18] OptiTrack - Prime 17W - Wide angle coverage for large volumes in smaller spaces. Retrieved April 11, 2018 from https://optitrack.com/products/prime-17w/

31st Florida Conference on Recent Advances in Robotics, May 10-11, 2018, University of Central Florida, Orlando, Florida

125